Thermochemical and electrochemical investigations of $Li(Ni,Mn,Co)O_2$ (NMC) as positive electrode material for lithium-ion batteries

zur Erlangung des akademischen Grades eines

Doktors der Ingenieurwissenschaften (Dr. -Ing.)

von der KIT-Fakultät für Maschinenbau des
Karlsruher Instituts für Technologie (KIT)

genehmigte

Dissertation

von

M.Sc. Maryam Masoumi

Tag der mündlichen Prüfung: 19. Dezember 2019
Hauptreferent: Prof. Dr. Hans Jürgen Seifert
Korreferent: Prof. Dr. Torsten Markus

Abstract

The worldwide demand for high energy and high power energy storage devices has been growing fast in the last decades. As a response to the existing demand, rechargeable lithium ion batteries have gained great attention. Lithium ion batteries found a wide range of applications in electronic devices, portable tools, hybrid and fully electric vehicles and large-scale grid storage facilities. Lithium mixed transition metal oxides, specifically $LiNi_xMn_yCo_zO_2$ ($x + y + z = 1$) compounds, often known as NMC or NCM materials, are one of the most important and widely investigated layered structured active compounds for lithium-ion battery cathodes.

The present dissertation aims at investigating the relationship between the chemical composition and the thermodynamic stability as well as the electrochemical performance of this family of oxides. For this purpose, two compositional series of NMC powder samples namely (i) manganese and nickel equimolar $LiNi_xMn_xCo_{1-2x}O_2$ (x = 0, 0.167, 0.333, 0.4 and 0.5) and (ii) Ni-rich $LiNi_{0.8-y}Mn_yCo_{0.2}O_2$ (y = 0, 0.1, 0.2, 0.3 and 0.4) are prepared by sol-gel method and high temperature calcination in air.

The synthesized samples are chemically characterized using inductively coupled plasma-optical emission spectroscopy (ICP-OES), carrier gas hot extraction (CGHE) and carbon analyzer. The average oxidation state of transition metals in each composition is determined by redox titration method. Based on the results of the chemical analysis, the formula of the prepared samples are determined and it is shown that the composition of all compounds are close to the nominal values. The powder X-ray diffraction (PXRD) patterns of the synthesized samples are obtained and analyzed by Rietveld refinement method, considering a rhombohedral layered α-$NaFeO_2$-type structural model ($R\bar{3}m$). The lattice parameters are determined and shown to be in a very good agreement with the literature data corresponding to the same compositions.

In addition, the optimum calcination temperature for $LiNi_{0.8-y}Mn_yCo_{0.2}O_2$ samples with y = 0 and 0.1 are determined.

The thermal stabilities of $LiNi_{0.8-y}Mn_yCo_{0.2}O_2$ samples for y = 0, 0.1, 0.2, 0.3 and 0.4 are investigated using simultaneous differential thermal analysis - thermal gravimetry (DTA / TG) under argon atmosphere. It is shown that by increasing Ni content in $LiNi_{0.8-y}Mn_yCo_{0.2}O_2$, the onset temperatures of decomposition reaction decreases and the mass loss resulted from the decomposition of the sample increases, indicating declined thermal stabilities. The phases emerged from the decomposition are investigated by means of PXRD.

The enthalpies of formation of all synthesized samples are determined using high temperature oxide melt drop solution calorimetry in a sodium molybdate solvent at 701 °C under argon atmosphere. The results are interpolated to the larger composition range in $LiNiO_2$-$LiCoO_2$-$LiNi_{0.5}Mn_{0.5}O_2$ system. A ternary contour, which demonstrates the standard enthalpy of formation from elements for the compositions to lie between the $LiNiO_2$, $LiCoO_2$ and $LiNi_{0.5}Mn_{0.5}O_2$ end members, is plotted to compare their relative thermodynamic stabilities. The results show a near-linear relationship between the standard enthalpy of formation value and the NMC composition. Moreover the direction of composition variation which leads to the maximum changes in the enthalpy values was determined and $LiNi_{0.5}Mn_{0.5}O_2$ was found as the most energetically stable compounds in this region.

To investigate the effect of chemical composition on the stability and cyclability upon electrochemical lithium intercalation, $LiNi_{0.8-y}Mn_yCo_{0.2}O_2$ compounds as well as $LiNi_{0.5}Mn_{0.5}O_2$ were subject of different electrochemical measurements. The electrochemical investigations include galvanostatic coulometry with potential limitations (GCPL) in the potential range of 3-4.2 V and 3-4.5 V, galvanostatic intermittent titration technique (GITT) in the voltage range of 3.0 V and 4.5 V, cyclic voltammetry (CV) over the potential range of 3.0 and 4.5 V and rate capability and cyclability tests over the potential range of 3.0 and 4.5 V at 25 °C.

Kurzfassung

Die weltweite Marktnachfrage nach energieintensiven und leistungsstarken Energiespeichern ist sehr stark in den letzten Jahrzehnten gestiegen. Als Folge der bestehenden Nachfrage haben wiederaufladbare Lithium-Ionen-Batterien große Aufmerksamkeit auf sich gezogen. Lithium-Ionen-Batterien fanden ein breites Anwendungsfeld in elektronischen Geräten, mobilen Werkzeugen, Hybrid- und Vollelektrofahrzeugen sowie in großen Netzspeichern. Lithium-Mischkristalloxide, insbesondere $LiNi_xMn_yCo_zO_2$ ($x + y + z = 1$) Verbindungen, auch bekannt als NMC- oder NCM-Materialien, sind eine der wichtigsten und am breitesten erforschten schichtstrukturierten aktiven Verbindungsklassen für Lithium-Ionen-Batteriekathoden.

Die vorliegende Dissertation zielt darauf ab, den Zusammenhang zwischen der chemischen Zusammensetzung und der thermodynamischen Stabilität sowie der elektrochemischen Leistung dieser Oxidfamilie zu untersuchen. Dazu wurden zwei Zusammensetzungsserien von NMC-Pulverproben, nämlich: 1) Mangan und Nickel äquimolares $LiNi_xMn_xCo_{1-2x}O_2$ (x = 0, 0,167, 0,333, 0,4 und 0,5) und 2) Ni-Reiches $LiNi_{0,8-y}Mn_yCo_{0,2}O_2$ (y = 0, 0,1, 0,2, 0,3 und 0,4) durch die Sol-Gel-Methode und Hochtemperaturkalzinierung unter Luft hergestellt.

Die synthetisierten Proben wurden chemisch mit induktiv gekoppelte plasma-optische Emissionsspektroskopie (ICP-OES), Trägergas-Heißextraktion (CGHE) und Kohlenstoffanalysator charakterisiert. Die durchschnittliche Oxidationszahl der Übergangsmetalle in jeder Zusammensetzung wurde durch die Redox-Titrationsmethode bestimmt. Ausgehend von den Ergebnissen der chemischen Analyse wurde die Formel der vorbereiteten Proben bestimmt und gezeigt, dass die Zusammensetzungen aller Verbindungen annähernd den Nominalwerten entsprachen. Die Pulver-Röntgendiffraktogramme (PXRD) der synthetisierten Proben wurden erhalten und mit der Rietveld-Verfeinerungsmethode unter Berücksichtigung eines rhomboedrisch geschichteten Strukturmodells vom Typ α-$NaFeO_2$ ($R\bar{3}m$) analysiert. Die

Gitterparameter wurden ermittelt und zeigten eine sehr gute Übereinstimmung mit den Literaturdaten, die den gleichen Zusammensetzungen entsprechen. Zusätzlich wurde die optimale Kalzinierungstemperatur für $LiNi_{0,8-y}Mn_yCo_{0,2}O_2$-Proben mit y = 0 und 0,1 festgelegt.

Die thermischen Stabilitäten von $LiNi_{0,8-y}Mn_yCo_{0,2}O_2$-Proben für y = 0, 0,1, 0,2, 0,3 und 0,4 wurden mittels simultaner Differenzthermoanalyse - Thermogravimetrie (DTA / TG) unter Argonatmosphäre untersucht. Es wurde gezeigt, dass durch die Erhöhung des Ni-Gehalts in $LiNi_{0,8-y}Mn_yCo_{0,2}O_2$ die Anfangstemperaturen der Zersetzungsreaktion abnehmen und der Gewichtsverlust durch die Zersetzung der Probe zunimmt, was auf verminderte thermische Stabilität hinweist. Die aus der Zersetzung hervorgegangenen Phasen werden mit Hilfe der PXRD untersucht.

Die Bildungsenthalpien aller synthetisierten Proben wurden mittels Hochtemperaturoxid-Einwurflösungskalorimetrie in einem Natriummolybdat-Lösungsmittel bei 701 °C unter Argonatmosphäre bestimmt. Die Ergebnisse wurden auf den größeren Zusammensetzungsbereich im $LiNiO_2$-$LiCoO_2$-$LiNi_{0.5}Mn_{0.5}O_2$-System interpoliert. Ein ternärer Konturplot wurde aufgetragen, welcher die Standardbildungsenthalpie aus Elementen für die Zusammensetzungen zwischen den Endgliedern $LiNiO_2$, $LiCoO_2$ und $LiNi_{0.5}Mn_{0.5}O_2$ zeigt, um ihre relativen thermodynamischen Stabilitäten zu vergleichen. Die Ergebnisse zeigen eine nahezu lineare Beziehung zwischen den Werten der Standardbildungsenthalpie und den NMC-Zusammensetzungen. Darüber hinaus wurde die Richtung der Zusammensetzungsvariation bestimmt, die zu den maximalen Veränderungen der Enthalpiewerte führt, und $LiNi_{0.5}Mn_{0.5}O_2$ wurde als die energiestabilste Verbindung in dieser Region gefunden.

Um den Einfluss der chemischen Zusammensetzung auf die Stabilität und Zyklabilität bei der elektrochemischen Lithium-Interkalation zu untersuchen, wurden $LiNi_{0,8-y}Mn_yCo_{0,2}O_2$-Verbindungen sowie $LiNi_{0.5}Mn_{0.5}O_2$ verschiedenen elektrochemischen Messungen unterzogen. Zu den elektrochemischen Untersuchungen gehörten die galvanostatische Coulometrie mit Potentialbegrenzungen (GCPL) im Potentialbereich von 3-4,2 V und 3-4,5 V, die galvanostatische intermittierende Titrationstechnik

(GITT) im Spannungsbereich von 3,0 V und 4,5 V, die zyklische Voltammetrie (CV) im Potentialbereich von 3,0 und 4,5 V sowie Leistungs- und Zyklenfestigkeitstests im Potentialbereich von 3,0 und 4,5 V bei 25 °C.

Acknowledgement

First, I would like to express my deepest gratitude to my supervisor Professor Dr. Hans J. Seifert for providing me with the opportunity to work on the present research topic under his supervision, and for his invaluable guidance, advice and support throughout my PhD study.

I would like to thank Prof. Dr. Torsten Markus for his willingness to accept the co-examination and for the many inspiring discussions during various workshops and conferences.

I appreciate all the past and present members of the Institute for Applied Materials–Applied Materials Physics (IAM-AWP) at Karlsruhe Institute of Technology for their support and help. It was a great pleasure to work with them. I would like to sincerely thank Dr. Thomas Bergfeldt for his enthusiastic guidance and many technical discussions. He and his group kindly supported me with the chemical analysis in the present work and helped me establish the redox titration set-up. I am grateful to Dr. Damian Cupid who introduced me to the world of drop solution calorimetry and made helpful suggestions and feedback on my thermodynamic experiments. I wish to thank Dr. Thomas Reichman who generously took time to advise me on PXRD measurements and Rietveld refinement. I am thankful to Dr. Weibin Zhang for sharing his insight on the present materials system. I would like also to thank Dr. Magnus Rohde, the head of thermodynamic and thermophysics group.

I am very thankful to Christoph Gebert, Alexandra Reif, Nils Uhlmann, Tatjana Kaiser, Tobias Weingärtner, Pirimze Khelashvili, Judith Jung, Ulrike Stegmaier und Koljia Erbes and other technical staff at IAM-AWP for all their help and assistance in the labs. I also thank undergraduate students who helped me with DTA-TG sample preparation.

I thank Wenjiao Zhang, Dr. Andreas Melcher and Dr. Yuantao Cui for the pleasant time as office mates.

I had the pleasure to work with some great people from IAM-ESS at KIT. I am grateful to Dr. Aiswarya Bhaskar for sharing her valuable experience on cell production and electrochemical testing. I would like to thank Dr. Raheleh Azmi for the XPS measurements and evaluation and Mr. Udo Geckle for SEM pictures of my samples.

I appreciate Dr. Keke Chang, Dr. Denis Music and Prof. Jochen M. Schneider from RWTH Aachen University, who did a great theoretical study in parallel to my experiments in the framework of a collaboration in WeNDeLIB project.

Financial support by the German Research Foundation (DFG) through the Priority Program 1473 WeNDeLIB (Materials with New Design for Improved Lithium Ion Batteries), subproject 3, “Design of an all solid state thin film lithium ion battery and their electrochemical-thermodynamic modeling and evaluation” for the second funding period is greatly acknowledged. My thank goes to all further WeNDeLIB doctoral candidates and members for the scientific exchange and the nice time during the numerous workshops.

Last but not least, I would like to express my gratitude to my family for all their love, patience and encouragement during my PhD time and all my study years. I thank all my friends who made my time at Karlsruhe enjoyable.

Finally, I would like to take the opportunity to thank all those who have ever helped and supported me before.

Karlsruhe, June 2019
Maryam Masoumi

Table of contents

List of publications

Journal publications

1. Masoumi, M., Cupid, D. M., Reichmann, T. L., Chang, K., Music, D., Schneider, J. M., Seifert, H. J. (2017). Enthalpies of formation of layered $LiNi_xMn_xCo_{1-2x}O_2$ ($0 \leq x \leq 0.5$) compounds as lithium ion battery cathode materials. *International Journal of Materials Research*, *108*(11), 869-878.

2. Azmi, R., Masoumi, M., Ehrenberg, H., Trouillet, V., Bruns, M. (2018), Surface analytical characterization of $LiNi_{0.8-y}Mn_yCo_{0.2}O_2$ ($0 \leq y \leq 0.4$) compounds for lithium ion battery electrodes, *Surface and Interface Analysis*, DOI: 10.1002/sia.6415.

Conference contributions

Oral Presentations:

1. Masoumi, M., Cupid, D.M., Seifert, H.J., Thermodynamic investigation of layer structured LiNixMnyCozO2 as lithium ion battery cathode materials, *EUROMAT2017*, 17-22.09.2017, Thessaloniki, Greece.

2. Masoumi, M., Cupid, D.M., Reichmann, T.L., Seifert, H.J., Thermochemistry of selected compositions in the $LiNiO_2$-$LiMnO_2$-$LiCoO_2$ system as promising lithium ion battery cathode materials, *Materials Science and Engineering (MSE)*, 27-29.09.2016, Darmstadt.

3. Masoumi, M., Cupid, D.M., Reichmann, T.L., Seifert, H.J., Enthalpies of formation of selected compositions in the $LiNiO_2$-$LiCoO_2$-$LiMnO_2$ system as promising lithium ion battery cathode materials, *Junior Euromat 2016*, 10-14.07.2016, Lausanne, Switzerland.

4. Masoumi, M., Cupid, D., Gotcu-Freis, P., Seifert, H. J., Thermal analysis of selected compositions in the $LiNiO_2$-$LiMnO_2$-$LiCoO_2$ system, *4th conference of the KIT Energy Center*, 20.05.2015, Karlsruhe.

5. Masoumi, M., Thermal analysis of selected compositions in the $LiNiO_2$-$LiMnO_2$-$LiCoO_2$ system, *29th Annual MSIT Meeting, International Seminar on Heterogeneous Multicomponent Equilibria*, 15-20.02.2015, Schloss Ringberg, Tegernsee.

6. Masoumi, M., Synthesis and phase stability of $LiMnO_2$, *Workshop im Schwerpunktprogramm 1473 der Deutschen Forschungsgemeinschaft*, 10-14.11.2014, Neunkirchen.

Poster Presentations:

1. Masoumi, M., Cupid, D.M., Reichmann, T.L., Seifert, H.J., Enthalpies of formation of layered $LiNi_xMn_xCo_{1-2x}O_2$ ($0<x\leq0.5$) compounds as promising Li-ion battery cathode materials, *IMLB 2016*, 19-24.06.2016, Chicago, USA.

2. Masoumi, M., Cupid, D.M., Reichmann, T.L., Gotcu-Freis, P., Seifert, H.J., Thermochemistry of selected compositions in the $LiNiO_2$-$LiMnO_2$-$LiCoO_2$ (NMC) system as positive electrode materials for Li-ion batteries, *EUROMAT2015*, 20-24.09.2015, Warsaw, Poland.

List of figures

List of tables

List of symbols and abbreviations

a_{Li}	Activity of lithium
A	Surface area of electrode
$\mathcal{A}$	Alkali element
AOS	Average oxidation state
BSE	Backscattered electrons
BCD	Battery Capacity Determination
C_C	Heat capacity of calorimeter cell
C-rate	Charge-discharge rate
CALPHAD	CALculation of PHAse Diagrams
CGHE	Carrier gas hot extraction
CV	Cyclic voltammetry
$\widetilde{D}$	Chemical diffusion coefficient
DMC	Dimethyl carbonate
DSC	Differential scanning calorimeter
DTA	Differential thermal analysis
dQ	First derivative of specific capacity
δ	Oxygen coefficient
$E^0(x)$	Equilibrium cell potential
$E_{(x)}$	Operating voltage (closed circiut voltage)
E^0	Average voltage
EC	Ethylene carbonate
ESB	Energy selective backscattered
EV	Electric vehicle
F	Faraday constant (96500 Coulombs·mole^{-1} = 26.8 Ah·mol^{-1})
FWHM	Full width at half maximum
FW	Formula weight of the sample
ϕ	Heat flow signal of calorimeter
GEFTA	Gesellschaft für thermische Analyse e.V (in German)
GCPL	Galvanostatic coulometry with potential limitations

GITT	Galvanostatic intermittent titration technique
HEV	Hybrid electric vehicle
HT	High temperature
I	Current
i	Current density
ICP-OES	Inductively coupled plasma-optical emission spectroscopy
ITS-90	The International Temperature Scale of 1990
IUPAC	International Union of Pure and Applied Chemistry
K	Calibration factor of the calorimeter
k	Coverage factor
λ	Thermal conductivity
LCO	$LiCoO_2$
LIB	Lithium-ion battery
LMO	$LiMnO_2$
LNO	$LiNiO_2$
M	3d transition metal
$\mathcal{M}$	Molar weight of the cathode materials
m-$LiMnO_2$	Monoclinic $LiMnO_2$
m_e	Weight of electrode disk
$\bar{m}_f$	Average weight of uncoated aluminum foil with the same diameter as electrode disc
m_a	Weight of active material
MTSE	Maximum Theoretical Specific Energy
μ_{Li}	Chemical potential of lithium
NIST	National Institute of Standards and Technology
NMC	$LiNi_xMn_yCo_{1-x-y}O_2$
NMP	N-methyl-2-pyrrolidinone
n	Sum of the moles of reactants of cell reaction
O-$LiMnO_2$	Orthorhombic $LiMnO_2$
OCV	Open circuit voltage
PHEV	Plug-in hybrid electric vehicle
PPMS	Physical Property Measurement System
PVDF	Poly(vinylidene fluoride)
PXRD	Powder X-ray diffraction
Q_{th}	Theoretical capacity

Q_p	Practical capacity
QOCV	Quasi open circuit voltage
q	Charge density or specific charge
RT	Redox titration
R	Universal gas constant (8.314 $J \cdot K^{-1} \cdot mole^{-1}$)
R_a	Mass fraction of the active material in cathode composite
R_{th}	Thermal resistance of the calorimeter block
s^2	Variance
SE	Secondary electrons
SEI	Solid electrolyte interface
SEM	Scanning electron microscopy
TEM	Transmission electron microscopy
TG	Thermogravimetry
TM	Transition metal
τ	Time of the pulse (in GITT measurements)
U	Expanded or overall uncertainty
$u(x_i)$	Standard uncertainty of x_i
u_c	Combined standard uncertainty
V	Voltage
V_1	Volume of $KMnO_4$ solution consumed by 20 ml of 0.05 N $Na_2C_2O_4$
V_2	Volume of $KMnO_4$ solution consumed by 20 ml of 0.05 N $Na_2C_2O_4$ in presence of a known weight of the sample
V_M	Molar volume
W	Energy density or specific energy
$\mathscr{w}$	Molecular weights of reactants of the cell reaction
XAS	X-ray absorption spectroscopic
XPS	X-ray photoelectron spectroscopy
XRD	X-ray diffraction
Z	Atomic number
z	Charge transfered by lithium in the electrolyte during the cell reaction
T	Absolute temperature
t	Time

ΔH_P	Enthalpy changes of calorimeter's cell
$\Delta G(x)$	Gibbs free energy change for the cell reaction
ΔS	Entropy changes

1 Basic concepts

1.1 Lithium-ion battery

In this section, first a brief summary on the history and development of lithium-ion battery is presented. Then the structure of the Li-ion cell and its components are described. Finally, positive electrode material as one of the most determining factors in the performance of the Li-ion cell is briefly reviewed.

1.1.1 History and development

Limited supply, uneven distribution, and unstable price of fossil fuels and the effect of CO_2 emissions from burning of fossil fuels on global warming, lead to a public interest in the production of electricity from renewable and clean energy sources. The transition to a sustainable energy economy requires not only generating clean energy but also an efficient energy storage [1–3]. A reliable utilization and distribution of intermittent electricity from renewable resources requires efficient, safe and low cost stationary power and energy storage options. In addition, in our highly mobile, energy-dependent society there is a growing demand for portable energy storage devices for applications such as computers, mobile phones, portable tools, as well as the emerging field of electric and hybrid electric vehicles (EVs and HEVs). Among various methods that are used for the storage of energy, electrochemical methods, that store and release electric energy through electrochemical reactions, generally termed as *batteries*, attracted the most attention. Battery technologies can be used for both energy and power applications.

Rechargeable lithium-ion batteries (LIBs) have emerged as the fastest-growing technology for electric energy storage [3] as they offer energy densities two to three times higher than their historical predecessors, lead acid and secondary alkaline (NiCd or Ni-metal-hybrid) batteries [4, 5]. In various other aspects,

this kind of lithium secondary battery show advantages over the conventional rechargeable systems. These advantages include high average output voltage, low self-discharge, no memory effect, excellent cycling behavior, high rate capability, high coulomb efficiency, wide possible working temperature range, easy measurement of the residual capacity, maintenance free and very few adverse effects on the environment [6]. The so-called Ragone chart depicting specific energy versus specific power (usually in logarithmic scale), as shown in Figure 1.1, is typically used to compare the performance of different types of battery [7].

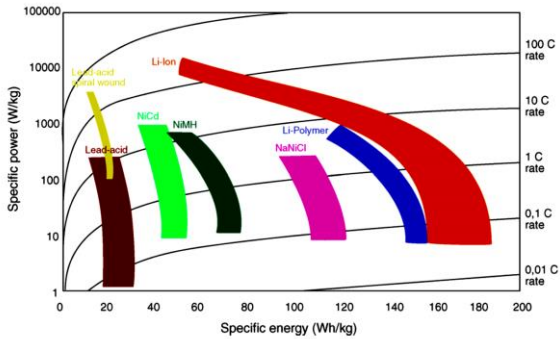

Figure 1.1: Ragone chart showing specific energy versus specific power for different types of battery [7].

The first commercial rechargeable (secondary) lithium battery reported by Exxon in 1975, had TiS_2 and LiAl as cathode and anode materials, respectively, and worked based on the reversible Li intercalation in Li_xTiS_2 [8]. These original cells were reported active with 2/3 of their capacity until 2014 [9], which is an evidence of intrinsic long life of lithium cells. However, the commercialization of rechargeable lithium batteries was not successful as the dendritic growth of lithium metal as the negative electrode resulted in serious safety problems, even in prototype scales [10]. One solution, which was proposed to overcome this problem, was the replacement of lithium anode (or its alloys) with a non-metallic compound capable of storing and exchanging

a large quantity of lithium ions. As in this system lithium ions rock between negative and positive electrode of a concentration cell, these cells have been termed as rocking-chair cell by M. Armand [11]. The feasibility of the rocking chair battery concept was investigated by Bonino et al. on small laboratory prototype cells with complicated electrode fabrication (original conference proceeding was not found) [10].

Although the concept of lithium-ion (shuttlecock) cell emerged in early 1980s by Goodenough and co-workers [12], it gained new attentions as an innovative secondary system about a decade later. The first commercially successful 4 V lithium-ion cell has been introduced in 1991 by Sony for portable electronic devices based on carbon as anode, a non-aqueous electrolyte, and lithium cobaltate ($LiCoO_2$) cathode [13]. As the lithium-ion concept worked very successfully, the next generation of lithium-based secondary batteries was developed based on this type of cell with intercalation compounds. Since then, for the past three decades, lithium-ion batteries became dominant for powering portable electronic devices.

Currently, LIB dominates the energy storage technology in consumer electronic market and is positioned as the energy storage device of choice for plug-in hybrid electric vehicles (PHEVs) and all-electric vehicles. Large-format cells and packs, which are used in transportation applications have energy capacities of 15–20 kWh for PHEVs and up to 85 kWh for all-electric vehicles [3].

These battery packs can also be incorporated into systems for grid applications. As an example, Li-ion systems prevail in the current setting for grid-scale electric energy storage in the United States [3].

Considering theoretical specific energy, researchers worldwide see high development potentials for new materials and cell chemistries such as Li/O_2 [14–16], Li/S [17, 18], Na-ion [19, 20], Mg-ion [21] and multi-electron phosphates [9, 22]. However, when it comes to analyzing the cost, volume and mass at the system-level, due to the requirements of the gaseous oxygen reactant, the best-case of nonaqueous lithium–oxygen batteries and the current lithium-based batteries using metal-oxide positive electrodes are found

comparable [23]. Therefore, advanced lithium-ion technology seems to be a moderate risk pathway to reach long-term automotive objectives. The competitive market demands the improvement in state-of-the-art Li-ion battery technology and optimization of energy density, power density, cycle life, thermal behavior, safety and costs for different applications. For instance, high energy is more important for electric vehicles, while hybrid vehicles foremostly need power. For portable electronics, where autonomy is essential, energy density measured in $Wh \cdot Kg^{-1}$ is primarily sought.

1.1.2 Lithium-ion cell; mechanisms and components

A lithium-ion cell is a galvanic cell that consists of two dissimilar electronic conductive electrodes, a reductant (anode) and an oxidant (cathode), separated by an ionic conductor electrolyte. The reversible chemical reaction responsible for the generation and storage of electricity, known as redox reaction, takes place at the interface of the electrodes and electrolyte. In galvanic cells, the redox reaction is divided in two half-cell electrochemical reactions: oxidation (release of electrons) at the anode and reduction (take in of electrons) at the cathode. Anode and cathode are conventionally defined based on their behavior during discharge. The electrolyte allows transfer of lithium ions between the electrodes but does not allow transport of any released electron, forcing them to pass an external electrical circuit outside of the cell through a current collector. When the cell is discharged, the output is an external current I at the voltage of V for a time of Δt [24]. By application of a charging I and V, the chemical cell reaction takes place in the reversed direction and a *cycle* is completed. When two or more of the galvanic cells are connected in series or parallel, depending on the required output voltage and capacity, a battery is assembled. Figure 1.2 shows a schematic picture of an electrochemical lithium-ion cell and its components.

In lithium-ion batteries, and generally in reversible electrochemical cells, the anode and cathode are switched depending on whether the cell is charging or discharging, because the half-cell reactions are reversed by the way the current is flowing. Hence, using the terms anode and cathode might be confusing as

they are consistent only with what happens during cell discharge. To avoid this confusion, it is preferred to label the electrodes as positive and negative, depending on their relative potential. However, as the convention is to refer the electrodes in terms of their behavior during discharge, in batteries the negative electrode is always called the anode and the positive electrode the cathode [6].

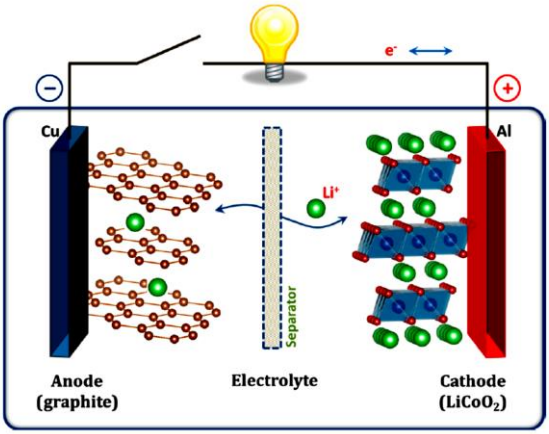

Figure 1.2: Schematic picture showing the main components of a lithium-ion cell [24].

There are different working concepts for lithium-ion batteries depending on the type of the overall cell reaction. The major types of reaction mechanisms in electrochemical cells are [6] (1) *formation* reaction, in which in one the electrodes a new phase is formed from its atomic constitutes (example of this type is the cell with lithium – antimony chemistry) (2) *conversion* reaction such as Cu_2O - Li system and (3) *insertion* or *intercalation* reaction which involves the insertion and extraction of guest species (lithium ions) into interstitial sites of the solid matrix of a host material without destructing the core structure. This mechanism is also referred as topotactic reaction. Intercalation based reactions provide the opportunity for the highest rates in solid electrodes because there is no need to build new structures on discharge and charge.

However, their capacity is restricted by the limitation of the host structure for holding lithium, as well as by the mass and volume of host material.

As mentioned in the previous section, the first lithium-ion battery from Sony was developed based on insertion mechanism and this type of electrochemical reaction is still the dominant system in the field. In the remaining part of this section, cathode materials with the intercalation mechanism are focused.

1.2 Electrochemical parameters of lithium-ion cells

There are different parameters used to describe and evaluate the performance of the cell and characterize the behavior of the electrode materials. The theoretical values of some of these parameters correspond to the equilibrium performance of the material. However, the practical values of these parameters vary from the maximum theoretical values, because of the presence of passive components and non-effective utilization of active components in the chemical reaction [6]. Theoretical parameters can be determined by the thermodynamics of the chemical reaction between the components in the electrodes whereas electrochemical techniques are used to evaluate the practical parameters and thereby the real performance of the cell. In the following, common terms frequently used in the evaluation of Li-ion cells, are described.

Cell potential is divided into the theoretical and the practical values. The equilibrium cell potential ($E^0(x)$) is the theoretical voltage of an electrochemical cell depending on the difference between the chemical potential of lithium in the anode and cathode material. This equilibrium potential is equal to the open circuit voltage (OCV), i.e. when no current is passing through the external circuit. The potential difference supplies the driving force for the transport of ions through the electrolyte, and electrons in the external circuit. The equilibrium cell potential is given by the Nernst equation [25, 26]:

$$E^0(x) = -\frac{1}{F}\cdot\left(\frac{\partial\Delta G(x)}{\partial x}\right)_{T,P} = -\frac{\mu_{Li}^{cathode}{}_{(x)} - \mu_{Li}^{anode}}{zF} = \frac{RT}{zF}\,ln\left(\frac{a_{Li}^{cathode}}{a_{Li}^{anode}}\right) \quad (1.1)$$

where $\Delta G(x)$ is the Gibbs free energy change for the cell reaction:

$$\square MeO_2 + xLi \rightarrow Li_xMeO_2 \quad (1.2)$$

and $E^0(x)$ is the open circuit voltage at *x* state of charge (lithium content in cathode). μ_{Li} and a_{Li} are the chemical potential and the activity of lithium, respectively in relevant electrode. *F* is the Faraday constant (96500 Coulombs·mole^{-1} = 26.8 Ah·mol^{-1}), *R* is the universal gas constant (8.314 J·K^{-1}·mole^{-1}) and z is the charge (in moles of electrons) transfered by lithium in the electrolyte during the cell reaction. For lithium intercalation in most nonelectronically conducting electrolytes z = 1 [25]. For a half-cell configuration with pure metallic lithium as anode material, $a_{Li}^{anode} = 1$.

The operating voltage ($E_{(x)}$) or the closed circiut voltage is the output voltage at which the battery operates during charge and discharge in its actual use. This voltage is a function of the state of charge. In most cases, it varies from the equilibrium voltage due to various kinetic factors.

Charge capacity is the amount of charge that a battery contains, often measured in mAh or Ah. As in the case of voltage, the maximum or the theoretical charge capacity is a thermodynamic quantity but unlike voltage, charge capacity is an extensive quantity. This means that the charge capacity of an electrode depends on the amount of material in it. It also depends on the chemistry of the battery. Theoretical capacity (Q_{th}) in Ah is calculated by Faraday's law as Equation (1.3) [27]:

$$Q_{th} = \frac{z\cdot F\cdot m}{3600\cdot\mathcal{M}} \quad (1.3)$$

where $\mathcal{M}$ is the molar weight of the cathode materials in g·mole^{-1}, *m* is the mass of the active material in cathode used in the cell in grams and F is 96500 coulombs·mole^{-1}.

The practical capacity in Ah is calculated as:

$$Q_p = \int_{t_1}^{t_2} I(t) \cdot dt \tag{1.4}$$

where *I(t)* in amperes is the current as a function of time and t_1 and t_2 stand for the begin and end of the considered interval in hour, respectively.

State of charge is the fraction of the maximum capacity that is still available.

Current density (*i*) is the ratio of the total current from an electrode (*I*) to its surface area (*A*):

$$i(t) = \frac{I(t)}{A} \tag{1.5}$$

Charge density or specific charge is the amount of theoretical (q_{th}) or practical (q_p) charge per unit weight of the reactants in $Ah \cdot g^{-1}$.

Energy density or specific energy (*W*) is the energy per unit weight (or volume) of a material or a device. It is often measured in $Wh \cdot kg^{-1}$ (gravimetric) or $Wh \cdot L^{-1}$ (volumetric). Maximum Theoretical Specific Energy (MTSE) according to Huggins [28] is the maximum value of specific energy that can be obtained from the respective electrochemical cell. The maximum storable energy from a cell equals the standard Gibbs free energy of the cell reaction ($\Delta_r G^0$) per mole of the reactants in $J \cdot mole^{-1}$:

$$\text{MTSE} = W_{th} = \frac{\Delta_r G^0}{n} = \frac{z \cdot F \cdot E^0}{n} \tag{1.6}$$

where n is the sum of the moles of reactants of cell reaction, E^0 is average voltage in volts and F is 96500 $coulombs \cdot mole^{-1}$. One Wh equals 3600 Joul. MTSE in $J \cdot g^{-1}$ or $kJ \cdot kg^{-1}$ can be calculated using the following equation:

$$\text{MTSE} = W_{th} = \frac{\Delta_r G^0}{w} = \frac{z \cdot F \cdot E^0}{w} \tag{1.7}$$

where w is the sum of the molecular weights of reactants of the cell reaction. Therefore, the accessible energy of a cell depends on the electrode material.

The practical energy contained in an electrochemical cell in $Wh \cdot g^{-1}$ is the integral of the voltage multiplied by the charge capacity:

$$W_p = \int E_{(x)} dq \tag{1.8}$$

where q is the amount of practical charge density in $Ah \cdot g^{-1}$ and $E_{(x)}$ is the voltage of the cell in volts. Layered transition metal oxides are suitable electrodes for high-energy-density applications thanks to their high cell voltage (about 4 V with respect to metallic lithium) combined with a relatively high capacity.

Cycle life is the number of cycles that a device can be effectively recharged before its performance, e.g. its capacity degrades to a specific degree.

1.3 Cathode materials

To increase the energy density, either specific capacity or the cell voltage should increase (as defined in Section 1.2.). Cell voltage is limited to the stability window of the conventional electrolytes. Therefore, the right strategy for the improvement of the energy density is using high capacity electrode materials. The fact that graphite is used predominantly in the lithium-ion batteries as the negative electrode means that the positive electrode material is the bottleneck in the improvement of the performance of lithium-ion cell and is being intensively investigated. In addition, by recent introduction of nanocomposites of Sn/C/Co alloys or Si-C led as major developments in anode material, there is a need for cathodes with higher capacities for optimum operation [29]

The host network compounds in the intercalation cathode of lithium-ion battery could be metal chalcogenides, transition metal oxides and polyanion compounds [30]. In general, current state-of-the-art positive electrode intercalation materials are categorized into three classes based on their structure and subsequently the dimensionality of the Li^+ ion diffusion in them [31]: (i) layered compounds like $LiCoO_2$ and its derivatives, (ii) spinel-like compounds such as $LiMn_2O_4$ and (iii) polyanion-based compounds with

olivine or tavorite structure as $LiMPO_4$ (M = Fe, Mn, Ni, Co, etc.) or Fluorophosphates. The representative structures of the three categories are depicted in Figure 1.3. Typically, the intercalation cathodes have 100–200 $mAh \cdot g^{-1}$ specific capacity and 3-5 V average voltage vs. Li/Li^+ [30].

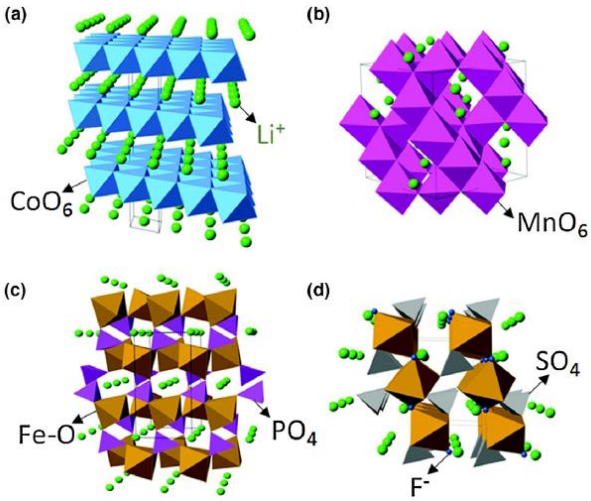

Figure 1.3: Crystal structures of different intercalation cathodes: (a) layered ($LiCoO_2$), (b) spinel ($LiMn_2O_4$), (c) olivine ($LiFePO_4$) and (d) tavorite ($LiFeSO_4F$) (From Ref. [30]).

Layered lithium metal oxides attracted interests for application as cathode due to their topotactic Li-interaction mechanism. This means that these oxides show a large stability region with respect to lithium content that in some cases might reach 1 to 0 Li without substantial changes of the structure of the material [25]. Therefore, the layered material shows higher capacity (a reversible capacity of 140 to 200 $mAh \cdot g^{-1}$) comparing the two other types of cathode structures. Layered materials are used as cathodes for high-energy systems, while spinel oxides and olivines are considered in the case of high-power lithium-ion batteries because of low cost and long-life requirements, respectively [31]. LMO_2 typically has a trigonal crystal system and the average

oxidation state of the M cation in LMO_2 is +3 [32]. In Chapter 2, major developments in layer structured lithium transition metal oxides, in particular $Li(Ni,Mn,Co)O_2$ material as cathodes for lithium-ion batteries will be reviewed.

2 Layer-structured $LiMO_2$ (M = Ni, Mn, Co)

The layered lithium transition metal oxides with the general formula $LiMO_2$ (M = Co or Ni or Mn or a combination of them) have been the most widely commercialized cathode material for LIBs [33, 34]. The purpose of this chapter is to review the state of the art on the challenges and progress in the development of this family of oxides as cathode material for lithium ion batteries and the related mechanism.

2.1 Crystallography of Li_xMO_2 phases

In this section, the main structures in Li_xMO_2 compounds appearing during synthesis or lithium deintercalation, namely layered (O1, O3, H1-3) and cubic (rock salt and spinel), will be discussed. The crystal structures of these relevant phases are depicted in Figure 2.1. An introduction of the crystallography of these phases is essential as the synthesis, operation and degradation of layered lithium oxide cathodes involve different transformations between such phases, that will be discussed in Section 2.3. The common feature of these structures is the presence of closed pack oxygen sublattice.

The layered crystal structure of the $\mathcal{A}MO_2$ composition ($\mathcal{A}$ = alkali, M = 3d element) has a close packed framework of oxygen anions. In Figure 2.1, the columns next to each structure with “A”, “B” and “C” characters denote the oxygen sheets and show the pattern according to which the stacking of oxygen anions is repeated within the structure. The $\mathcal{A}^+$ and the M^{3+} cation are ordered in interstitial sites of alternating (111) planes of the rock salt type structure [35, 36]. The (111) ordering induces a slight distortion of the lattice to a hexagonal symmetry. From the layers filled by M cations, MO_2 slabs are formed consisting of edge-sharing MO_6 octahedrals. The $\mathcal{A}$ cations, which can be intercalated, are located in the layers between the MO_2 sheets.

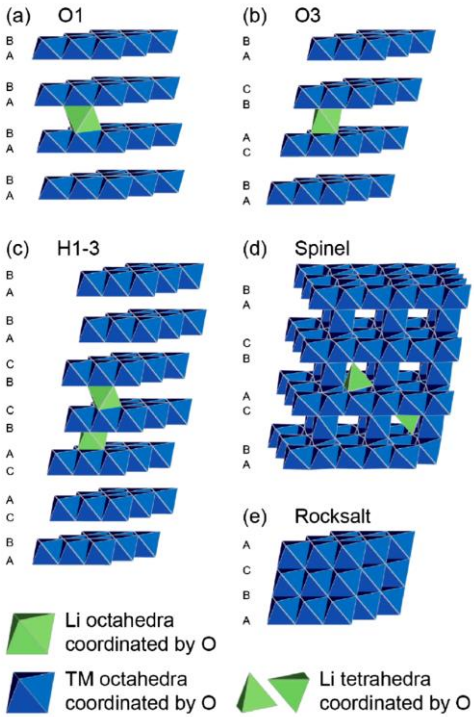

Figure 2.1: The crystal structure of (a) O1, (b) O3, (c) H1-3, (d) spinel and (e) rock salt phases, which are relevant in lithium (de)intercalation of Li_xMO_2. Blue and green octahedra represent MO_6 units and Li sites, respectively [37].

The $\mathcal{A}$ cations can occupy octahedral (O), prismatic (P), or tetrahedral (T) sites, based on the relative stacking of the MO_2 slabs [36]. When the oxygen layers of neighboring MO_2 slabs stack directly on top of each other around the layer of $\mathcal{A}$ cations, prismatic sites emerge. A shift in this relative stacking results in the formation of octahedral and tetrahedral sites within the $\mathcal{A}$ layer. The octahedral sites form a planar triangular lattice with face-sharing tetrahedral sites connecting neighboring octahedral sites.

According to the classification introduced by Delmas et al. [36], a letter is used to indicate the coordination of $\mathcal{A}$ cations by oxygen anions, i.e. either O for octahedral, P for prismatic, or T for tetrahedral. A number that indicates the number of MO_2 sheets repeated in a unit cell follows the letter. The unit cell here describes the translational symmetry along an axis vertical to the MO_2 sheets. The five "primitive" stacking sequences are O1, O3, P3, O2, and P2. These structures are divided into two main groups: the O3/O1/P3 and the O2/P2 group [37]. Transformations between structures of each group is easily possible through gliding of the MO_2 layers while transformations between structure from two different groups require the breaking of metal–oxygen bonds, which needs more energy than gliding transformations. Therefore, cathode structures usually remain in the same family during cycling [38].

In the O3 structure, the oxygen layers are stacked in an AB CA BC pattern, forming a rhombohedrally distorted *fcc* oxygen lattice with three MO_2 slabs required to complete the unit cell. The O3 structure is commonly referred to by its prototype structures: α-$NaFeO_2$ with the space group of $R\bar{3}m$. [39]. Similarly, in the O1 structure the oxygen layers are stacked in an ABAB pattern, forming an hcp oxygen lattice with a single MO_2 sheet repeated in the unit cell. Hybrid H1-3 phase consists of alternating blocks of O1 and O3 structures and is observed upon partial delithiation [40–42]. The P2 and O2 structures can also be synthesized for $\mathcal{A}MO_2$ compounds but are metastable [43, 44]. If monoclinic distortions is present in layered oxides, a prime symbol is added to the structure name [45]. In O3 structure, such distortions reduce the space group from $R3m$ to $C2/m$, which is designated as O′3. The distortion happens either due to collective Jahn–Teller distortions (like in $LiMnO_2$ [46]) or lithium-vacancy ordering (like in $Li_{0.5}CoO_2$ [41, 47]).

The spinel and disordered rock salt structures have the same *fcc* oxygen framework as O3 but the arrangement of $\mathcal{A}$ and M cations in octahedral and tetrahedral interstitial sites is different. Therefore, O3 is sometimes referred to as layered rock salt. Figure 2.2 shows how cation-ordering on (111) planes of the rock salt structure form the O3 structure. Rock salt phases forming from the degradation of layered oxides are rich in transition-metal, with compositions close to MO. The transformation from the delithiated layered

MO_2 to a rock salt MO takes place by oxygen release and diffusion of transition-metal ions back into the material (referred to as densification) [37]. If the O3 structure transforms into spinel, one quarter of the metal ions migrate from the transition-metal layer to particular octahedral sites in the Li layer (metal ordering within the *fcc* oxygen lattice with cubic symmetry) and, as a result, the Li ions rearrange. If the Li concentration in $Li_{\alpha}MO_2$ is close to α = 1, the Li ions either reside in the remaining octahedral sites in spinel and if the Li concentration *x* is less than 0.5, Li ions occupy a subset of tetrahedral sites that do not share faces with MO_6 octahedra [48, 49].

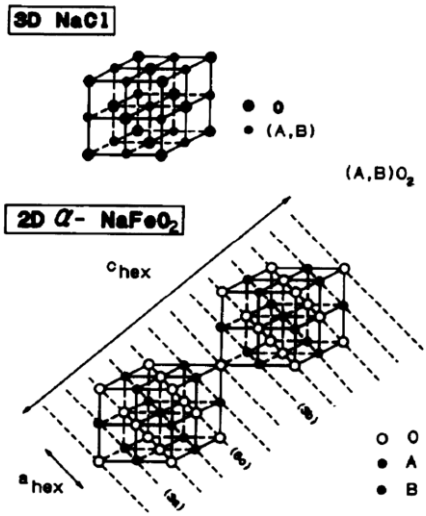

Figure 2.2: The layered structure is formed by cation ordering in rock salt structure [35].

The phase transformation of O3 to rock salt and spinel, which are more facile at higher temperatures, are irreversible. However, due to kinetic limitations in interlayer migrations of the transition metal ions [50, 51], the O3 structure usually undergoes a number of reversible phase transformations when cycled at room temperature. Upon deintercalation of lithium in layered $Li_{\alpha}MO_2$,

depending on the extent of preserving the host structure, the phase transformations are categorized in three types.

1) If the host crystal structure remains unchanged, the phase transformation is least destructive. An example of this type is from O3-$Li_{0.95}CoO_2$ to O3-$Li_{0.75}CoO_2$ with slight changes in lattice parameters, which is an insulator-to-metal electronic transition [52–54].

2) If the host crystal structure preserves original network, but a structural distortion along with reduction in symmetry happens, the phase transformation is more destructive. Such transformations are caused by the Jahn-Teller distortions and / or lithium-vacancy ordering and result in rhombohedral O3 to a monoclinic O′3 transformation, as shown in Figure 2.3 [41, 46, 47, 55, 56]. Transformations driven by Jahn– Teller distortions can lead to dramatic changes in lattice parameter and are more destructive comparing those associated with lithium vacancy ordering.

3) If the stacking of MO_2 slabs changes upon delithiation, the phase transformation is more disruptive. An important example of such transformation is the transformation from the O3 to O1 host structure after complete lithium removal. Transformations to one or more hybrid O1/O3 phases such as H1-3 may also happen at intermediate compositions.

Phase transformations can be also categorized as first-order or continuous. However, the first-order (a two-phase coexistence) and continuous transitions (changes in symmetry) in battery materials are often difficult to distinguish [37].

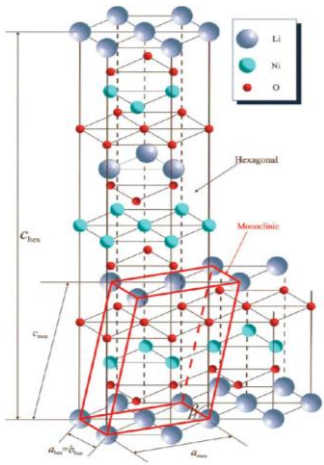

Figure 2.3: The crystallographic relationship between hexagonal and monoclinic description for $Li_{\alpha}NiO_2$. The pictures taken from Ref. [57, 58].

2.1.1 Characteristics of layered structure

The relative size of transition metal (M) against alkaline ($\mathcal{A}$) cations in $\mathcal{A}MO_2$ compounds is the determining factor for the layered structure characteristics of these compounds and the possibility of cation mixing [35]. The size difference should be large enough to increase the two-dimensional ordering characteristics of the structure. It is worth reminding that, mismatch in the ionic size can result in lattice strains and material instability [59]. Figure 2.4, retrieved from a review paper by Rozier and Tarascon [60], compares the ionic radii of stable valance states of $\mathcal{A}$ (Li, Na) and M (Co, Ni and Mn) species. It shows that all $NaMO_2$ ternary oxides crystalize in such a well ordered layered structure due to the large difference in size between Na^+ and M^{3+} cation. However, in lithium derivatives, only Ni and Co in their trivalent state meet the requirements for a 2D layered structure. The size difference between larger Mn^{3+} ions in high spin state and lithium ions is not high enough for a 2D order. Nevertheless, smaller tetravalent Mn ions can meet the criteria for a layered structure. It should be mentioned that these results concern only stable

materials prepared at high temperatures. Metastable-layered $LiMO_2$ can be obtained by chemical exchange at low temperatures from the parent sodium phases, but are decomposed when heated to around 300 °C.

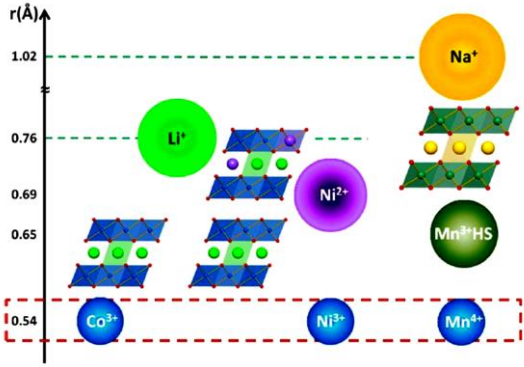

Figure 2.4: Comparison of the ionic radii of stable valance states of $\mathcal{A}$ (Li, Na) and M (Co, Ni and Mn) species [60].

The second parameter for predicting the possibility of a stable 2D structure in the $\mathcal{A}MO_2$ compounds is the stability of the valence state of the transition metals (M) [35]. The stability means that the desired valence state of M cations in respect to the first parameter needs to be thermodynamically stable at the synthesis conditions such as temperature and partial pressure of oxygen. These two parameters will be used to describe the layered structure characteristics of different compounds in the following of this chapter.

There are some features of the x-ray diffractogram of a sample with $LiMO_2$ composition that are related to the extent of cation mixing and thus the layered characteristics of the structure. Ohzuku et al. [57] pointed out that the integrated intensity ratio of I(003) / I(104) Bragg peaks for $LiNiO_2$ could be a key factor. The mixing between Ni ions at octahedral 3a sites and Li ions at 3b sites in the space group $R\bar{3}m$ decreases the intensity of the (003) line, while such a displacement does not affect the intensity of the (104) peak. When the

integrated intensity ratio of (003) to (104) lines (I(003) / I(104)) is below 1.2, the (108) and (110) doublets become difficult to distinguish from each other [61]. $LiNiO_2$ is reported to be inactive in nonaqueous lithium cells if the intensity ratio is below 1.0 [61]. The integrated intensity itself can be determined by two methods, either by measuring the area under the peak (enclosed by the estimated background) or estimated by multiplying the maximum peak height at full width at half maximum (FWHM) of the peak. The measurement of peak areas may not be very accurate as the level of the background is an uncertain feature of the peak as a triangle and the area may change noticeably with small changes of background. Therefore, the product of the peak height and the width at half peak height is considered as the most satisfactory method for the measurement of integrated intensity [62].

2.2 Exploration of the NMC chemistry

To gain an understanding of the $LiNi_xMn_yCo_{1-x-y}O_2$ (NMC) materials as a combination of $LiCoO_2$, $LiNiO_2$ and $LiMnO_2$ systems, a brief review of the end members, i.e. $LiCoO_2$, $LiNiO_2$ and $LiMnO_2$ as well as their binary combinations, i.e. $LiCoO_2$-$LiNiO_2$, $LiCoO_2$-$LiMnO_2$ and $LiNiO_2$-$LiMnO_2$ systems is necessary.

2.2.1 Parent materials

2.2.1.1 $LiCoO_2$

$LiCoO_2$ (LCO), the parent compound of the $LiMO_2$ family, was first reported by Goodenough and co-workers [12] and after its commercialization in 1991 it received great research attentions. High temperature form of $LiCoO_2$ (HT-$LiCoO_2$), adopts the α-$NaFeO_2$ type structure (space group: $R\bar{3}m$, No. 166) as described in Section 2.1. In LCO compound cobalt is trivalent in the low spin state with the electronic configuration of $(t_{2g})^6(e_g)^0$ [31]. Despite the high theoretical capacity of the layered $LiCoO_2$ (274 $mAh \cdot g^{-1}$), its reversible capacity is limited to only 50% of the theoretical value, i.e. cut-off voltage should be limited to 4.2 vs. Li/Li^+ [47]. Further delithiation results in

irreversible structural changes [60, 63, 64], large shape and volume changes during (de)intercalation leading to mechanical damage [65–69], loss of oxygen due to a reduced stability of delithiated phase [66], electrolyte decomposition [70], transformation to the spinel phase [65], the formation of an SEI (solid-electrolyte interface)-like film on LCO [71] and dissolution of cobalt in electrolyte [72], thereby leading to severe capacity loss. Manthiram et al. [73] suggested that by extracting more than half of the lithium from LCO, chemical instability occurs due to a significant overlap of the redox active $Co^{3+/4+}$:t_{2g} band with the top of the O^{2-}:2p band as shown in Figure 2.5. Co is also rather expensive and toxic, both of which hinder its use in large-scale batteries for electric vehicles and grid storage applications. Furthermore, low thermal stability of LCO leading to thermal runaway at around 200 °C makes it an unsafe cathode option for larger batteries [30, 74]. Although doping and substitution of Co with Mn, Al, Fe or Cr [75–78] or coating with Al_2O_3, B_2O_3, TiO_2 or ZrO_2 [79, 80] have shown to be promising in the improvement of the performance of LCO, alternative chemistries to $LiCoO_2$ especially for large-scale applications are necessary.

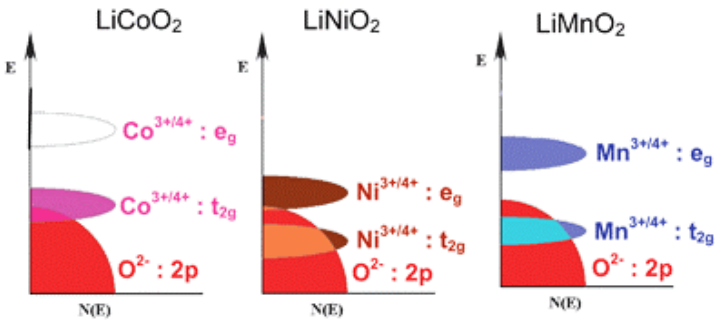

Figure 2.5: Comparison of the energy diagrams of $LiCoO_2$, $LiNiO_2$, and $LiMnO_2$ [73].

2.2.1.2 $LiNiO_2$

$LiNiO_2$ (LNO) with the same structure and similar theoretical specific capacity, was initially considered as an alternative to LCO because of

environmental benignity and lower cost of Ni comparing Co [81]. In LNO, nickel is trivalent with low-spin $(t_{2g})^6(e_g)^1$ electronic configuration. Unlike in the case of LCO, in LNO the t_{2g} orbitals remain completely filled during the charge/discharge process. However, a strong Ni-O-Ni covalence result in a reasonably high conductivity with a semi-conducting behavior [82]. In LNO there is no significant overlap of the redox active $Ni^{3+/4+}$: e_g band with the top of the O^{2-}: $2p$ band, as can be seen in Figure 2.5. Therefore, the extraction of one lithium-ion per Ni (reaching higher capacity) is possible without encountering the release of oxygen from the lattice [73].

$LiNiO_2$-based cell has a higher energy density and reversible capacity (ca. 200 $mAh \cdot g^{-1}$) [29] while having a lower operating voltage (about 250 mV less) than those based on $LiCoO_2$ [83]. Dahn's group [74, 81, 84–86] and later Ohzuku et al. [57, 61] and Delmas et al. [56, 87–90] performed a great deal of research on the preparation condition, cation distribution and performance of $LiNiO_2$.

However, for several issues LNO was not successful in supplanting LCO. First, the synthesis of stoichiometric $LiNiO_2$ is difficult [90, 91]. The closest synthesized sample to stoichiometry to the best of our knowledge is $Li_{0.996}Ni_{1.006}O_2$ [92]. In practice, during the synthesis process by different routes, it is difficult to stabilize Ni as Ni^{3+} valence state, even by calcination in flowing oxygen at the lowest possible temperature (~700 °C). Instead the off-stoichiometric $Li_{1-y}Ni_{1+y}O_2$ phase ($0.00 < y \leq 0.20$) is formed in which 1+y Ni^{3+} is decomposed to 2y Ni^{2+} and (1-y) Ni^{3+} with simultaneous volatilization of y Li from the reaction mixture [90]. The Ni^{2+} ions present in the products have a similar size to the Li^+ ion (r_{Ni2+} = 0.69 Å, r_{Li+} = 0.76 Å and r_{Ni3+} = 0.56 Å) [93]. As a result, the excessive yNi^{2+} occupy the Li interlayer sites, resulting in cation site disorder. The parts where Ni has contaminated the Li^+ site are regarded as local NiO disordered array halite layers (space group: $Fm\bar{3}m$) [94].

Furthermore, during the first charge of $LiNiO_2$, after oxidation of Ni ions in the transition-metal layer, with further delithiation, Ni^{2+} ions in the Li layer oxidize to smaller Ni^{3+} ions. The smaller size of Ni^{3+} than Ni^{2+} results in a local

contraction of the interslab distance and these ions act as local pinning centers restricting the diffusion of Li^+ ions during the first discharge and leading to significant irreversible capacity loss [88, 92, 95, 96] and slower lithium diffusion in LNO compared to LCO [97, 98]. This phenomenon is schematically demonstrated by Delmas et al. as in Figure 2.6 [88]. Another problem associated with LNO is the safety concern. As thermal gravimetric analysis has shown, the thermal stability of delithiated LNO is inferior to that of LCO [74].

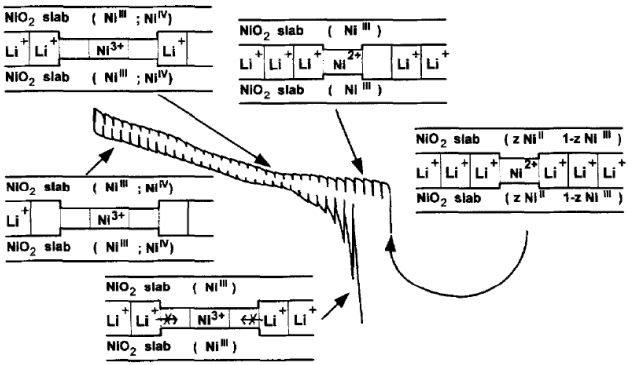

Figure 2.6: The mechanism of irreversible capacity loss during the first electrochemical cycle of $LiNiO_2$. The oxidation of Ni^{2+} ions in the Li layer results in local pinning centers restricting the diffusion of Li^+ ions during first discharge [88].

2.2.1.3 $LiMnO_2$

From an economical and environmental point of view, layered $LiMnO_2$ (here referred as LMO) with the same structure as LCO is a very attractive material. However, layered $LiMnO_2$ does not form through conventional solid-state synthesis routes which are used in the synthesis of layered Co or Ni analogues. instead, using high temperature firing, $LiMnO_2$ crystalize in the form of an orthorhombic phase, o-$LiMnO_2$ with the *Pmmn* space group [99, 100]. As described in Section 2.1 and shown in Figure 2.4, the layer-structured $LiMnO_2$ is not stable due to the small ionic radii difference between Mn^{3+} in high spin

configuration (r_{Mn3+} = 0.65 Å) and Li^+ (r_{Li+} = 0.76 Å). O-$LiMnO_2$ shows poor electrochemical activity [101].

The metastable well-layered $LiMnO_2$, has been produced almost two decades ago using ion exchange of the thermodynamically stable layered $NaMnO_2$ with Li^+, as independently reported by Dahn et al. [102], Bruce et al. [103] and Delmas et al. [104]. Wang and Navrotsky [105] experimentally showed that the orthorhombic structure is thermodynamically more stable than the monoclinic layered structure. The resulting layered materials does not have a perfect α-$NaFeO_2$ structure, but a monoclinic unit cell with lower symmetry (space group: *C2/m*) with angles and lattice constants distorted from the rhombohedral due to cooperative Jahn–Teller effect of high spin Mn^{3+} ions. Although most researchers suggest that m-$LiMnO_2$ can only be prepared by meta-stable soft chemical routes, the results from Jang et al. [106, 107] show that m-$LiMnO_2$ is stable at 1050 °C in air and can be maintained at room temperature by quenching in water.

Nevertheless, the layered $LiMO_2$ is no practical option for a cathode material for three reasons. First, because layered $Li_{0.5}MnO_2$ rapidly converts to the more stable $LiMn_2O_4$ spinel structure upon cycling, resulting in an irreversible loss of capacity and a spinel-like drop in the voltage profile [49, 108–110]. In Mn-based $LiMO_2$ phases, Mn^{3+} ions undergo a disproportionation reaction favored by the contact with the electrolyte, to form Mn^{2+} and Mn^{4+}. The mobile Mn^{2+} ions can easily diffuse from Mn to Li layer via the dumbbell mechanism [50, 51, 111]. This mechanism is quite fast because of the high stability of Mn^{2+} in the tetrahedral sites, which serve as an intermediate step in the interlayer migration. The layer to spinel phase transformation will be discussed further in Section 2.3. To prevent the transformation into spinel, layered $LiMnO_2$ with different oxygen layers stacking sequences, such as O2 type instead of O3 type (see Section 2.1 and 2.3 for the definition of different types) was proposed. However, these compounds presented poor electrochemical performances [112].

Secondly, the cycling performance of LMO was not satisfactory because of the Mn dissolution in the electrolyte [113, 114]. Mn^{2+} from the disproportion reaction is thought to be soluble in the electrolyte, and destabilize the anode

SEI [115–118]. Thirdly, during delithiation, the distortion of the monoclinic phase is removed resulting in large mechanical stresses that could fracture the material [37].

2.2.2 Binary combinations

As mentioned in the previous section, each lithium single transition metal oxide faces certain limitations. To minimize these limitations, mixing them and coming up with different compositional variation could be an effective solution. There are a few works that systematically investigated the possibility of the formation of a substitutional solid solution for different binary combinations of $LiMO_2$ (M = Ni, Co, Mn, etc.) [59, 119–121].

The changes in the composition are accompanied by the changes in the size and the valence state of cations present in the layered structure. As discussed in Section 2.1, the size mismatch of the cations results in lattice strains and structural instability of the layered $LiMO_2$ oxides. Bond valance model presents an empirical correlation between the bond length and the bond valence (formal oxidation state of the atoms) for a given cation-anion pair [122–124]. Noticeable deviation from the expected bond distances indicates the steric strain in the lattice (or problems in the determination of crystal structure). Therefore, this model is able to analyze and predict the lattice strains from the experimental interatomic distances and evaluate material stability.

Based on the bond valence model, Levi and Aurbach obtained a direct correlation between the length of transition metal-oxygen (TM-O) bonds and the valence state of the transition metal for unstressed TM-O bonds [125]. They used such correlation to evaluate the lattice strains in layered structure $LiMO_2$ (M = Ni, Co, Mn, etc.) arising due to the cation substitution in the TM layer by introducing a tolerance factor. Being a function of chemical composition (substitution level) and the size difference of the substituted cations, the tolerance factor estimates the stability of the solid solution of two lithium single TM oxides during synthesis and electrochemical deintercalation [59]. The prediction of solid solution stability ranges made by the tolerance factor of Levi and Aurbach are in very good agreement with the experimental data

for the $LiCoO_2$-$LiNiO_2$, $LiCoO_2$-$LiMnO_2$ and $LiNiO_2$-$LiMnO_2$ binary combinations, indicating the effectiveness of this model [59].

Koyama et al. [119] conducted first-principles calculations on the $LiCoO_2$-$LiNiO_2$-$LiMnO_2$ system to investigate the solid solution behavior of the different binary combinations of end members. It is shown that $LiNi_{1-x}Co_xO_2$ is a solid solution between $LiCoO_2$ and $LiNiO_2$. However, no stable solid solution forms between $LiCoO_2$ and $LiMnO_2$, instead phase separation is predicted. $LiNi_yMn_{1-y}O_2$ is found stable only when $y \geq 0.5$ and the compound is considered as a solid solution of $LiNiO_2$ and $LiNi_{0.5}Mn_{0.5}O_2$, not $LiMnO_2$, due to the charge distribution between Mn and Ni. Figure 2.7 shows the summary of their calculations on phase triangle of $LiCoO_2$-$LiNiO_2$-$LiMnO_2$.

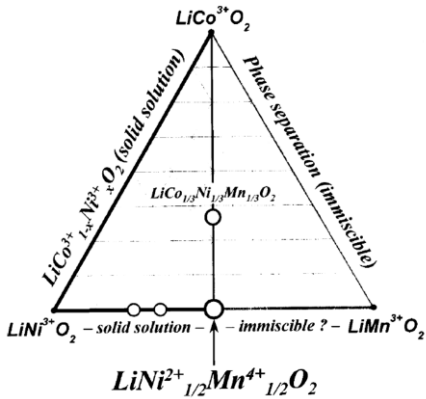

Figure 2.7: The summary of the prediction of solid solution formation for all binary combinations of the $LiCoO_2$-$LiNiO_2$-$LiMnO_2$ system based on first principle calculations [119].

2.2.2.1 $LiCoO_2$-$LiNiO_2$

$LiCoO_2$ and $LiNiO_2$ form a complete solid solution with the layered structure [126]. It means that the Ni and Co cations can be mixed randomly in transition metal layers in all ratios to form a single phase. The realization of $LiNi_{1-x}Co_xO_2$

solid solution for the entire range of x ($0 \leq x \leq 1$) is due to the following facts: (i) $LiCoO_2$ and $LiNiO_2$ are isostructural, (ii) Co and Ni ions are trivalent with very similar ionic radius (r_{Co3+} = 0.545 Å and r_{Ni3+} = 0.56 Å, both low spin), (iii) $LiCoO_2$ and $LiNiO_2$ can be synthesized under flowing oxygen, and (iv) the electronegativity of Ni (1.91) is similar to that of Co (1.88) [127]. $LiNi_{1-x}Co_xO_2$ solid solutions have lower insertion potentials compared to that of the pure $LiCoO_2$ phase [128, 129].

For low substitution amounts ($x \leq 0.2$), off-stoichiometry, similar to $LiNiO_2$ was observed [35]. However, by substituting more Ni with Co (for $x \geq 0.3$), even without flowing oxygen during calcination, the formation of Ni^{2+} is prohibited resulting in reduced cation disorder. This leads to stabilization of the two dimensional character of the layered structure (increase in the trigonal distortion of the cubic lattice) and consequently, improvement of the reversibility of lithium intercalation [35, 130]. For Ni-rich compositions ($0 \leq x \leq 0.4$), by increasing Co content, there is a small decrease in potential while the shape of the voltage curve does not change dramatically [126]. For cell voltages of 3.5 – 4 V, up to 0.6 lithium atom per $LiNi_{1-x}Co_xO_2$ can be reversibly deintercalated [126]. However the solid-state properties and battery performances of $LiNi_{1-x}Co_xO_2$ vary depending on the synthesis method [94, 131–133]

It is suggested that among all $LiNi_{1-x}Co_xO_2$ compounds, $LiNi_{0.8}Co_{0.2}O_2$ has the best electrochemical charge-discharge behavior due to a balance between low lithium deficiency and high nickel content [94, 134].

2.2.2.2 $LiCoO_2$-$LiMnO_2$

The layered $LiNi_{1-z}Co_zO_2$ ($0 \leq z \leq 0.5$) cannot be prepared using the conventional solid-state method. Instead, it has been prepared by Armstrong et al. [135–137] using a solution-based route coupled with ion exchange. When $0 \leq z \leq 0.1$, localized high spin Mn^{3+} induces a Jahn-Teller distortion resulting in a monoclinic structure ($C2/m$) with lower symmetry than rhombohedral structure ($R3$-m). By more substitution, for $0.1 \leq z \leq 0.5$, the distortion is suppressed and a continuous range of solid solutions with rhombohedral symmetry exists. Substitution of as little as 10% of Mn by Co in m-$LiMnO_2$,

increases the capacity up to 200 mAh·g^{-1}. Higher Co contents show lower capacities but less capacity fading. However, similar to the case of m-$LiMnO_2$, layered structure of $LiNi_{1-z}Co_zO_2$ converts to a spinel-like structure upon cycling. The rate of conversion depends on the cobalt content and is slower with increasing Co content.

Nevertheless, the successful preparation of a thermodynamically stable layered material based on a $LiCoO_2$-$LiMnO_2$ solid solution has not been reported to our knowledge. Koyama et al. used first principle calculations to confirm the instability of layered $LiNi_{1-z}Co_zO_2$ with hexagonal symmetry for the entire range ($0 \leq z \leq 1$) [119]. The stoichiometric solid solutions between $LiCoO_2$ and $LiMnO_2$ show phase separation at processing temperatures commonly used for either end members.

2.2.2.3 $LiNiO_2$-$LiMnO_2$

Single phase layered $LiNi_yMn_{1-y}O_2$, the solid solution of $LiNiO_2$ and $LiMnO_2$, can only be formed when $y > 0.5$. This was first investigated by Rossen and Dahn [138]. For $y > 0.5$, they successfully obtained $LiNi_yMn_{1-y}O_2$ materials through solid-state reaction of rock salt MnO and NiO precursors. Spahr et al. [139] also reported the preparation of layered $LiNi_yMn_{1-y}O_2$ ($y > 0.5$) by an oxidative co-precipitation process and calcination between 450 °C and 800 °C. However, their material showed poor capacity retention. Nevertheless, given the beneficial effect of manganese on cost reduction and improvement of thermal stability at the highly delithiated states, finding a promising composition and synthesis conditions for the optimized electrochemical performance was still an active research topic [140–142].

In 2001, Ohzuku et al. synthesized layered $LiNi_{0.5}Mn_{0.5}O_2$ at 1000 °C from a co-precipitated process as a successful alternative to $LiCoO_2$ [143]. Their material demonstrated a smooth sloping voltage profile and a promising capacity of about 150 mAh·g^{-1} [143] and 200 mAh·g^{-1} [144] with little capacity fading when charged to 4.3 and 4.5 V, respectively. After that, among other compositions in this series, $LiNi_{0.5}Mn_{0.5}O_2$ was most widely investigated. $LiNi_{0.5}Mn_{0.5}O_2$ with good electrochemical performance was also prepared by Dahn et al. at 900 °C in air and reported as a part of their works on

$Li[Ni_xLi_{(1/3-2x/3)}Mn_{(2/3-x/3)}]O_2$ system [145]. The improvement of electrochemical performance of $LiNi_{0.5}Mn_{0.5}O_2$ relates to the calcination temperature of more than 800 °C during synthesis.

Unlike $LiNi_{1-y}Co_yO_2$ in which both transition metals are in +3 valence state, in $LiNi_{0.5}Mn_{0.5}O_2$, charge separation between nickel and manganese forms Ni^{2+} and Mn^{4+}, as suggested by Rossen and Dahn [138] and later confirmed by X-ray absorption spectroscopy [146] and first principle calculations [119, 147]. Mn in tetravalent ions improves the cycling stability of the layered structure oxides [148]. $LiNi_{0.5}Mn_{0.5}O_2$ possesses the α-$NaFeO_2$ type structure (space group: $R\bar{3}m$, 166) [145]. The presence of Ni^{2+} leads to around 10% anti-site mixing between Li^+ and Ni^{2+} in $LiNi_{0.5}Mn_{0.5}O_2$ [149, 150]. From magnetic measurements it is derived that 7% of the nickel occupies the (3*a*) Wyckoff position in Li sites, constituting a Ni^{2+}(3*a*) defect [151]. To suppress cation mixing, Ceder's group prepared $LiNi_{0.5}Mn_{0.5}O_2$ employing an ion-exchange method, which demonstrated an acceptable rate capability at higher C-rates [152].

For the $LiNi_yMn_{1-y}O_2$ system (y > 0.5), alternatively represented as $LiNi^{3+}{}_{1-2y}Ni^{2+}{}_yMn^{4+}{}_yO_2$, the anti-site mixing between Li^+ and Ni^{2+} decreases from 10% to 3% as y changes from 0.5 to 0.1 [153, 154]. While Mn is tetravalent, the oxidation state of Ni changes from purely 3+ to purely 2+ as y increases from 0 to 0.5, to provide charge neutrality of the compound [153]. The capacity decreases as Mn is substituted for Ni. This behavior is attributed to the combined effects of cation mixing and the presence of inactive Mn^{4+} [138]. However, the capacity retention and thermal stability improves by increasing Mn content [154].

2.2.3 $LiNi_xMn_yCo_{1-x-y}O_2$ (NMC)

Early studies on layered lithium mixed nickel manganese cobalt oxide ($LiNi_xMn_yCo_{1-x-y}O_2$) focused on the Ni-rich composition ($0.5 \leq x \leq 1$) in the framework of substitution of Ni with both Mn and Co. Such substitution showed to be effective in reducing off-stoichiometry and cation mixing in $LiNiO_2$ even if the calcination is performed in air instead of oxygen [155, 156].

Attempts to apply solid-solution approach to mix $LiCoO_2$ with other compounds having the same crystal family of α-$NaFeO_2$, led to the emergence of a layered lithium Ni–Mn–Co oxide $LiNi_xMn_yCo_{1-x-y}O_2$ (NMC, aka NCM) in the early 2000s [157, 158]. NMCs are attractive active materials as they offer similar or higher achievable specific capacity, similar operating voltage, lower cost, and improved safety compared to the $LiCoO_2$. The presence of Co reduces the degree of Li/Ni off-stoichiometry, though a Li/Ni site mixing of 1%–6% is still observed [63, 159]. Mn in general improves the cyclability [143, 155–157] and thermal stability [157, 160].

He et al. [32] used the triangular compositional phase diagram of $LiCoO_2$-$LiNiO_2$-$LiMnO_2$ from Ohzuku et al. [119] and marked the stability ranges of hexagonal structure by full lines while the dash lines show where immiscibility occurs, as shown in Figure 2.8. Moreover, Ni-rich layered NMC oxides are shown in this diagram. However, there are some ambiguities in this phase diagram; (i) no reference is mentioned regarding the oxidation state of transition metal oxides on the line between the center of triangle (NMC111 as will be described in next paragraph) and LNO, (ii) no reference is mentioned regarding solubility region for LCO-LMO mixture close to LCO corner (iii) the stability range of layered structure inside the triangle is not clearly discussed.

The NMC compound with the composition $LiNi_{1/3}Mn_{1/3}Co_{1/3}O_2$ referred to as NMC111 (or sometimes NMC333) is the most common and already commercialized form of NMC. This compound was first synthesized by Ohzuku et al. [158] by heating at 1000 °C in air and delivered capacity of 150 $mAh \cdot g^{-1}$ and 200 $mAh \cdot g^{-1}$ when charged to 4.2 and 5 V vs. lithium, respectively [158]. Later on they modified the synthesis process containing a mixed hydroxide of TMs and achieved the same high capacity at the cut-off voltage of 4.6 V [160].

Various synthesis routes such as solid-state [158], sol–gel [161, 162] and modified co-precipitation of mixed hydroxides [155, 160, 163] have been employed to improve the phase-purity and uniformity of the cation distribution. Currently, co-precipitation is the most common process for the synthesis of NMC in laboratory as well as industrial scales. Despite differences

between the products of different synthesis methods, NMC111 synthesized at temperatures around 900 °C has demonstrated best electrochemical performance [164]. This material has reversible capacity of 160 mAh·g^{-1} and 200 mAh·g^{-1} when charged to 4.3 and 4.6 V vs. Li^+/Li, respectively [158, 165–168].

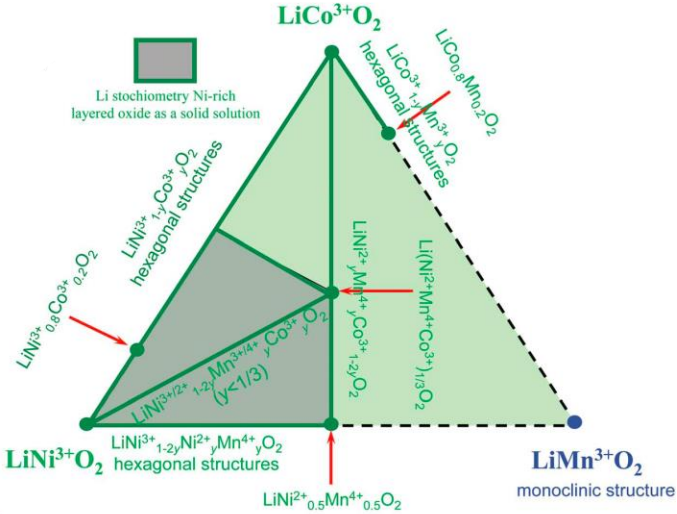

Figure 2.8: The compositional phase diagram of lithium-stoichiometric layered transition metal oxide [32].

First principles calculations indicated the presence of transition metal ordering in $LiNi_{1/3}Mn_{1/3}Co_{1/3}O_2$ [169]. However, experimental studies detected only a short-range ordering [170–172]. Cation mixing between Li and Ni is likely to occur but the degree of mixing in NMC111 is lower than in Ni-rich compositions [173]. The presence of Ni, Mn, and Co also suppresses lithium/vacancy ordering, leading to a smooth voltage curve. Similar to what described for $LiNi_{0.5}Mn_{0.5}O_2$, the nominal valence states of transition metals in pristine $LiNi_{1/3}Mn_{1/3}Co_{1/3}O_2$ is +2, +3, and +4, for Ni, Co, and Mn, respectively [161, 169, 174]. However, Li et al. [175] showed that for $LiNi_{1/3}Mn_{1/3}Co_{1/3}O_2$

when annealed at 700 °C, about 30% of Mn is trivalent and therefore a deviation of stoichiometry for oxygen was considered.

Computational (Density Functional Theory) studies [161], X-ray absorption spectroscopic (XAS) investigations [161, 172, 176–178] and magnetic measurements (Nuclear Magnetic Resonance [172], Superconducting Quantum Interference Device and Electron Paramagnetic Resonance [179] revealed that during intercalation/deintercalation of NMC111, Ni^{2+}/Ni^{4+} is the main redox process while Mn^{4+} is electrochemically inactive [161, 172, 176–179]. It is suggested that Co^{3+}/Co^{4+} redox does not significantly contribute to the redox reaction. Instead near the end of charge (4.5 V vs Li^{+} /Li), charge compensation takes place on O [161, 169, 172, 180] resulting in oxygen release [178, 181]. Therefore, the optimum value for the cut-off voltage of NMC111 is suggested as 4.3-4.4 V.

However, moving toward lower costs by decreasing the Co content, $LiNi_xMn_xCo_{1-2x}O_2$ compositions within a narrower range of $0.33 \leq x \leq 0.5$ have been investigated comprehensively [182–184]. Among them, $LiNi_{0.4}Mn_{0.4}Co_{0.2}O_2$ (NMC442) with high discharge capacity of 180 $mAh \cdot g^{-1}$ showed the optimum electrochemical properties. In NMC442 at room temperature, transition metals are randomly distributed in the transition metal layer [185]. Katana Ngala et al. [182] found the optimum temperature for synthesis of NMC442 to be 800-900 °C. They performed XPS investigations and found out that the oxidation state of Mn and Ni are mainly +4 and +2, respectively. However, about 20% of Ni and Mn are in the 3+ oxidation state. In compositions such as NMC111 and NMC442, where Ni and Mn content are matched, only Ni and Co are electroactive and Mn in its +4 valence state remains inactive [161, 169]. Therefore, compositions with higher Ni content, e.g. $LiNi_{0.5}Mn_{0.3}Co_{0.2}O_2$ (NMC532), are found attractive for increasing the specific capacity. Therefore, there is a recent trend toward these compositions in the NMC research. Compositions containing 40% or more Ni in the transition metal layer are usually referred to as Ni-rich NMC [186]. In such oxides, because the Ni and Mn contents are not matched, charge neutrality is achieved by the partial oxidation of Ni^{2+} to Ni^{3+} [187, 188]. NMC532 is one of the most-studied compositions due to its high discharge capacity (214 $mAh \cdot g^{-}$

[1] and 175 mAh·g^{-1} when charged to 4.6 V and 4.3 V, respectively) and good rate capability [189].

Increasing the nickel content in $LiNi_xMn_yCo_{1-x-y}O_2$ to x = 0.6 – 0.8 can result in higher practical capacities at moderate operating voltages but may also decrease the thermal stability of charged NMC [190–194]. In addition, Ni-rich NMC face difficulties similar to $LiNiO_2$ regarding off-stoichiometry during synthesis. In $LiNi_{0.6}Mn_{0.4-x}Co_xO_2$ compositions, an increase in cobalt content leads to a decrease in the tap-density of the powders and increase of discharge capacity and increase of capacity fading [195–197]. This behavior is attributed to the enhancement of the Ni^{3+}/Ni^{2+} ratio. Among these compositions, $LiNi_{0.6}Mn_{0.2}Co_{0.2}O_2$ (NMC622) containing same Co and Mn content had the highest tap density [195] and exhibited the optimum combination of reversible capacity and capacity retention as well as minimum polarization [195–200]. It delivers an initial discharge capacity of 172 mAh·g^{-1} when charged to 4.3 V and more than 94% of the capacity is retained after 100 cycles [195].

Increasing nickel content to higher values such as x = 0.7 [201–203] and x = 0.8 (like NMC811) [191, 204–207], if optimal synthesis conditions are satisfied, can result in high initial discharge capacities of about 180 and 190 mAh·g^{-1} using an upper cutoff voltage of 4.3 V vs Li^+/Li, respectively. Such NMC compositions can achieve capacities of more than 200 mAh·g^{-1} after charging to 4.5 V [208, 209]. The synthesis of Ni-rich NMCs is complicated and requires optimization of several variables including amount of excess lithium, annealing temperature, duration, and atmosphere that all influence morphology, stoichiometry and defect structure and consequently electrochemical performance [205, 210]. However, Ni-rich layered oxides such as NMC811 still suffer from long-term cycling and thermal instabilities [191, 207, 211–213].

Li_2MnO_3 stabilized $LiMO_2$ (where M = Mn, Ni, Co) can deliver high capacities (> 200 mAh·g^{-1}) when charged to high cut-off voltages (4.5 V) [214]. NMCs, blended with spinel oxides, are used commercially in electric vehicles such as the Nissan Leaf and Chevrolet Volt [215]. The two latter are out of the scope of the present work and will not be discussed further.

2.3 Phase transition upon cycling

For lithium-ion batteries with high-energy densities, in addition to high operating voltage and large rechargeable capacity, high cyclability and rate-capability are essential. Reversible capacity and cyclability depend on the structural stability of the host lattice in lithium insertion materials. In a stable electrode that realizes a lithium ion cell with long life (i.e. high cyclability), lattice strain or lattice volume change during lithium extraction/ insertion is ideally zero. When the changes in the lattice parameters during delithiation are considerable, the host structure undergoes a phase transformation which deteriorates its ability to reinsert lithium and leads to a lower cyclability. Cyclability generally depends on the cut-off voltage. Therefore, studying the delithiation/ lithiation reaction mechanism and the possible resulting phase transformations is of great importance.

The shape of the equilibrium voltage curve vs. state of charge provides insight about the thermodynamic behavior of the electrode material based on the relation between voltage and lithium chemical potential as stated in Equation (1.1). High-slope parts of the voltage curve relate to single-phase solid solutions, while plateaus correspond to two-phase regions. A two-phase region is commonly due to a first-order phase transition, while continuous phase transitions can be identified at inflection points in the voltage curve with no region of two-phase coexistence. In practice, continuous transitions are often difficult to differentiate from weak first-order transitions. Figure 2.9 shows and compares the voltage curve for $LiCoO_2$, $LiNiO_2$ and NMC111.

One interesting feature to notice in the interpretation of voltage curves in Figure 2.9 is the presence of a shift in voltage curves. In LNO (de)intercalation occurs at voltages about 0.2–0.3 V lower than those of LCO because nickel redox reactions involve e_g orbitals rather than t_{2g} orbitals [37]. Accordingly, charging to 4.2 V extracts 90% of the Li from LNO but only 50% of the Li from LCO.

As can be seen in Figure 2.9, the voltage curve of LCO exhibits many bumps and kinks indicating numerous phase transitions during (de)intercalation. The

reaction mechanism of Li_xCoO_2 upon Li deintercalation is intensively investigated by means of electrochemical studies, in situ and ex situ X-ray diffraction and can be summarized as follows: as Li is extracted from O3-$LiCoO_2$, the material first undergoes a first-order transformation from an insulating phase to a metallic phase [53, 54] resulting in a large plateau in the voltage curve. The voltage curve after the plateau is somewhat steeper showing a single-phase region. However, two bumps exist within this single-phase region, near $x = 0.5$ that correspond continuous (or nearly continuous) order-disorder phase transitions. These transformations are due to row ordering of Li^+ ions, which reduces the symmetry from rhombohedral to monoclinic (M or O3') [47, 216].

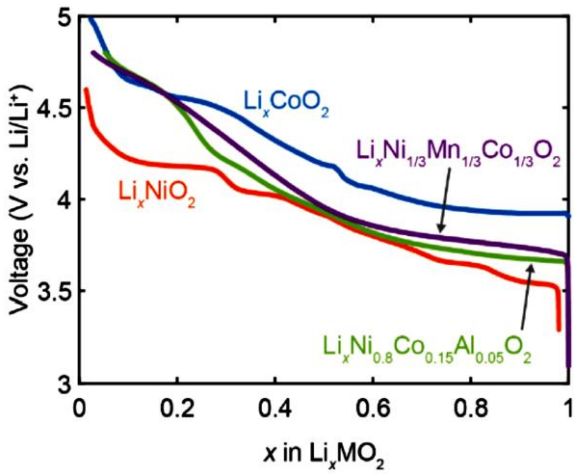

Figure 2.9: Voltage curve of the first charge of different lithium layered oxides. The graph is taken from Ref. [37] which takes the experimental data of Ref. [89] for $LiNiO_2$ and Ref. [217] for $LiCoO_2$.

By further delithiation, the transformation to an intermediate phase, $Li_{0.12}CoO_2$, (H1-3) occurs [40, 42]. This phase is a hybrid host structure that contains both the O3 and O1 stacking sequences. A voltage plateau which

appears as a small step around $x = 0.2$ relates to the two-phase coexistence of the O3 and H1-3 solid solutions. Delithiation proceeds via a two-phase region of H1-3 and O1. Finally, a transformation of the O3 phase into the O1-Li_xCoO_2 phase happens at $x \approx 0.05$ [64, 218].

Abe and Koyama [219] have developed the thermodynamic description of the O3-$LiCoO_2$–CoO_2 system using the CALPHAD approach with the estimated heat capacity based on the Neumann–Kopp rule. Cheng et al. [220] remodeled the same system using experimental heat capacity of O3-$LiCoO_2$ from Kawaji et al. [221], Emelina et al. [222], and Menetrier et al. [223]. Figure 2.10 compares the phase diagram of the O3-$LiCoO_2$-CoO_2 pseudo-binary system at 298 K based on the experimental studies [47, 64, 217, 224, 225], *ab initio* and Monte Carlo simulations [41, 226] and CALPHAD modeling [219, 220]. Although in experiments five phases including O3, O3(II), M or O3', H1-3 and O1 have been detected, both thermodynamic models consider the two O3 and O3(II) phases as the same O3 phase, due to lack of thermodynamic information.

However, it should be noted that the Li content on the x-axis in Figure 2.10 could be misleading because in each study, x is calculated from simple Coulomb counting (based on the passed current and mass of active material in electrode). This assumption can lead to systematic errors in estimating the state of charge because for example, a part of the cathode particles may not be electrically connected or there might be some uncertainty in the initial composition [47]. Radin et al. [37] has aligned the phase boundaries of $LiCoO_2$-CoO_2 pseudo-binary system with the features of the voltage curve of O3-$LiCoO_2$ to resemble the connection between the shape of the voltage curve and intercalation thermodynamics.

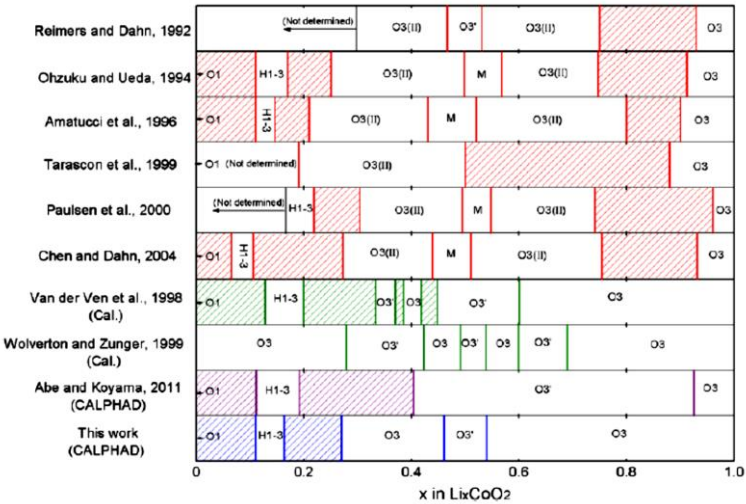

Figure 2.10: Phase diagram of the O3-$LiCoO_2$-CoO_2 pseudo-binary system at 298 K comparing the experimental studies by Reimers and Dahn [47], Amatucci et al. [64], Tarascon et al. [225] Paulsen et al. [224] and Chen and Dahn [217], *ab initio* and Monte Carlo simulations by Van der Ven et al. [41] and Wolverton and Zunder [226] and CALPHAD modeling by Abe and Koyama [219] and Chang et al. [220]. The diagram is taken from Ref. [220].

$LiNiO_2$ (LNO) also exhibits similar phase transitions upon delithiation that lead to plateaus and steps on the voltage curve, as can be seen in Figure 2.9. It is worth mentioning that the voltage curve of LNO in Figure 2.9 starts from x values less than one due to the presence of an inevitable off-stoichiometry in LNO. By deintercalation, O3 phase first goes through a first order phase transition to a monoclinic (M) phase, which is due to the Jahn–Teller effect of the Ni^{3+} ions and the ordering of Li ions [55, 56]. By further delithiation, another (first order) transition to a hexagonal phase and then a transition to the O1 phase takes place. The formation of the two-phase region of the hexagonal and O1 phase significantly changes the interlayer distance [57]. Chang et al. [58] used CALPHAD method and *ab initio* calculations for thermodynamic modeling of the $LiNiO_2$–NiO_2 pseudo binary system. The results of their calculations compared with the experimental studies [56, 84, 227–230] is

shown in Figure 2.11. The hexagonal phase termed as H3 in [84] corresponds to the O1 phase. Since the monoclinic distortion is quite small [84], the M phase is treated as ordered O3 phase in Chang's model. There are discrepancies between the structures reported by different researchers for the phase, which exists at x = 0.15-0.35 range in Li_xNiO_2. This structure is reported as a hexagonal phase with $R\bar{3}m$ space group and has been referred to as H2 [84, 228], R2 [56] or O3 phase [37, 231]. However, in the assessment of Chang et al. this phase has been described as H1-3 to keep an analogy with the $LiCoO_2$–CoO_2 system. It is important to notice that once a two-phase region consisting of the H1-3 and O1 coexists, as a result of a roughly 0.3 Å discontinuous gap in the interlayer distance between the two phases, the reversible lithium insertion/extraction into/from the structure becomes difficult, resulting in capacity loss [57, 95].

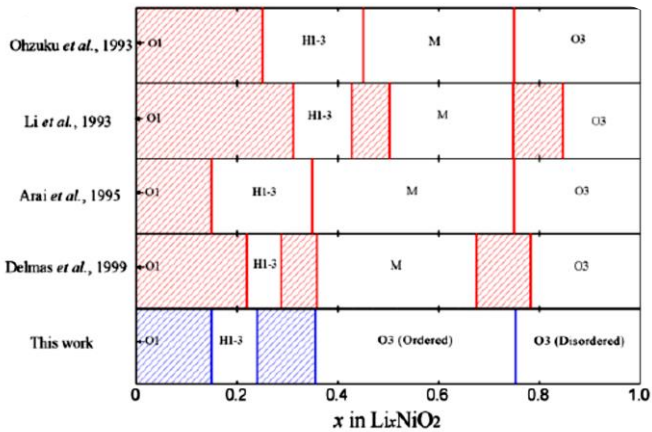

Figure 2.11: Phase diagram of the $LiNiO_2$-NiO_2 pseudo-binary system at 298 K comparing the experimental studies by Ohzuku and Ueda [57], Li et al. [84], Arai et al. [228], Delmas et al. [56] , and CALPHAD modeling [58]. The diagram is taken from Ref. [58] in which monoclinic phase is modeled as O3 ordered phase.

As can be seen in Figure 2.11, the phase boundaries and the state of charge corresponding to each phase transition vary among different studies. The

discrepancies between different experiments could be due to systematic errors in the calculation of state of charge, as described earlier for LCO. In addition, in Ni-based $LiMO_2$ cathodes this could originate from differences in the used XRD technique. Yang et al. [232, 233] found that there is a lag in the state of charge between the features of the voltage curve and phase transitions detected by in-situ XRD. They concluded that if the XRD diffraction patterns are collected in the transmission mode, the structural changes related to the bulk are reflected.

However, electrochemical information is related to structural changes on the surface. Yang et al. [232, 233] suggested using the XRD diffraction patterns in both transmission and reflection mode to solve this problem. Therefore, it seems reasonable to correlate the phase stability ranges to the features of voltage curve as suggested by Radin et al. [37] for both LCO and LNO. The pseudo-binary phase diagram of LCO and LNO by Radin et al. [37] is shown in Figure 2.12.

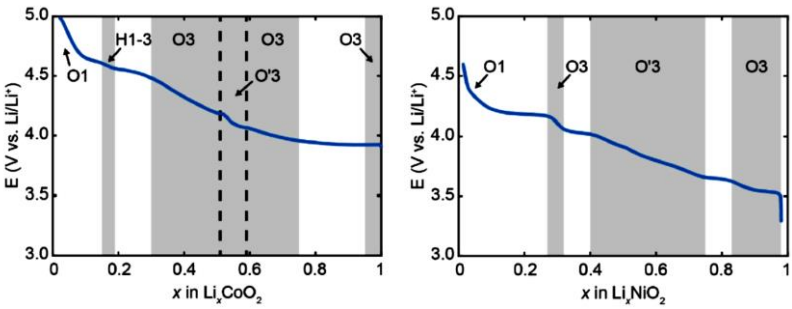

Figure 2.12: Relevant phase stability ranges shown on voltage curves of (a) the $LiCoO_2$-CoO_2 [217] (b) the $LiNiO_2$-NiO_2 [89] pseudo-binary systems. Grey and white regions represent single phase and two-phase equilibria, respectively. Picture taken from Ref. [37].

In the binary or ternary solid solutions of $LiNiO_2$-$LiMnO_2$-$LiCoO_2$ system, the phase transitions during lithium deintercalation becomes less complicated as the random distribution of transition metal cations on the transition metal layer

suppress the ordering between lithium vacancies and single transition metals. The redox potential of $Co^{3+/4+}$ in the layered structure is similar to that of $Ni^{3+/4+}$, leading to a continuous charge/discharge slope without any pronounced voltage plateaus, as can be seen in Figure 2.9 [127].

Phase transition upon delithiation in the $Li(Ni,Co)O_2$ solid solution are investigated by studying the chemically delithiated [234, 235] or electrochemically delithiated samples [134]. Chemically delithiated $Li_xNi_{0.85}Co_{0.15}O_2$ preserves the initial O3 structure over a wide region of $0.23 \leq x \leq 1$. At $x = 0.23$, a second hexagonal phase with smaller lattice parameters is formed resulting in a two-phase region when $x \leq 0.23$ [235]. Comparing the lattice parameters of the second hexagonal phase appeared at x = 0.23 with those of O1 phase in $LiNiO_2$-NiO_2 system [58], it seems that the new phase is of an O1 type and when $x \leq 0.23$, O3 and O1 coexist. Delmas et al. investigated $Li_xNi_{0.8}Co_{0.2}O_2$ upon electrochemical intercalation over the range of $0.4 \leq x \leq 1$ and found no phase transition during charge and discharge processes, but only a slight variation in cell parameters [134].

The structural phase transitions of $LiNi_{0.5}Mn_{0.5}O_2$ during extraction and insertion of Li were extensively studied by many groups [149–151, 232, 236–240]. Yang et al. [232] reported that , similar to LNO, $LiNi_{0.5}Mn_{0.5}O_2$ undergoes a phase transition from O3-$LiNi_{0.5}Mn_{0.5}O_2$ to another O3 phase (H2) with shorter "*a*" axis and longer "*c*" axis which is reversible on cycling. However, contrary to the $LiNiO_2$-NiO_2 system where H3 phase forms above 4.3 V, in $LiNi_{0.5}Mn_{0.5}O_2$ by further delithiation to 4.6 V the formation of a third hexagonal phase (H3 or O1) does not occur.

Arachi et al. observed a second order phase transition in $Li_{1-x}Ni_{0.5}Mn_{0.5}O_2$ from O3 to monoclinic phase (*C2/m*) between x = 0.2 and 0.3 [149, 240]. For $0 \leq x \leq 0.5$, $Li_{1-x}Ni_{0.5}Mn_{0.5}O_2$ can be represented as $Li_{1-x}(Ni^{2+}{}_{0.5-x}Ni^{3+}{}_{x}Mn^{4+}{}_{0.5})O_2$, i.e. a valence state change of Ni ions from Ni^{2+} to Ni^{3+}. Arachi et al. introduced a characteristics mechanism of lithium deintercalation for Li in $Li_{1-x}Ni_{0.5}Mn_{0.5}O_2$ which is different from LCO and LNO and involves migration of lithium ions from the octahedral 2a site to the tetrahedral 4i sites [239]. However, Manthiram et al. [150] reported that chemically delithiated $Li_xNi_{0.5}Mn_{0.5}O_2$ maintain the initial O3 structure for the full range of $0 \leq x \leq 1$.

Bréger et al. [237] used a combined experimental and first principle calculation approach and investigated the structural changes and the extraction of Li ions from different sites in $Li_xNi_{0.5}Mn_{0.5}O_2$ which is charged to voltages above 4.5 V. In later investigations by Yabuuchi et al. [236] and Li et al. [238] on the same material, it was found that by charging the Li / $LiNi_{0.5}Mn_{0.5}O_2$ cells to voltages as high as 5.3 V, nearly all of the nickel ions migrate from the lithium layer to the transition metal layer and O3 phase (cubic-close-packed oxygen array) transforms to O1 structure (hexagonal-close-packed oxygen array). Although a part of the nickel returns to the lithium layer upon discharge, such a high voltage charging permanently reduces the interlayer mixing of lithium and nickel, increases the layered character of $Li_xNi_{0.5}Mn_{0.5}O_2$ and improves its reversible capacities in the voltage range between 4.5 and 2.0 V.

$Li_{1-x}Ni_{1/3}Mn_{1/3}Co_{1/3}O_2$ (NMC111) has also been studied for structural stability during lithium deintercalation. Studies performed by Yin et al. [241] on the chemically delithiated samples suggest that the initial O3 phase retains its original stacking with only ~1% volume change until about 0.7-0.75 Li per formula unit is extracted. Choi and Manthiram also reported that $Li_{1-x}Co_{1/3}Ni_{1/3}Mn_{1/3}O_2$ is structurally stable for at least $(1-x) > 0.23$ by maintaining the parent O3 structure and chemically stable up to $(1-x) = 0.35$ without tendency for oxygen release [242]. Further delithiation results in an irreversible transition to O1 phase (trigonal; $P\bar{3}m1$) which exhibits a 5.3% decrease in *c* axis [241–243]. To prevent irreversible structural changes, an optimum cutoff voltage of 4.3-4.4 is suggested [241].

Yabuuchi and Ohzuku [160] found around 1.9% increase in *a* axis and 1.4% decrease in *c* axis by electrochemical removing of up to 0.67 Li per formula unit of NMC111, resulting in an almost constant unit cell volume. Even beyond this level of delithiation, later ex-situ XRD and electrochemical investigations by Yabuuchi et al. [167] and neutron diffractions by Kim and Chung [176] found negligible volume changes during charge/discharge. They claimed that there is no evidence of formation of any phase with O1 stacking in the entire range of *x* in $Li_xCo_{1/3}Ni_{1/3}Mn_{1/3}O_2$ during electrochemical delithiation; instead, the reaction proceeds topotactically in the O3 phase over the entire range of *x*. Ohzuku et al. attributed the different behavior observed for the formation of

O1 phase during chemical and electrochemical delithiation to the oxidation method. The electrochemical oxidation in 1 M $LiPF_6$ EC/DMC under a galvanostatic condition is milder than the chemical oxidation with NO_2BF_4 in acetonitrile [167].

During the lithium deintercalation of NMC532, no formation of O1 phase was detected, although transformation to spinel and rock salt phase at high cut-off voltage (≈ 4.8 V) was observed on the surface of the NMC particles. The absence of O1 phase could be attributed to less sliding of the MO_2 slabs due to higher degree of Li-Ni mixing [244]. The *dQ/dV* curve resulting from the galvanostatic cycling of NMC532 half cells (vs. Li anode) in the voltage window of 3.0 V and 4.6 V exhibits a couple redox peak at around 3.75 and 3.72 V [245].

Shu et al. [186] studied the structural evolution in layered $LiNi_{0.5}Mn_{0.2}Co_{0.3}O_2$ by in-situ XRD for two cut-off voltages of 4.3 V (0.606 Li per formula) and 4.9 V (0.979 Li per formula). They found that the structural changes in the higher working potential region is more irreversible and electrochemical properties is poorer. This behavior is attributed to the formation of hexagonal phase H3 (equivalent to O1 phase) and electrolyte irreversible decomposition in high potential regions. Based on in-situ XRD results, H3 phase starts forming at around 4.7 V in the charge process corresponding to 0.681 Li per formula or a specific capacity of 188.2 $mAh \cdot g^{-1}$. This phase is considered to be the main "structure destroyer" resulting in poor cyclability and low reversible capacity.

Structural changes of $Li_xNi_{0.6}Mn_{0.15}Co_{0.25}O_2$ during cycling (3–4.5 V vs. Li^+/Li) investigated by in-situ synchrotron XRD also showed a solid-solution reaction with only 4% lattice volume change. No new H2 phase formation is detected in this potential region, contrary to $LiCoO_2$ and $LiNiO_2$ [246]. In the differential capacity curves of $LiNi_{0.6}Mn_{0.4-x}Co_xO_2$ (x = 0.05–0.3, 2.8–4.5 V vs. Li^+/Li), only one pair of redox peaks appeared in the voltage range of 3.7- 4.1 V [195].

$Li_xNi_{0.8}Mn_{0.1}Co_{0.1}O_2$ (NMC811) cathode materials synthesized by solid-state reaction are studied using ex-situ structural studies including X-ray diffraction

and Raman scattering. It is found that the host layered structure is maintained during the electrochemical lithiation–delithiation processes in the 3–4.5 V range and only the lattice parameters change systematically [247]. However, Yang et al. [248, 249] reported that the destructive H2 to H3 phase transition occurs during the discharge of $LiNi_{0.8}Co_{0.1}Mn_{0.1}O_2$ at about 4.2V and showed that small amounts of Li_2MnO_3 can suppress the destructive phase transition.

Noh et al. [250] investigated the fundamental electrochemical properties of different NMC compositions between 3.0 and 4.3 V at 0.1 C-rate in half cell configurations. The initial charge- discharge curves of different NMC and corresponding differential curves are shown in Figure 2.13. As can be seen, an increase of the Ni content resulted in a decrease in capacity retention. The differential curve of NMC 811 cell (Figure 2.13-f) showed four distinct redox peaks which are attributed to the multiphase transitions of hexagonal to monoclinic (H1 / M), monoclinic to hexagonal (M / H2), and hexagonal to hexagonal (H2 / H3) phases [250].

Despite the profitable effects of solid solution approach for mixing of Ni, Mn and Co in NMCs, these compounds still suffer from irreversible phase transitions on the surface and mechanical degradations. Various techniques such as XAS [251], S/TEM [252] and X-ray photoelectron spectroscopy (XPS) [253] have been used to detect surface transitions to spinel and rock salt phases after electrochemical cycling. Mechanical degradation like micro cracks, similar to those found in the other layered oxides, has been observed in NMC materials using SEM and TEM [254]. Another degradation mechanism, the dissolution of transition-metal ions and their deposition on the anode has also been observed [114, 118].

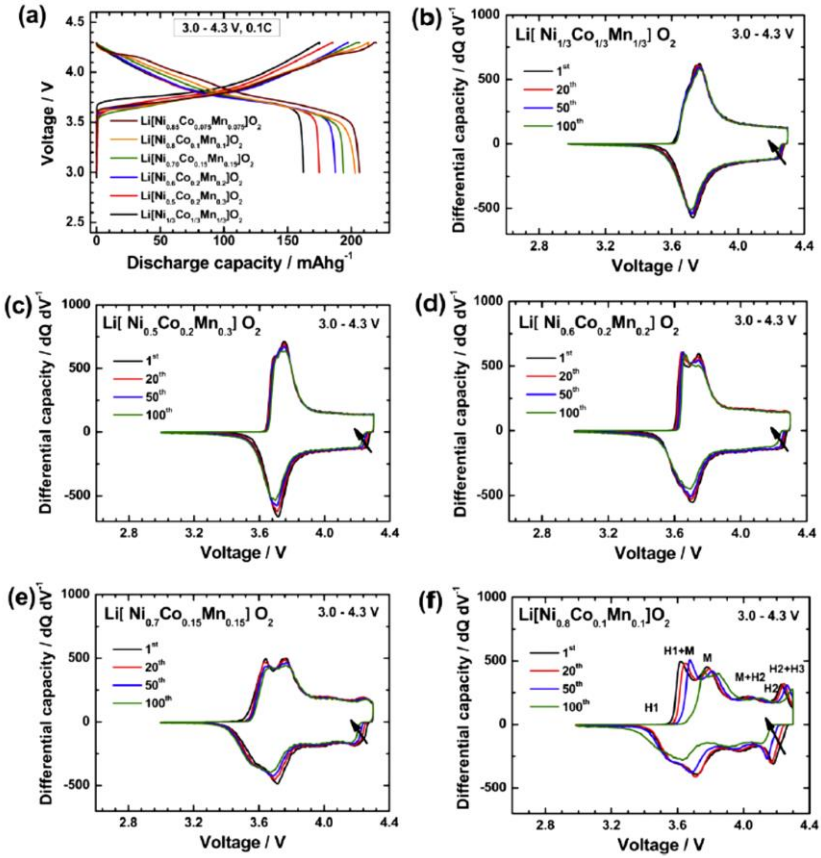

Figure 2.13: The graph retrieved from Ref. [250] showing (a) the initial charge- discharge curves of NMC versus Li anode between 3.0 and 4.3 V at 0.1 C-rate and corresponding differential curves versus voltage for (b) $LiNi_{1/3}Co_{1/3}Mn_{1/3}O_2$, (NMC111), (c) $LiNi_{0.5}Co_{0.2}Mn_{0.3}O_2$ (NMC532), (d) $LiNi_{0.6}Co_{0.2}Mn_{0.2}O_2$ (NMC622), (e) $LiNi_{0.7}Co_{0.15}Mn_{0.15}O_2$ and (f) $LiNi_{0.8}Co_{0.1}Mn_{0.1}O_2$ (NMC811).

2.4 Thermodynamic properties

As described in Section 2.3, the lithiation/delithiation mechanisms in electrodes during electrochemical cycling of Li-ion batteries is generally

investigated using conventional physical-chemical techniques such as X-ray and neutron diffraction or physical spectrometry. However, it has been shown that thermodynamic studies can also be employed as a useful tool in the characterization of electrode materials and revealing useful information about the structural evolution in active materials [6].

In spite of the relatively large amount of research performed on the electrochemistry of the $LiNi_xMn_yCo_{1-x-y}O_2$ materials, there are limited data reported on the thermodynamic properties of selected layer-structured compositions in the $LiNiO_2$– $LiMnO_2$–$LiCoO_2$ system. Thermodynamic data are important as an input for the thermodynamic modelling of the multicomponent systems. These data are correlated with the open circuit voltages, based on the Gibbs free energy descriptions of the assessed phases [255]. In addition, thermodynamic properties, such as the heat capacities of active materials are important input data for the modelling of the thermal behavior of lithium ion cells and batteries and the development of thermal management systems.

Hertz et al. [256] determined the low temperature heat capacities of Li_xCoO_2 and its chemically delithiated compounds (x = 1.00, 0.78, 0.70, 0.62, 0.58, and 0.51) from 2 to 15 K using a physical property measurement system (PPMS) from Quantum Design. The heat capacity of stoichiometric $LiCoO_2$ in a wider range is measured by Kawaji et al. from 13 to 300 K using an adiabatic calorimetry [221] and by Menetrier et al. from 1.8 to 300 K using the relaxation method in a helium Quantum Design PPMS cryostat [223]. In addition, Miyoshi et al. used a similar method to measure the heat capacity of a single crystal $Li_{0.66}CoO_2$ from 100 to 200 K [257]. Emelina et al. [222] measured the heat capacity of both low- and high-temperature modifications of $LiCoO_2$ using differential scanning calorimetry from 140 to 570 K and from 180 to 570 K, respectively. Gotcu-Freis et al. [258] also used differential scanning calorimetry with three different devices and continuous and step methods to conduct a more comprehensive measurement of the heat capacity of $LiCoO_2$ (commercial sample with $Li_{0.977}CoO_2$ composition) in a more extended temperature range of 160 to 953 K. In addition, the enthalpy increment of $LiCoO_2$ was measured using transposed temperature drop calorimetry at

T = 974.15 K and showed good agreement with the enthalpy increment derived from heat capacity function. Lately, Jankovsky et al. [259] experimentally determined the heat capacity of stoichiometric $LiCoO_2$ using PPMS from 2 to 257 K and using the DSC with step method from 261 to 358 K. In the latter work, also the enthalpy increments of $LiCoO_2$ from room temperature to final temperatures between 573 and 1273 K is measured using drop calorimetry which showed very good agreement with the results of Gotcu-Freis et al. [258].

First principle calculations have been used to obtain the constant volume heat capacity of $LiCoO_2$ from 0 to 340 K [260] and from 0 to 800 K [261]. Heat capacity of $LiCoO_2$ is estimated and assessed in some works. To estimate the heat capacity of $LiCoO_2$ based on heat capacity of binary oxides, Zhang et al. [262] assumed that $LiCoO_2$ is an ideal solution between Li_2O and Co_2O_3. The heat capacity of unstable Co_2O_3 is calculated from the available data for Co_3O_4 and CoO. As described in Section 2.3, in the thermodynamic description of the O3-$LiCoO_2$–CoO_2 system developed by Abe and Koyama, the heat capacity of LiCoO2 is estimates by assuming the Neumann-Kopp rule based on the assessed heat capacities of Li, Co, and O_2, while in the assessment of Chang et al. [220] experimental heat capacity of O3-$LiCoO_2$ from Kawaji et al. [221], Emelina et al. [222], and Menetrier et al. [223] are used. Figure 2.14 retrieved from Ref. [258], outlines the thermal dependency of heat capacity of $LiCoO_2$ determined through different experimental measurements by Kawaji et al. [221], Menetrier et al. [223], Emelina et al. [222], Gotcu-Freis et al. [258], and assessed heat capacites by Zhang et al. [262], Abe and Koyama [219] and Chang et al. [220].

Kawaji et al. measured the heat capacity of $LiNiO_2$ (real stoichiometry of $Li_{0.99}Ni_{1.01}O_2$) from 13 to 300 K using adiabatic calorimetry [263]. There is no experimental heat capacity data of $LiNiO_2$ above room temperature. First principles calculations were used to calculate the constant volume heat capacities of $LiNiO_2$ and $LiMnO_2$ with monoclinic structures (*C2/m* space group) from 0 to 800 K [261].

Although no experimental data are available for the delithiated phases, the enthalpies of formation for the ordered O3–Li_xNiO_2 ($0 < x < 1$) phases relative to O3–NiO_2 and O3–$LiNiO_2$ have been obtained by *ab initio* calculations by

Ceder et al. [55]. Chang et al. used *ab initio* calculation [264] and CALPHAD modelling [58] to obtain enthalpy of formation at 0 K and 298 K, respectively for O3, H1-3 and O1 phases in the NiO_2–$LiNiO_2$ system [10]. In Chang's model [58], the Gibbs free energy function of $LiNiO_2$ was developed by the assessed Gibbs energies of the pure elements Li, Ni, and O_2. However, an extra term was added that enabled fitting the calculated heat capacity of $LiNiO_2$ at 300 K to the measured data from Kawaji et al. [263].

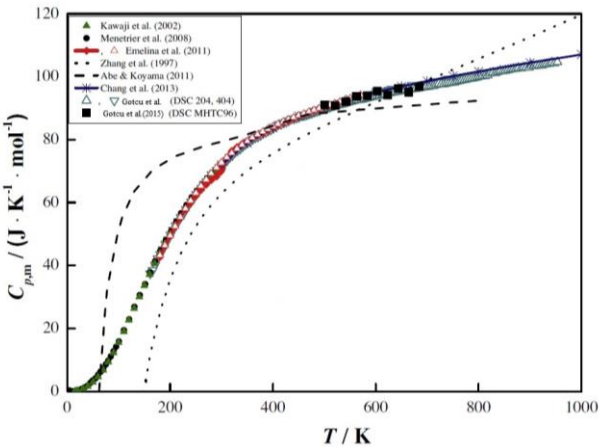

Figure 2.14: The graph retrieved from Ref. [258] summarizing the thermal dependence of heat capacity of $LiCoO_2$ determined through different experimental measurements by Kawaji et al. [221], Menetrier et al. [223], Emelina et al. [222], Gotcu-Freis et al. [258], and assessed heat capacities by Zhang et al. [262], Abe and Koyama [219] and Chang et al. [220].

The temperature dependence of the heat capacity of $LiNi_{0.5}Mn_{0.5}O_2$ was measured by Chernova et al. [265] using a Quantum Design PPMS system (Physical Property Measurement System) in temperature range from 300 to 2 K and compared with the heat capacity data of isostructural compounds, $LiCoO_2$ [221] and $Li_{0.99}Ni_{1.01}O_2$ [263], as shown in Figure 2.15. In a work similar to Ref. [261] for $LiCoO_2$, $LiNiO_2$ and $LiMnO_2$, constant volume heat

capacities for $LiMn_{0.5}Ni_{0.5}O_2$ and $LiCo_{0.5}Ni_{0.5}O_2$ chemistries from 0 to 800 K were also calculated [266].

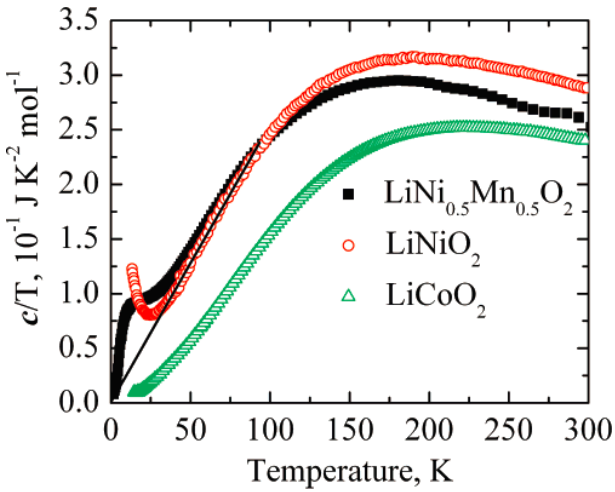

Figure 2.15: The experimentally measured specific heats of $LiNi_{0.5}Mn_{0.5}O_2$ by Chernova et al. [265] compared with those of isostructural compounds, $LiCoO_2$ [221] and $Li_{0.99}Ni_{1.01}O_2$ [273] by Kawaji et al. The graph is taken from Ref. [265].

As shown in Figure 2.16, the heat capacity of Li_2MnO_3 was determined by Cupid et al. [267] using differential scanning calorimetry on three devices with the step method and the obtained specific heat capacity was compared with that estimated based on stoichiometric amounts of Li_2O and MnO_2 according to the Neumann-Kopp approximation.

In an interlaboratory study comprising of five laboratories with different operators, and different employed methods, devices, temperature ranges, gas atmospheres and crucible materials, the heat capacity of a commercial NMC111 sample was determined using differential scanning calorimetry. The heat capacity of the NMC111 sample from 315 K to 1020 K is obtained based on evaluation of the data from each laboratory, with an expanded reproducibility uncertainty of less than 1.22%, as shown in Figure 2.17. The

heat capacity of the NMC sample with the composition of $Li_{1.04}Ni_{0.33}Mn_{0.32}Co_{0.31}O_2$ was measured using the continuous method on two differential scanning calorimeters from 273 to 573 K in the framework of a transport properties study of cathode materials [268].

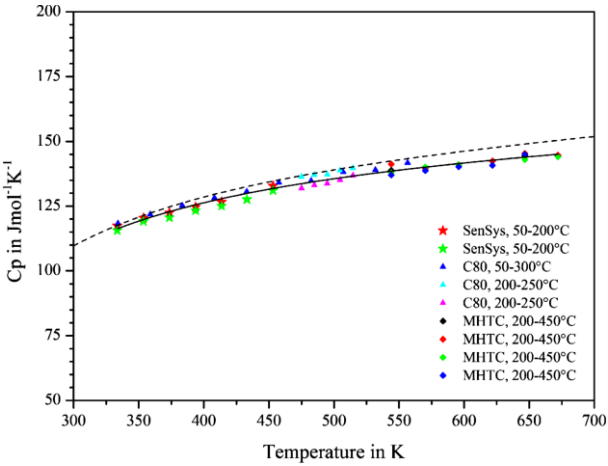

Figure 2.16: Experimentally-determined heat capacity of Li_2MnO_3 by Cupid et al. [267] from 323 to 673K using three different DSCs. The evaluated Maier-Kelley polynomial description for heat capacity and the Neumann-Kopp estimated heat capacity are shown as solid line dashed line, respectively.

The enthalpy of formation of $LiCoO_2$ and its chemically delithiated compounds at 298 K has been determined using high temperature oxide melt drop solution calorimetry by Wang et al. [269], Wang and Navrotsky [270] and Gotcu-Freis et al. [258]. Figure 2.18 taken from Wang et al. [269] summarizes the experimental values of enthalpies of formation from oxides as a function of x in Li_xCoO_2 determined in the above-mentioned work. The enthalpy of formation for stoichiometric $LiCoO_2$ is also determined by *ab initio* calculations by Ceder et al. [271] and Chang et al. [272] and assessed by CALPHAD method by Abe and Koyama [219] and Change et al. [220]. The

enthalpy of formation of $LiNiO_2$ at 298 K has been determined by Wang and Navrotsky [7] using drop solution calorimetry.

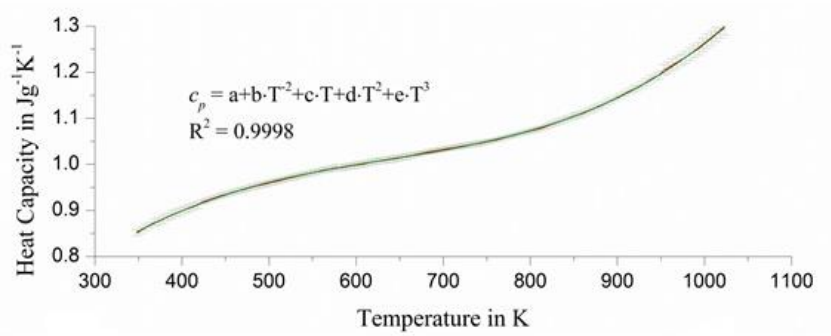

Figure 2.17: Analytic function based on Shomate equation, expressing the heat capacity of the NMC 111 sample and fits to the measured data from all laboratories taken from Ref. [273]. Coefficients of the equation are as follows: A = 0.36069, B = -1.06982×10^4, C= 0.00291, D = -4.49104×10^{-6}, E = 2.49066×10^{-9}.

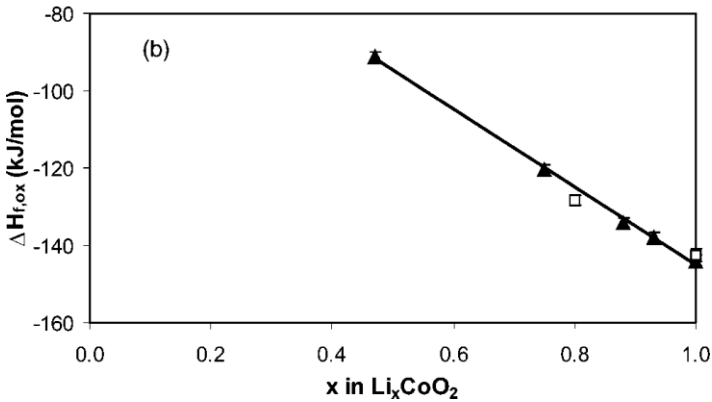

Figure 2.18: The enthalpy of formation from oxides and oxygen as a function of *x* in Li_xCoO_2 taken from Ref. [269]. The filled and open symbols represents samples prepared with NO_2BF_4 in acetonitrile medium and with acid delithiation, respectively. Line is the least-squares fit for the filled symbol data points.

The enthalpies of formation of $LiNi_{1-x}Co_xO_2$ (x = 0, 0.25, 0.5, 0.75, 1) stoichiometries were determined by Wang and Navrotsky [270] using high temperature oxide melt drop solution calorimetry in molten $3Na_2O{\cdot}4MoO_3$ and $2PbO{\cdot}B_2O_3$ solvents at 701 °C. The obtained values of enthalpies of formation from the oxides are shown in Figure 2.19. The determined enthalpies of formation from the elements are -678.2 ± 2.2 kJ·mol^{-1} and -593.0 ± 1.6 kJ·mol^{-1} for $LiCoO_2$ and $LiNiO_2$, respectively. These results showed that $LiCoO_2$ is significantly more stable than $LiNiO_2$ and that both compounds form an almost ideal solid solution with a small positive enthalpy of mixing.

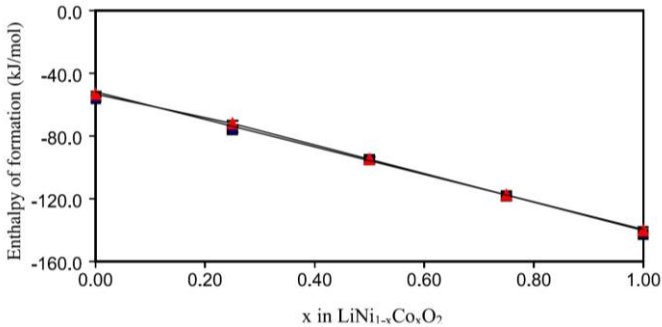

Figure 2.19: The enthalpies of formation of $LiNi_{1-x}Co_xO_2$ in kJ·mol^{-1} as a function of x for selected compositions (x = 0, 0.25, 0.5, 0.75, 1) determined by Wang and Navrotsky [270] using high temperature oxide melt drop solution calorimetry in molten $3Na_2O{\cdot}4MoO_3$ and $2PbO{\cdot}B_2O_3$ solvents at 701 °C. Triangular and circular data points are related to lead borate calorimetry and sodium molybdate calorimetry, respectively.

The enthalpy of formation of $LiNi_{1/3}Mn_{1/3}Co_{1/3}O_2$ was determined by Idemoto and Matsui [274] using acid solution calorimetry as -649.74 ± 2.05 kJ·mol^{-1}, showing a more positive value than that of $LiCoO_2$. This result [274] would suggest reduction in stability and electrochemical performance due to partial substitution of Co with Mn and Ni. However, this observation is in contrast with the works from Reed and Ceder [147], Ammundsen and Paulsen [148], Makimura and Ohzuku [57, 144, 216] and Martha et al. [275] and who all

indicated improved structural stability and capacity retention of the NMC electrodes comparing $LiCoO_2$. Hence, the enthalpy of formation data obtained by Idemoto and Matsui [274] needs to be revisited.

The enthalpy of formation of Li_2MnO_3 was measured by Cupid et al. [267] using high temperature oxide solution calorimetry in molten $3Na_2O{\cdot}4MoO_3$. The enthalpy of formation of this compound per one mole of total atoms is compared in Figure 2.20 with the same experimentally determined parameter for other $LiMO_2$ compounds, including $LiCoO_2$, $LiNiO_2$, and the $LiNi_{1-x}Co_xO_2$ solid solutions by Wang and Navrotsky [270], orthorhombic and monoclinic $LiMnO_2$ by Wang and Navrotsky [105], and $Li_{1+x}Mn_{2-x}O_4$ spinels by Wang and Navrotsky [276] and by Cupid et al. [277]. The results shows the Li_2MnO_3 has the lowest enthalpy of formation comparing investigated layered and spinel compounds, indicating its higher thermodynamic stability.

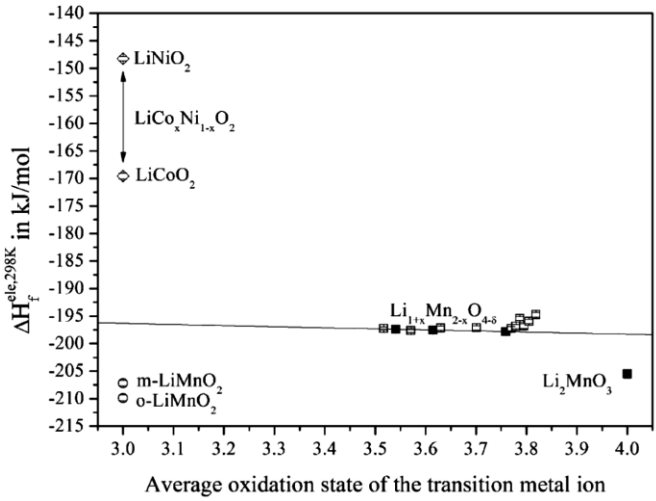

Figure 2.20: Enthalpy of formation from the elements per mole of atoms vs. average oxidation state of the transition metal cation for Li_2MnO_3 [267], $LiCoO_2$, $LiNiO_2$, and the $LiNi_{1-x}Co_xO_2$ solid solutions [270], and $Li_{1+x}Mn_{2-x}O_4$ spinels [277] (filled squares) and [276] (open squares), and orthorhombic and monoclinic $LiMnO_2$ [105]. The graph is taken from Ref. [267].

Measurements of the temperature dependence of open circuit voltage (OCV) or entropy term or potentiometric measurements has been used by Bach et al. [278] and Yazami's group [279, 280] to correlate the evolved ΔS function with the structural changes in the active materials during charge and discharge and get a better understanding of the electrochemical behavior of lithium transition metal oxides. Yazami [279] has developed an electrochemical thermodynamic measurement system (ETMS) to measure the temperature dependence of the open circuit voltage of lithium ion batteries at different state of charges. Using this measurement system, Yazami [279] and Reynier et al. [280] determined the entropy changes of the lithiation reaction of Li_xCoO_2 for $0.5 < x \leq 1.0$, as shown in Figure 2.21.

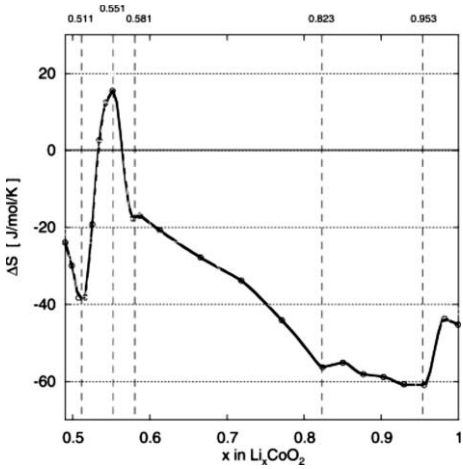

Figure 2.21: Entropy changes of the reaction of lithiation of $LiCO_2$ as a function of lithium concentration (x). The graph is retrieved from Ref. [279].

In this graph, six areas can be recognized. While sharp decreases and increases in the $\Delta S(x)$ function show phase transitions boundaries, uniform changes indicate solid-solution behavior. A plateau-shape entropy change is attributed to a two-phase region. As a conclusion, their studies show that entropy measurements enable higher accuracy in definition of transition boundaries

comparing in situ techniques such as XRD and X-ray absorption spectrometry, due to quasi-equilibrium condition of these thermodynamic measurements. Entropy studies are even more sensitive to phase transitions than OCV measurements. Lepple [281] performed similar measurement on $LiCoO_2$ with similar cell chemistry and configuration, yet using a sensitive temperature chamber to change the temperature of the cell and a high accuracy electrochemical cycler to read the OCV. The results of Lepple [281] has quite good agreement with those of Reynier et al. [280].

To the best of my knowledge, the entropy measurements on NMC compounds using the potentiometric method have been reported only by Viswanathan et al. [282], Williford et al. [283] and Eddahech et al. [284]. In addition a new method was developed by Schmidt et al. [285]. Though, they utilized the results mainly for developing a thermal model to predict the heat generation in LIBs during cycling and not much attention is paid to the interpretation of entropy profile. Besides, in these reports it is not stated which composition of NMC was investigated.

3 General Experimental Techniques

3.1 Synthesis method: Sol-Gel

Lithium mixed transition metal oxides were traditionally synthesized using the conventional solid-state method. This includes thoroughly mixing lithium salts such as lithium hydroxide, lithium carbonate or lithium nitrate with oxides, hydroxides or carbonates of the respective transition metals, pelletizing and firing the pellet at higher temperatures. However, this method usually requires several cycles of intermittent grinding, re-pelletizing and heating for a relatively long calcination time to ensure a complete reaction and a homogenous product. In addition, the final product usually has large grain size with a wide-ranging size distribution. Electrochemical studies have shown that a smaller particle size of active material in cathode greatly improves the capacity, reversibility, and polarization [286].

Solution-based methods, also referred to as wet chemistry or soft chemistry ("chemie doux" in French) routes, offer the advantages of homogenous mixing of the starting materials at the atomic or molecular level, shorter heating times, lower synthesis temperatures, uniform particle distributions, better crystallinity and smaller particle size at submicron level of the final powder product in comparison to solid state reactions [287–289]. Sol-gel is one of the most popular and commonly used solution techniques in the laboratory scale since it does not require specific reactors as in the case of coprecipitation method. Sol-gel relies on hydroxylation and condensation of molecular precursors and obtaining a metal oxide network [290]. The main steps of the method [287] can be summarized as shown in Figure 3.1.

In the sol-gel process, a gel, which is a viscous three-dimensional polymeric network, is formed upon gentle heating of a sol, which is a suspension of small particles dispersed in a liquid phase. The gel is then dried to obtain the

precursor for further heat treatments. In acid-assisted sol-gel process, in general a carboxylic acid serves as the chelating agent.

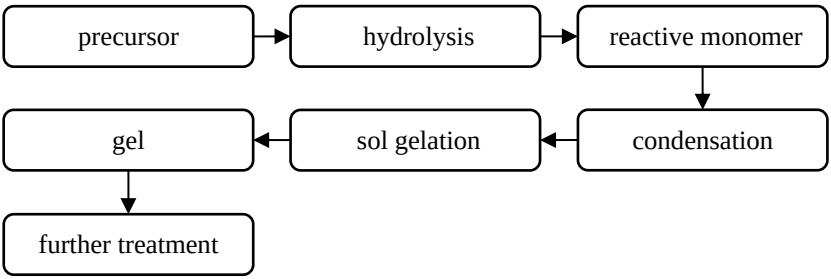

Figure 3.1: The main steps of the sol-gel method [287].

Sol-gel method has shown great improvement in the preparation of cathode active materials such as $LiMn_2O_4$ [291], $LiCoO_2$, $LiNiO_2$, $LiNi_{0.8}Co_{0.2}O_2$ [83] and different NMC compositions. Lee et al. [292] successfully used acetates as lithium and transition metal salts and adipic acid as chelating agent in their sol-gel process to prepare $LiMn_2O_4$. The mechanism of gel formation is described as a chemical bonding between carboxylic group in the adipic acid and the metal ions so that they become extremely viscous gelled polymeric resins [292].

In the present work, the sol-gel method similar to the work of Lee et al. [292] and Cupid et al. [293] using metal acetates and adipic acid as the chelating agent was used to synthesize the investigated self-made samples.

In our preparation method, first the required amounts of $Li(CH_3COO)\cdot 2H_2O$, $Mn(CH_3COO)_2\cdot 4H_2O$, $Ni(CH_3COO)_2\cdot 4H_2O$ and $Co(CH_3COO)_2\cdot 4H_2O$, and adipic acid $(CH_2)_4(COOH)_2$ were dissolved in distilled water. The amounts of the metal acetate were chosen based on the final stoichiometries of the NMC compounds, whereas the amount of adipic acid was selected to yield an acid to total metal ion ratio of 1:1. The origin and purities of the starting chemicals are listed in Table 3.1

Table 3.1: Details of the raw materials used in the sol-gel process.

raw material	chemical formula	source	mass fraction purity
Lithium acetate di-hydrate	$Li(CH_3COO)\cdot 2H_2O$	Alfa Aesar	≥ 99.9%
Manganese (II) acetate tetrahydrate	$Mn(CH_3COO)_2\cdot 4H_2O$	Merck KGaA	≥ 99.0%
Nickel acetate tetrahydrate	$Ni(CH_3COO)_2\cdot 4H_2O$	Sigma-Aldrich	≥ 99.0%
Cobalt acetate tetrahydrate	$Co(CH_3COO)_2\cdot 4H_2O$	Merck KGaA	≥ 99.0%
Adipic acid	$C_6H_{10}O_4$	Merck Schu-chardt OHG	≥ 99%

[a] Purity expressed in mole fraction

The pH value of the resulting solution at room temperature was adjusted to approximately 6.5 by dropwise addition of ammonium hydroxide. The solution was kept at 80-90 °C under constant stirring for 5-6 hours to obtain a viscous gel. The gel was dried in a vacuum drying oven (Thermo Scientific, Heraeus) at 120 °C for 1 day and then ground using an agate mortar. Afterwards, the ground precursor was placed in an alumina crucible with silica lining and pre-calcinated at 500 °C for 10 hours in air using a box furnace (Nabertherm P330, Germany). Such a heat treatment with a heating rate of 2 °C/min from room temperature to 500 °C serves to remove the organic content. The obtained powder was then ground and placed in a pure alumina crucible for final calcination. The final calcination temperature was chosen between 700 and 1000 °C, depending on the respective NMC composition. Unless stated otherwise, all samples used in this study are heat treated at only one optimum final temperature to achieve pure single-phase material. In some cases, different final calcination temperatures are tried for the sample to study the effect of heat treatment condition on the properties of the NMC material. In all cases, the samples were heated for 15 hours at the final temperature and then quenched in air by removing from the hot furnace.

In the present work, two series of NMC samples are produced including $LiNi_xMn_xCo_{1-2x}O_2$ with equimolar amounts of Mn and Ni cations and $LiNi_{0.8-y}Mn_yCo_{0.2}O_2$ with constant Co mole amount while altering Ni and Mn amounts. The $LiNi_xMn_xCo_{1-2x}O_2$ samples, and the $LiNi_{0.8-y}Mn_yCo_{0.2}O_2$ samples with y = 0, 0.1, 0.2, 0.3 and 0.4 were synthesized by the sol-gel method using metal acetates and adipic acid, as described above. For convenience, a common abbreviation convention is employed here to express the composition of samples. In this way, each composition is shown in an "NMCxyz" form, where the ratio of Ni, Mn and Co in the NMC compound is x:y:z and x, y and z are smallest whole numbers. For examples, $LiNi_{0.6}Mn_{0.2}Co_{0.2}O_2$ and $LiNi_{0.5}Mn_{0.5}O_2$ are labeled as NMC622 and NMC110, respectively. In Figure 3.2 the experimentally investigated compositions are shown on the Gibbs triangle by red squares and blue circles for the first and second series, respectively. The sample with x = 1/3 and samples with y = 0.2, 0.3 and 0.4 correspond to the commercially-important compositions NMC111, NMC622, NMC532 and NMC442, respectively.

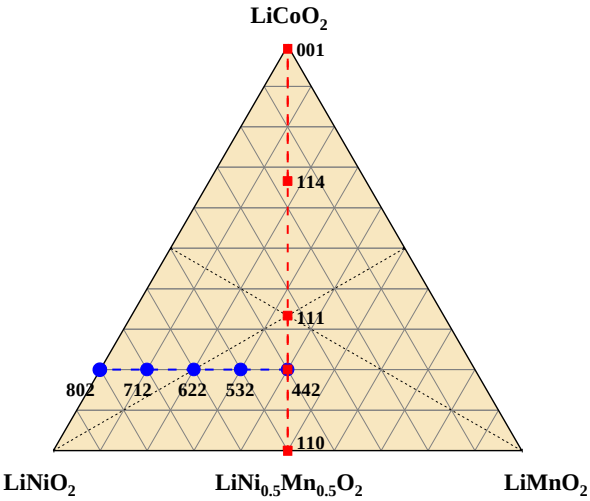

Figure 3.2: Compositional Gibbs triangle for the $LiNiO_2$-$LiMnO_2$-$LiCoO_2$ (NMC) system showing the $LiNi_xMn_xCo_{1-2x}O_2$ series (red squares) and the $LiNi_{0.8-y}Mn_yCo_{0.2}O_2$ series (blue circles).

In the $LiNi_xMn_xCo_{1-2x}O_2$ sample series, that were prepared and studied firstly, lithium acetate was added to the initial mixture in a stoichiometric ratio. However, as some deviation from the stoichiometric lithium were observed after final calcination and because of the importance of excess lithium for the preparation of stoichiometric $LiNiO_2$ [294, 295] for the preparation of the Ni-rich NMCs (second series), 3 mol% of excess lithium was added to the initial sol-gel ingredients. The use of excess lithium compensated for lithium loss during preparation and heat treatment processes [209]. The reason of lithium loss is still subject of debate. Some researchers believe that there is a lithium loss at higher temperatures because of volatilization of Li salts [296].

3.2 Materials characterization

In the following, the methods used for the characterization of the studied material in the present work are generally described. Specific parameters and test programs corresponding to different chapters are declared in the same chapter.

3.2.1 Inductive coupled plasma - optical emission spectrometry (ICP-OES)

The Li, Ni, Mn, and Co contents in the $LiNi_xMn_yCo_{1-x-y}O_2$ samples after the final calcination were accurately determined by inductively coupled optical emission spectroscopy (ICP-OES). For the preparation of the solution, about 50 mg (triplicate, weighing accuracy ± 0.05 mg) of the powder sample were dissolved in 6 mL hydrochloric acid and 2 mL nitric acid at T = 80 °C for 4 h in Teflon container with closed lid and heated in a graphite furnace. An iCAP 7600 Duo from Thermo Fisher Scientific with an echelle spectrometer equipped with segmented-array charge-coupled detector was used for the ICP-OES measurements. This allowed for the measurement of the different emission lines of analytic and internal standards simultaneously. For each sample, three solutions are made and the measurements are repeated three

times. The analysis of the main components was accomplished with four different calibration solutions and two internal standards (Na, Sc).

3.2.2 Carrier gas hot extraction (CGHE)

The oxygen content of the $LiMO_2$ sample is analyzed by the method of carrier gas hot extraction (CGHE) using a commercial oxygen/nitrogen analyzer TC600 (LECO). The oxygen concentration is calibrated with the certified standard steel powder JK 47. The calibration is verified with Mn_3O_4, NiO and Co_3O_4. The calibration range was close to the concentration of the samples. The weight of the standards and the samples were in the range of 2 to 100 mg (weighing accuracy ± 0.05 mg). Samples are weighed in Sn crucibles (9-10 mm) together with a Sn pellet (about 200 mg) and wrapped. The wrapped samples are put into a Ni crucible and are loaded in an outgassed (5500 W) high temperature graphite crucible. The measurements take place at 5000 W. The evolving gases, CO_2 and CO, were swept out by helium as an inert carrier gas and measured by infrared detectors.

3.2.3 Carbon analysis

The carbon content is analyzed with the CS600 (LECO), calibrated with at least three different iron certified standards, and verified with another iron standard. The calibration range was close to the concentration of the samples. The standard and the samples were weighed in a range of 5-100 mg (weighing accuracy ± 0.05 mg) in baked out ceramic crucibles. About 1 g of accelerator material (W with Sn) is added to the sample and the standard. After loading into the furnace, the sample is purged with oxygen to remove the residual atmosphere gas. The combustion took place at about 2200 K while all material is oxidized. The carbon reacts with oxygen to CO or CO_2. CO is converted to CO_2 and then the gas is detected in the infrared cells.

3.2.4 Redox titration

The average oxidation state (AOS) of the transition metal ions (M) in the $LiMO_2$ (M = Mn, Ni, Co) samples is determined by redox titration [297, 298]. In this method, the sample reacts with a known excess amount of sodium oxalate and the unreacted sodium oxalate is titrated with potassium permanganate. The detailed procedure is as follows. About 20 mg of the $Li[M]O_2$ sample is mixed with 20 mL of 4 N (2 M) H_2SO_4 (reagent grade, 95-97 wt%, Sigma-Aldrich) and 20 mL of 0.05 N (0.025 M) $Na_2C_2O_4$ (≥ 99.99% trace metals basis, Sigma Aldrich, dried overnight before the preparation of the solution) in a Teflon container with lead and heated in a graphite furnace set at 70 °C for around 4 hours, until the powder sample is completely dissolved. For each sample, three independent sample measurements are performed. Blind samples are prepared by mixing 20 mL of 4 N (2 M) H_2SO_4 and 20 mL of 0.05 N (0.025 M) $Na_2C_2O_4$ and are heated in the same way as samples. The blind samples serve as samples for determination of titration factor as described further below.

During the process of heating the sample in sodium oxalate solution, all $M^{(2+\varepsilon)+}$ cations are reduced to M^{2+} (e.g., Mn^{2+}, Co^{2+}, Ni^{2+}) according to the reaction given below:

$$\varepsilon C_2O_4{}^{2-} + 2M^{(2+\varepsilon)+} \rightarrow 2M^{2+} + 2\varepsilon CO_2 \tag{3.1}$$

The unreacted $C_2O_4^{2-}$ in the solution is then determined by titrating the warm solution with a 0.1, 0.05 or 0.025 N $KMnO_4$ solution. Potassium permanganate with different concentrations is tested on the standard sample to find the optimum concentration considering the accuracy of the burette used for titration. The burette is a 50 ml / 0.1 with ± 0.05 ml accuracy at 20 °C. The warm solution resulted from the dissolving of the sample is transferred to a 100 ml beaker and stirred using a magnet stirrer during titration with potassium permanganate. At the end point of the titration, the solution turns from colorless into a very light pink color. During this process, the following reaction occurs:

$$5(C_2O_4)^{2-} + 2M^{7+} \rightarrow 2M^{2+} + 10CO_2 \tag{3.2}$$

The volume of the unreacted $Na_2C_2O_4$ can be calculated using the following equation:

$$2(C \cdot V)_{\mathrm{Na_2C_2O_4}} = 5(C \cdot V)_{\mathrm{KMnO_4}} \ or \ (N \cdot V)_{\mathrm{Na_2C_2O_4}} = (N \cdot V)_{\mathrm{KMnO_4}} \quad (3.3)$$

where *C* is the molarity of the solution and *N* is the normality of the solution. For blind sample, the volume of the unreacted sodium oxalate is known which is equal to the initially added sodium oxalate, i.e. 20 ml. Therefore, theoretically 10 ml potassium permanganate (or 40 ml for diluted potassium permanganate) is required to titrate the blind sample. However, in practice, the obtained value might be slightly different. The ratio of the theoretical volume to the used volume of titrant is referred to as the titration factor.

In titration of the samples, the volume of unreacted $Na_2C_2O_4$ ($V_{\mathrm{Na_2C_2O_4}}$) is calculated from the volume of consumed $KMnO_4$, considering the volume required for titrating blind sample. The consumed volume of sodium oxalate is then:

$$V_{\mathrm{Na_2C_2O_4}} = N_{\mathrm{KMnO_4}} \cdot \frac{(V_2 - V_1)_{\mathrm{KMnO_4}}}{N_{\mathrm{Na_2C_2O_4}}} \quad (3.4)$$

where

V_1 = volume of $KMnO_4$ solution (ml) consumed by 20 ml of 0.05 N $Na_2C_2O_4$.

V_2 = volume of $KMnO_4$ solution (ml) consumed by 20 ml of 0.05 N $Na_2C_2O_4$ in presence of a known weight of the sample.

The reduction reaction of all $M^{(2+\varepsilon)+}$ to M^{2+} (Equation (3.1)) can be written as follows:

$$\varepsilon \cdot \mathrm{mol}_{\mathrm{M}^{(2+\varepsilon)+}} = 2(C \cdot V)_{\mathrm{Na_2C_2O_4}} \quad (3.5)$$

By substituting *V* from Equation (3.5) we can calculate the value of ε as shown below:

$$\varepsilon = \frac{[(\text{Normality of } \mathrm{KMnO_4}) \cdot (V_1 - V_2) \cdot \mathrm{FW}]}{\text{sample weight (mg)}} \quad (3.6)$$

where FW is the formula weight of the sample ($g \cdot mol^{-1}$). From the value of ε, the average oxidation state of the transition metal ions and hence the oxygen content of the sample was determined from the charge neutrality principle.

3.2.5 Powder X-ray diffraction (PXRD)

Phase identification is realized and precise lattice parameters are obtained by powder X-ray diffraction (PXRD). The PXRD measurements are performed using a D8 Advance flat-plate Bragg-Brentano diffractometer of pseudo-focusing geometry (Bruker-AXS GmbH, Karlsruhe, Germany) with CuKα radiation. The data are recorded with a LynxEye silicon strip detector in the angle range of $10 < 2\theta < 110$ with a step size increment of 0.02 and a collection time of 6 s per step. The respective samples are ground to a fine powder using an agate mortar and fixed on a low-background sample holder made from Si wafer (Bruker, Germany) with the help of a very thin layer of Vaseline. The samples were rotated during the XRD measurements.

3.2.6 Rietveld refinement

The powder XRD patterns were analyzed by Rietveld refinements [299, 300]. Structure-related, profile-related and instrument-related parameters were used for peak profile modelling. Refinements of the collected data sets were done with TOPAS 4.2 software (Bruker, Germany). TOPAS [301] is a graphics-based profile analysis program built around a general nonlinear least square fitting system written specifically to integrate various types of powder diffraction and single crystal analyses.

3.2.7 Scanning electron microscopy

Scanning electron microscopy (SEM) in the present work is carried out by Mr. Udo Geckle from IAM-ESS. SEM is performed using a Zeiss Merlin (Carl Zeiss SMT AG, Oberkochen) scanning electron microscope equipped with a Schottky field emission source. The SEM delivers primary electron beam width energies in the range of 0.02-30 keV. The interaction of primary electron

beam with the electrons of the sample produces a large number of backscattered electrons (BSE) when elastically scattered as well as secondary electrons (SE) and characteristic X-rays when inelastically scattered. For SEM images, the SE and BSE are detected with a SE detector and an energy selective backscattered (ESB) detector, respectively. Details and benefits of the ESB technique, e.g. for characterizing the binder and carbon black, are explained in Ref. [302]. For the topographical contrast in electron micrographs secondary electrons were used as they are generated only in near surface regions (≤ 50 nm). The backscattered electrons reveal the chemical contrast in the images. This is due to the fact that the backscattering coefficient depends on the atomic number (Z), i.e. the backscattering coefficient increases with the increase of the atomic number. Therefore, the brighter regions displayed in the BSE images correspond to the species with higher Z elements [303].

3.2.8 X-ray photoelectron spectroscopy (XPS)

X-ray photoelectron spectroscopy measurements on powder NMC samples as well as pristine and charged electrodes were performed and evaluated by Ms. Raheleh Azmi from IAM-ESS of KIT. The results of these spectropic studies is partly published in a journal paper by Azmi et al. [304]. The measurements are carried out using a K-Alpha+ instrument (Thermo Fisher Scientific, East Grinstead, UK), applying a micro-focused, monochromated Al Kα X-ray source with 400 µm spot size. To prevent the buildup of any localized charge, the K-Alpha+ charge compensation system was employed using electrons of 8 eV energy and low-energy argon ions. Data acquisition and processing using the Thermo Avantage software were performed by fitting the spectra with one or more Voigt profiles according to [305]. Full details of the spectroscopy and evaluation method can be found in [304].

3.3 Thermal analysis

3.3.1 Simultaneous thermal analysis

Using simultaneous differential thermal analysis / thermogravimetry analysis (DTA / TG), the calorific effects and the mass changes of the sample during a controlled temperature program in a specific atmosphere are measured at the same time as a function of time and temperature [306]. For this purpose, a temperature program is given to the furnace, in which the sample and a reference material are placed in respective inert crucibles. In DTA mode, the temperature difference between the sample and a reference material (ΔT) is measured by thermocouples connected to the reference and the sample crucibles and recorded as an electric voltage. If the sample goes through a reaction, the temperature difference changes and this is reflected as an exothermic or endothermic peak in the DTA signal [307]. In TG mode, the changes in the mass of the sample and temperature are measured as a function of time by means of a thermo-balance. The advantage of simultaneous DTA / TG is that the observed mass changes of the sample can be correlated to the respective exothermic or endothermic peaks on DTA signals. To distinguish between the reactions involving mass changes and the reactions, which do not include a mass change, one can compare the DTA signal with the first derivation of TG with respect to time. The latter shows peaks only where a reaction with mass changes occurs, while the former has peaks where both types of reactions take place [306–308].

Simultaneous DTA / TG in the present work is carried out using SetSys Evolution 2400 from Setaram (Setaram, Cailure, France) [309]. In SetSys Evolution 2400 a symmetrical and hang-down electro-balance is designed for TGA application which enables the measurement of mass changes up to a 0.03 µg resolution. In this device, the crucibles are of freestanding type and the outer bottom of the crucibles is placed on the protective tube of the thermocouples. The furnace is a graphite furnace. In the measurements head of the device, thermocouples of type S are implemented to enable acceptable accuracy of measurements at lower temperatures. The device is equipped with

active cooling using flowing water. On this device it is possible to apply either Ar or Ar / 20 vol. % O_2 flowing gases during the experiments as the purge gas which enables the DTA / TG measurements under different atmospheres.

It is known that the changes of the density of the working gas by temperature lead to the Buoyancy force resulting in apparent mass changes. To compensate the Buoyancy effect, it is necessary to measure a blank experiment to make a baseline before the measurement of each sample. To run a baseline, the same temperature program and gas conditions as of the desired sample measurement are applied to empty reference and sample crucibles. Then for the processing of the measurement data, the respective signals of the baseline measurement are subtracted from the signals of sample measurements. The CALISTO software presented by Setaram is used for acquisition and processing of the measured data.

DSC / DTA devices are not absolute measuring instruments as they measure heat and heat flow rates dynamically and not at a thermal equilibrium condition. Therefore, it is necessary to convert the relative measured values to absolute values by using a suitable calibration procedure. By definition, calibration is establishing a quantitative relationship between the measured value of a quantity by an instrument and the true value of the respective quantity [310]. In a DTA / TG device, the heating rate affects the measured temperature during dynamic heating/cooling steps. Besides, as we measure the sample inside a crucible connected to the thermocouples, the heat transfer between the sample and the crucible and between the crucible and the thermocouples causes a deviation from the real temperature.

To calibrate the temperature of our DTA / TG device, the recommendations by GEFTA (Gesellschaft für thermische Analyse e.V) [310] and IUPAC (International Union of Pure and Applied Chemistry) [311] are employed. The calibration reference materials from Netzsch are used with the following materials and purities: Al (99.999 %), Au (99.999 %) and Ag (99.99 %). The calibration measurements are performed using alumina crucibles and argon atmosphere (99.999% purity) with 20 ml/h flowing rate, similar to the desired measurements. The temperature program includes four consecutive heating and cooling cycles with a heating and cooling rate of 10 $K \cdot min^{-1}$. The Al, Ag

and Au samples are heated up to 710 °C, 1000 °C and 1100 °C, respectively, during the heating cycles and cooled down to 580 °C, 870 °C and 870 °C, during the cooling cycles, respectively. In the last cooling round, the samples are cooled down to room temperature.

For the evaluation of the calibration results, the true melting temperature of the calibration reference material are taken from ITS-90 (The International Temperature Scale of 1990) [312]. The measured melting temperature corresponding to the onset temperature of the endothermic peak appears on the baseline-subtracted DTA signal of the respective heating cycle. According to NIST Recommended Practice Guide, DTA and Heat-flux DSC Measurements of Alloy Melting and Freezing [313], the onset temperature is the beginning of the deviation from the baseline.

The onset temperature as defined here can be read in two ways using the evaluation tools of Calisto program (Setaram, France); once by drawing the baseline of the heat flow signal in the peak range and read the first point where the signal deviates from the baseline. The second way is using the first derivative of heat flow signal then reading the first point where the curve deviates from zero. In our measurements, the first method resulted in melting temperatures closer to the literature data and therefore, this method is used for any onset temperature determination. The results including the true melting point from the literature (T_m) and the onset temperatures of the melting peaks of second, third and fourth heating cycles for each reference material are listed in Table 3.2. The first heating round is not considered in the evaluation.

Table 3.2: Melting temperatures of the calibration material used for the temperature calibration of the DTA / TG device, temperatures from the literature [312] and three time measurements are listed.

Calibration material	T_m (°C) [312]	T_2 (°C)	T_3 (°C)	T_4 (°C)
Al	660.323	656.3	656.2	656.6
Ag	961.78	958.3	958.0	958.1
Au	1064.18	1060.8	1060.5	1060.6

To construct the calibration equation, the temperature difference between the real melting point from the literature and the measured melting temperatures (ΔT_i) is plotted versus true melting temperature as shown in Figure 3.3, where T is in °C.

$$\Delta T_i = T_m - T_i \tag{3.7}$$

The data points of Figure 3.3 are fitted to a second order polynomial with the following formula using Origin program by the least squares method with the R-square value of 0.617:

$$\Delta T(T) = (5.29 \pm 2.76) - (0.00268 \pm 0.00676) \cdot T + (9.9 \pm 4.0)10^{-7} \cdot T^2 \tag{3.8}$$

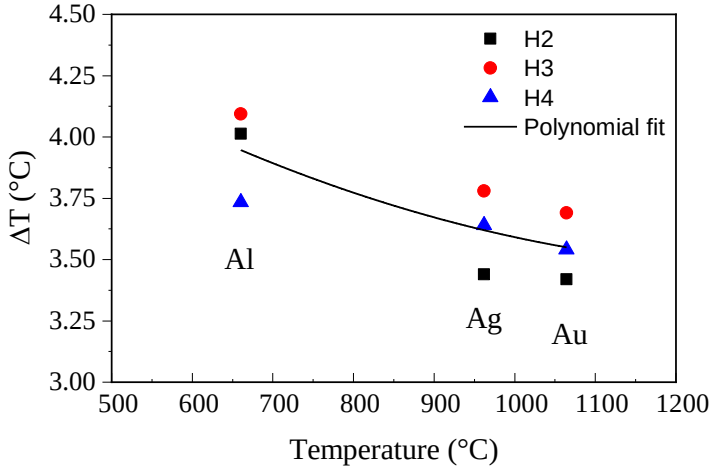

Figure 3.3: The difference between measured and true melting temperature of the calibration materials vs. true melting temperatures used for the temperature calibration of the DTA / TG device for a heating rate of 10 K·min^{-1}. The equation of the polynomial fit is presented in Equation (3.8).

The latter relation can be used to convert each measured temperature to the real value as given by:

$$T_{real} = T_{measured} + \Delta T \tag{3.9}$$

3.4 Calorimetry

Accurate thermodynamic data for oxide materials can be obtained by several methods, i.e. by measurement of oxidation-reduction equilibria using either gas mixture or electrochemical cells and also by direct calorimetry [314].

Calorimetry is the measurement of the thermal effects. A calorimeter is a container in which the investigated thermal phenomena takes place. The calorimeter is wrapped in an external jacket. Depending on the magnitude of the thermal conductivity (λ) of the medium of the external jacket, calorimeters are classified as (i) *adiabatic calorimeter*, when λ = 0 and there is no heat exchange with the environment (ii) *isothermal calorimeter* when λ is very large and all the heat produced in the calorimeter container is rapidly transferred to the outer jacket (iii) *Tian-Calvet calorimeter* when the heat flux between the calorimeter and the external jacket is measured by a bank of thermocouples surrounding the calorimeter container [315]. Calorimetry methods consist of two major categories: the measurement of heat capacities and the determination of enthalpies of chemical reactions [314]. The isoperibolic Calvet-type calorimeter used for solution calorimetry in molten oxide solvent (sodium molybdate) is utilized in this project to determine the enthalpies of formation of NMC oxides. This devise is briefly introduced in the following section.

3.4.1 High temperature oxide melt solution calorimetry

High temperature solution calorimetry in molten oxide solvents has proven to be a suitable method for the determination of enthalpies of formation of a wide range of compounds [314, 316, 317]. This technique has been used since 1964

for different minerals [318–320]. The Calvet-type microcalorimeter [315] is modified by Kleppa [321] for high temperature applications and is further improved by Navrotsky for a wide range of materials [314, 316, 317], while keeping the same working principles.

In the present work, high temperature oxide melt drop solution calorimetry was performed on a Setaram AlexSys-1000 (Setaram Instrumentation, Caluire-et-Cuire, France) [322], which is a commercial Tian–Calvet calorimeter operating under isoperibolic conditions. AlexSys-1000 calorimeter is constructed based on the custom-built calorimeters developed by Navrotsky [314, 316, 317]. The installation and set-up of the AlexSys-1000 calorimeter at the KIT lab is described by Cupid et al. [277]. High temperature calorimetry here refers to calorimeters operating at temperatures higher than 400 °C [317].

A schematic picture of the calorimeter and the components of the calorimeter cells are depicted in Figure 3.4. The calorimeter basically consists of two sample chambers each surrounded by a thermopile of 56 Pt-Pt13%Rh thermocouples in series. The two thermopiles are connected in opposite, which reduces the fluctuations in the measured base-line caused by temperature changes in the calorimeter block [315]. The thermopiles are embedded in a large block of Hastelloy X. As the calorimeter works based on isoperibolic condition, the temperature of the calorimeter block is kept constant at T_B by a cylindrical heater on the sides, and plate heaters on the top and bottom. The calorimeter is insulated from the surrounding environment by a thermal insulation cover.

In Figure 3.4 the calorimeter cell is enlarged. This cell consists of a platinum crucible (11 cm long, 1.5 cm diameter) placed in silica crucible. The solution is put inside the platinum crucible. Both crucibles are then placed inside a long silica glass tube to minimize thermal radiation heat transfer. The sample dropping tube and the tubes carrying bubbling and flushing gas are also connected to the long glass tube. The flushing gas serves to maintain a constant gaseous environment above the solution. The bubbling gas is driven inside the molten solution through a thin tube and serves to stir the solution, thereby further enabling sample dissolution and preventing local solvent saturation.

Both flushing and bubbling gases determine the activity of oxygen in the molten solution.

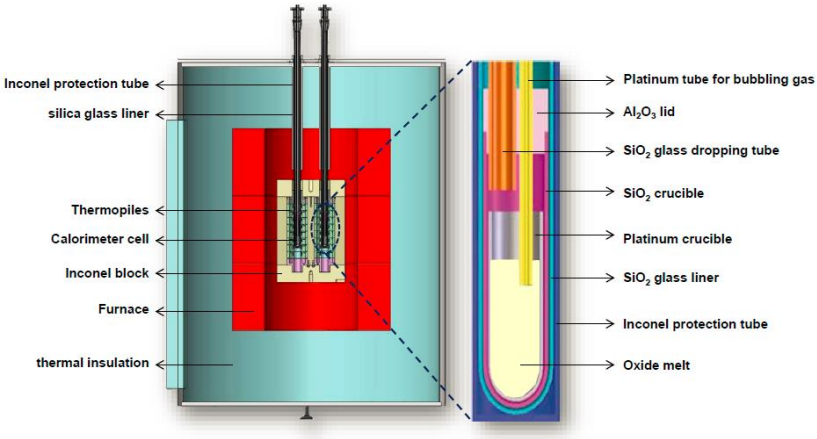

Figure 3.4: Schematic structure of the AlexSys 1000 calorimeter from SETARAM. On the left-hand side, the vertical cross-section of calorimeter chamber is illustrated and on the right-hand side different components of the calorimeter cell are shown.

Before the start of the measurements, the calorimeter cells are in thermal equilibrium with the block and this is reflected as a stable heat flow signal (ϕ in µV) over time. When a sample is dropped into the calorimeter cell, the signal starts to rapidly deviate from the baseline, as depicted in Figure 3.5, and after reaching an extremum at the end of chemical reaction, the signal slowly returns to the baseline level, creating a peak. In fact, when a sample is dropped into the calorimeter, the enthalpy of the cell changes by ΔH_P. The heat released or absorbed by the sample during the dropping process includes the heat content of the sample from the room temperature to the temperature of calorimetry and the heat of dissolution in the oxide melt.

The purpose of calorimetry is to determine ΔH_P and find the relationship between ΔH_P and the measured heat flow signal as described in the following.

The released or absorbed heat results in a temperature difference between the calorimeter cell and calorimeter block:

$$\Delta T(t) = T_C(t) - T_B \tag{3.10}$$

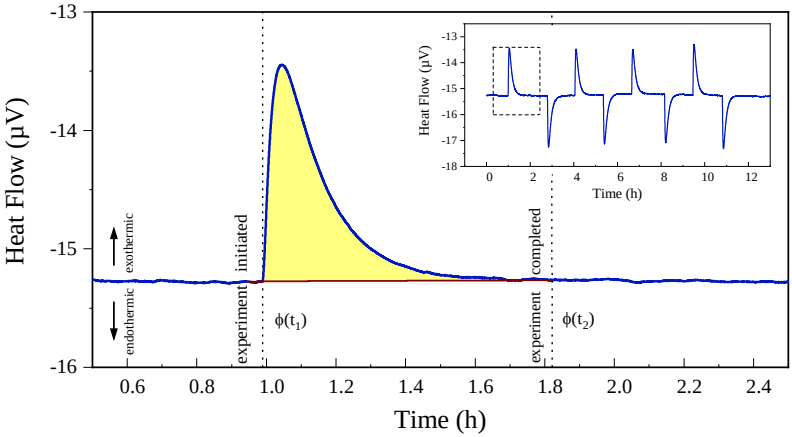

Figure 3.5: The calorimetric measurement curves showing heat flow signal (ϕ) against time when a sample is dropped into the calorimeter. The base line (in red) linearly connects the beginning and the end point of the measurements such that $\phi(t_1) - \phi(t_2) = 0$. The peak area is shown in yellow. Inset graph: overview of the repeated calorimetric measurements by samples of the same NMC material.

$\Delta T(t)$ is measured by the thermopiles as a voltage (heat flow) signal which is proportional to the temperature difference:

$$\phi(t) = \frac{1}{K} \cdot \Delta T(t) \tag{3.11}$$

where K is the calibration factor of the calorimeter. The enthalpy changes of the calorimeter cell by time is given by the following equation [315]:

$$\frac{dH(t)}{dt} = \Delta H_P - \frac{\Delta T(t)}{R_{th}} \tag{3.12}$$

where R_{th} is the thermal resistance of the calorimeter block and $\frac{\Delta T(t)}{R_{th}}$ is the heat flow between the calorimeter container and the block. As $dH = d(C_C \cdot T_C(t))$, where C_C is the heat capacity of the calorimeter cell, the previous equation can be written as:

$$\Delta H_P - \frac{\Delta T(t)}{R_{th}} = \frac{d(C_c \cdot T_c(t))}{dt} \tag{3.13}$$

The thermal capacity of the calorimeter stays constant due to the small size of the sample comparing the calorimeter cell; therefore, the equation can be rewritten as the Tian's equation as follows [308]:

$$\frac{d\Delta T(t)}{dt} = \frac{\Delta H_P}{C_c} - \frac{\Delta T(t)}{C_c \cdot R_{th}} \tag{3.14}$$

Considering the relation between the voltage signal $\phi(t)$ and ΔT, the equation turns into the following:

$$\frac{d\phi(t)}{dt} = \frac{\Delta H_P}{K \cdot C_c} - \frac{\phi(t)}{C_c \cdot R_{th}} \tag{3.15}$$

By integrating both sides:

$$\int_{t_1}^{t_2} d\phi(t) = \frac{\Delta H_P}{K \cdot C_c} - \frac{1}{C_c \cdot R_{th}} \int_{t_1}^{t_2} \phi(t)\, dt \tag{3.16}$$

As $\phi(t_1) = \phi(t_2)$:

$$\Delta H_P = \frac{K}{R_{th}} \int_{t_1}^{t_2} \phi(t)\, dt \tag{3.17}$$

Therefore, ΔH_P can be calculated using Equation (3.17) through measuring the area under the peak which is highlighted in yellow in Figure 3.5. $\frac{K}{R_{th}}$ should be determined through calibration using a material with well-known heat capacity.

In the course of the present work, the average temperature inside the platinum crucibles located inside the calorimeter cells is set to 974.0 ± 0.1 K. Both calorimetric chambers were calibrated independently using 7 mg sapphire

spheres (origin and purity in Table 3.3) with a diameter of 1.5 mm. The sapphire spheres were dropped from room temperature (298 ± 1) K into the empty platinum crucibles of the calorimeter (no oxide melt) at 974 K. The measured heat content of sapphire with known heat capacity is then used to determine the calibration factor of the calorimeter.

In the present work, solution calorimetry was performed in a sodium molybdate ($3Na_2O{\cdot}4MoO_3$) melt as solvent. For this purpose, the required amounts of sodium molybdate dihydrate ($Na_2MoO_4{\cdot}2H_2O$) and molybdenum (IV) oxide are thoroughly mixed. The origin and purity of the chemicals are listed in Table 3.3. The mixture was heated at 973K for 5h in air and after cooling inside the furnace, ground to powder. About 28 g of the sodium molybdate mixed powder is put inside each platinum crucible and heated again at 700 °C for 2 hours and slowly cooled in the turned-off furnace to set inside the platinum crucible. The crucible is then assembled as shown in Figure 3.4. By inserting the tubes inside the calorimeter chamber, the sodium molybdate powder melts and is usually ready to use after 4 hours if the baseline is stable. The oxide melt is a buffer solution and below approximately one mole percent of solute oxide (sample) in solvent oxide, no dependence of the measured heat on the concentration was observed and the presence of one cation did not affect the solution of other compounds with different cations [319].

Table 3.3: Details of the chemicals, reference material and the gas used in the calorimetry experiments.

raw material	chemical formula	source	mass fraction purity
Sodium molybdate dihydrate	$Na_2MoO_4{\cdot}2H_2O$	Merck KGaA	≥ 99.5%
Molybdenum trioxide	MoO_3	Merck KGaA	≥ 99%
Sapphire spheres	Al_2O_3	Alfa Aesar	99.99%
Argon	Ar	Air Liquide	99.999% [a]

[a] Purity expressed in mole fraction

For the high temperature drop solution measurements, all powder samples were pressed into pellets of 3 mm diameter and dropped from ambient temperature into liquid sodium molybdate at 974 K. The masses of the pellets varied between 5 and 9 mg (accuracy of weighing ± 0.005 mg). To estimate the uncertainty related to the repeatability of the experiments, several samples of each material were dropped into the calorimeter, reflecting as consecutive peaks in Figure 3.5 insert picture. The individual drops were performed in approximately 1.5 hours intervals to ensure complete dissolution of the sample in the sodium molybdate solvent and the attainment of a steady-state equilibrium after each drop. Ar gas (origin and purity in Table 3.3) with flow rates of 50 $ml \cdot min^{-1}$ and 5 $ml \cdot min^{-1}$ were used as a flushing and bubbling gas, respectively.

3.5 Electrochemical characterization

This section focuses on the preparation method of electrodes out of synthesized NMC powder, assembly of coin cells, electrochemical instrumentation and the techniques used to investigate the electrochemical performance of the cells.

3.5.1 Fabrication of electrodes

The electrodes sheets composed of synthesized NMC powder of different compositions as active material, carbon black as electronically conductive filler (SUPER C65, TIMICAL) and polyvinylidene fluoride (PVDF) as binder (purity ≥ 99.0 %, MTI, USA) with the weight ratio of 80:10:10, respectively. The fabrication process is as follows: first, PVDF powder is dried for 2 hours in a vacuum oven at 100 °C and dissolved in appropriate amount of N-methyl-2-pyrrolidinone (NMP, purity ≥ 99.5 %, Alfa Aesar) to prepare 5 wt% solution of PVDF in NMP. The required amounts of active material and carbon black were weighed and ground thoroughly three times in an agar mortar by adding acetone. The mixture is then dried in a drying oven at 60 °C for 30 min. The required amount of PVDF solution is added to the active material and carbon black mixture and stirred using a magnet stirrer overnight to ensure a

homogenous slurry. As the viscosity and consistency of the slurry was suitable for coating, no additional NMP was added.

The composite NMC electrodes were produced by casting the prepared slurry on aluminum foil (20 µm thickness, Targray) using a doctor blade coating machine (AFA-III Automatic Thick Film Coater, MTI Corp., USA). The blade clearance (wet coating thickness) was set to 150 µm and the moving speed of the blade was 10 mm/s. The coated sheets were dried in a vacuum oven (mBRAUN-MB VOH-250) at 80 °C overnight. The electrode disks with a diameter of 13 mm were punched out of the dried sheets using a punching machine (El-Cut 13, El-Cell, Hamburg, Germany). The electrode disks were subsequently pressed using a hydraulic hand press by 8 tones in a press die of 20 mm diameter in a replacement to industrial calendaring process to improve the particle to particle contact in the electrode and the adhesion of the electrode to the aluminum substrate.

Knowing the measured weight of the mixed active material, carbon black and PVDF in the slurry, their real ratio was calculated and the actual mass fraction of the active material in cathode composite (R_a) in each slurry mixture was determined. The weight of electrode disk (m_e) and the average weight of uncoated aluminum foil with the same diameter as electrode disc ($\overline{m}_f$) were measured before the cell assembly. The weight of active material (m_a) for each cell was calculated through Equation (3.18).

$$m_a = (m_e - \overline{m}_f) \cdot R_a \tag{3.18}$$

3.5.2 Electrochemical cells: assembly and disassembly

Electrochemical measurements were performed on coin cells of type CR2032, with a diameter of 20 mm and a height of 3.2 mm, made of composite NMC as working (positive) electrode and metallic lithium disk (diameter of 12 mm, thickness of 0.38 mm, 99.99 %, trace metal basis, Sigma Aldrich, United States) as negative and counter electrode. The coin cell casing was made of stainless steel and cases were equipped with O-rings (Pi-KEM, MTI

Corporation). The electrolyte was 1M solution of lithium hexafluorophosphate ($LiPF_6$) salt in ethylene carbonate (EC) /dimethyl carbonate (DMC) with weight ratio 1:1 (LP30, water content < 20 ppm, HF as free acid < 50 ppm, BASF, Germany). In each coin cell 90 µl of electrolyte was added, using a volumetric pipette. As separator, glass fiber (diameter of 15 mm, thickness of 260 µm, GF/A Filter, Whatman,) was used. The coin cells were constructed in an argon-filled glovebox (O_2 < 0.1 ppm, H_2O < 0.3 ppm; mBRAUN-LAB master sp, Garching, Germany) using MT 160 D coin-cell pressing machine (MTI Corp, USA). Before the cell assembly, the stainless-steel parts, the cathode disks and the separator were dried under vacuum at 110 °C for 24 h. Separators have been dried earlier at 120 °C under vacuum for two additional days and stored inside the glovebox. The electrochemical measurements started at least three hours after the assembly of cell to ensure homogenous permeation of electrolyte.

3.5.3 Techniques

The electrochemical tests in the present work were performed using MPG2, a multi-channel battery cycler from Bio-Logic (Bio-Logic Science Instruments SAS, Seyssinet-Pariset, France). In this device each channel is an independent potentiostat / galvanostat, enabling to control either current or voltage on multiple channels simultaneously. These settings as well as some post data analysis were performed with the help of the EC-Lab software from Bio-Logic. To keep a constant temperature during electrochemical investigations, all cell and cell holders were placed in a temperature chamber (KT 53 E6, Binder GmbH, Tuttlingen, Germany) and the temperature was set at 25 °C for all measurements. For each NMC composition, at least two corresponding cells have been assembled and tested.

3.5.3.1 Galvanostatic coulometry

In the galvanostatic measurements also known as chronopotentiometry, a constant-current pulse is applied to the working and counter electrodes and the variation of potential with time is measured. The current is applied by a galvanostat with very large internal resistance. In this technique, the potential

is usually limited in a specific range. Therefore, these measurements are usually referred to as galvanostatic coulometry with potential limitations (GCPL). When the applied current is positive, the working electrode oxidizes and once the maximum voltage limit is reached, the current becomes negative to reduce the electrode to the minimum voltage limit. This consecutive charge and discharge process forms a galvanostatic *cycle*. Galvanostatic measurements are important as the constant applied current provides a working condition similar to the real working condition of the battery. An example of four GCPL cycles on a fresh cell with NMC532 cathode versus metallic lithium anode is shown in Figure 3.6. As mentioned earlier, the voltage curve is characteristic of the cell reaction.

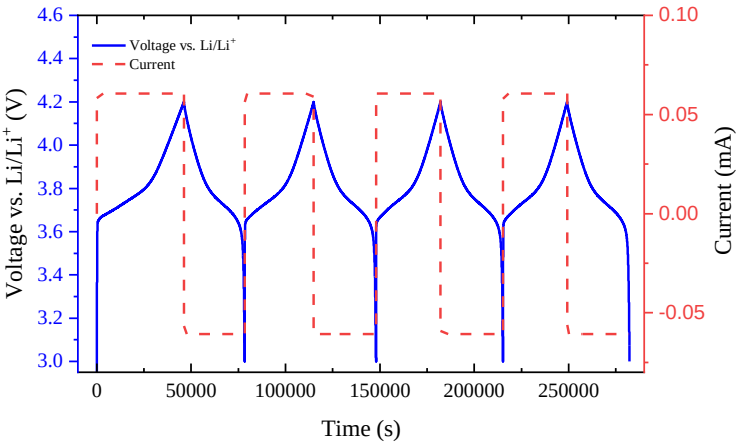

Figure 3.6: An example from the present work showing four GCPL cycles on a fresh cell with NMC532 cathode vs. metallic lithium anode. In this measurement, constant current (nominal C/10 charge and discharge) is applied and variations of voltage between 3.0 V and 4.2 V is measured.

For an intercalation/deintercalation of lithium as the guest species in a host structure according to the reaction in Equation (3.19), the amount of Li can be calculated by Equation (3.20).

$$A_x \cdot Host + \Delta x \cdot A^+ + \Delta x \cdot e^- \leftrightarrow A_{x+\Delta x} \cdot Host \tag{3.19}$$

$$\Delta x = \frac{I \cdot \Delta t \cdot \mathcal{M}}{m_a} \tag{3.20}$$

where I is the applied current (A), Δt is the time interval (s), $\mathcal{M}$ is the molecular weight of the host material (g·mol^{-1}) and m_a is the mass of active material in the electrode (g).

3.5.3.2 Galvanostatic intermittent titration technique (GITT)

Galvanostatic intermittent titration technique (GITT) combines transient and steady-state measurements to obtain both kinetic and thermodynamic information about solid solution electrodes [323]. GITT method is a well-known electrochemical method to measure the quasi open circuit voltage (QOCV) at different states of charge (lithium content) which is a close estimation of open circuit voltage (OCV) or equilibrium cell potential as introduced is Section 2.2. OCV measurements are important as other thermodynamic properties can be directly derived from OCV data. In addition, GITT method or current pulse method proposed by Weppner and Huggins [324] is the standard electrochemical method employed to obtain the chemical diffusion coefficient $\widetilde{D}$ of Li^+ ions in the insertion electrodes of lithium-ion battery. Other electrochemical methods include potentiostatic intermittent titration technique (PITT) [325], electrochemical impedance method [326] and cyclic voltammograms (CV) [327]. For high power density batteries, it is important that the solid electrodes incorporate electroactive species fast from the electrolyte into their crystal structures and the local compositional (stoichiometric) gradient inside the electrode can rapidly reach the compositional equilibration (relaxation). Therefore, study of the transport of the mobile species and its quantitative expression in terms of chemical diffusion coefficient $\widetilde{D}$ is of great importance.

Using the GITT method, the electrode is subjected to a small constant current pulse followed by an open circuit stand for a long enough period of time that allows the cell potential to relax and reach its steady-state value. During the measurement, the potential responses to the current changes are measured as a

function of time. This procedure is repeated until the cell potential reaches the upper limit of the desired voltage range. The intermittent charging of the cell leads to step-wise variation of the electrode's composition, i.e. x in Li_xMO_2 electrode. The voltage of the electrode at the end of each relaxation time is the QOCV for the corresponding state of charge (x value). The evolution of QOCV versus x in Li_xMO_2 is obtained from the GITT measurements and is equivalent to OCV at varying x. An example of a GITT measurement exhibiting the current and voltage changes as a function of time is shown in Figure 3.7. The insets of Figure 3.7 show enlarged views of the current pulses and voltage responses during charge and discharge courses as well as QOCV of the respective steps.

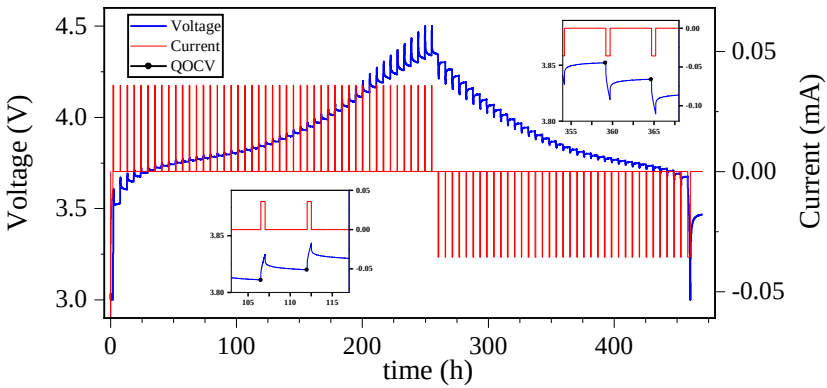

Figure 3.7: An example from the present work showing a GITT measurement on a coin cell with NMC110 as positive electrode. The measurements program includes intermittent charge and discharge between 3.0 V and 4.5 V with 30 minutes of current application and 5 hours of relaxation. The inserts show the shape of respective voltage response to each current pulse during charge/ discharge courses as well as quasi open circuit voltage (QOCV) as the working voltage at the end of each relaxation period corresponding to lithium content after each electrochemical titration step.

Figure 3.8 shows the enlarged view of a single current pulse and its respective voltage changes from the same measurement of Figure 3.7. The set parameters

of the GITT including current of the pulse (I_p), time of the pulse (τ) and relaxation time ($t_{relaxation}$) as well as the features of the voltage curve that are used for the calculation of the diffusion coefficient are specified in the picture.

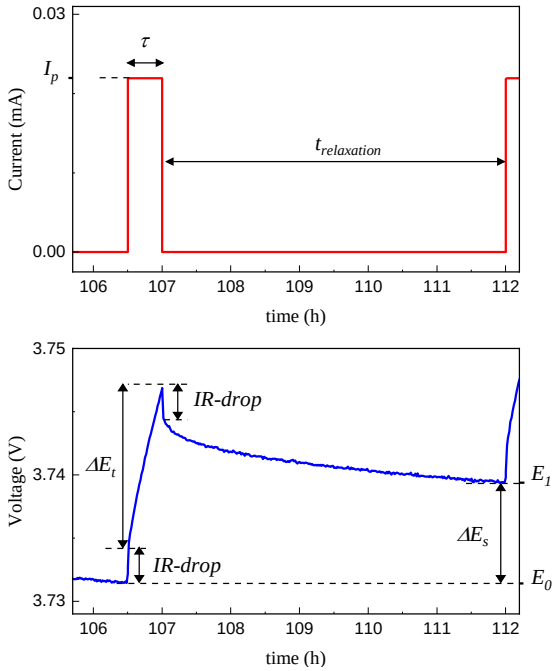

Figure 3.8: A single current pulse and its respective voltage changes as a function of time. The set parameters of the GITT measurement including current of the pulse (I_p), time of the pulse (τ), relaxation time ($r_{elaxation}$) as well as the features of the voltage curve including ΔE_t (the total transient change in the cell voltage after subtraction of *IR-drop*) and ΔE_s (the change in the steady-state voltage between two consecutive titration steps) are shown. The graphs are taken from the measurements preformed in the present work.

Assuming that lithium transport in the electrode is according to Fick's second law and considering the phenomenon as one-dimensional diffusion (without consideration of ohmic potential drop, double-layer charging, charge-transfer

kinetics, and phase transformation) a lithium diffusion coefficient can be calculated using the following equation:

$$D_{Li}^{GITT} = \frac{4}{\pi\tau}\left(\frac{m_a V_M}{\mathcal{M} S}\right)^2 \left(\frac{\Delta E_s}{\Delta E_t}\right)^2 \quad (\tau \ll L^2/D_{Li}) \tag{3.21}$$

Where m_a, V_M and $\mathcal{M}$ are the active mass, molar volume and molar mass of the insertion electrode material, respectively. S is the total contact area between the electrolyte and the electrode, and L is the thickness of the electrode. The V_M value is deducted from the crystallographic data for each compound. ΔE_s is the total transient change in the cell voltage, after subtraction of *IR-drop*, and ΔE_t is the change in the steady-state voltage between two consecutive titration steps. These values are obtained from the voltage response curve for each step as shown in Figure 3.8.

3.5.3.3 Cyclic voltammetry

In voltametric methods, the voltage of the cell varies with the time within a defined voltage window and with a specific sweep rate. Concurrently, the changes of the current generated by the consequent electrochemical reactions of the electrode is measured. In cyclic voltammetry (CV), the voltage changes linearly with time with a prescribed $\pm\, dE/dt$ (ranging from $\mu V \cdot s^{-1}$ to $mV \cdot s^{-1}$). CV is the most widely used technique to obtain quantitative information about the redox potentials of electroactive species. In the present work, the cyclic voltammetry investigations are performed on the coin cells after GITT tests. The measurement is performed after 5 hours of open circuit voltage stand of the cell and is recorded between 3.0 and 4.5 V with a sweep rate of 0.01 $mv \cdot s^{-1}$. An example of such a measurement is shown in Figure 3.9-a. The results of the CV measurements are presented in form of current versus voltage graphs. Such graphs are known as cyclic voltammograms, an example of which is shown in Figure 3.9-b.

3.5.3.4 Rate capability

In high power applications, it is important for the battery to exhibit good cyclability at different C-rates. This feature is known as high rate capability. To investigate the rate capability, the battery is usually cycled using

subsequently varied C-rates while each C-rate is applied for a specific number of cycles. In the present work, the rate capability investigations are performed after GITT and CV tests, using C/20, C/20, C/5, C/2, C, 2C, 5C charges and discharged for 5 cycles with each C-rate as shown in the step No. 10 in Figure 3.10.

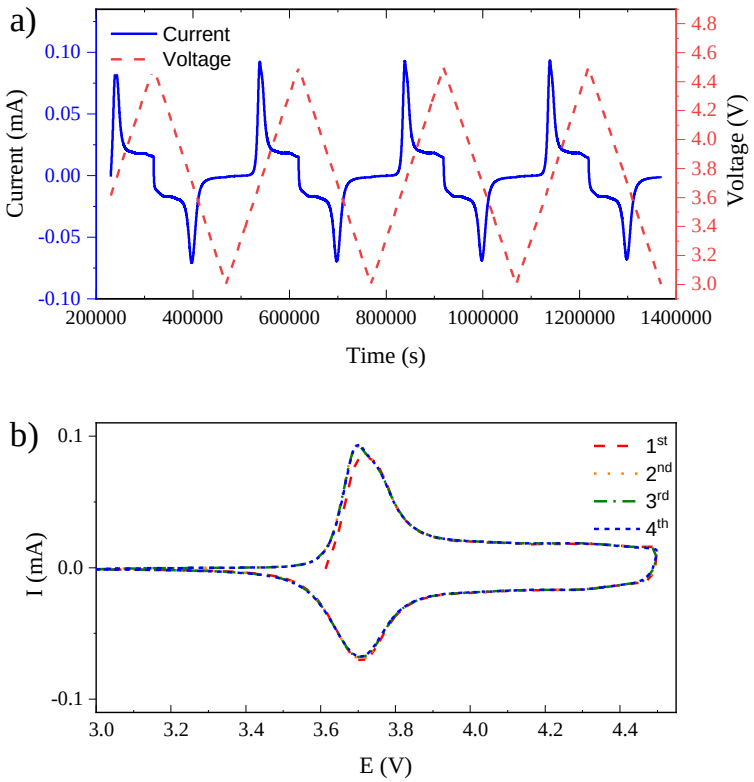

Figure 3.9: An example from the present work showing a CV measurement on a coin cell with NMC532 as positive electrode. The measurement is performed after 5 hours of open circuit voltage stand on the cell and is recorded between 3.0 and 4.5 V with a sweep rate of 0.01 mv/s. a) current and voltage versus time graphs, b) Cyclic voltammogram of the measurement.

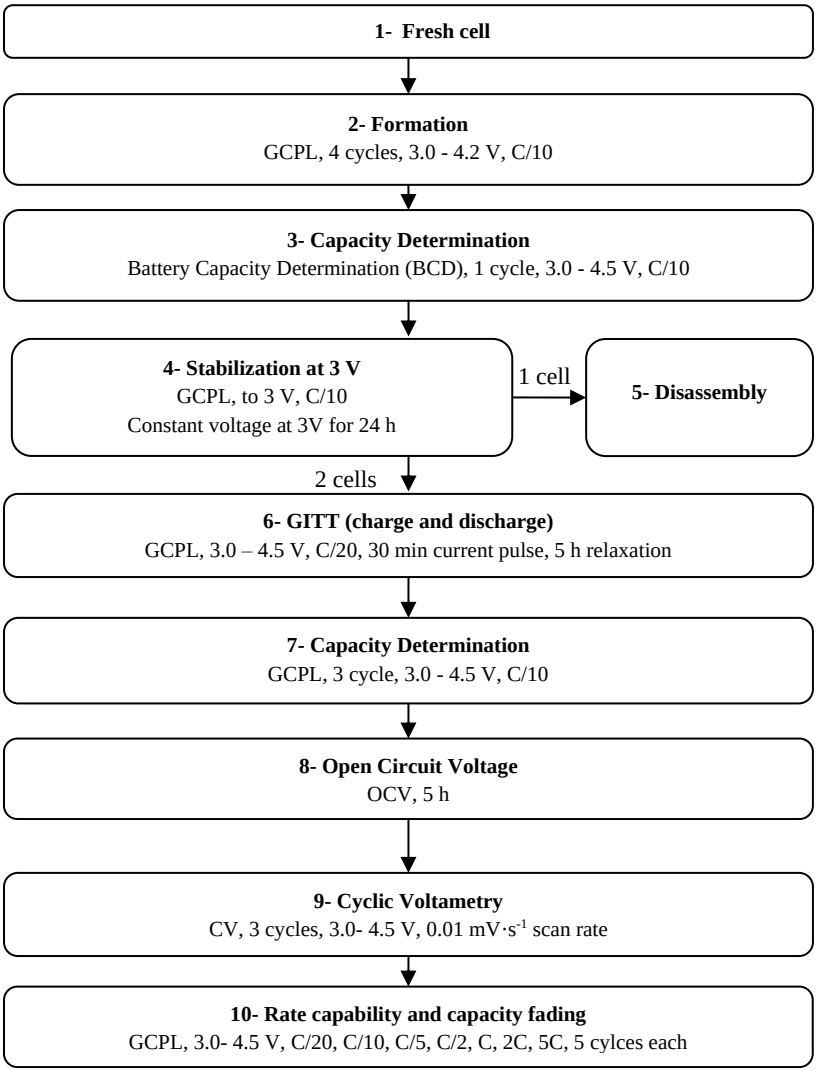

Figure 3.10: Flow diagram showing the techniques, parameters and sequences used for testing coin cells made of different NMC material as active material of positive electrode.

3.6 Uncertainty of measurements

In general, the result of a *measurement* of a physical quantity or a *measurand* is only an *estimate* of its value. The result of a measurement is complete only when accompanied by the evaluation and expression of the *uncertainty* of the estimated value. Statement of the uncertainty provides a quantitative indication of the quality of the result and makes any comparison with other measurements or with the reference values possible. The evaluation of uncertainties in the measurements of the present work follows the rules of the "Guide to the Expression of Uncertainty in Measurements (GUM)" [328].

The term *uncertainty* of the result of a measurement is a parameter that reflects the lack of exact knowledge of the value of the measurand and shows the dispersion of the values that could be attributed to the measurand. The result of a measurement is usually determined based on a series of observations of the same measurand. If the results are obtained by successive measurements carried out under the same conditions, then the *repeatability* of the measurement is evaluated. Repeatability conditions consist of the same measurement procedure, the same measuring instrument, the same observer, the same location and repetition over a short period of time. If the measurements are carried out under specific changed conditions, then the *reproducibility* of the measurement is evaluated. The changed conditions may consist of method of measurement, observer, measuring instrument, reference standard, location or time.

Differences in repeated observations under repeatability conditions are supposed to exist because of inconstant influence quantities, i.e. quantities other than the measurand which affect the result of the measurement. Random effects of a measurement result are usually decreased by increasing the number of observations. Similarly, systematic effects can also be reduced but not removed. If an influence quantity leading to a significant systematic effect (relative to the required accuracy of the measurement) is recognized, a correction or correction factor can be applied to compensate for the effect. The uncertainty has different components arising from random effects and from imperfect correction of the result for systematic effects. The uncertainty of an

applied correction is the uncertainty of the result due to imperfect knowledge of the required value of the correction. Adjustment and calibration using standards and reference materials is usually a measure to eliminate systematic effects. Still, the uncertainties accompanying these standards and materials need to be taken into account.

Standard uncertainty is the uncertainty of a measurement, which is expressed as a standard deviation. In general, there are two types of evaluation of uncertainty. This classification is based on the methods, by which the uncertainty components are evaluated rather than the components themselves. Type A evaluation is a method using statistical analysis of series of observations and Type B is a method using other means. However, both types of evaluations are on the basis of probability distributions, and the uncertainty components resulting from each type are expressed by variances or standard deviations.

When uncertainty components are determined from repeated observations, Type A evaluation is practiced. A measurand Y is usually obtained from n input quantities X_1, X_2, ..., X_n through a functional relationship f:

$$Y = f(X_1, X_2, \dots, X_n) \tag{3.22}$$

The function f contains all corrections and correction factors. To determine y which is the estimated value of the measurand Y, x_i, the estimated value of input quantities X_i, need to be determined. Thus, y can be calculated by Equation (3.23).

$$y = f(x_1, x_2, \dots, x_n) \tag{3.23}$$

Where x_i is usually determined based on the statistical analysis of series of observations and estimated by the arithmetic mean of n independent repeated observations of input quantity X_i as obtained from Equation (3.24).

$$x_i = \bar{X}_i = \frac{1}{n}\sum_{k=1}^{n} X_{i,k} \tag{3.24}$$

The variance σ^2 of the probability distribution of x_i is estimated by the experimental variance of the observations ($s^2(x_i)$) given by:

$$s^2(x_i) = \frac{1}{n-1}\sum_{k=1}^{n}(X_{i,k} - \bar{X}_i)^2 \tag{3.25}$$

The standard uncertainty of x_i, $u(x_i)$ equals the experimental standard deviation (positive square root of experimental variance) of the observations, $s(\bar{X}_i)$, where $s^2(\bar{X}_i)$ calculated according to Equation (3.26).

$$u^2(x_i) = s^2(\bar{X}_i) = \frac{s^2(x_i)}{n} \tag{3.26}$$

When the input quantities are independent or uncorrelated, the *combined standard uncertainty* denoted by u_c is calculated using the standard uncertainty $u(x_i)$ of each input estimate x_i by Equation (3.27).

$$u_c{}^2(y) = \sum_{i=1}^{n}\left(\frac{\partial f}{\partial x_i}\right)^2 u^2(x_i) \tag{3.27}$$

However, it is not an economic investigation to obtain all of the uncertainty components by Type A evaluation. Therefore, many uncertainty components must be evaluated by other means i.e. by Type B. In Type B evaluation, other available information is discussed which cannot be obtained by statistical evaluation. This information includes mathematically determinate distributions, imported input values and measured input values. The uncertainties from mathematically determinate distribution can arise from the resolution of the digital indication, hysteresis or finite-precision arithmetic. In these cases, standard uncertainty is $u = 0.29\ \delta x$, where δx could be the resolution of the indicating device, the range of possible hysteresis or smallest change in the output quantity by increasing small increments in the most important input quantity, respectively. Another Type B uncertainties come from imported quantities with known or estimated uncertainties or from input quantities measured by single observation with the uncertainty obtained by calibration of the device against a standard or a verified device.

To define an interval that covers a large fraction of the values attributed to the measurand, the *expanded* or *overall uncertainty (U)* is used. The fraction is

known as the coverage probability or the level of confidence of the interval. The combined standard uncertainty is multiplied by a factor known as *coverage factor* (k) typically in the range of 2 to 3 to obtain expanded uncertainty.

$$U = ku_c(y) \tag{3.28}$$

The result of a measurement is expressed as $Y = y \pm U$, which means that the best estimate of the value attributable to the measurand Y is y, and it is expected that a large fraction of the distribution of values that could reasonably be attributed to Y lies in $y - U$ to $y + U$ interval. In the present work, the coverage factor of 2 is chosen. Assuming that the dispersion of the measured values has a normal distribution, the coverage factor $k = 2$, covers 95.4% of the values which is equivalent to a confidence level of $p \approx 95\%$.

4 Synthesis and characterization

The layer-structured NMC samples synthesized and investigated in the present work consist of two compositional series including: 1) manganese and nickel equimolar $LiNi_xMn_xCo_{1-2x}O_2$ (x = 0, 0.167, 0.333, 0.4 and 0.5) and 2) Ni-rich $LiNi_{0.8-y}Mn_yCo_{0.2}O_2$ (y = 0, 0.1, 0.2, 0.3 and 0.4). Figure 3.2 showed the investigated compositions on the Gibbs triangle by red squares and blue circles for the first and second series, respectively. The compositions of the samples are designed so that they cover the area of commercial interest of the NMC materials while making possible a systematic investigation of compositional changes. The samples whose synthesis is discussed in this chapter are subject of further investigations including thermal analysis (Chapter 5), determination of enthalpy of formation (Chapter 6) and electrochemical studies (Chapter 7). The main purpose of the synthesis and characterization of these materials is to ensure that the composition of the samples are as close to the nominal compositions as possible. In this chapter, based on the results of the chemical analysis, a general method for the determination of chemical formula of the NMC material is proposed. Rietveld refinement of the XRD patterns of the samples is used to characterize the structures present in the samples. The average oxidation state of transition metals in each composition is determined by redox titration method. The presence of oxygen vacancy is investigated by comparing oxygen content obtained through different methods including carrier gas hot extraction (CGHE), redox titration and Rietveld refinement of the corresponding powder XRD pattern (only for $LiNi_{0.8-y}MnyCo_{0.2}O_2$ series). For samples in which different preparation conditions are experimented, the optimum synthesis condition is detected. After all, the effect of changes in the Ni:Mn:Co ratio on chemical formula and structural properties of the NMC samples is discussed in this chapter.

4.1 Experimental

The $LiNi_xMn_xCo_{1-2x}O_2$ samples with x = 0, 0.167, 0.333, 0.4 and 0.5, and the $LiNi_{0.8-y}Mn_yCo_{0.2}O_2$ samples with y = 0, 0.1, 0.2, 0.3 and 0.4 (see Figure 3.2 for sample notations) were synthesized by the sol-gel method using metal acetates and adipic acid, as described in Section 3.1. The first series of samples, namely $LiNi_xMn_xCo_{1-2x}O_2$ samples with x = 0, 0.167, 0.333, 0.4 and 0.5 were prepared using stoichiometric lithium acetate added to the initial solution. The final calcination temperature was chosen at 900 °C for the samples with x = 0, 0.167, 0.333 and 0.4, and 1000 °C for the sample with x = 0.5 to achieve pure single-phase material. The sample with x = 0.5 when calcinated at 900 °C, contained Li_2MnO_3 (space group: *C2/m*) as impurity phase. This impurity phase disappeared when the calcination temperature was raised to 1000 °C. The calcination temperatures were chosen based on the best agreement of temperatures suggested in different works [143, 182, 184, 204, 275, 329].

For the second series of samples, namely $LiNi_{0.8-y}Mn_yCo_{0.2}O_2$, samples with y = 0, 0.1, 0.2, 0.3 and 0.4, 3 mol% of excess lithium acetate was used to compensate for lithium loss during the calcination process and preventing the lithium deficiency. It is know that the lithium deficiency is undesirable and harmful for the electrochemical performance [228]. The lithium insufficiency seems to be due to the high vapor pressure of lithium at high calcination temperatures [330]. Hence, adding excess lithium is suggested to compensate for the lithium loss during the calcination [228] and to reduce the undesirable site mixing of Li and Ni in $LiNiO_2$ and Ni-rich layered compounds [331].

It has been proposed that there is an optimum thermal treatment condition for each composition of a transition-metal oxide electrode materials, which leads to optimized electrochemical properties [332, 333]. In the case of Ni-rich compounds, as Mn content increased, calcination temperature has increased to suppress the oxidation of Ni^{2+}. A similar trend was reported on the optimum firing temperature for $LiNi_{0.4}Mn_{0.5}Co_{0.1}O_2$ and $Li(Ni_{0.45}Mn_{0.45}Co_{0.1})O_2$ synthesized by a coprecipitation method [334] and the Co-free Ni-rich $Li(Ni_{1-x}Mn_x)O_2$ layered compounds [154].

The final calcination temperature was chosen at 900 °C for the samples with y = 0.2, 0.3 and 0.4. For the sample with y = 0.1 (NMC712), the calcination temperatures of 850 °C was used. Hereafter this sample is called NMC712-850. To investigate the effect of calcination temperature, a part of NMC712-850 was calcinated at 900 °C. This sample is called NMC712-900. In the same way, sample with y = 0 was first calcinated at 725 °C, making NMC802-725 sample. To investigate the effect of different calcination temperatures and to find the optimum temperature, NMC802-725 sample was divided into four parts, three of them were calcinated at 750 °C, 800 °C and 900 °C, respectively. In each calcination course, the samples were heated for 15 hours at the final temperature and then cooled in air by removing the crucible from the hot furnace. The samples were characterized chemically and structurally by different characterization methods already described in Chapter 3.

4.2 Results and discussion

4.2.1 $LiNi_xMn_xCo_{1-2x}O_2$ series

4.2.1.1 Chemical analysis

The chemical compositions of the $LiNi_xMn_xCo_{1-2x}O_2$ samples in weight percent, determined by ICP-OES and CGHE, are listed in Table 4.1. It should be mentioned that the numbers after the "±" sign in Table 4.1 represent the repeatability of the experiments and are calculated using type A combined uncertainty analysis and Equation (3.28) with a coverage factor of 2 (confidence level of p ≈ 95%). This does not contain the uncertainties associated with using different sample batches and different devices or operators. It is expected that the total uncertainty of each value is larger than the uncertainty related to repeatability. The results were found to be very close to the nominal values. However, small Li losses were observed, which can be attributed to lithium evaporation during synthesis of these materials. These Li losses depend on the heat treatment temperatures and the employed procedures, and are not uncommon for the preparation of these materials [185]. As the deviations of the measured compositions from the nominal values are

small, only the nominal compositions were used for the refinements of the powder XRD patterns and the evaluation of the enthalpy of formation data of these series of samples in Chapter 6. The effect of neglecting Li loss on the calculation of enthalpies will be discussed in Chapter 6.

Table 4.1: Chemical analysis of the layered $LiNi_xMn_xCo_{1-2x}O_2$ ($0 < x \leq 0.5$) samples. The values in brackets correspond to the nominal compositions. The uncertainties are expanded uncertainties of three sample repetition with a confidence level of p ≈ 95% (k = 2).

sample \ method	(ICP-OES) / wt%				CGHE / wt%
	Li	Ni	Mn	Co	O
$LiCoO_2$	6.78 ± 0.16 [7.09]	---	---	59.7 ± 0.6 [60.21]	28.1 ± 2.6 [32.69]
$LiNi_{0.17}Mn_{0.17}Co_{0.66}O_2$	6.91 ± 0.04 [7.14]	9.55 ± 0.06 [10.07]	9.36 ± 0.2 [9.42]	39.6 ± 0.2 [40.43]	32.9 ± 0.6 [32.93]
$LiNi_{0.33}Mn_{0.33}Co_{0.33}O_2$	7.00 ± 0.18 [7.20]	19.4 ± 0.6 [20.28]	19.1 ± 0.6 [18.98]	19.9 ± 0.6 [20.37]	30.9 ± 4.4 [33.17]
$LiNi_{0.4}Mn_{0.4}Co_{0.2}O_2$	6.89 ± 0.12 [7.22]	23.1 ± 0.6 [24.41]	22.6 ± 0.6 [22.85]	11.8 ± 0.2 [12.25]	34.3 ± 1.2 [33.27]
$LiNi_{0.5}Mn_{0.5}O_2$	6.73 ± 0.04 [7.25]	30.8 ± 0.08 [30.65]	28.2 ± 0.06 [28.69]	---	32.6 ± 0.8 [33.42]

The average oxidation state (AOS) of transition metals is determined by redox titration method as described in Section 3.2.4. The results are summarized in Table 4.2 and show that the AOS for the samples with x = 0.167, 0.333, 0.4 and 0.5 are about 3, i.e. the nominal value for oxidation state of M in $LiMO_2$ compound. The AOS for $LiCoO_2$ sample is 2.67 which is lower than the expected +3 oxidation state. However, the uncertainty of the obtained value for $LiCoO_2$ sample is also higher than the other samples.

The chemical formula in general is described as $Li_\alpha MO_{2-\delta}$ and should satisfy two rules; First, the sum of the cation occupations on the 3(b) sites (in the transition metal layer) should equal one [157]. Second, the sample should be electrically neutral. This means that the sum of the oxidation state of each element multiplied by its occupation must equal zero. Knowing the content of lithium and transition metals through ICP-OES and the content of oxygen,

either through direct measurement using carrier gas hot extraction method or through calculation using average oxidation state of transition metals, one can determine the coefficients of the chemical formula for each sample. The chemical formula of all $LiNi_xMn_xCo_{1-2x}O_2$ samples based on the two assumptions for the content of oxygen are listed in Table 4.3.

Table 4.2: Summary of the results of redox titration of the layered $LiNi_xMn_xCo_{1-2x}O_2$ ($0 < x \leq 0.5$) samples. For each composition, three samples (Nr. 1 to Nr. 3) are measured.

sample	Nr.	NMC 001[1]	NMC 114	NMC 111	NMC 442 [2]	NMC 110
sample mass	1	20.48	20.519	19.913	---	20.221
	2	20.375	20.299	20.47	20.302	20.358
	3	19.801	20.442	20.767	20.616	20.146
formula weight		96.18	96.18	96.18	96.18	95.76
titration factor		1.098	1.098	1.098	1.098	1.083
N of $KMnO_4$		0.055	0.055	0.055	0.055	0.054
V_1 [3]		18.21	18.21	18.21	18.21	18.47
V_2 [4]	1	15.85	14.2	14.2	---	14.55
	2	15.55	14.2	14.1	14.15	14.6
	3	15.6	14.2	14.1	14	14.55
ε	1	0.61	1.03	1.06	---	1.01
	2	0.69	1.04	1.06	1.06	0.99
	3	0.70	1.04	1.05	1.08	1.01
average ε		0.67	1.04	1.06	1.07	1.00
standard deviation		0.049	0.006	0.010	0.016	0.012
two standard error		0.056	0.007	0.011	0.022	0.014
error %		8.46	0.63	1.07	2.09	1.44
AOS		2.67	3.04	3.06	3.07	3.00

[1] $LiCoO_2$

[2] NMC442 of $LiNi_xMn_xCo_{1-2x}O_2$ series (without excess Li).

[3] Average value for three blind samples.

[4] From titration of the sample.

As can be seen in Table 4.3, in almost all samples the coefficient of Li is close to one which indicates negligible Li loss during the synthesis process. Only

NMC110 sample has the highest lithium loss which is possibly due to its higher calcination temperature (1000 °C) than the other samples (900 °C). To compare two methods for the determination of oxygen coefficient, namely redox titration and carrier gas hot extraction, the Δδ parameter is introduced and calculated as follows:

$$\Delta\delta = \frac{\delta_{RT} - \delta_{CGHE}}{\delta_{RT}} \cdot 100 \tag{4.1}$$

Where δ_{RT} and δ_{CGHE} are oxygen coefficient determined by redox titration and carrier gas hot extraction methods, respectively. The values of Δδ are listed in Table 4.3 and the oxygen coefficients are also depicted in Figure 4.1 for all samples.

Table 4.3: Real chemical formula of $LiNi_xMn_xCo_{1-2x}O_2$ ($0 < x \leq 0.5$) samples determined based on ICP-OES results and either redox titration or CGHE measurements.

sample	real composition (redox titration)	real composition (CGHE)	Δδ (%) [1]
NMC001	$Li_{0.96}CoO_{1.81}$	$Li_{0.96}CoO_{1.73}$	4.42
NMC114	$Li_{0.99}Ni_{0.16}Mn_{0.17}Co_{0.67}O_{2.01}$	$Li_{0.99}Ni_{0.16}Mn_{0.17}Co_{0.67}O_{2.05}$	1.99
NMC111	$Li_{0.99}Ni_{0.33}Mn_{0.34}Co_{0.33}O_{2.02}$	$Li_{0.99}Ni_{0.33}Mn_{0.34}Co_{0.33}O_{1.90}$	5.94
NMC442	$Li_{0.99}Ni_{0.39}Mn_{0.41}Co_{0.20}O_{2.02}$	$Li_{0.99}Ni_{0.39}Mn_{0.41}Co_{0.20}O_{2.13}$	5.45
NMC110	$Li_{0.93}Ni_{0.51}Mn_{0.49}O_{1.97}$	$Li_{0.93}Ni_{0.51}Mn_{0.49}O_{1.96}$	0.51

[1] Relative difference between oxygen coefficients determined by two methods (redox titration and carrier gas hot extraction).

As can be seen in Table 4.3, a maximum of 6% difference between two methods is observed, which is a quite good agreement between two very different ways of determination of oxygen coefficient. All samples except $LiCoO_2$ has oxygen coefficients close to ideal value, i.e. 2. In the case of $LiCoO_2$, higher oxygen deficiency of δ = 0.2-0.3 is measured. This is in agreement with the lower AOS of M (Co) in this sample. This is probably the reason of preparing of $LiCoO_2$ under flowing oxygen in many reports [221, 223, 256]. However, in the present work we did not aim to change the partial

pressure of oxygen in the synthesis process. In Chapter 6, we will see that although the synthesized $LiCoO_2$ sample has the highest deviation from the stoichiometry among other samples, its enthalpy of formation has a very good agreement with the literature values. Therefore, the prepared samples could be considered as stoichiometric with good approximation.

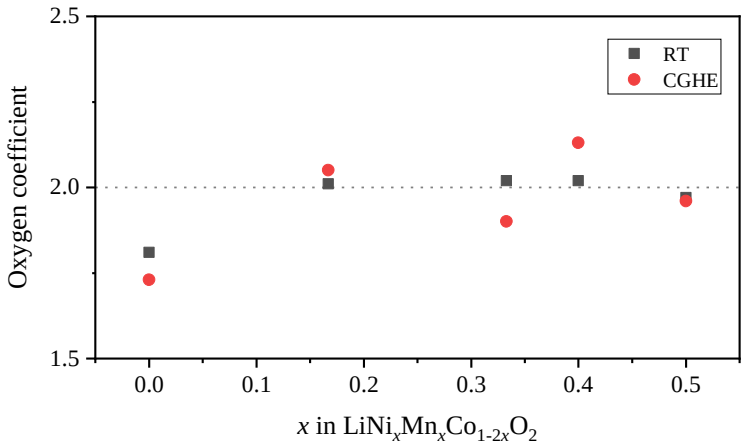

Figure 4.1: Oxygen coefficient in $LiNi_xMn_xCo_{1-2x}O_2$ samples as a function of x, determined by redox titration (RT) or carrier gas hot extraction (CGHE) methods.

4.2.1.2 XRD

The powder X-ray diffraction patterns of the synthesized $LiNi_xMn_xCo_{1-2x}O_2$ samples for different x values are shown in Figure 4.2. For each pattern, all reflections were indexed according to the rhombohedral layered α-$NaFeO_2$-type structure ($R\bar{3}m$ space group, No. 166) which is the common structure for $LiCoO_2$.

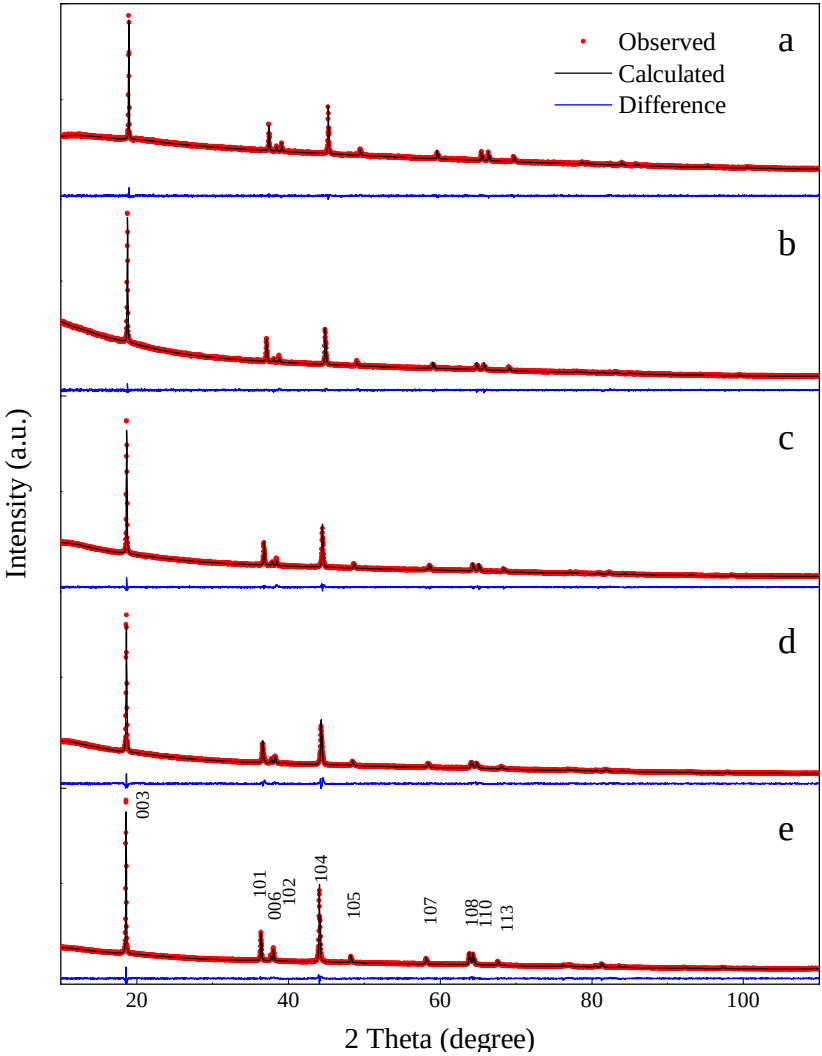

Figure 4.2: Powder XRD patterns for $LiNi_xMn_xCo_{1-2x}O_2$; a) $x = 0$, b) $x = 0.167$, c) $x = 0.333$, d) $x = 0.4$ and e) $x = 0.5$.

By increasing *x*, through substitution of Co^{3+} by equimolar amounts of Mn^{4+} and Ni^{2+}, the $LiNi_xMn_xCo_{1-2x}O_2$ series maintains isotopy with $LiCoO_2$. Comparing the patterns, one can see that the characteristic intensity reflections shift to lower 2 Theta values by increasing *x*, indicating a change in the lattice parameters. A distinctive peak splitting between the (006) and (102) and also the (108) and (110) pairs is a result of the distortion of the oxygen sub-lattice in the hexagonal *c* direction and indicates presence of the layered structure [335]. An obvious reflection splitting can be seen in all XRD patterns. However, it seems that with increasing *x* the degree of splitting decreases. This is possibly related to the overall increase of lattice parameters which leads to a shift of all reflections to smaller angle values. However, there is still a reasonable splitting of the above mentioned doublets in the XRD pattern of the sample with $x = 0.5$ ($LiNi_{0.5}Mn_{0.5}O_2$).

In addition, in XRD patterns, the value of the integrated intensity ratios of (003) peak to (104) peak is used as an indicator of the degree of the cation mixing in the layered compounds [336]. The smaller the I(003) / I(104) ratio is, the higher is the disordering. Generally, the disorder of the layer occupancy takes place when the I(003) / I(104) ratio is below 1.2 [61]. As shown in Table 4.4, the intensity ratio of I(003) / I(104) first increases when *x* in the $LiNi_xMn_xCo_{1-2x}O_2$ materials increases from 0 to 0.167. By further increasing *x*, the I(003) / I(104) ratio decreases. It is noticed that the intensity ratio of I(003) / I(104) in $LiNi_xMn_xCo_{1-2x}O_2$ samples, $x = 0$, 0.167, 0.333, and 0.4, is larger than 1.2, meaning that no undesirable cation mixing has taken place. But at $x = 0.5$, the I(003) / I(104) value is smaller than 1.2, implying that the undesired cation mixing may occur in this sample.

The measured diffractograms were analyzed by the Rietveld refinement method, considering a $LiMO_2$ structural model ($R\bar{3}m$), isotypic to $LiCoO_2$, where the Li ions occupy the 3(*a*) sites, M represents the Ni^{2+}, Mn^{4+} and Co^{3+} ions randomly occupying 3(*b*) sites and O locates on 6(*c*) sites. Occupancies are considered according to nominal stoichiometries. Mixing between Li and transition metal cations did not lead to significant improvement of the residual values and therefore was not considered in the refinements of the present compounds. The measured and calculated patterns are shown in Figure 4.2.

Table 4.4: Summary of X-ray diffraction and Rietveld refinement of the layered $LiNi_xMn_xCo_{1-2x}O_2$ ($0 < x \leq 0.5$) samples. Phase fraction is 100 wt% $LiMO_2$ phase with $R\bar{3}m$ space group, for all samples.

sample	NMC 001[1]	NMC 114	NMC 111	NMC 442	NMC 110
x	0	0.167	0.333	0.4	0.5
I(003) / I(104)	1.49	2.00	1.73	1.62	1.13
a (Å)	2.81607(4)	2.83800(5)	2.86428(4)	2.87646(5)	2.89434(3)
c (Å)	14.0531(5)	14.1810(6)	14.2618(5)	14.2900(6)	14.3245(4)
c/*a*	4.9903(5)	4.9968(6)	4.9791(5)	4.9678(6)	4.9491(4)
Cell volume (Å^3)	96.514(4)	98.915(6)	101.330(5)	102.395(5)	103.923(3)
		(Structural parameters)			
R_p	0.85	1.22	1.43	1.59	1.56
R_{wp}	1.09	1.60	1.95	2.34	2.17
Li_{3a}					
x	0	0	0	0	0
y	0	0	0	0	0
z	0	0	0	0	0
$Occ._{Li}$	1	1	1	1	1
M_{3b}					
x	0	0	0	0	0
y	0	0	0	0	0
z	0.5	0.5	0.5	0.5	0.5
$Occ._{Ni}$	0	0.66	0.33	0.2	0.5
$Occ._{Mn}$	0	0.17	0.33	0.4	0.5
$Occ._{Co}$	1	0.17	0.33	0.4	0
O_{6c}					
x	0	0	0	0	0
y	0	0	0	0	0
z	0.2343(3)	0.2421(6)	0.2427(5)	0.2351(9)	0.2384(8)
Occ.	1	1	1	1	1

[1] $LiCoO_2$

The summary of Rietveld parameters are listed in Table 4.4. Based on the powder-XRD results, all studied samples were considered as single phase with a well-developed layered structure. The lattice constants *a* and *c*, as well as the *c/a* ratio are depicted in Figure 4.3 as functions of *x* in $LiNi_xMn_xCo_{1-2x}O_2$.

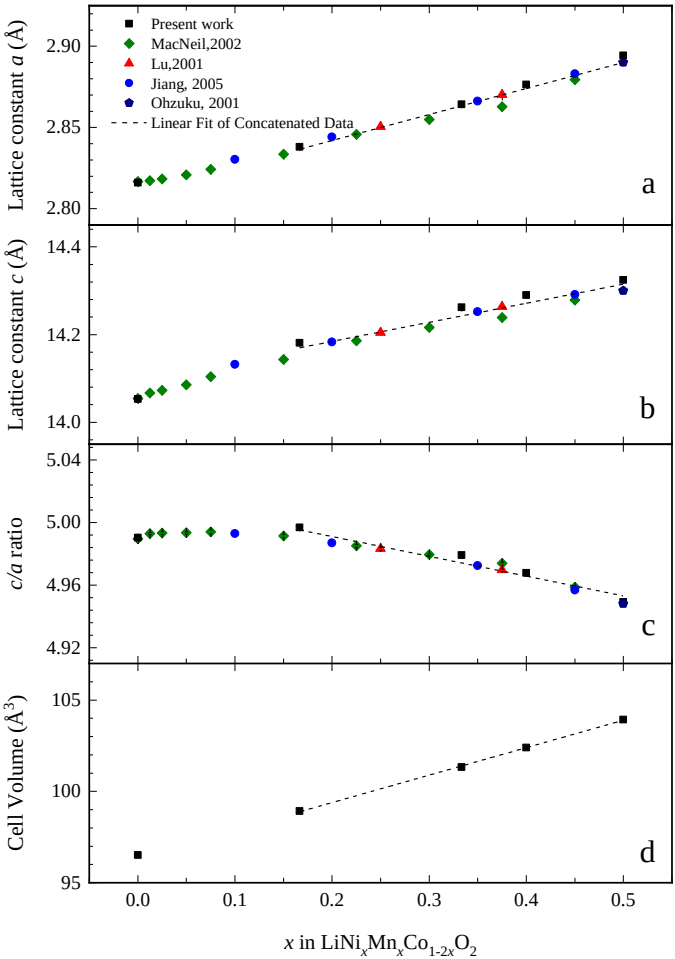

Figure 4.3: Chemical dependency of lattice constants a) *a*, b) *c*, c) *c/a* ratio and d) cell volume vs. *x* in $LiNi_xMn_xCo_{1-2x}O_2$ samples compared with the experimental data from MacNeil et al. [337], Lu et al. [157], Jiang et al. [329] and Ohzuku and Makimura [143]. The linear fits of concatenated data are as Y = α + βX with the residual sum of squares (RSS) while the parameters are as follows a) α = 2.8099 ± 0.00299, β = 0.16024 ± 0.00852, and RSS = 0.0034, b) α = 14.09748 ± 0.0128, β = 0.43499 ± 0.03647 and RSS = 0.02618, c) α = 5.01632 ± 0.00307, β = -0.12635 ± 0.00875 and RSS = 0.00216, d) α = 96.38154 ± 0.079, β = 15.02624 ± 0.21325 and RSS = 13.302.

Both *a* and *c* values increase steadily with increasing *x*, indicating that the lattice expands with the substitution of Co^{3+} in the transition metal layer with equimolar amounts of Mn^{4+} and Ni^{2+} cations. This is mainly attributed to the larger Ni^{2+} cations (ionic radius of 0.69 Å [93]) replacing half of the Co^{3+} cations (ionic radius of 0.545 Å [93]). Replacing Co^{3+} ions by Mn^{4+} ions (ionic radius of 0.53 Å [93]) is not expected to significantly influence the lattice parameters since both ions have similar cationic radii.

The *c*/*a* ratio increases slightly as *x* increases up to $x = 0.167$, and then decreases sharply for $0.167 \leq x \leq 0.5$. Nevertheless, the *c*/*a* ratio of all the materials was observed to be above 4.94 suggesting good layered characteristics [338, 339]. When *x* increases from 0 to 0.167, the lattice expands preferentially in the *c*-direction. This could be explained considering the non-substituted $LiCoO_2$, in which the O^{2-} ions are placed on the general 6(*c*) position with the site coordination of (0,0,*z*) and $z = 0.23951(15)$ [340]. The deviation of *z* from an ideal value of ¼ is possibly due to the relatively strong bonding tendency of oxygen to the transition metal, which fills up the open spaces in distorted octahedra formed by O^{2-} ions. When Co is substituted by small equimolar amounts of Mn^{4+} and Ni^{2+}, the lattice preferentially expands in the *c*-direction to approach to the ideal $z = ¼$. Consequently, the distortion of the O^{2-} octahedra is lowered, indicating an improved layered nature of the crystal structure in $LiNi_{0.167}Mn_{0.167}Co_{0.666}O_2$. This sample possesses the highest *c*/*a* ratio showing the most layered structure. As the *x* value increases beyond 0.167, the structure expands more in the *a*,*b*-direction, then the *c*/*a* ratio decreases. The observed behavior of the *c*/*a* ratio is in accordance with the changes of I(003) / I(104) in these samples. The trend of the change in the lattice parameters with *x* is almost linear, which is common for a substitution mechanism that is not accompanied by significant attractive or repulsive electronic effects. As can be seen in Figure 4.3, the lattice parameters determined by Rietveld refinement are in a very good agreement with the literature data [157, 329, 337]. The linear trend is also observed by Shizuka et al. for $0.3 \leq x \leq 0.5$ [341].

4.2.2 Effect of calcination temperature on the Ni-rich NMCs

As described in Section 4.1, in order to prepare $LiNi_{0.8-y}Mn_yCo_{0.2}O_2$ samples with the closest chemical formula to the nominal values, the optimum calcination temperatures for the samples with y = 0 and 0.1 were investigated. In each calcination course, the samples were heated for 15 hours at the final temperature and then cooled in air by removing the crucible from the hot furnace. The chemical formula and the structural properties of the samples are evaluated and used as the criteria for choosing the best calcination temperature.

4.2.2.1 $LiNi_{0.8}Co_{0.2}O_2$

A sample with y = 0 was first calcinated at 725 °C, making NMC802-725 sample. The NMC802-725 sample was then calcinated at 750 °C, 800 °C and 900 °C, creating NMC802-750, NMC-800 and NMC802-900 samples, respectively.

4.2.2.1.1 Chemical analysis

The chemical compositions of the NMC802-725, NMC802-750, NMC-800 and NMC802-900 samples, determined by ICP-OES, carbon analyzer and CGHE are listed in Table 4.5 in weight percent. The results show that by increasing the calcination temperature the deviation of lithium contents from the nominal values increases, while carbon content decreases. The observed increase of lithium loss could be explained by more severe volatilization of lithium at higher synthesis temperatures [185, 342]. The reduction in carbon content by increasing the firing temperature will be discussed later.

The average oxidation state (AOS) of transition metals in calcinated samples are determined by redox titration method. The results are summarized in Table 4.6 and show that the AOS of transition metals slightly increases as the calcination temperature increases. However, the AOS in the sample which is heat treated at 725 °C is much lower than the nominal value of 3. This is possibly due to the fact that at 725 °C, a part of the Ni cations are still in +2 oxidation state and not completely oxidized to Ni^{3+} ions.

Table 4.5: Chemical analysis of the NMC802 samples heat-treated at different calcination temperatures along with the nominal compositions. The uncertainties are expanded uncertainties of three sample repetition with a confidence level of p ≈ 95% (*k* = 2).

Calcination temperature (°C)	ICP-OES (wt%)			Carbon analyzer (wt%)	CGHE (wt%)
	Li	Ni	Co	C	O
725	7.07 ± 0.04	46.1 ± 0.2	11.60 ± 0.06	0.737 ± 0.006	28.3 ± 1.2
750	6.98 ± 0.06	46.7 ± 0.2	11.84 ± 0.02	0.310 ± 0.010	30.8 ± 1.0
800	6.79 ± 0.04	47.5 ± 0.4	12.0 ± 0.2	0.138 ± 0.006	29.3 ± 1.2
900	6.16 ± 0.04	48.8 ± 0.2	12.36 ± 0.04	0.047 ± 0.003	31.3 ± 1.0
Nominal	7.11	48.07	12.07	0	32.76

The chemical formula is determined in the same way as described in Section 4.2.1.1 for $LiNi_xMn_xCo_{1-2x}O_2$ samples. In $Li_\alpha MO_{2-\delta}$ formula two rules should be satisfied; first, the sum of the cation occupations on the 3*b* sites (in the transition metal layer) should equal one [157]. Second, the sample should be electrically neutral. This means that the sum of the oxidation state of each element times its occupation must equal zero. Yet as the carbon contents for $LiNi_{0.8-y}Mn_yCo_{0.2}O_2$ samples were determined, it was assumed that the carbon in the sample is in the form of lithium carbonate. Therefore, the amount of Li_2CO_3 in each sample is calculated based on C wt%. The amount of lithium and oxygen present in lithium carbonate phase are subtracted from the total lithium and oxygen content. Then the remained lithium and oxygen are used for the calculation of lithium and oxygen coefficients in the $Li_\alpha MO_{2-\delta}$ phase. Here similar to what done in Section 4.2.1.1 for the $LiNi_xMn_xCo_{1-2x}O_2$ samples, the coefficients of oxygen is determined by direct measurement using carrier gas hot extraction method as well as by calculation using average oxidation state of transition metals. The chemical formula of the NMC802 samples as well as their lithium carbonate content are listed in Table 4.7. The variations of Li coefficients and oxygen coefficients determined by two methods and the values of Li_2CO_3 phase in wt% as a function calcination temperature in NMC802 sample are depicted in Figure 4.4 a-c.

Table 4.6: Summary of the results of redox titration of the NMC802 samples heat-treated at different calcination temperatures. For each sample with specific calcination temperature, three samples (Nr. 1 to Nr. 3) are experimented by redox titration.

Calcination temperature (°C)		725	750	800
sample mass	Nr. 1	20.48	20.519	19.913
	Nr. 2	20.375	20.299	20.47
	Nr. 3	19.801	20.442	20.767
formula weight		96.18	96.18	96.18
titration factor		1.098	1.098	1.098
N of $KMnO_4$		0.055	0.055	0.055
V_1 [1]		18.21	18.21	18.21
V_2 [2]	Nr. 1	15.85	14.2	14.2
	Nr. 2	15.55	14.2	14.1
	Nr. 3	15.6	14.2	14.1
ε	Nr. 1	0.61	1.03	1.06
	Nr. 2	0.69	1.04	1.06
	Nr. 3	0.70	1.04	1.05
average ε		0.67	1.04	1.06
standard deviation		0.049	0.006	0.010
two standard error		0.056	0.007	0.011
error %		8.46	0.63	1.07
AOS		2.67	3.04	3.06

[1] Average value for three blind samples

[2] From titration of the sample

As displayed in Table 4.7 and Figure 4.4 a, when the calcination temperature increases, the lithium coefficient initially increases to reach the nominal value of one (the dashes line) in NMC802-750 sample. Then in NMC-800 the Li coefficients decreases slightly. By further increasing the calcination temperature, the Li coefficient noticeably deviates from the ideal value, showing a considerable Li evaporation by calcination at 900 °C.

Table 4.7: Real chemical formula of $LiNi_xMn_xCo_{1-2x}O_2$ ($0 < x \leq 0.5$) samples determined based on ICP-OES results and either redox titration or CGHE measurements.

nominal composition	real composition (redox titration)	real composition (CGHE)	Li_2CO_3 (wt%)
725	$Li_{0.91}Ni_{0.8}Co_{0.20}O_{1.88}$	$Li_{0.91}Ni_{0.8}Co_{0.20}O_{1.61}$	4.53
750	$Li_{0.96}Ni_{0.8}Co_{0.20}O_{1.93}$	$Li_{0.96}Ni_{0.8}Co_{0.20}O_{1.85}$	1.91
800	$Li_{0.94}Ni_{0.8}Co_{0.20}O_{1.92}$	$Li_{0.94}Ni_{0.8}Co_{0.20}O_{1.77}$	0.85
900	---	$Li_{0.84}Ni_{0.8}Co_{0.20}O_{1.87}$	0.29

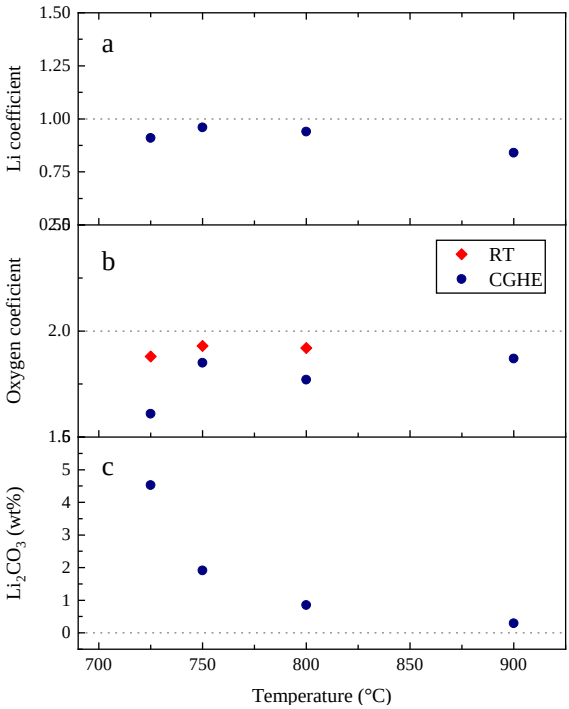

Figure 4.4: The variations of a) Li coefficients, b) oxygen coefficients determined by two methods, namely redox titration (RT) and carrier gas hot extraction (CGHE) and c) the values of Li_2CO_3 phase in wt% as a function of calcination temperature in NMC802 sample. The dashed lines show the ideal values for each parameter.

As can be seen in Figure 4.4 b, the oxygen coefficients generally increase as the calcination temperature increases. It is to be noticed that the values of oxygen coefficient determined by redox titration are larger than the coefficients determined by CGHE for all samples, although the trend of changes of oxygen coefficients against *y* is nearly the same in both methods. The oxygen coefficients approach the nominal value of 2 when the calcination temperature is above 750 °C and stay almost constant up to the calcination temperature of 900 °C. Nonetheless, the NMC802-725 sample has the lowest oxygen coefficient value. Li et al. performed XPS analysis of two NMC111 samples, annealed at 700 °C and 900 °C and also indicated that a lower annealing temperature results in the formation of oxygen deficiency [175].

As shown in Figure 4.4 c, the content of Li_2CO_3 decreases constantly as the calcination temperature increases. It is known that Li_2CO_3 is a reaction intermediate of the sol-gel process which melts at about 723 °C and reacts with the transition metal oxides to produce the lithiated layered structure. Therefore, when the calcination temperature is lower, there would be more unreacted Li_2CO_3 phase present in the final product.

4.2.2.1.2 XRD

The powder X-ray diffraction patterns of the NMC802 samples with different calcination temperatures are depicted in Figure 4.5. The measured diffractograms were analyzed by Rietveld refinement method, considering a $LiMO_2$ structural model ($R\bar{3}m$), isotypic to $LiNiO_2$, where the Li ions occupy the 3(*a*) sites and M represents the transition metal cations including Co and Ni randomly occupying 3(*b*) sites. Oxygen anions reside on 6(*c*) sites with (0, 0, *z*) coordinates. The occupancy of Li ions at 3(*a*) sites and Ni and Co at 3(*b*) sites were obtained from the chemical formula based on ICP-OES data. The measured and calculated patterns are shown in Figure 4.5. In this figure the red circles are the collected experimental data and the solid black lines are the calculated patterns. The summary of Rietveld parameters are listed in Table 4.8. The lattice constants *a* and *c*, the *c/a* ratio as well as the cell volume are depicted in Figure 4.6 as functions of calcination temperature.

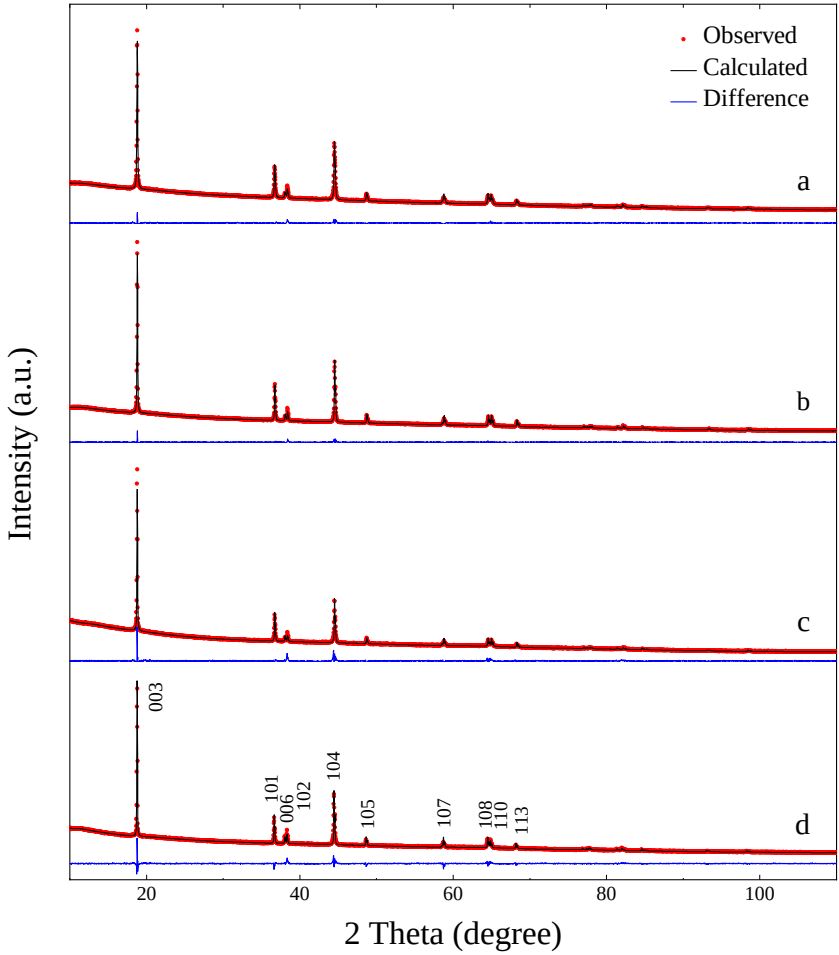

Figure 4.5: Powder XRD pattern for NMC802 sample heat-treated at a) 725 °C, b) 750 °C, c) 800 °C, and d) 900 °C.

Table 4.8: Summary of X-ray diffraction and Rietveld refinement of the layered NMC802 sample heat-treated at 725 °C, 750 °C, 800 °C, and 900 °C. Phase fraction is 100 wt% $LiMO_2$ phase with $R\bar{3}m$ space group, for all samples.

Calcination temperature (°C)	725	750	800	900
I(003) / I(104)	1.50	1.54	1.94	1.59
a (Å)	2.86987(3)	2.86755(2)	2.86809(3)	2.87301(3)
c (Å)	14.1820(4)	14.1694(3)	14.1783(3)	14.1812(3)
c/*a*	4.9417(4)	4.9413(4)	4.9435(4)	4.9360(4)
Cell volume (Å^3)	101.156(3)	100.903(2)	101.004(3)	101.372(3)
		(Structure parameters)		
R_p	0.93	0.98	1.25	1.31
R_{wp}	1.42	1.46	1.86	2.31
Li_{3a}				
x	0	0	0	0
y	0	0	0	0
z	0	0	0	0
Occ.	0.91	0.91(54)	0.94	0.84
M_{3b}				
x	0	0	0	0
y	0	0	0	0
z	0.5	0.5	0.5	0.5
$Occ._{Ni}$	0.8	0.80(5)	0.8	0.8
$Occ._{Mn}$	0	0	0	0
$Occ._{Co}$	0.2	0.2	0.2	0.2
O_{6c}				
x	0	0	0	0
y	0	0	0	0
z	0.2432(4)	0.2438(3)	0.2432(5)	0.2424(5)
Occ.	0.888(8)	0.889(7)	0.8948(97)	0.822(12)

[1] Pre-calcinated powder is calcinated at 800 °C for 15 hours in air.

[2] Pre-calcinated powder is calcinated at 850 °C for 15 hours in air.

In each pattern, all peaks were indexed according to the rhombohedral layered α-$NaFeO_2$-type structure ($R\bar{3}m$ space group, No. 166) which is the common structure for the layered $LiNiO_2$. For all samples, the peak with the highest

intensity was observed to be the (003) line. By increasing the calcination temperature, the samples remain single phase with an α-$NaFeO_2$-type structure. If lithium carbonate is present in the studied samples, its amount is less than the detection limit of XRD, which is typically 5 wt%.

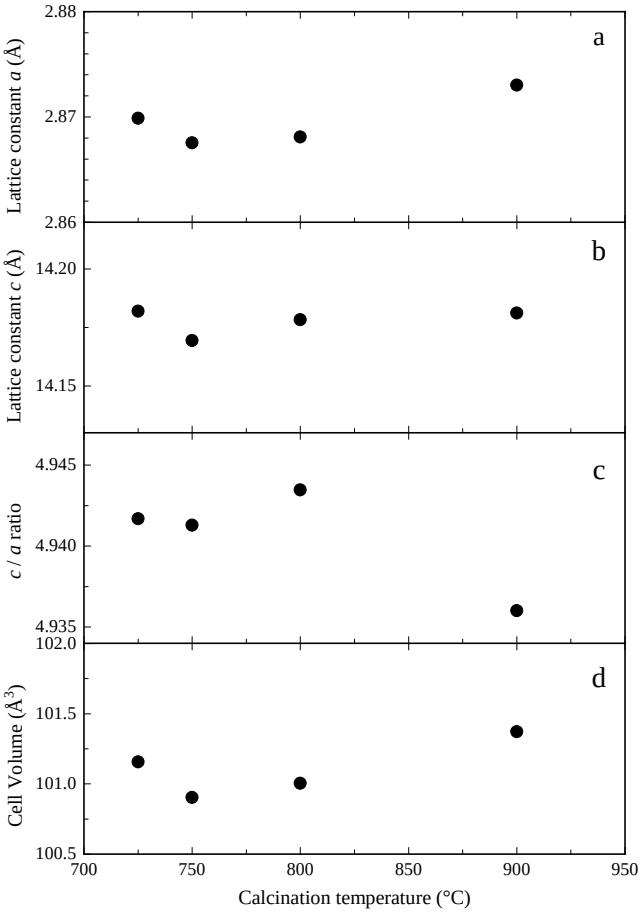

Figure 4.6: Variations of the lattice constants a) *a*, b) *c*, c) *c/a* ratio and d) cell volume by calcination temperature in the NMC802 sample.

An obvious peak splitting between the (006) and (102) as well as between the (108) and (110) pairs is observed for all samples indicating the presence of the layered structure. Here similar to Section 4.2.1.2 , the value of the integrated intensity ratios of (003) peak to (104) peak is evaluated as an indication of the degree of cation mixing in the layered compounds [336]. A larger I(003) / I(104) ratio implies that the sample is more highly ordered [343]. Generally, the disorder of the layer occupancy takes place when the I(003) / I(104) ratio is below 1.2 [61]. As shown in Table 4.8, the intensity ratio of I(003) / I(104) first increases as the calcination temperature increases up to 800 °C. However, in the NMC802 sample heat treated at 900 °C, the I(003) / I(104) value drops drastically. The NMC802-800 sample shows the highest I(003) / I(104) value of 1.94 indicating the minimum cation mixing.

By increasing the calcination temperature, *a* , *c* and cell volume first decreases up to 750 °C and then increases with further increase of calcination temperature. The *c*/*a* ratio of all the materials was observed to be above 4.94 for all samples suggesting good layered characteristics [338, 339]. However, the *c*/*a* ratio increases to its maximum value in NMC802-800 sample and then decreases when the sample is heat treated at 900 °C, indicating the best 2D character and the highest layered structure among other NMC802 samples.

4.2.2.2 $LiNi_{0.7}Mn_{0.1}Co_{0.2}O_2$

For the samples with $y = 0.1$, initially the calcination temperatures of 850 °C was used (NMC712-850 sample) and subsequently a part of the NMC712-850 sample was calcinated at 900 °C (NMC712-900).

4.2.2.2.1 Chemical analysis

The chemical compositions of the NMC712-850 and NMC712-900 samples in weight percent, determined by ICP-OES, carbon analyzer and CGHE along with the nominal values are listed in Table 4.9. The results reveal reductions in lithium and carbon contents that increase by increasing the calcination temperature. Similar to the previous samples, the Li losses here are also attributed to volatilization of lithium at the high synthesis temperature [185, 342].

Table 4.9: Chemical analysis of the NMC712 samples heat-treated at different calcination temperatures and the nominal compositions. The uncertainties are expanded uncertainties of three sample repetition with a confidence level of p ≈ 95% (*k* = 2).

Calcination temperature (°C)	ICP-OES (wt%)			Carbon analyzer (wt%)	CGHE (wt%)
	Li	Ni	Co	C	O
850	7.01 ± 0.06	41.2 ± 0.2	12.00 ± 0.06	0.187 ± 0.006	29.5 ± 1.6
900	6.19 ± 0.06	43.0 ± 0.2	12.48 ± 0.06	0.0431 ± 0.010	29.8 ± 0.8
Nominal	7.13	42.22	12.11	0	32.88

The average oxidation state (AOS) of transition metals in NMC712-850 is determined by redox titration method as 2.95. The chemical formula are determined in the same way as described in Section 4.2.2.1.1. The chemical formula of the NMC712 samples calculated based on carrier gas hot extraction method as well as by calculation using average oxidation state of transition metals together with their lithium carbonate content are listed in Table 4.10. As shown in Table 4.10, by increasing the calcination temperature from 850 °C to 900 °C, the decline of lithium coefficients and oxygen coefficients from their nominal values increases. Therefore, it seems that the NMC712-850 sample is closer to the nominal composition.

Table 4.10: Real chemical formula of NMC712 samples heat-treated at different calcination temperatures, determined based on ICP-OES results and either redox titration (RT) or carrier gas hot extraction (CGHE) measurements.

Calcination temperature (°C)	real composition (redox titration)	real composition (CGHE)	Li_2CO_3 (wt%)
850	$Li_{0.97}Ni_{0.7}Mn_{0.1}Co_{0.2}O_{1.96}$	$Li_{0.97}Ni_{0.7}Mn_{0.1}Co_{0.2}O_{1.79}$	1.15
900	--- [1]	$Li_{0.84}Ni_{0.7}Mn_{0.1}Co_{0.2}O_{1.76}$	0.27

[1] Not determined

4.2.2.2.2 XRD

The powder X-ray diffraction patterns of the NMC712 samples with two different calcination temperatures are depicted in Figure 4.7. The measured diffractograms were analyzed using the Rietveld refinement method, similar to NMC802 samples. The measured and calculated patterns are shown in Figure 4.7. The summary of Rietveld parameters are listed in Table 4.11.

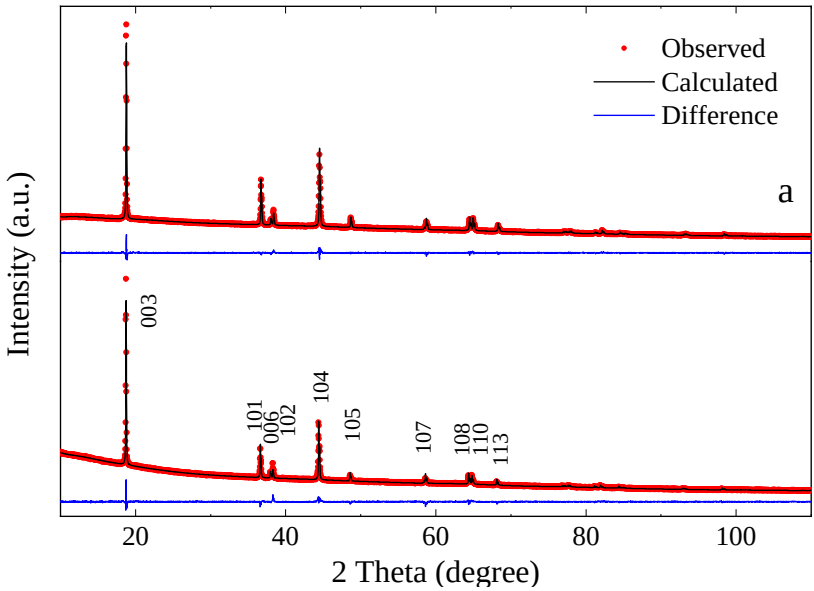

Figure 4.7: Powder XRD pattern for $LiNi_{0.7}Mn_{0.1}Co_{0.2}O_2$ sample heat treated at a) 850 °C (NMC712-850 sample) and b) 900 °C (NMC712-900 sample).

For each pattern, all peaks were indexed according to the rhombohedral layered α-$NaFeO_2$-type structure ($R\bar{3}m$ space group, No. 166). For both samples, the peak with the highest intensity was observed to belong to the (003) line. By increasing the calcination temperature, the NMC712 samples remain single phase with α-$NaFeO_2$-type structure. An obvious peak splitting between

the (006) and (102) as well as between the (108) and (110) pairs is an indication of the presence of the layered structure.

Table 4.11: Summary of X-ray diffraction and Rietveld refinement of the $LiNi_{0.7}Mn_{0.1}Co_{0.2}O_2$ sample heat treated at 850 °C and 900 °C. Phase fraction is 100 wt% $LiMO_2$ phase with $R\bar{3}m$ space group, for all samples.

Calcination temperature (°C)	850	900
I(003) / I(104)	1.37	1.56
a (Å)	2.86870(2)	2.87520(3)
c (Å)	14.1978(3)	14.2145(3)
c/a	4.9492(3)	4.9438(3)
Cell volume (Å^3)	101.186(3)	101.765(3)
	(Structure parameters)	
R_p	0.91	1.26
R_{wp}	1.41	2.01
Li_{3a}		
x	0	0
y	0	0
z	0	0
Occ.	0.97	0.84
M_{3b}		
x	0	0
y	0	0
z	0.5	0.5
$Occ._{Ni}$	0.7	0.7
$Occ._{Mn}$	0.1	0.1
$Occ._{Co}$	0.2	0.2
O_{6c}		
x	0	0
y	0	0
z	0.2436(3)	0.2432(5)
Occ.	0.913(7)	0.865(11)

In addition, the value of the integrated intensity ratios of the (003) peak to the (104) peak revealed in Table 4.11 increases as the calcination temperature

increases, indicating less cation mixing [336]. However, the intensity ratio of I(003) / I(104) is greater than 1.2 for both samples, meaning that no undesirable cation mixing took place. The *c*/*a* ratio decreases slightly by increasing the calcination temperature from 850 °C to 900 °C. The *c*/*a* ratio of both samples was still above 4.94, showing good layered characteristics [338, 339].

Overall, considering the chemical formula and the structural properties, it seems that for NMC712 sample calcination at 750 °C is a more optimized synthesis condition.

4.2.3 $LiNi_{0.8-y}Mn_yCo_{0.2}O_2$ series

4.2.3.1 Chemical analysis

The chemical compositions of the $LiNi_{0.8-y}Mn_yCo_{0.2}O_2$ samples determined by ICP-OES, carbon analyzer and CGHE are listed in Table 4.12 in weight percent. The results for transition metals were found to be very close to the nominal values with a maximum of 2.9 % relative difference in Ni content of the NMC442 sample. However, there were small Li losses. The highest Li losses were observed in the NMC622 and NMC802 samples with 5.59 % and 6.33 % relative difference with nominal values, respectively. Similar to previous samples, the Li losses here are also attributed to volatilization of lithium at the high synthesis temperature and are common for the preparation of Ni-rich compositions [185, 342]. The oxygen contents determined by CGHE are up to 10.4 % (in sample NMC712) less than the nominal values. This is similar to the trend observed for $LiNi_xMn_xCo_{1-2x}O_2$ samples.

The average oxidation state (AOS) of transition metals is determined by redox titration method as described in Chapter 3. The results are summarized in Table 4.13 and show that as *y* in $LiNi_{0.8-y}Mn_yCo_{0.2}O_2$ increases, the AOS of transition metals slightly increases. However, in all samples, the AOS values are within a small range in the vicinity of the nominal value of 3.

Table 4.12: Chemical analysis of the layered $LiNi_{0.8-y}Mn_yCo_{0.2}O_2$ ($0 < y \leq 0.4$) samples. The values in brackets correspond to the nominal compositions. The uncertainties are expanded uncertainties of three sample repetition with a confidence level of p ≈ 95% (k = 2).

sample \ method	ICP-OES (wt%)				carbon analysis (wt%)	CGHE (wt%)
	Li	Ni	Mn	Co	C	O
NMC442 [1]	7.24 ± 0.12 [7.22]	23.7 ± 0.4 [24.41]	22.51 ± 0.40 [22.85]	12.03 ± 0.22 [12.25]	0.090 ± 0.008	31.8 ± 0.8 [33.3]
NMC532	7.09 ± 0.06 [7.19]	29.73± 0.10 [30.39]	16.78 ± 0.08 [17.07]	12.07 ± 0.04 [12.21]	0.060 ± 0.004	31.8 ± 1.8 [33.1]
NMC622	6.76 ± 0.02 [7.16]	36.13 ± 0.08 [36.33]	11.33 ± 0.02 [11.34]	12.24 ± 0.02 [12.16]	0.046 ± 0.004	29.9 ± 1.0 [33.0]
NMC712 [2]	7.01 ± 0.06 [7.13]	41.2 ± 0.2 [42.22]	5.53 ± 0.02 [5.65]	12.00 ± 0.06 [12.11]	0.187 ± 0.006	29.5 ± 1.6 [32.9]
NMC802 [3]	6.66 ± 0.04 [7.11]	48.01 ± 0.16 [48.07]	0	12.09 ± 0.04 [12.07]	0.130 ± 0.001	--- [4]

[1] NMC442 of $LiNi_{0.8-y}Mn_yCo_{0.2}O_2$ series (with excess Li)

[2] Calcinated at 850 °C for 15 hours in air.

[3] Calcinated at 800 °C for 15 hours in air.

[4] Not determined.

In general, the chemical formula is determined in the same way as described in Section 4.2.1.1 for $LiNi_xMn_xCo_{1-2x}O_2$ samples. In $Li_\alpha MO_{2-\delta}$ formula two rules should be satisfied; first, the sum of the cation occupations on the 3*b* sites (in the transition metal layer) should equal one [157]. Second, the sample should be electrically neutral. This means that the sum of the oxidation state of each element multiplied by its occupation must equal zero. Yet, as the carbon content for $LiNi_{0.8-y}Mn_yCo_{0.2}O_2$ samples were determined, it was assumed that the carbon in the sample is in the form of lithium carbonate. Therefore, the amount of Li_2CO_3 in each sample is calculated based on C wt%. The amount of lithium and oxygen present in lithium carbonate phase are subtracted from the total lithium and oxygen content. Then the remained lithium and oxygen are used for the calculation of lithium and oxygen coefficient in the $Li_\alpha MO_{2-\delta}$ phase.

Table 4.13: Summary of the results of redox titration of the layered $LiNi_{0.8-y}Mn_yCo_{0.2}O_2$ ($0 < y \leq 0.4$) samples. For each composition, three samples (Nr. 1 to Nr. 3) are measured.

Sample	Nr.	NMC 442 [1]	NMC 532	NMC 622	NMC 712 [2]	NMC 802 [3]
sample mass	1	20.267	20.339	19.997	20.137	20.168
	2	20.884	20.351	20.445	20.2	20.284
	3	20.841	20.731	20.17	20.424	---
formula weight		96.18	96.55	96.93	97.31	97.68
titration factor		1.075	1.075	1.075	1.078	1.098
N of $KMnO_4$		0.054	0.054	0.054	0.054	0.055
V_1 [4]		18.60	18.60	18.60	18.55	18.21
V_2 [5]	1	14.55	14.55	14.8	14.85	14.75
	2	14.45	14.5	14.8	14.85	14.7
	3	14.5	14.55	14.85	14.9	---
ε	1	1.03	1.03	0.99	0.96	0.92
	2	1.03	1.05	0.97	0.96	0.93
	3	1.02	1.01	0.97	0.94	---
average ε		1.03	1.03	0.98	0.95	0.92
standard deviation		0.008	0.016	0.012	0.014	0.006
two standard error		0.009	0.018	0.014	0.017	0.008
error %		0.92	1.79	1.47	1.75	0.86
AOS		3.03	3.03	2.98	2.95	2.92

[1] NMC442 of $LiNi_{0.8-y}Mn_yCo_{0.2}O_2$ series (with excess Li)

[2] Calcinated at 850 °C for 15 hours in air.

[3] Calcinated at 800 °C for 15 hours in air.

[4] Average value for three blind samples

[5] From titration of the samples.

Here similar to Section 4.2.1.1 for $LiNi_xMn_xCo_{1-2x}O_2$ samples, the coefficient of oxygen is determined by direct measurement using carrier gas hot extraction method as well as by calculation using average oxidation state of transition metals. The chemical formula of $LiNi_{0.8-y}Mn_yCo_{0.2}O_2$ samples calculated based on both methods as well as their lithium carbonate content are listed in Table

4.14. The values of Li_2CO_3 phase in wt% along with the oxygen coefficients in $LiNi_{0.8-y}Mn_yCo_{0.2}O_2$ samples determined by two methods, namely redox titration and carrier gas hot extraction, are depicted in Figure 4.8.

Table 4.14: Real chemical formula of $LiNi_{0.8-y}Mn_yCo_{0.2}O_2$ ($0 < y \leq 0.4$) samples determined based on ICP-OES and carbon analysis results and either redox titration or CGHE measurements.

Sample	real composition (redox titration)	real composition (CGHE)	Li_2CO_3 (wt%)
NMC442 [1]	$Li_{1.01}Ni_{0.4}Mn_{0.4}Co_{0.2}O_{2.02}$	$Li_{1.01}Ni_{0.4}Mn_{0.4}Co_{0.2}O_{1.93}$	0.55
NMC532	$Li_{0.99}Ni_{0.5}Mn_{0.3}Co_{0.2}O_{2.01}$	$Li_{0.99}Ni_{0.5}Mn_{0.3}Co_{0.2}O_{1.94}$	0.37
NMC622	$Li_{0.94}Ni_{0.6}Mn_{0.2}Co_{0.2}O_{1.96}$	$Li_{0.94}Ni_{0.6}Mn_{0.2}Co_{0.2}O_{1.80}$	0.28
NMC712 [2]	$Li_{0.97}Ni_{0.7}Mn_{0.1}Co_{0.2}O_{1.96}$	$Li_{0.97}Ni_{0.7}Mn_{0.1}Co_{0.2}O_{1.79}$	1.15
NMC802 [3]	$Li_{0.92}Ni_{0.8}Co_{0.2}O_{1.92}$	--- [4]	0.80

[1] NMC442 of $LiNi_{0.8-y}Mn_yCo_{0.2}O_2$ series (with excess Li)

[2] Pre-calcinated powder is calcinated at 850 °C for 15 hours in air.

[3] Pre-calcinated powder is calcinated at 800 °C for 15 hours in air.

[4] Not determined.

As can be seen in Table 4.14 and Figure 4.8, in almost all samples the coefficient of Li is close to one which shows negligible Li loss during the synthesis process. The NMC802 sample has the lowest lithium coefficient of 0.92 despite its lowest calcination temperature (800 °C) compared to the other samples. This is possibly due to its higher Ni content and the complications associated with the preparation of stoichiometric $LiNiO_2$ phase [90]. The values of oxygen coefficient determined by redox titration are larger than the coefficients determined by CGHE for all samples, even though the trend of changes of oxygen coefficients against y is almost the same in both methods. The oxygen coefficients in the formula of samples with y = 0.4, 0.3, 0.2 and 0.1 are closer to the nominal value of 2 (shown by dashed line in Figure 4.8). Nonetheless, in the NMC802 sample (y = 0), the oxygen coefficient has the lowest value. This is due to the difficulty of stabilizing trivalent nickel cations through high temperature calcination in air. The average oxidation state of

transition metal in NMC802 sample which is less than +3 is compensated by oxygen deficiency.

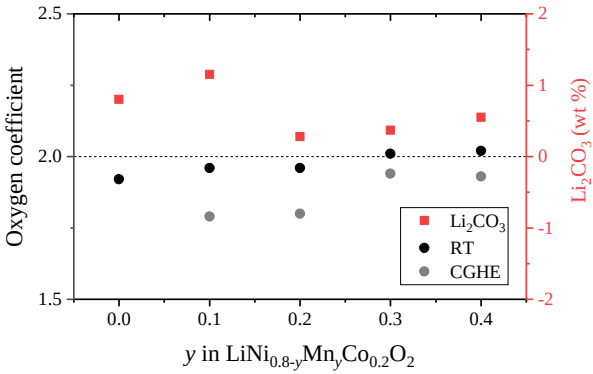

Figure 4.8: The oxygen coefficients in $LiNi_{0.8-y}Mn_yCo_{0.2}O_2$ samples determined by two methods, namely redox titration and carrier gas hot extraction (left Y axis) and the values of Li_2CO_3 phase in wt% (right Y axis) as a function of *y*.

It has been shown that the lithium residual species are present on the surface of $LiNiO_2$ and its analogues NMC compounds [344–346]. There are two possible sources for the Li_2CO_3 impurity phase. The first source is related to the fact that the excess of lithium is required for preparing highly ordered Ni-rich layer compounds [61, 228], residual lithium which is not incorporated into the layered structure can remain on the surface of the active materials. This lithium reacts with the moisture and CO_2 from air, in the case of present work during grinding and transfer processes thus forming LiOH and Li_2CO_3 [347]. In addition, as mentioned before, Li_2CO_3 is a reaction intermediate of the sol-gel process which melts at about 723 °C and reacts with the transition metal oxides to produce the lithiated layered structure. If the calcination temperature and time is not enough, depending on the composition and morphology of the synthesized powder, there might be some unreacted Li_2CO_3 phase present in the final product.

Comparing the amount of lithium carbonate in samples heat treated at 900 °C, namely NMC442, NMC532 and NMC622, the content of Li_2CO_3 increases slightly as *y* increases. This could be attributed to higher residual excess lithium in samples with lower Ni content. NMC802 and NMC712 contain higher amounts of lithium carbonate. This might be related to the lower calcination temperatures of these samples which are closer to the decomposition temperature of lithium carbonate and higher residual carbonate from the synthesis process. However, the amount of Li_2CO_3 impurity phase in all samples is maximum 1.2 wt%. These amounts of impurity phase are negligible considering their effect of the further thermal and thermochemical investigations performed on powder samples in the present work.

4.2.3.2 Morphology

The scanning electron microscopy (SEM) micrographs with secondary electron detector are displayed in Figure 4.9- a-e. These figures show the surface morphology of as-calcinated $LiNi_{0.8-y}Mn_yCo_{0.2}O_2$ samples. Two different magnifications are given for each sample. The SEM images of the sol-gel products show that the as-calcinated powders are secondary particles agglomerated from highly packed primary particles. The primary particles are almost uniform and spherical crystalline grains. The particle size gradually increases as *y* in $LiNi_{0.8-y}Mn_yCo_{0.2}O_2$ decreases. The NMC442 sample has a small particle size about 200 nm while the particle size of NMC802 sample is up to 1 µm. The particles have defined edges consistent with the high crystallinity resulting from the high temperature heating, which was also indicated by sharp X-ray diffraction reflections. At high magnification, the SEM pictures of the surface of the sample reveal very small dust-like particles on the surface of primary NMC particles in NMC622, NMC712 and NMC802 samples. However, these small particles were not evenly distributed on the surface of agglomerates. It was speculated that these are lithium carbonate phase forming on the surface of NMC particles. These impurity phases are possibly formed through the reaction of lithium from the NMC phase with the carbon dioxide or humidity from the air during calcination and/or grinding processes. As can be seen in Figure 4.9, the amount of lithium carbonate generally increases as *y* in $LiNi_{0.8-y}Mn_yCo_{0.2}O_2$ decreases. This means that the

samples with higher Ni content are more prone to the contamination with air and to the formation of superficial impurity phases.

4.2.3.3 XRD

The powder X-ray diffraction patterns of the as-calcinated $LiNi_{0.8-y}Mn_yCo_{0.2}O_2$ samples for different *y* values are depicted in Figure 4.10. For each pattern, all reflections were indexed according to the rhombohedral layered α-$NaFeO_2$-type structure ($R\bar{3}m$ space group, No. 166) which is the common structure for the layered $LiNiO_2$. For all samples prepared in this series, the strongest line was observed as being the (003) line. By increasing *y*, through substitution of Mn^{4+} and Ni^{2+} for Ni^{3+}, the $LiNi_{0.8-y}Mn_yCo_{0.2}O_2$ series remains single phase with α-$NaFeO_2$-type structure. Comparing the patterns, one can see that by increasing *y*, the characteristic intensity reflections shift slightly to lower 2 Theta values, indicating a change in the lattice parameters. An obvious peak splitting between the (006) and (102) as well as between the (108) and (110) pairs is the indication of the presence of the layered structure due to the distortion of the oxygen sub-lattice in the hexagonal *c* direction [335]. Based on the powder-XRD results, all synthesized $LiNi_{0.8-y}Mn_yCo_{0.2}O_2$ samples were considered as single phase with a well-developed layered structure.

Similar to Section 4.2.1.2, the value of the integrated intensity ratios of (003) peak to (104) peak is evaluated as an indication of the degree of cation mixing in the layered compounds [336]. A larger I(003) / I(104) ratio implies that the sample is more highly ordered [343]. Generally, the disorder of the layer occupancy takes place when the I(003) / I(104) ratio is below 1.2 [61]. As shown in Table 4.15, the intensity ratio of I(003) / I(104) is greater than 1.2 for all samples, meaning that no undesirable cation mixing has taken place. The NMC622 sample shows the lowest I(003) / I(104) value of 1.29. However, no clear correlation between the I(003) / I(104) value and *y* in $LiNi_{0.8-y}Mn_yCo_{0.2}O_2$ was found.

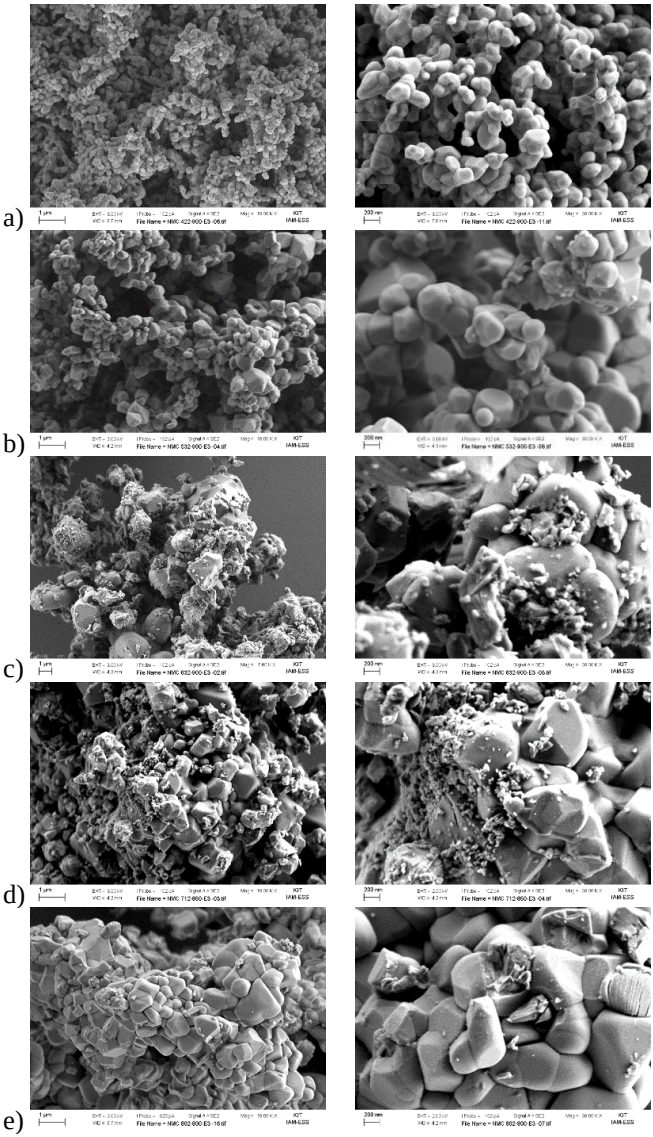

Figure 4.9: SEM micrographs of $LiNi_{0.8-y}Mn_yCo_{0.2}O_2$ as-calcinated powders; a) NMC442, b) NMC532, c) NMC622, d) NMC712 and e) NMC802 taken by secondary electron detector. Pictures on the right are at circa 5 times higher magnification.

In the previously reported works on NMC samples with constant Co contents, different trends were observed. Liao et al. [197] reported that the intensity ratio of I(003) / I(104) decreases in the $LiNi_{0.75-y}Mn_yCo_{0.25}O_2$ materials as *y* increases. Gu et al. [348] however found a non-linear behavior between the intensity ratios of I(003) / I(104) and *y* increases in the $LiNi_{0.85-y}Mn_yCo_{0.15}O_2$ sample which was different from the behavior observed in the present work. The discrepancy between different reports might be related to the difference in the investigated compositions. It may also be explained by the fact that in the present work different calcination temperatures are employed for different studied compositions while the above references [197, 348] calcinated all samples at 900 °C.

The measured diffractograms were analyzed by the Rietveld refinement method, considering a $LiMO_2$ structural model ($R\bar{3}m$), isotypic to $LiNiO_2$, where the Li ions occupy the 3*a* sites and M represents the transition metal cations including Mn, Co and Ni randomly occupying 3*b* sites. Oxygen anions reside on 6*c* (0, 0, *z*) sites. The occupancy of Li ions at 3*a* sites and Ni, Mn and Co at 3*b* sites were introduced from chemical formula based on ICP-OES data. The measured and calculated patterns are shown in Figure 4.10. The red circles are the collected experimental data and the solid black lines are the calculated pattern. The summary of Rietveld parameters are listed in Table 4.15.

The lattice constants *a* and *c*, the *c/a* ratio as well as the cell volume are depicted in Figure 4.11 as functions of *y* in $LiNi_{0.8-y}Mn_yCo_{0.2}O_2$. For all graphs in Figure 4.11 a-d, the same scale as in the Figure 4.3 are used to facilitate the comparison. By increasing *y*, *a* value does not change considerably while *c* value shows a steady increase. This suggests that when *y* increases, the lattice expands preferentially in the *c*-direction. The cell volume also increase gradually as *y* increases for the entire range of $0 \leq y \leq 0.4$. This indicates that by increasing *y*, the lattice expands with the substitution of Ni^{3+} with Mn^{4+} and Ni^{2+} cations in the transition metal layer. This is mainly attributed to the larger Ni^{2+} cations (ionic radius of 0.69 Å [93]) replacing Ni^{3+} cations (ionic radius of 0.56 Å [93]) with smaller cationic radii.

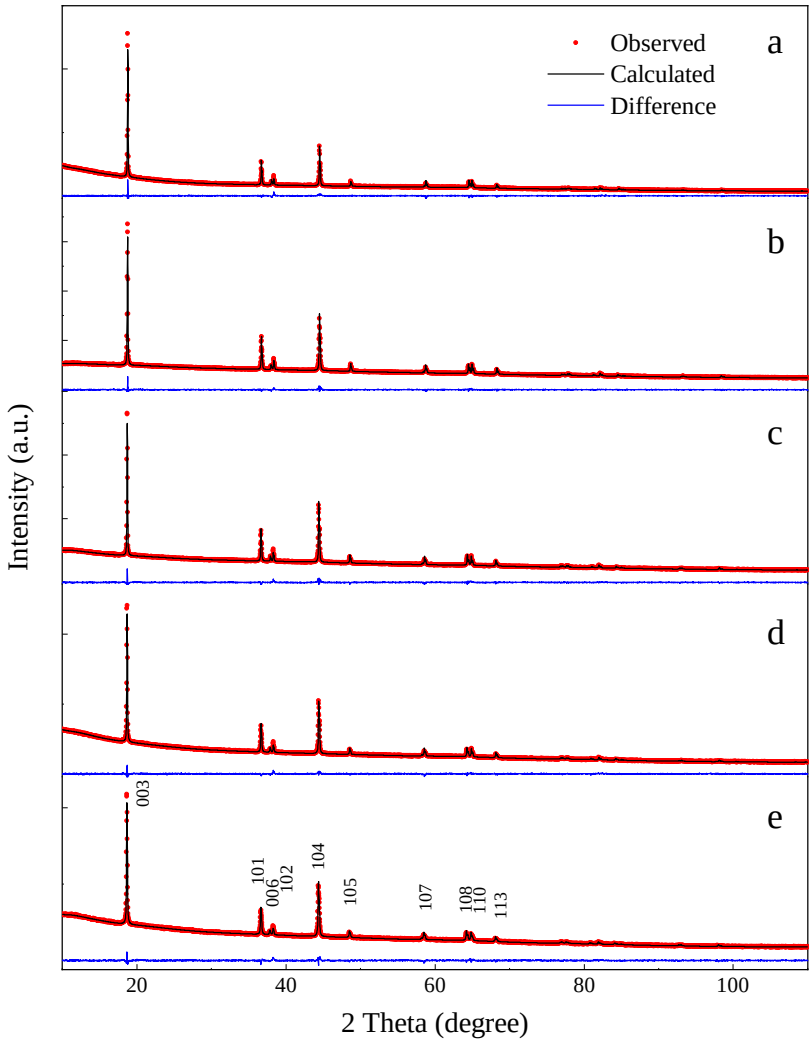

Figure 4.10: Powder XRD pattern for $LiNi_{0.8-y}Mn_yCo_{0.2}O_2$; y = (a) 0, (b) 0.1, (c) 0.2, (d) 0.3 and (e) 0.4.

Table 4.15: Summary of X-ray diffraction and Rietveld refinement of the layered $LiNi_{0.8-y}Mn_yCo_{0.2}O_2$ ($0 < y \leq 0.4$) samples. Phase fraction is 100 wt% $LiMO_2$ phase with $R\bar{3}m$ space group, for all samples.

Sample	NMC 802 [1]	NMC 712 [2]	NMC 622	NMC 532	NMC 442
y	0	0.1	0.2	0.3	0.4
I(003) / I(104)	1.87	1.37	1.29	1.42	1.35
a (Å)	2.86935(3)	2.86870(2)	2.87352(3)	2.87284(3)	2.87465(4)
c (Å)	14.1764(3)	14.1978(3)	14.2328(3)	14.2477(4)	14.2674(5)
c/a	4.9406(3)	4.9492(3)	4.9531(3)	4.9595(5)	4.9632(6)
Cell volume (Å^3)	101.080(3)	101.186(3)	101.777(3)	101.836(3)	102.105(5)
		(Structure Parameters)			
R_p	1.58	0.91	1.02	1.12	1.13
R_{wp}	2.39	1.41	1.62	1.55	1.59
Li_{3a}					
x	0	0	0	0	0
y	0	0	0	0	0
z	0	0	0	0	0
Occ.	0.92	0.97	0.94	0.99	1.01
M_{3b}					
x	0	0	0	0	0
y	0	0	0	0	0
z	0.5	0.5	0.5	0.5	0.5
$Occ._{Ni}$	0.8	0.7	0.6	0.5	0.4
$Occ._{Mn}$	0	0.1	0.2	0.3	0.4
$Occ._{Co}$	0.2	0.2	0.2	0.2	0.2
O_{6c}					
x	0	0	0	0	0
y	0	0	0	0	0
z	0.2430(4)	0.2436(3)	0.2429(4)	0.2425(4)	0.2439(4)
Occ.	0.892(9)	0.913(7)	0.910(9)	0.943(9)	0.941(10)

[1] Pre-calcinated powder is calcinated at 800 °C for 15 hours in air.

[2] Pre-calcinated powder is calcinated at 850 °C for 15 hours in air.

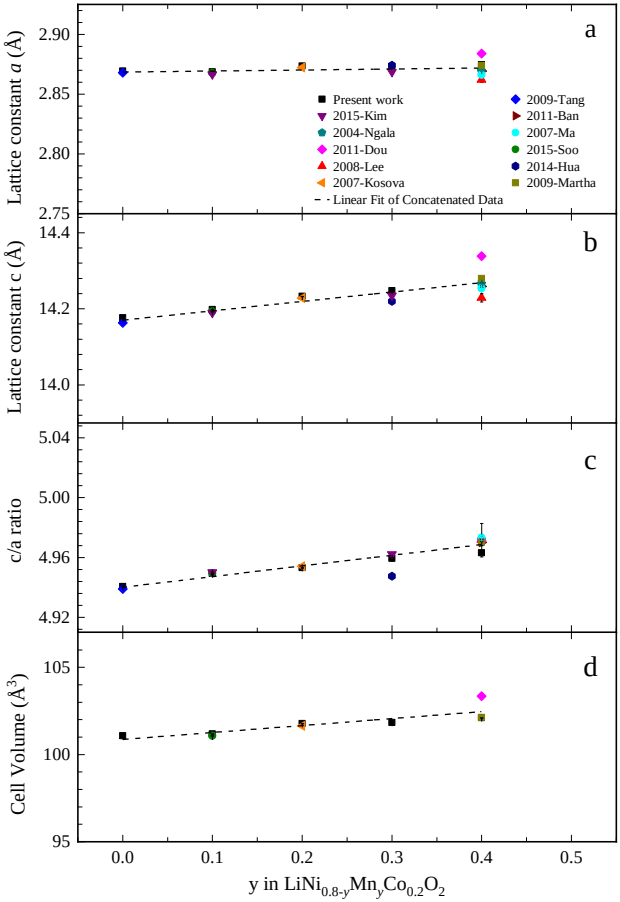

Figure 4.11: Chemical dependency of lattice constants a) *a*, b) *c*, c) *c/a* ratio and d) cell volume vs. *y* in $LiNi_{0.8-y}Mn_yCo_{0.2}O_2$ samples compared with the experimental data from Kim et al. [349], Ngala et al. [182] , Dou and Wang [350] , Lee et al. [351], Kosova et al. [352], Tang et al. [353], Ban et al. [354], Ma et al. [185], Soo et al. [355], Hua et al. [245], Martha et al. [275]. The linear fits of concatenated data are as Y = α + βX with the residual sum of squares (RSS) while the parameters are as follows a) α = 2.86844 ± 0.00238, β = 0.0085 ± 0.00801, and RSS = 0.0004, b) α = 14.17003 ± 0.01134, β = 0.24679 ± 0.03818 and RSS = 0.0079, c) α = 4.94011 ± 0.00221, β = 0.07127 ± 0.00745 and RSS = 0.0003, d) α = 100.86784 ± 0.26176, β = 3.98259 ± 0.95937 and RSS = 1.15968.

The *c*/*a* ratio also increases by increasing *y*. The *c*/*a* ratio was observed to be above 4.94 for all samples, suggesting good layered characteristics [338, 339]. Increasing *y*, the distortion of the O^{2-} octahedra is lowered, indicating an increase in the 2D character and an increased layered nature of the crystal structure. The trend of the changes in the lattice parameters with *y* is almost linear, which is common for a substitution mechanism that is not accompanied by significant attractive or repulsive electronic effects. As can be seen in Figure 4.11, the lattice parameters determined by Rietveld refinement are in a very good agreement with the literature data.

5 Thermal stabilities of $LiNi_{0.8-y}Mn_yCo_{0.2}O_2$

In this chapter, thermal stabilities of $LiNi_{0.8-y}Mn_yCo_{0.2}O_2$ compounds for y = 0, 0.1, 0.2, 0.3 and 0.4 are investigated using simultaneous differential thermal analysis - thermal gravimetry (DTA / TG). The amount of mass losses and the temperatures of decomposition are compared for different compositions. In addition, the phases which are formed after the decomposition reaction are determined by X-ray diffraction data.

5.1 Experimental

DTA / TG measurements are performed using a Setaram-SETSYS device which is introduced in Section 3.3.1. For the measurements, pellets of 3 mm diameter and an approximate mass of 15 mg from the calcinated powders were prepared. The powder was pressed using a hand press and an applied pressure of approximately 150 MPa. High purity argon gas (mass fraction purity of 99.9999 %) was used as the purge gas and the measurements were performed in alumina crucibles. In the measurement, the samples were heated and cooled according to the temperature program shown in Figure 5.1 with the heating rate of 10 $K \cdot min^{-1}$ and gas flow rate of 20 $mL \cdot min^{-1}$. The program includes two cycles of heating up to 720 °C to check the thermal stability of different compositions up to the temperature used for high temperature drop solution calorimetry experiments which is described in Chapter 3. The next two cycles, heated the sample up to a higher threshold, i.e., 1000 °C to examine the possibility of decomposition and the resulting mass loss.

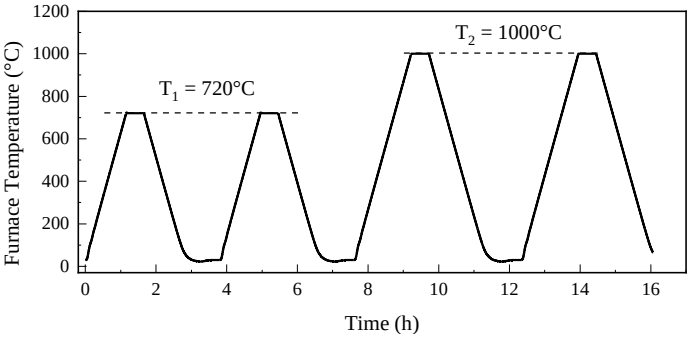

Figure 5.1: Furnace temperature recorded in DTA / TG experiments including two heating / cooling cycles up to 720 °C followed by two cycles up to 1000 °C.

5.2 Results and discussion

Figure 5.2 shows the results of simultaneous DTA / TG experiments on $LiNi_{0.8-y}Mn_yCo_{0.2}O_2$ compounds for y = 0.4 (NMC442), 0.3 (NMC532), 0.2 (NMC622), 0.1 (NMC712) and 0 (NMC802). Looking at the first two heating / cooling cycles which have a maximum temperature of 720 °C, there is no evidence of any peaks on the heat flow signal for none of the compositions. The mass losses at the end of the second cycles are below 1 % for NMC442, NMC532, NMC622 and NMC712. In the case of NMC802, the respective mass loss is about 1.15 wt%.

The mass loss during the first heating cycle starts at around 100 °C for all compositions and could be attributed to the removal of different water contents from the samples. At around 25 - 140 °C the mass loss might be due the lattice water and at about 140 - 240 °C, due to coordinated water [356]. Apart from this low temperature mass loss, no other considerable mass loss happened up to 720 °C for all samples. During the first cooling, and the second heating and cooling cycles there was no considerable mass changes. Therefore, it could be concluded that $LiNi_{0.8-y}Mn_yCo_{0.2}O_2$ samples do not decompose in argon atmosphere up to 720 °C and are stable samples for the high temperature drop solution calorimetry experiments.

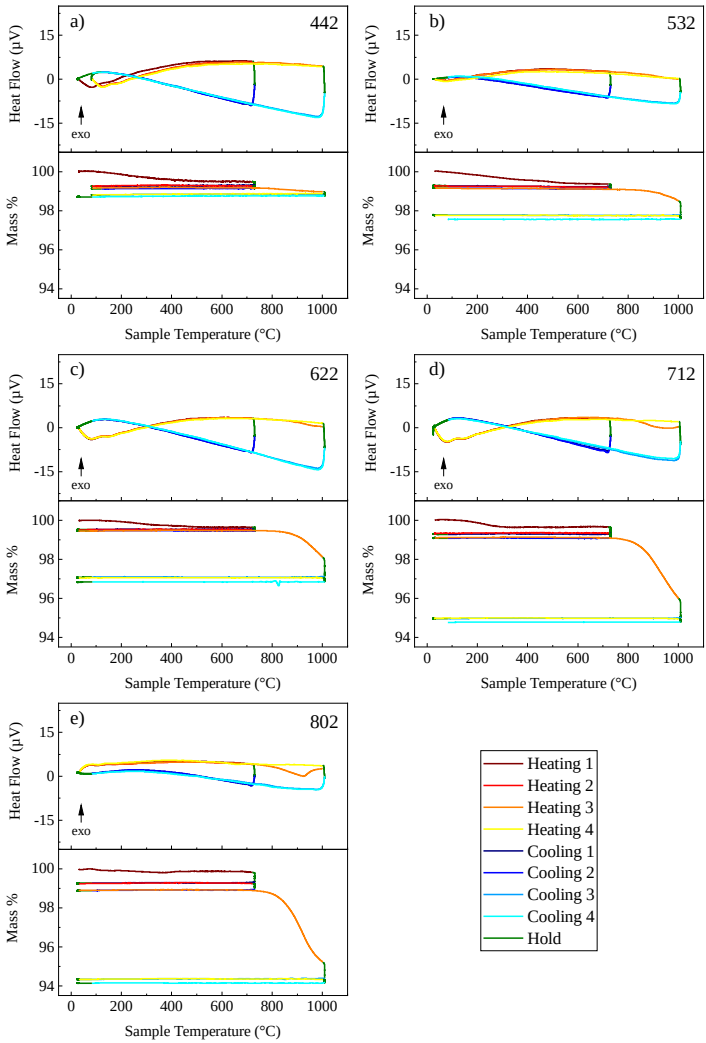

Figure 5.2: The results of simultaneous DTA / TG measurements including heat flow signal (upper graph) and mass changes (lower graph) for (a) NMC442, (b) NMC532, (c) NMC622, (d) NMC712, (e) NMC802 samples. All signals are corrected by subtracting the respective zero measurement from the sample measurements, except the heat flow signal of NMC802, due to unsatisfactory baseline quality. The measurements are performed under flowing argon.

By increasing the temperature, the behavior of the samples with different compositions differ from each other. In the case of NMC442 and NMC532, the heat flow signals of third heating cycles, which heat up the sample up to 1000 °C, show no obvious peak. The mass loss during third heating cycle is about 0.2 % and 0.7 % for NMC442 and NMC532, respectively. The results may indicate that the initial O3 phase in NMC442 and NMC532 is stable up to 1000 °C under flowing argon.

However, in the case of NMC622 sample, the heat flow signal of the third heating cycle shows a wide endothermic peak initiating at around 823 °C and the signal does not return to its baseline level even until 1000 °C. During the third heating cycle of NMC622, an accompanying mass loss of approximately 1.4 % takes place. This mass loss may be attributed to the mass of released oxygen during decomposition of the initial layered structure. Over holding time at 1000 °C, the mass loss continues for about 1 % which shows that the decomposition reaction is not complete during dynamic heating to 1000 °C using the applied heating rate. During subsequent cooling and heating cycles, no considerable mass change and no evident reaction takes place. The absence of reverse reaction is due to the fact that the experiments are performed in flowing argon where the reaction products are purged and no oxygen is available for the reaction to occur in the reverse direction.

A similar peak is observed on the heat flow signal of the third heating cycle for NMC712 and NMC802, starting at approximately 748 °C and 720 °C, respectively. The corresponding mass losses during the third heating courses are 3.2 % and 3.7 % for NMC712 and NMC802, respectively. During holding at 1000 °C, NMC 712 loses 1 % of its weight while this value is 0.8 % for NMC 802. This indicates a more complete decomposition reaction until 1000 °C for NMC 802, as confirmed by a complete peak on the heat flow signal of the third heating cycle for this sample.

As mentioned in Section 3.3.1, the reactions related to mass changes are reflected as peaks in the DTA curve as well as in both the direct and first derivative of TG curves with respect to time (or temperature, if the heating rate is constant). The heat flow signal and the first derivative of the mass loss with

respect to sample temperature for the third heating cycle of all samples are depicted against sample temperature in Figure 5.3.

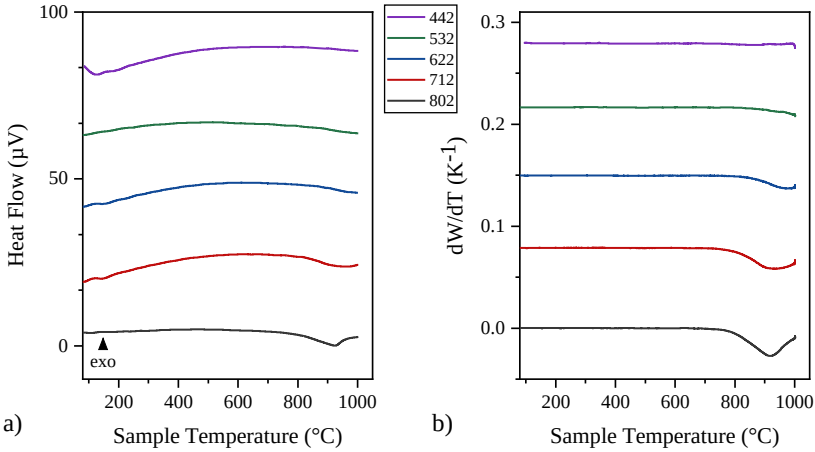

Figure 5.3: Results of simultaneous DTA / TG measurements: a) Heat flow signal of third heating cycle, as in Figure 5.2 and b) the first derivative of mass loss signal W (see Figure 5.2) with respect to sample temperature, depicted versus sample temperature for respective NMC samples. In b) the dW/dT signal is smoothed using adjacent averaging method (500 points).

The peaks discussed above are visible in both curves, and are even more obvious in the dW/dT curves. Therefore, for the more accurate determination of the onset temperature of the decomposition reaction the dW/dT curves are used. The values of mass losses during different cycles as well as the corresponding onset temperatures of the decomposition reaction are listed in Table 5.1. The uncertainties of the onset temperatures are calculated as combined Type B uncertainty based on the uncertainty of the calibration equation of the device (Equation (3.8)) and the uncertainty of the resolution of the signal.

Table 5.1: The values of the mass losses during different cycles of DTA / TG experiments and the corresponding decomposition temperatures extracted from Figure 5.2.

Sample	Mass loss of 1st heating (%)	Mass loss of 3rd heating (%) [1]	Mass loss at 1000 °C (%) [2]	Onset temperature (TG) [3] (°C)
NMC442	0.50	0.18	0.11	---
NMC532	0.64	0.69	0.69	865.8 ± 3.0
NMC622	0.36	1.37	0.98	823.0 ± 2.7
NMC712	0.35	3.14	0.98	748.3 ± 2.4
NMC802	0.18	3.71	0.82	719.4 ± 2.5

[1] Normalized with respect to sample's mass at the beginning of third heating cycle.

[2] The mass loss during holding time at 1000 °C after third dynamic heating.

[3] Determined as the temperature at which the first derivation of mass loss against temperature (third heating cycle) starts deviating from zero.

In order to investigate the decomposition reaction and explore the products of the decomposition, the samples were studied after DTA / TG measurements by powder-XRD and Rietveld refinement. The measured XRD patterns and the calculated patterns are shown in Figure 5.4. In the case of NMC442, NMC532 and NMC622 the samples are found to be single phase structures with $R\bar{3}m$ space group. However, the intensity ratio of (003) to (104) Bragg peaks has a descending trend from NMC442 sample to NMC532 and then to NMC622 sample. In NMC712 and NMC802 samples, a phase with $Fm\bar{3}m$ space group is found to be present as the main phase while the $R\bar{3}m$ phase comprises the second phase. The weak diffraction lines marked by asterisks in Figure 5.4 (d) and (e) could stem from the traces of Li_2O. The origin of the peak marked by inverse triangle (at $2\theta \approx 23.5°$) in Figure 5.4 (e) is not clear and it could not be attributed to cubic spinel structure ($Fd\bar{3}m$). The details of Rietveld refinement of all samples are presented in Table 5.2. In the case of NMC442, NMC532 and NMC622, which are single phase samples, the occupancy of oxygen in 6*c* site as well as oxygen positional parameter (*z*) are refined, similar to the refinement process for the pristine samples (see Chapter 4).

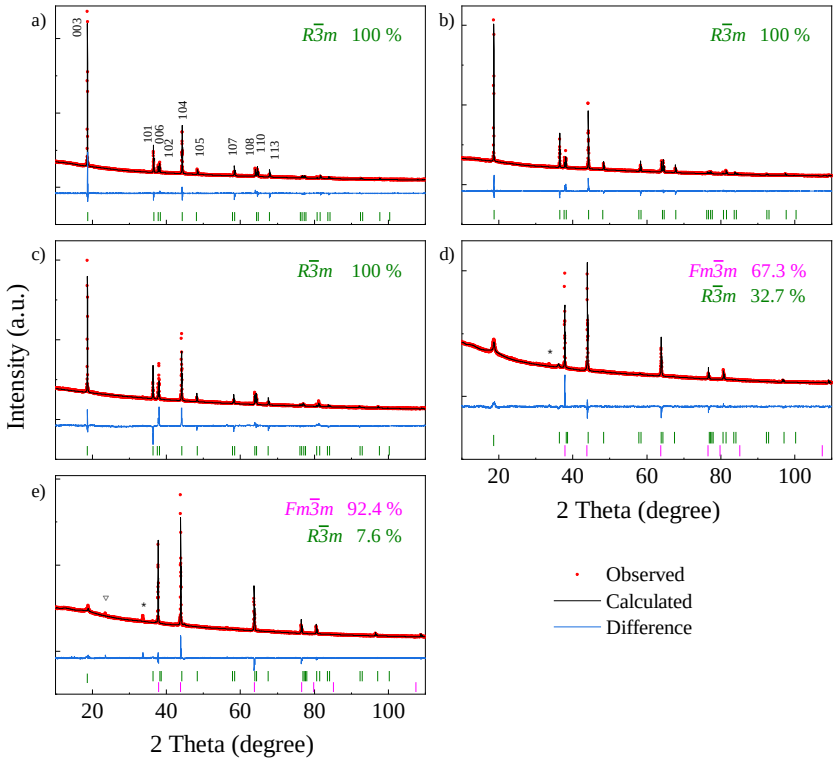

Figure 5.4: The measured XRD patterns, the calculated patterns and the detected phases of the $LiNi_{0.8-y}Mn_yCo_{0.2}O_2$ samples after DTA / TG measurements. a) NMC442, b) NMC532, c) NMC622, d) NMC712, e) NMC802.

Table 5.2: Structural parameters from of Rietveld refinement of PXRD from the $LiNi_{0.8-y}Mn_yCo_{0.2}O_2$ samples after DTA / TG measurements.

Sample	NMC442	NMC532	NMC622	NMC712		NMC802	
Phases	$LiMO_2$	$LiMO_2$	$LiMO_2$	$LiMO_2$	NiO	$LiMO_2$	NiO
Phase fraction (wt%)	100	100	100	32.7(9)	67.3(9)	7.6(7)	92.4(7)
Space group	$R\bar{3}m$	$R\bar{3}m$	$R\bar{3}m$	$R\bar{3}m$	$Fm\bar{3}m$	$R\bar{3}m$	$Fm\bar{3}m$
I(003) / I(104)	1.73	1.08	1.00	---	---	---	---
a (Å)	2.88358(2)	2.88914(2)	2.89718(5)	2.916(9)	4.120(1)	2.844(2)	4.130(1)
c (Å)	14.2869(3)	14.2925(3)	14.2955(5)	14.265(9)	---	14.158(9)	---
Cell volume ($Å^3$)	102.880(3)	103.318(3)	103.915(5)	105.04(9)	69.917(9)	99.2(2)	70.44(1)
			(Structure parameters)				
R_p	1.46	1.30	2.21	1.38		1.10	
R_{wp}	3.06	2.41	4.29	2.47		2.07	
Li_{3a}							
x	0	0	0	0	---	0	
y	0	0	0	0	---	0	
z	0	0	0	0	---	0	
Occ.	1	1	1	1	---	1	
M_{3b}							
x	0	0	0	0	0	0	0
y	0	0	0	0	0	0	0
z	0.5	0.5	0.5	0.5	0	0.5	0
$Occ._{Ni}$	0.4	0.5	0.6	0.7	1	0.8	1
$Occ._{Mn}$	0.4	0.3	0.2	0.1	---	0	---
$Occ._{Co}$	0.2	0.2	0.2	0.2	---	0.2	---
O_{6c}							
x	0	0	0	0	0.5	0	0.5
y	0	0	0	0	0.5	0	0.5
z	0.2286(3)	0.2371(3)	0.2365(6)	0.24	0.5	0.24203	0.5
Occ.	0.967(9)	0.951(8)	0.74(2)	1	1	1	1

The integrated intensity ratio of (003) to (104) Bragg peaks for NMC442, NMC532 and NMC622 is reported in Table 5.2. The intensity ratio is calculated based on the product of FWHM (full width at half maximum) and maximum height of the peak. For NMC442 sample, I(003) / I(104) is 1.73 which is greater than 1.2 (see Section 4.2.1.2) and suggests that the well-ordered layered structure is preserved after the DTA / TG experiments. The intensity ratios have lower values of 1.08 and 1.00 for NMC532 and NMC622 samples, respectively. It is known that in $LiNiO_2$, the displacement between Li^+ ions at 3*a* and Ni^{3+} ions at 3*b* sites weakens the intensity of (003) reflection while it does not affect the intensity of (104) line. Therefore, the observed drift in I(003)/ I(104) from NMC442 to NMC 622 shows the increased Li and Ni site mixing and the decreased layered characteristics of the initial O3 phase. Thus, it seems that by increasing Ni content from NMC442 to NMC 622, the layered O3 phase becomes less stable against heating and loses its ordering and structural stability more severely. In addition, the refined oxygen occupancy decreases from NMC442 (0.97) to NMC622 (0.74). This result combined with the observed mass losses suggests that the sample with higher nickel content is chemically less stable and starts partially reducing Ni^{3+} to Ni^{2+} and releasing lattice oxygen at a lower temperature.

If the Li and Ni ions are mixed completely, then the intensity of (003) Bragg peak should be zero. In the case of NMC712 and NMC802, it can be seen that the (003) reflection is almost faded out. In these samples, the structural and chemical instability of O3 phase has proceeded to the decomposition of initial rhombohedral phase (O3) and the formation of a new rock-salt cubic phase.

Based on the detected phases, the decomposition reaction could be speculated as follows:

$$\mathrm{LiMO}_{2-\delta} \rightarrow \mathrm{LiM'O}_{2-\delta'} + \mathrm{NiO} + \mathrm{O}_2 \tag{5.1}$$

Where $\mathrm{LiMO}_{2-\delta}$ is the initial O3 phase, which is characterized for all NMC samples in Chapter 4. $\mathrm{LiM'O}_{2-\delta'}$ and NiO are the altered $R\bar{3}m$ and the new $Fm\bar{3}m$ phases found in the XRD characterization of the sample after DTA / TG measurements. The new rock-salt cubic structure might be lithiated NiO as its lattice constant is smaller than NiO (*a* = 4.185 Å) [357]. This difference is

due to the presence of Ni^{3+} in lithiated NiO ($Li_xNi_{2-x}O_2$) with smaller ionic radius than Ni^{2+} (r_{Ni3+} = 0.56 Å vs. r_{Ni2+} = 0.68 Å). However, considering Li in Ni site in our refinement did not improve the refinement considerably and hence is not applied. Additionally, X-ray diffraction is not accurate enough for such a refinement and one needs neutron diffraction, for example, to be able to accurately refine Li sites and occupancies in this phase. Oxygen as the reaction product is the released gas which causes the observed mass losses. M describes the initial ratio of transition metals in 3*b* sites, while M' denotes the new and possibly different arrangement, as a part of the Ni ions might locate at the other phase. It is worth mentioning that for convenience, for the NMC712 and NMC802 samples that consist of two phases, occupancy of oxygen in *6c* site and the position of "O" atoms are kept fixed and M' is supposed to be equal to M. It should be mentioned that the equation is not balanced due to many unknown parameters.

This decomposition reaction is similar to the decomposition mechanism of $LiNiO_2$ in the absence of oxygen studied by Kanno et al. [92], Tao et al. [358] and Li et al. [359]. The decomposition temperature of $LiNiO_2$ in argon atmosphere is found to be 750 °C [92] and 619.5 °C (real stoichiometry: $Li_{0.86}NiO_2$) [358] and between 725 °C to 818 °C depending on the heating rate and the particle size [359]. The decomposition reaction of layered $LiNiO_2$ is considered to be the reduction of Ni^{3+} to Ni^{2+} state, formation of rock salt structure and release of oxygen gas.

6 Determination of the enthalpies of formation

This chapter aims at finding the relationship between the composition of the NMC compounds and their relative thermodynamic stabilities. For this purpose, the enthalpies of formation of two series of the NMC samples with selected stoichiometries, which were characterized in Chapter 14, are determined by high temperature oxide melt drop solution calorimetry in $3Na_2O{\cdot}4MoO_3$ solvent at 701 °C under argon atmosphere. The enthalpies of formation of two experimented series of compounds are then extrapolated to a larger composition range of NMC as an attempt to generalize the results to a wider range of parameters. Part of the results presented in this chapter, which are associated with the $LiNi_xMn_xCo_{1-2x}O_2$ ($0 \leq x \leq 0.5$) compounds are published by Masoumi et al. in a peer-reviewed journal paper [360].

6.1 Calibration with sapphire

As described in Section 3.4.1, both chambers of the Alexys calorimeter are calibrated independently using 7 mg sapphire spheres. The enthalpy changes of sapphire spheres from room temperature to the temperature of calorimeter is calculated using the heat capacity of sapphire, taken from Ref. [311]. The calibration factors for the right and left side of the calorimeter are determined as 0.00467593 and 0.00464650, respectively. The corresponding calibration factors are multiplied to the area under each peak, resulted from drop solution experiment of the NMC sample, to obtain the enthalpy of drop solution of the respective dropped sample. The calculation process for the determination of the enthalpy of drop solution based on the results of high temperature oxide solution calorimetry are extensively described for NMC622 sample as an example in the Appendix.

6.2 $LiNi_xMn_xCo_{1-2x}O_2$ series

The standard enthalpies of formation of various $LiNi_xMn_xCo_{1-2x}O_2$ ($0 \leq x \leq 0.5$) compositions from their constituent binary oxides are calculated with respect to binary oxides i.e. Li_2O, MnO_2, NiO and CoO and oxygen. A thermodynamic cycle as shown in Table 6.1 is used which shows the reactions involved in the calculation of the enthalpies of formation. Reactions (1) to (4) represent drop solution calorimetry of the binary oxides in $3Na_2O{\cdot}4MoO_3$ solvent at 701 °C (974 K) under argon atmosphere while reaction (6) shows the drop solution calorimetry of the $LiNi_xMn_xCo_{1-2x}O_2$ compound at the same solvent and temperature. Reaction (5) corresponds to heating up the gaseous oxygen from room temperature to the temperature of calorimetry. Then reaction (7) shows the formation reaction of $LiNi_xMn_xCo_{1-2x}O_2$ compound from its constituent binary oxides and oxygen. It should be noted that for the formation reaction those binary oxides are chosen that are stable at room temperature and pressure with available data of their enthalpies of drop solution. It is also worth mentioning that heat of dissolution of heated gaseous oxygen (701 °C) in the solvent is neglected in the current thermodynamic cycles due to unfeasibility of such a measurement; since the set-up of the calorimeter is an open system for gaseous components.

Concerning the reactants and the products of the reactions in Table 6.1, the oxidation states are outlined for the transition metal cations. In Section 2.2.3, the main oxidation state of transition metals in NMC compound are already discussed. Specifically for $LiNi_xMn_xCo_{1-2x}O_2$ series, Lu et al. [157] and Ammundsen and Paulsen [148] proposed that Ni^{2+} and Mn^{4+} substitute for Co^{3+} in the $LiNi_xMn_xCo_{1-2x}O_2$ ($0 \leq x \leq 0.5$) series. Later, differential capacity measurements [337], X-ray absorption near-edge spectroscopy (XANES) [146] and magnetic measurements [185] verified that indeed, the oxidation states of Ni, Co, and Mn are mainly +2, +3, and +4, respectively. Therefore, here also these oxidation states are considered to exist in the studied $LiNi_xMn_xCo_{1-2x}O_2$ samples.

Table 6.1: Thermodynamic cycle showing the reactions used for the determination of the enthalpy of formation of $LiNi_xMn_xCo_{1-2x}O_2$ compounds from binary oxides and oxygen using drop solution calorimetry in $3Na_2O{\cdot}4MoO_3$ solvent at 701 °C (974 K) under argon atmosphere.

Reaction	ΔH
1) $Li_2O_{(s,25°C)} \rightarrow [2Li^+ + O^{2-}]_{(sol,701°C)}$	$\Delta_{ds}H_{(Li_2O)}$
2) $Ni^{2+}O_{(s,25°C)} \rightarrow [Ni^{2+} + O^{2-}]_{(sol,701°C)}$	$\Delta_{ds}H_{(NiO)}$
3) $Mn^{4+}O_{2(s,25°C)} \rightarrow [Mn^{2+} + O^{2-}]_{(sol,701°C)}$	$\Delta_{ds}H_{(MnO_2)}$
4) $Co^{2+}O_{(s,25°C)} \rightarrow [Co^{2+} + O^{2-}]_{(sol,701°C)}$	$\Delta_{ds}H_{(CoO)}$
5) $O_{2(g,25°C)} \rightarrow O_{2(g,701°C)}$	$\Delta H_{(O_2)}$
6)$LiNi^{2+}{}_xMn^{4+}{}_xCo^{3+}{}_{1-2x}O_{2(s,25°C)} \rightarrow {}^1/_2\,[2Li^+ + O^{2-}]_{(sol,701°C)} + x[Ni^{2+} + O^{2-}]_{(sol,701°C)} + x[Mn^{2+} + O^{2-}]_{(sol,701°C)} + {}^x/_2\,O_{2(g,701°C)}$	$\Delta_{ds}H_{(LiNi_xMn_xCo_{1-2x}O_2)}$
7) ${}^1/_2\,Li_2O_{(s,25°C)} + xNi^{2+}O_{(s,25°C)} + xMn^{4+}O_{2(s,25°C)} + (1-2x)Co^{2+}O_{(s,25°C)} + {}^{(1-2x)}/_4\,O_{2(g,25°C)} \rightarrow LiNi^{2+}{}_xMn^{4+}{}_xCo^{3+}{}_{1-2x}O_{2(s,25°C)}$	$\Delta_f H^{\theta,oxides}{}_{(LiNi_xMn_xCo_{1-2x}O_2)}$

The products of the reactions 1– 4 and 6 in Table 6.1, show the species (cations and anions) formed from the dissolution of oxide samples in the solvent. Navrotsky and Kleppa [361] fully described the chemistry of dissolution in sodium molybdate ($3Na_2O{\cdot}4MoO_3$) solution which consists of sodium and molybdenum oxides. Accordingly, through decomposition of Na_2O at the temperature of calorimetry, the following reaction takes place:

$$3Na_2O \rightarrow 6Na^+ + 3O^{2-} \tag{6.1}$$

MoO_3 reacts with the produced O^{2-} ions and form two species of Mo oxides:

$$3O^{2-} + 4MoO_3 \rightarrow 2MoO_4{}^{2-} + Mo_2O_7{}^{2-} \tag{6.2}$$

Two charged Mo oxides, i.e. ${MoO_4}^{2-}$ and ${Mo_2O_7}^{2-}$ are in equilibrium with each other inside the solution and create a buffer system for oxygen anions according to reaction (6.3):

$$O^{2-} + {Mo_2O_7}^{2-} \rightleftharpoons 2{MoO_4}^{2-} \tag{6.3}$$

When oxide samples are dropped into molten $3Na_2O{\cdot}4MoO_3$, depending on whether they are basic, acidic or transition metal oxides, they may dissolve, react with oxygen anions to form complex anions or undergo a redox reaction, respectively. In the case of simple acidic and basic oxides dissolution, the introduction of oxide sample changes the amount of oxygen anions inside the solution. This may shift the direction in buffer equilibrium reaction (6.3) so that the reaction constant remains unchanged. Therefore, in these cases, the drop solution experiments can be performed under argon atmosphere.

However, when transition metal oxides are introduced into the molten solvent, their oxidation state may change. Navrotsky's group has shown that, for instance the oxidation state of Co, Mn, Ni and Cu oxides in sodium molybdate at 700 °C change to Co^{+2} [362], Mn^{+2} [276], Ni^{+2} [270] and Cu^{2+} [363]. As an example, we consider M as a trivalent transition metal that reduces to divalent M through dissolving in molten sodium molybdate. By dissolving M_2O_3 in the solvent, first the oxide decomposes according to reaction (6.4), similar to other oxides

$$M_2O_3 \rightarrow 2M^{3+} + 3O^{2-} \tag{6.4}$$

The produced oxygen anions shift the position of the buffer reaction to the right to consume the additional oxygen anions. Then, the redox reaction takes place; the transition metal cations M^{3+} reduce to M^{2+} through dissolving in the solvent (reduction reaction):

$$2M^{3+} + 2e^- \rightarrow 2M^{2+} \tag{6.5}$$

The electrons required for the reduction are provided through oxidation of oxygen anions present in the buffer solution according to the following reaction (oxidation reaction):

$$O^{2-} \rightarrow 2e^{-} + \frac{1}{2}O_2 \tag{6.6}$$

The complete reaction would be:

$$2M^{3+} + O^{2-} \rightarrow 2M^{2+} + \frac{1}{2}O_2 \tag{6.7}$$

This reaction is accompanied by releasing oxygen gas. Therefore, in order to shift the position of the reaction to the right, i.e. complete dissolution, the partial pressure of oxygen should be reduced. As a conclusion, if the transition metal is reduced by dissolution in the solvent, the drop solution experiments should be performed under argon gas. Obviously, the consumed oxygen anions in reaction (6.6) are adjusted by the buffer reaction (6.3).

In the case of NMC compounds, the main oxidation state of constituting transition metals, Ni, Mn and Co in the sodium molybdate solvent under argon atmosphere at 701 °C has been determined by Navrotsky's group using thermal analysis experiments and are found to be mainly in the forms of Co^{+2} [362], Mn^{+2} [276] and Ni^{+2} [270]. Therefore, the dissolution of $LiNi_xMn_xCo_{1-2x}O_2$ with Ni^{2+}, Mn^{4+} and Co^{3+} valence states involves the reduction of Co and Mn cation and should be performed using argon bubbling and protecting gas.

As described in Section 3.4.1, a number of pellets from each compound are dropped into the sodium molybdate solvent at 701 °C and the average value of enthalpy of drop solution of respective compound is calculated. The values of the enthalpy of drop solution for the $LiNi_xMn_xCo_{1-2x}O_2$ ($0 \leq x \leq 0.5$) compounds from the presents work along with the values for binary oxides from the literature are listed in Table 6.2. The numbers of individual drops of each compound as well as the uncertainty of the repeated measurements are also listed. Among the cited references in Table 6.2, those marked by asterisk (*) are employed in the calculations of the present work. These values are those that were used by Wang and Navrotsky [270] for determination of the enthalpies of formation of $LiNi_xCo_{1-x}O_2$ series. In the case of MnO_2, the enthalpy of drop solution value of Ref. [276] is chosen which is cited in the latest review paper of Navrotsky [316].

Table 6.2: Values of enthalpy of drop solution of binary (upper rows, from literature) and ternary oxides (lower rows, from present work) in $3Na_2O{\cdot}4MoO_3$ solvent at 701 °C (974 K) under argon atmosphere. Those of binary oxides marked by asterisk are used in the calculation of enthalpies of formation from oxides based on the thermodynamic cycle in Table 6.1.

	sample	$\Delta_{ds}H^{974}$/ kJ·mol^{-1} (drops)	source
binary oxides	Li_2O	-93.02 ± 2.24 [1, *]	Wang & Navrotsky [270]
		-90.3 ± 2.5 [2]	McHale & Navrotsky [364]
	MnO_2	128.92 ± 0.91 (11) [*]	Wang & Navrotsky [276]
		124.80 ± 1.03 (8)	Birkner & Navrotsky [316, 365]
	NiO	35.73 ± 0.95 (8) [*]	Wang & Navrotsky [270]
	CoO	15.35 ± 0.46 (7) [*]	Wang & Navrotsky [270]
		16.45 ± 0.69 (14)	Mayer et al. [366]
		16.50 ± 0.70	Ma & Navrotsky [367]
		15.66 ± 0.59 (8)	Wang et al. [362]
ternary oxides	$LiCoO_2$	118.90 ± 0.84 (12)	This work
		116.82 ± 1.18 (10)	Wang & Navrotsky [270]
		118.27 ± 0.66 (10)	Wang et al. [269]
		118.26 ± 0.89 (10)	Gotcu-Freis et al. [258]
	$LiNi_{0.167}Mn_{0.167}Co_{0.666}O_2$	112.10 ± 1.53 (12)	This work
	$LiNi_{0.333}Mn_{0.333}Co_{0.333}O_2$	100.70 ± 1.08 (13)	This work
	$LiNi_{0.4}Mn_{0.4}Co_{0.2}O_2$	98.86 ± 1.09 (18)	This work
	$LiNi_{0.5}Mn_{0.5}O_2$	95.89 ± 0.62 (21)	This work

[1] Calculated by drop solution calorimetry on Li_2CO_3 and other related thermodynamic data[270].

[2] Calculated by drop solution calorimetry on the carbonate [364].

[*] Reference values used for the purpose of calculations of the present work.

The enthalpy changes of reaction (5) at Table 6.1 equals the heat content of gaseous oxygen from room temperature to the temperature of calorimetry taken from the SGTE Gibbs energy descriptions of the pure elements [368]. Adding oxygen in reaction (7) is necessary, because binary oxide of Co with +3 oxidation state cannot be prepared as a stable phase that can be used for the

drop solution calorimetry experiments and Co^{2+} as the reactant (CoO) needs to be oxidized to +3 state in the product (NMC).

The thermodynamic cycle shown in Table 6.3 is used by Wang and Navrotsky [270] to determine the enthalpy of drop solution of Li_2O through drop solution experiments of Li_2CO_3 ($\Delta_{ds}H^{974}$ = 162.76 ± 0.77 kJ·mol^{-1} from 8 drops) and thermodynamic data of CO_2 from Ref. [369]. The reason is that Li_2O is a reactive sample and difficult to be prepared and handled.

Table 6.3: Thermodynamic cycle used by Wang and Navrotsky [270] for the calculation of enthalpy of drop solution of Li_2O based on drop solution calorimetry of Li_2CO_3 and heat capacity of CO_2. In the original cycle of Ref. [270], $Li_2O_{(sol,701°C)}$ is used instead of $[2Li^+ + O^{2-}]_{(sol,701°C)}$.

Reaction	ΔH
$Li_2CO_{3(s,25°C)} \rightarrow [2Li^+ + O^{2-}]_{(sol,701°C)} + CO_{2(g,701°C)}$	$\Delta_{ds}H_{(Li_2CO_3)}$
$CO_{2(g,25°C)} \rightarrow CO_{2(g,701°C)}$	$\Delta H_{(CO_2)}$
$Li_2O_{(s,25°C)} + CO_{2(g,25°C)} \rightarrow Li_2CO_{3(s,25°C)}$	$\Delta_f H^{\theta,oxides}{}_{(Li_2CO_3)}$

The standard enthalpy of formation from oxides is equal to the enthalpy changes of the reaction (7) in Table 6.1 and is calculated according to Equation (6.8). The obtained values are listed in Table 6.4.

$$\Delta_f H^{\theta,oxides}{}_{(LiNi_xMn_xCo_{1-2x}O_2)} = \frac{1}{2}\,\Delta_{ds}H_{(Li_2O)} + x\,\Delta_{ds}H_{(NiO)} + x\,\Delta_{ds}H_{(MnO_2)} + (1-2x)\Delta_{ds}H_{(CoO)} + \frac{0.5-x}{2}\int_{298}^{974} c_{p(O_2)} - \Delta_{ds}H_{(LiNi_xMn_xCo_{1-2x}O_2)} \quad (6.8)$$

The standard enthalpy of formation of the $LiNi_xMn_xCo_{1-2x}O_2$ ($0 \leq x \leq 0.5$) composition from their elements is then calculated using quation (6.9). The results are summarized in Table 6.4.

$$\Delta_f H^{\theta,elements}{}_{(LiNi_xMn_xCo_{1-2x}O_2)} = \Delta_f H^{\theta,oxides}{}_{(LiNi_xMn_xCo_{1-2x}O_2)} + \frac{1}{2}\,\Delta_f H_{(Li_2O)} + x\,\Delta_f H_{(NiO)} + x\,\Delta_f H_{(MnO_2)} + (1-2x)\Delta_f H_{(CoO)} \quad (6.9)$$

The standard enthalpies of formation of the constituent binary oxides from the elements ($\Delta_f H$) are taken from Glushko et al. [370] as shown in Table 6.4. The standard enthalpies of formation of the binary oxides from the NIST-JANAF compilations [371] could not be used for the calculations because this reference has no data available for NiO and MnO_2, although there are data for CoO and Li_2O.

Table 6.4: Enthalpy of formation from binary oxides (MnO_2, NiO and CoO) and oxygen for ternary oxides and enthalpy of formation from elements at 298 K for binary oxides from the literature and for ternary oxides ($LiNi_xMn_xCo_{1-2x}O_2$ compounds) determined experimentally and compared with literature data.

sample (nominal composition)	$\Delta_f H^{0,oxides}$ (298K)/ kJ·mol^{-1}	$\Delta_f H^{0,elements}$ (298K)/ kJ·mol^{-1}	source
Li_2O		-597.935 ± 0.334	[370]
MnO_2		-521.493 ± 0.836	[370]
NiO		-239.743 ± 0.543	[370]
CoO		-238.906 ± 1.255	[370]
$LiCoO_2$	-144.61 ± 1.47	-682.49 ± 1.94	This work
	-142.54 ± 1.69	-679.4 ± 2.4	[270] / [105]
	-143.99 ± 1.38	-681.84 ± 1.96	[269] / [258]
	-142.79 ± 1.52	-673.06 ± 2.68	[258]
$LiNi_{0.167}Mn_{0.167}Co_{0.666}O_2$	-117.30 ± 1.93	-702.41 ± 2.12	This work
$LiNi_{0.333}Mn_{0.333}Co_{0.333}O_2$	-85.39 ± 1.62	-717.74 ± 1.72	This work
	---	-649.74 ± 2.05 [1]	[274]
	---	-652.49 ± 0.45 [2]	[274]
$LiNi_{0.4}Mn_{0.4}Co_{0.2}O_2$	-75.35 ± 1.65	-726.59 ± 1.72	This work
$LiNi_{0.5}Mn_{0.5}O_2$	-60.07 ± 1.44	-739.66 ± 1.53	This work

[1] Solid-state synthesized sample.

[2] Solution method-synthesized sample.

Although lithium losses were observed during synthesis of $LiNi_xMn_xCo_{1-2x}O_2$ sample as shown in Section 4.2.1.1, the nominal stoichiometric formula are used for the calculations of enthalpies, because the effect of this assumption on the derived enthalpies is negligible. For examples in a similar experimental work of Wang and Navrotsky [270], in spite of observed lithium loss, the

nominal compositions of $Li(Ni,Co)O_2$ samples are used for the calculation of enthalpies. Lithium deficiency is neglected in another work from the same group [269] investigating $LiCoO_2$ sample with slightly different synthesis conditions. In the latter work [269], 2 atom% excess lithium in the starting material and higher calcination temperature of 900 °C are used in the synthesis process, comparing no excess lithium in starting material and 800 °C calcination for the sample in the prior work [270]. Nevertheless, in both investigations the samples were treated as stoichiometric $LiCoO_2$ samples, i.e. Li / Co = 1. The enthalpies of drop solution for the two $LiCoO_2$ samples are reported as 116.82 ± 1.17 and 118.27 ± 0.66 in Ref. [270] and Ref. [269], respectively. In another similar experiment by Gotcu-Freis et al. [258] which used Alexys device at KIT, the same device as in the present work, commercial $LiCoO_2$ sample with unknown synthesis route is investigated. In Ref. [258], the measured composition of $LiCoO_2$ sample which is Li / Co = 0.977 ± 0.006 is used for the calculations of enthalpies. The enthalpy of drop solution by Gotcu-Freis et al. [258] is determined to be 118.26 ± 0.89 which is very close to the data of Wang et al. [269], indicating the two samples are very similar to each other. Even though in Ref. [258] the nonstoichiometric composition is used for further calculations of enthalpies of formation from oxides and elements from respective thermodynamic cycles, their obtained enthalpy values deviate only about 1% from those of Ref. [270] and Ref. [269] who assumed that samples have nominal stoichiometry. Therefore, in the present work also the nominal compositions are used for the calculation of enthalpies.

The uncertainties expressed for the derived enthalpies are the combined expanded uncertainties (k = 2, 95% confidence interval) calculated from the uncertainties of the enthalpies of drop solution for the constituent oxides and the NMC compounds.

The enthalpy of formation of $LiCoO_2$ from the elements obtained in the present work is in a very good agreement with the results of Wang and Navrotsky [105, 270], Wang et al. [269] and Gotcu-Freis et al. [258] as can be seen in Figure 6.1-a. Comparing the enthalpies of formation from elements for $LiCoO_2$ sample of the present work with the literature data, one should note that the samples used in different studies are slightly different in terms of preparation

condition and chemical composition and consequently enthalpy values. Yet, the relative difference is lower than 1.5% which is still a very good agreement. It should be mentioned that the numbers after the "±" sign in Table 6.4 and error bars in Figure 6.1 express the repeatability of the experiments and are calculated using type A combined uncertainty analysis. This does not include the uncertainties associated with using different sample batches and different calorimeters and operators. It is expected that the total uncertainty of each measurement is larger than the uncertainty related to repeatability.

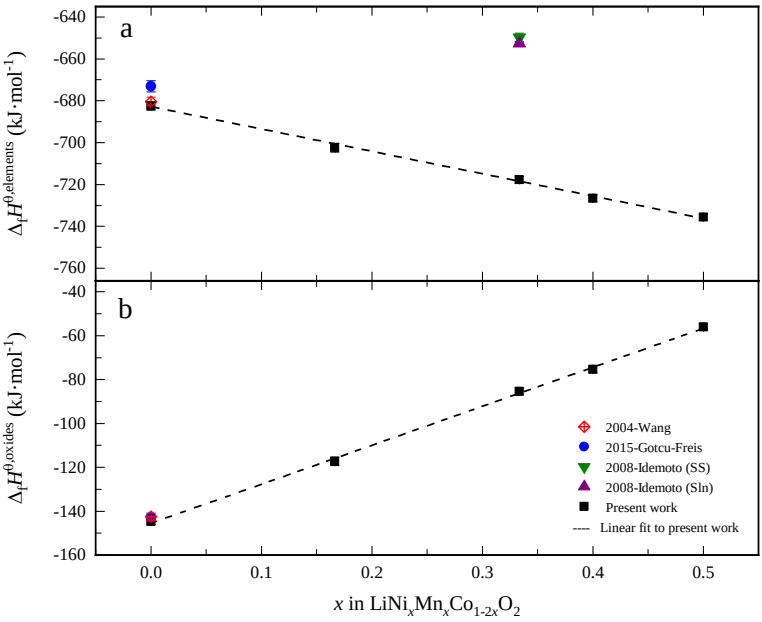

Figure 6.1: Enthalpy of formation (a) from the elements at 298.15 K (kJ·mol^{-1}) and (b) from the constituent oxides at 298.15 K (kJ·mol^{-1}) vs. x in $LiNi_xMn_xCo_{1-2x}O_2$ compared to those of $LiCoO_2$ from Wang and Navrotsky [270] and from Gotcu-Freis et al. [258] and $LiNi_{1/3}Mn_{1/3}Co_{1/3}O_2$ from Idemoto and Matsui [274]. The purple and green triangular data points from Idemoto and Matsui [274] show the related values for samples synthesized by solution and solid-state methods, respectively.

By increasing *x*, the standard enthalpies of formation of the various compositions of $LiNi_xMn_xCo_{1-2x}O_2$ from the elements become more exothermic. This indicates that by substitution of Co^{3+} with equimolar amounts of Mn^{4+} and Ni^{2+} cations on 3(*b*) sites (the transition metal layer), the layer structured compound becomes energetically more stable. When the experimental error is taken into account, for compositions along the line from $LiNi_{0.5}Mn_{0.5}O_2$ to $LiCoO_2$, the relationship between the enthalpies of formation from elements and *x* could be considered as linear.

The higher thermodynamic stabilities of $LiNi_xMn_xCo_{1-2x}O_2$ compounds with increasing Ni and Mn contents might contribute to their improved electrochemical and thermal stabilities as observed by many researchers. Makimura and Ohzuku [372] reported that $LiNi_{0.5}Mn_{0.5}O_2$ discharged at slow rates has a rechargeable capacity of approximately 200m Ah·g^{-1} in the voltage range of 2.5-4.5 V vs. Li with 99% coulombic efficiency over 30 cycles, while $LiCoO_2$ and $LiNiO_2$ have higher and faster capacity fading when charged to such high voltages [57, 216]. According to the comprehensive investigations of Ohzuku's group [143, 158, 372], the operating voltage of a $Li/LiNi_{0.5}Mn_{0.5}O_2$ cell is even slightly higher than that of a $Li/LiNi_{1/3}Mn_{1/3}Co_{1/3}O_2$ cell. There are also similar reports showing higher discharge capacity and better capacity retention of $LiNi_xMn_xCo_{1-2x}O_2$ cathode materials ($0.33 \leq x \leq 0.5$) by increasing *x* when cycled between 3.0-4.5 V [373], 2.5-4.5 V [275] and 2.5-4.4 V [350].

The higher capacity and improved cycle performance of Ni/Mn-rich $LiNi_xMn_xCo_{1-2x}O_2$ active materials could be attributed to the presence of octahedrally coordinated Mn^{4+} cations, which serve as an electrochemically inactive filler, making the structure more stable by preventing the transformation to spinel structure as proposed by Reed and Ceder [147] and Ammundsen and Paulsen [148]. Nevertheless, one needs to note that the electrochemical performance of layered lithium transition metal oxides as cathode materials depends strongly on the heat treatment history (including calcination temperature, duration, and cooling method), which in turn affects the lattice constants, cation mixing, oxygen non-stoichiometry, and morphology of the synthesized material. All these parameters directly affect

the electrochemical behavior of the cathode material and might be the source for some controversies in the literature.

The increased energetic stability of the layer-structured $LiNi_xMn_xCo_{1-2x}O_2$ phases with increasing x may also clarify why the O3-type structure is preserved in $LiNi_{0.5}Mn_{0.5}O_2$ after complete chemical delithiation as shown by Choi et al. [374], whereas the stable structures for the chemically delithiated end member of $LiNi_xMn_xCo_{1-2x}O_2$ were of O1 type and P3 type structures for $x = 1/3$ and $x = 0$, respectively [374].

The improved thermal stability of delithiated phases of $LiNi_xMn_xCo_{1-2x}O_2$ electrode materials with increasing x may also be related to their higher thermodynamic stabilities. This aspect is studied by Jiang et al. [329] for $LiNi_xMn_xCo_{1-2x}O_2$ with $0.1 \leq x \leq 0.5$, which was charged to 4.2 and 4.4 V vs. Li and then exposed to the reaction with ethylene carbonate/ diethyl carbonate (EC/DEC) solvent or electrolyte (1 M $LiPF_6$ in EC/DEC) in an accelerating rate calorimeter (ARC). It is observed that for $LiNi_xMn_xCo_{1-2x}O_2$ with $x \geq 0.2$ charged to 4.2 or 4.4 V vs. Li, the exothermic reaction between the sample and the solvent begins at about 190 °C, which is higher than the onset temperature of 140 °C for $LiCoO_2$. By increasing x the main exothermic peak associated with the reaction is also shifted to higher temperatures [329]. For samples that are charged to 4.2 V and allowed to react with the electrolyte, the onset temperature of the exothermal reaction and the thermal runaway in sample with $x = 0$ are 170 °C and 230 °C with a self-hearing rate of 0.15 $K \cdot min^{-1}$. For $LiCoO_2$ ($x = 0$) the above-mentioned parameters are 140 °C, 240 °C and 0.2 $K \cdot min^{-1}$, respectively. By increasing x above 0.2, even higher thermal stabilities are attained.

It should be mentioned that the enthalpy of formation of $LiNi_{1/3}Mn_{1/3}Co_{1/3}O_2$ reported by Idemoto and Matsui [274] is different from the value determined in the present work. This might be due to the heat of dissolution of Co_2O_3 that they employed in their calculations. As Co_2O_3 is unstable under normal conditions, Idemoto and Matsui [274] have estimated its heat of dissolution by calculating the lattice energy using the Born–Landé equation with the Madelung constant and internuclear distance taken from a DVX-α calculation. The standard enthalpy of formation of Co_2O_3 is calculated as -175.43 $kJ \cdot mol^{-1}$

by the Born–Haber cycle [274]. Moreover, the presence of point defects, impurity phases and/or second order phase transitions may also lead to the reported differences. Nevertheless, in our paper [360] the experimentally determined data of the present work are compared with the theoretical enthalpies of formation of respective compositions at 0 K determined by *ab initio* calculations (density functional theory)[1] and showed that they are consistent with each other. Furthermore, these results are congruent with the experimentally observed improved discharge capacity and better capacity retention [275, 350, 373] by increasing *x*.

In Figure 6.1-b the enthalpies of formation of the compounds with respect to the constituent oxides are depicted which also show a linear trend. The standard enthalpies of formation of $LiNi_xMn_xCo_{1-2x}O_2$ compounds from oxides become less exothermic with increasing *x*. The observed trend in enthalpy of formation from the oxides is mainly due to the change in the oxidation state of cobalt in the constituent oxide (Co^{2+}) to its oxidation state in the final NMC compound (Co^{3+}), as described earlier. With decreasing Co content (increasing *x*), the contribution of the exothermic oxidation of Co^{2+} to Co^{3+} to the overall enthalpy of formation decreases. Therefore, the enthalpies of formation become less exothermic. It could be concluded that, in formation reactions where the oxidation states of the transition metals in the reactants and products are dissimilar, the enthalpy of formation data from the constituent oxides may not reflect the real energetic trend. Instead the enthalpy of formation from the elements should be considered as a more reliable criterion for assessing the relative thermodynamic stabilities in such systems.

[1] The *ab initio* calculations have been performed by Dr. Keke Chang at RWTH Aachen in the framework of a collaborative project funded by the German Research Foundation (DFG) Priority Program 1473 WeNDeLIB – Materials with New Design for Improved Lithium Ion Batteries.

6.3 $LiNi_{0.8-y}Mn_yCo_{0.2}O_2$ series

The standard enthalpies of formation of various $LiNi_{0.8-y}Mn_yCo_{0.2}O_2$ ($0 \leq y \leq 0.4$) compositions from their constituent binary oxides are calculated with respect to binary oxides i.e. Li_2O, MnO_2, NiO and CoO and oxygen. The respective formation reaction and reactions representing drop solution calorimetry are shown in the thermodynamic cycle of Table 6.5. Reactions (1) to (4) similar to Section 6.2, represent drop solution calorimetry of the binary oxides while reaction (6) shows the drop solution calorimetry of the $LiNi_{0.8-y}Mn_yCo_{0.2}O_2$ compound at the same solvent and temperature. Reaction (5) is related to heating up the gaseous oxygen from room temperature to the temperature of calorimetry and reaction (7) corresponds to the formation reaction of $LiNi_{0.8-y}Mn_yCo_{0.2}O_2$ compound from its constituent binary oxides and oxygen. The criteria for choosing constituent binary oxides and other assumptions are similar to Section 6.2.

Concerning the reactions in Table 6.5, the oxidation states are outlined for the transition metal cations in reactants as well as the products. The oxidation states of transition metal cations in $LiNi_{0.8-y}Mn_yCo_{0.2}O_2$ powder samples synthesized in the present work are analyzed by Raheleh Azmi utilizing X-ray photoelectron spectroscopy. The results which are published in a joint paper [304] show that the Co and Mn are mainly trivalent and tetravalent, respectively. It was also demonstrated that the oxidation state of Ni changes gradually from Ni^{3+} to Ni^{2+} with increasing y in $LiNi_{0.8-y}Mn_yCo_{0.2}O_2$. The Ni^{2+} content is determined to be 0%, 13%, 35%, 62%, and 100% of total Ni ions for y = 0. 0.1, 0.2. 0.3 and 0.4, respectively [304]. These results fits quite well with the expected ratio of Ni^{2+} ions to the total Ni ions (0%, 14.3%, 33.3%, 60% and 100% for y = 0. 0.1, 0.2. 0.3 and 0.4, respectively) according to the theoretical formula of $Li({Ni^{3+}}_{0.8-2y}{Ni^{2+}}_y{Mn^{4+}}_y{Co^{3+}}_{0.2})O_2$ as shown in reaction (6) and (7) in Table 6.5.

The oxidation states of the species in the molten sodium molybdate under argon atmosphere at 701 °C are mainly Co^{+2} , Mn^{+2} and Ni^{+2}, similar to what described earlier in Section 6.2. Therefore, the dissolution of $LiNi_{0.8-y}Mn_yCo_{0.2}O_2$ samples with Ni^{3+}/ Ni^{2+}, Mn^{4+} and Co^{3+} valence states

involves the reduction of Co, Mn and part of Ni cation and should be performed using argon bubbling and protecting gas.

Table 6.5: Thermodynamic cycle showing the reactions used for the determination of the enthalpy of formation of $LiNi_{0.8-y}Mn_yCo_{0.2}O_2$ compounds from binary oxides and oxygen using drop solution calorimetry in $3Na_2O{\cdot}4MoO_3$ solvent at 701 °C (974 K) under argon atmosphere.

Reaction	ΔH
1) $Li_2O_{(s,25°C)} \rightarrow [2Li^+ + O^{2-}]_{(sol,701°C)}$	$\Delta_{ds}H_{(Li_2O)}$
2) $Ni^{2+}O_{(s,25°C)} \rightarrow [Ni^{2+} + O^{2-}]_{(sol,701°C)}$	$\Delta_{ds}H_{(NiO)}$
3) $Mn^{4+}O_{2\,(s,25°C)} \rightarrow [Mn^{2+} + O^{2-}]_{(sol,701°C)}$	$\Delta_{ds}H_{(MnO_2)}$
4) $Co^{2+}O_{(s,25°C)} \rightarrow [Co^{2+} + O^{2-}]_{(sol,701°C)}$	$\Delta_{ds}H_{(CoO)}$
5) $O_{2\,(g,25°C)} \rightarrow O_{2\,(g,701°C)}$	$\Delta H_{(O_2)}$
6) $Li(Ni^{2+}{}_{0.8-2y}Ni^{2+}{}_yMn^{4+}{}_yCo^{3+}{}_{0.2})O_{2\,(s,25°C)} \rightarrow {}^1/_2\,[2Li^+ + O^{2-}]_{(sol,701°C)} + (0.8-y)[Ni^{2+} + O^{2-}]_{(sol,701°C)} + y[Mn^{2+} + O^{2-}]_{(sol,701°C)} + 0.2[Co^{2+} + O^{2-}]_{(sol,701°C)} + {}^1/_4\,O_{2\,(g,701°C)}$	$\Delta_{ds}H_{(LiNi_{0.8-y}Mn_yCo_{0.2}O_2)}$
7) ${}^1/_2\,Li_2O_{(s,25°C)} + (0.8-y)Ni^{2+}O_{(s,25°C)} + yMn^{4+}O_{2\,(s,25°C)} + 0.2Co^{2+}O_{(s,25°C)} + {}^{(1-2y)}/_4\,O_{2\,(g,25°C)} \rightarrow Li(Ni^{3+}{}_{0.8-2y}Ni^{2+}{}_yMn^{4+}{}_yCo^{3+}{}_{0.2})O_{2\,(s,25°C)}$	$\Delta_f H^{\theta,oxides}{}_{(LiNi_{0.8-y}Mn_yCo_{0.2}O_2)}$

The values of the enthalpy of drop solution for the $LiNi_{0.8-y}Mn_yCo_{0.2}O_2$ (y = 0, 0.1, 0.2, 0.3 and 0.4) compounds are listed in Table 6.6. The numbers of individual drops of each sample as well as the uncertainty of the repeated measurements are also indicated.

The enthalpy of drop solution values of binary oxides as well as the heat content of oxygen gas from room temperature to the temperature of calorimetry used for the determination of the enthalpies of formation from oxides are the same as Section 6.2. For comparison, the enthalpy of formation from oxides for $LiNi_{0.8}Co_{0.2}O_2$ composition is calculated from linear interpolation of the enthalpy of formation from oxides of $LiNi_{1-x}Co_xO_2$ series determined by Wang

and Navrotsky [270] for x = 0, 0.25, 0.5, 0.75 and 1. The linear equation is calculated as $\Delta_f H^{\theta,oxides}$ = (-54.60 ± 1.66) + (-85.98 ± 2.71) x (R^2 = 0.9970).

Table 6.6: The values of enthalpy of drop solution of $LiNi_{0.8-y}Mn_yCo_{0.2}O_2$ (y = 0, 0.1, 0.2, 0.3 and 0.4) samples in $3Na_2O{\cdot}4MoO_3$ at 701 °C (974 K) under argon atmosphere.

	sample	$\Delta_{ds}H^{974}$/ kJ·mol^{-1} (drops)	source
ternary oxides	Li $Ni_{0.8}Co_{0.2}O_2$ [1]	61.39 ± 0.56 (13)	This work
		62.38 ± 2.20 [2]	Wang and Navrotsky [270]
	$LiNi_{0.7}Mn_{0.1}Co_{0.2}O_2$ [3]	72.16 ± 0.55 (12)	This work
	$LiNi_{0.6}Mn_{0.2}Co_{0.2}O_2$	80.24 ± 0.70 (12)	This work
	$LiNi_{0.5}Mn_{0.3}Co_{0.2}O_2$	89.79 ± 0.59 (11)	This work
	$LiNi_{0.4}Mn_{0.4}Co_{0.2}O_2$	97.97 ± 0.65 (12)	This work

[1] Final heat treatment at 800 °C.

[2] Calculated by linear interpolation of the enthalpy of drop solution values determined by Wang and Navrotsky for $LiNi_{1-x}Co_xO_2$ series.

[3] Final heat treatment at 850 °C.

The standard enthalpy of formation from oxides equals the enthalpy changes of the reaction (7) in Table 6.5 and is calculated according to Equation (6.10). The obtained values are listed in Table 6.7 and depicted in Figure 6.2.

$$\Delta_f H^{\theta,oxides}{}_{(LiNi_{0.8-y}Mn_yCo_{0.2}O_2)} = \frac{1}{2}\,\Delta_{ds}H_{(Li_2O)} + (0.8-y)\,\Delta_{ds}H_{(NiO)} + y\,\Delta_{ds}H_{(MnO_2)} + 0.2\,\Delta_{ds}H_{(CoO)} + \frac{1-2y}{4}\int_{298}^{974} c_{p(O_2)} - \Delta_{ds}H_{(LiNi_{0.8-y}Mn_yCo_{0.2}O_2)} \quad (6.10)$$

The standard enthalpy of formation of the $LiNi_{1-x}Co_xO_2$ (x = 0, 0.25, 0.5, 0.75 and 1) compositions from their elements were not reported in the original work of Wang and Navrotsky [270]. Therefore, the enthalpy of formation from elements for $LiNi_{0.8}Co_{0.2}O_2$ composition is here calculated using respective enthalpy of formation from oxides and Equation (6.11) with the same input values as our own calculation. Similar to Section 6.2, the standard enthalpies of formation of the constituent binary oxides from the elements ($\Delta_f H$) are taken

from Glushko et al. [370] as shown in Table 6.4. The results are summarized in Table 6.7 and represented in Figure 6.2.

$$\Delta_f H^{\theta,\text{elements}}{}_{(LiNi_{0.8-y}Mn_yCo_{0.2}O_2)} = \Delta_f H^{\theta,\text{oxides}}{}_{(LiNi_{0.8-y}Mn_yCo_{0.2}O_2)} + \frac{1}{2}\,\Delta_f H_{(Li_2O)} + (0.8-y)\,\Delta_f H_{(NiO)} + y\,\Delta_f H_{(MnO_2)} + 0.2\,\Delta_f H_{(CoO)} \quad (6.11)$$

Table 6.7: Enthalpy of formation from binary oxides (MnO_2, NiO and CoO) and enthalpy of formation from elements at 298 K for binary oxides from the literature and $LiNi_{0.8-y}Mn_yCo_{0.2}O_2$ (y = 0, 0.1, 0.2, 0.3 and 0.4) compounds determined experimentally and compared with the literature data.

sample (nominal composition)	$\Delta_f H^{\theta,\text{oxides}}$ (298K)/ kJ·mol^{-1}	$\Delta_f H^{\theta,\text{elements}}$ (298K)/ kJ·mol^{-1}	source
Li $Ni_{0.8}Co_{0.2}O_2$ [1]	-70.80 ± 1.47	-609.34 ± 1.56	This work
	-71.79 ± 2.20 [2]	-610.33 ± 2.64 [3]	Wang and Navrotsky [270]
$LiNi_{0.7}Mn_{0.1}Co_{0.2}O_2$ [4]	-73.34 ± 1.42	-640.05 ± 1.50	This work
$LiNi_{0.6}Mn_{0.2}Co_{0.2}O_2$	-73.19 ± 1.45	-668.08 ± 1.53	This work
$LiNi_{0.5}Mn_{0.3}Co_{0.2}O_2$	-74.46 ± 1.40	-697.58 ± 1.46	This work
$LiNi_{0.4}Mn_{0.4}Co_{0.2}O_2$	-56.09 ± 1.56	-725.70 ± 1.49	This work

[1] Final heat treatment at 800 °C.

[2] Calculated by linear interpolation of the enthalpy of formation from oxides values determined by Wang and Navrotsky for $LiNi_{1-x}Co_xO_2$ series.

[3] As this value is not reported in the original work (Ref. [270]), here it is calculated using respective enthalpy of formation from oxides and Equation (6.11) with the same input values as our own calculation.

[4] Final heat treatment at 850 °C.

Despite observed lithium losses for $LiNi_{0.8-y}Mn_yCo_{0.2}O_2$ sample as shown in Section 4.2.3.1, the nominal stoichiometric compositions are used for the calculations of enthalpies, because the effect of this assumption on the derived enthalpies is negligible. The uncertainties stated for the derived enthalpies are the combined expanded uncertainties (k = 2, 95% confidence interval)

calculated based on the uncertainties of the enthalpies of drop solution for the constituent oxides and the NMC compounds.

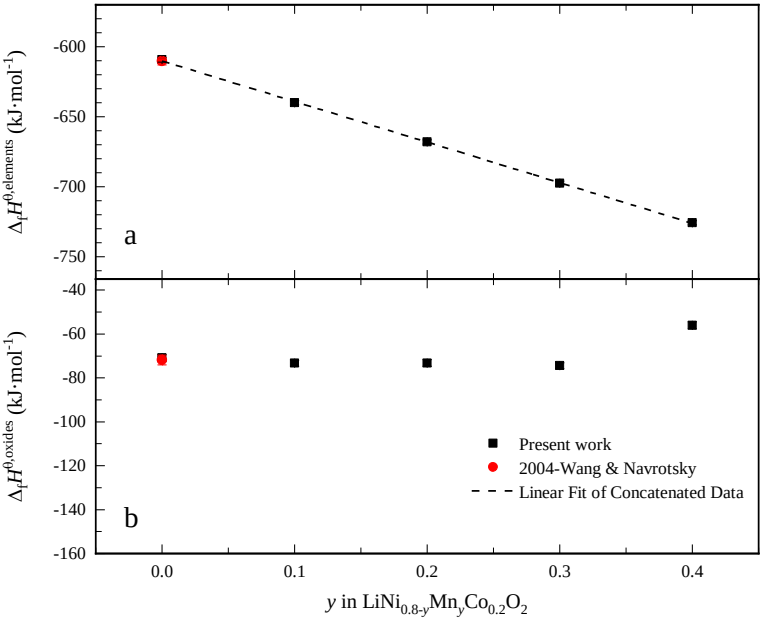

Figure 6.2: Enthalpy of formation (a) from the elements at 298.15 K (kJ·mol^{-1}) and (b) from the constituent oxides at 298.15 K (kJ·mol^{-1}) vs. y in $LiNi_{0.8-y}Mn_yCo_{0.2}O_2$ (y = 0, 0.1, 0.2, 0.3 and 0.4) compounds determined experimentally and compared to those of $LiNi_{0.8}Co_{0.2}O_2$ from Wang and Navrotsky [270].

Comparing the enthalpies values for $LiNi_{0.8}Co_{0.2}O_2$ sample of the present work with those of Wang and Navrotsky [270], a relative differences of 0.16 - 1.6 % is to observe. This indicates a very good agreement between our measurements and literature data despite differences in investigated samples of different studies in terms of preparation condition and chemical composition.

By increasing y, the standard enthalpies of formation of the various compositions of $LiNi_{0.8-y}Mn_yCo_{0.2}O_2$ from the elements become more

exothermic. This means that by substitution of Ni^{3+} with equimolar amounts of Mn^{4+} and Ni^{2+} cations on 3(*b*) sites (the transition metal layer), the layer structured compound becomes energetically more stable. The relationship between the enthalpies of formation from elements and *y* for $LiNi_{0.8-y}Mn_yCo_{0.2}O_2$ compositions along the line from $LiNi_{0.8}Co_{0.2}O_2$ to $LiNi_{0.4}Mn_{0.4}Co_{0.2}O_2$ could be considered as linear. The linear equation is calculated as $\Delta_f H^{\theta,elements} = (-610.19 \pm 0.42) + (-289.96 \pm 1.88)\, x$ ($R^2 = 0.9998$).

The higher thermodynamic stabilities of $LiNi_{0.8-y}Mn_yCo_{0.2}O_2$ compounds with increasing *y* is speculated to contribute to their improved structural stability and cycling performance that will be extensively examined and discussed in the next chapter, Chapter 67.

6.4 $LiNiO_2$ - $LiCoO_2$- $LiNi_{0.5}Mn_{0.5}O_2$ system

The values of standard enthalpies of formation from elements of $LiNi_xMn_xCo_{1-2x}O_2$ (x = 0, 0.17, 0.33, 0.4. 0.5) and $LiNi_{0.8-y}Mn_yCo_{0.2}O_2$ (y = 0, 0.1, 0.2, 0.3 and 0.4) compounds which are experimentally determined in the present work are plotted into a contour plot on ternary coordinate i.e. on the $LiNiO_2$-$LiCoO_2$-$LiMnO_2$ Gibbs triangle. The enthalpy values of $LiNi_{1-x}Co_xO_2$ (y = 0, 0.25, 0.5, 0.75 and 1) compositions from their elements are also calculated based on the experiments of Wang and Navrotsky [270] and incorporated. Figure 6.3 illustrates the ternary contour plot of the standard enthalpy of formation from elements for the left side of the NMC triangle; the compositions lie between the $LiNiO_2$, $LiCoO_2$ and $LiNi_{0.5}Mn_{0.5}O_2$ end members. The graph is plotted using Origin program's ternary contour graph without smoothing.

The contour lines (iso-enthalpy compositions) are almost linear, indicating a near-linear relationship between the standard enthalpy of formation value and the composition of the NMC compound in this region. The direction perpendicular to the contour lines show the path of composition variation which leads to the maximum changes in the enthalpy values. This direction is shown by an arrow in Figure 6.3. By changing the composition of the NMC

compound in the direction of the arrow, the standard enthalpies of formation from the elements become more exothermic, indicating improved energetic stability of the layer structured compound. It could be concluded that in the investigated area, $LiNi_{0.5}Mn_{0.5}O_2$ and $LiNiO_2$ are the most and the least energetically stable compounds, respectively.

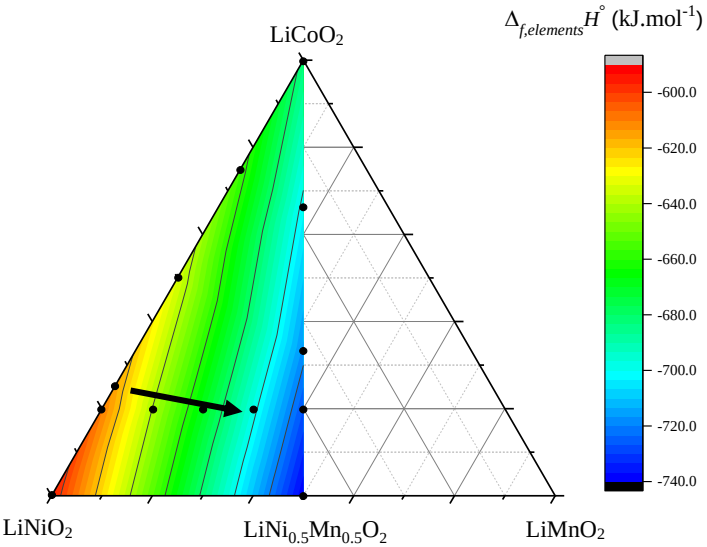

Figure 6.3: Ternary contour plot of the standard enthalpy of formation from elements for the compositions lie between the $LiNiO_2$, $LiCoO_2$ and $LiNi_{0.5}Mn_{0.5}O_2$ end members. The black arrow shows the direction of compositional variation which leads to the maximum changes in the enthalpy values. For sample notation please see Figure 3.2.

The higher thermodynamic stabilities of the NMC compounds is believed to contribute to the improved structural stability and cyclability upon electrochemical lithium intercalation. This theory is supported by the results of electrochemical experiments on $LiNi_{0.8-y}Mn_yCo_{0.2}O_2$ and $LiNi_{0.5}Mn_{0.5}O_2$ half cells in the following chapter of the present dissertation.

7 Electrochemical studies

In this chapter, the results of the electrochemical investigation on $LiNi_{0.8-y}Mn_yCo_{0.2}O_2$ compounds as well as $LiNi_{0.5}Mn_{0.5}O_2$ are presented. For this purpose, half coin cells with composite electrodes made of synthesized NMC as active material of cathode are subject of different electrochemical measurements techniques. Through these measurements, the redox behavior and cyclability of different compositions are compared.

7.1 Coated electrodes

To examine the distribution of the particles of active material in the coated electrodes, the In-lens (secondary electron) and energy selective backscattered images of the pristine electrodes are obtained. The SEM micrographs of the samples using in-lens detector (right) and ESB detector (left) are shown in Figure 7.1 a-e. As can be seen from the ESB images which reveal the chemical contrast, the very small particles formed on the surface of the coated electrodes are much darker than the NMC particles in all samples. These particles are probably the organic compounds originated from PVDF or carbon black. They also might be impurities made of light elements like C, such as lithium carbonate or H, such as lithium hydroxide.

These impurity phases are possibly formed through the reaction of excess lithium of NMC phase with the carbon dioxide or humidity from air during the casting process. As can be seen in Figure 7.1, the amount of light phases increases as y in $LiNi_{0.8-y}Mn_yCo_{0.2}O_2$ decreases. This means that the samples with higher Ni content are more prone to the contamination with air and to the formation of superficial impurity phases.

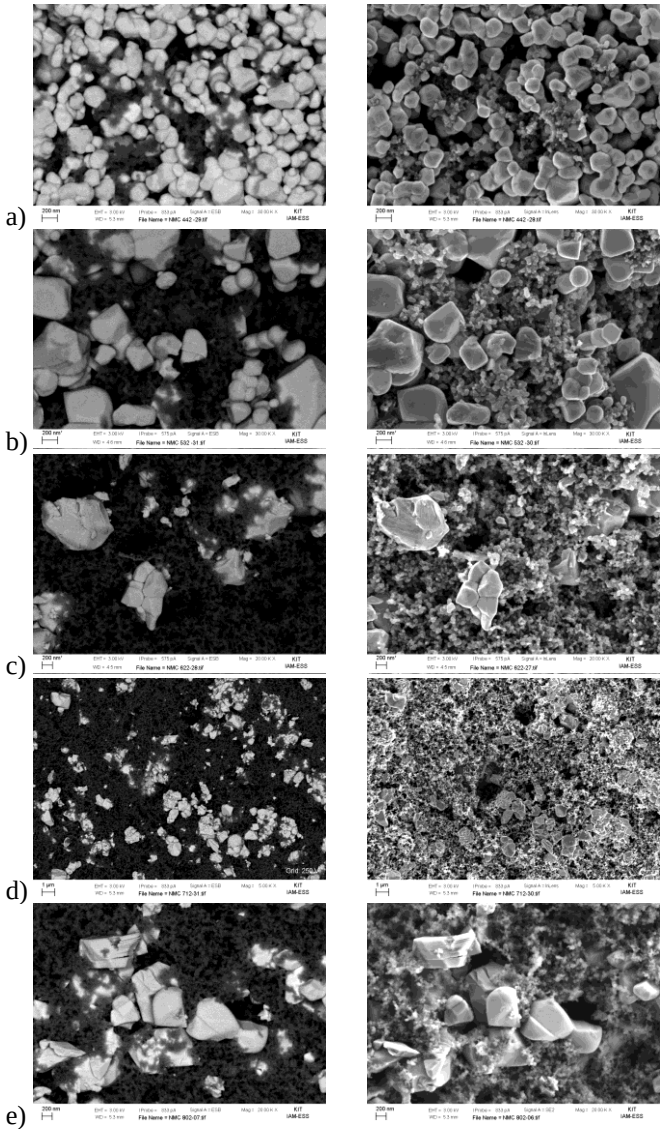

Figure 7.1: Energy selective backscattered (left) and in-lens secondary electron (right) micrographs of $LiNi_{0.8-y}Mn_yCo_{0.2}O_2$ coated electrodes; a) NMC442, b) NMC532, c) NMC622, d) NMC712 and e) NMC802. (Pictures courtesy of IAM-ESS, KIT)

Moshtev et al. [375] discussed that when $LiNiO_2$ is in contact with air, the water from air humidity is absorbed and can cause chemical delithiation according to the following reaction:

$$LiNiO_2 + \frac{x}{2}H_2O \rightarrow Li_{1-x}NiO_{2-\frac{x}{2}} + xLiOH \tag{7.1}$$

Another possibility is that due to their larger particle sizes, the $LiNi_{0.8-y}Mn_yCo_{0.2}O_2$ with higher Ni content are more difficult to mix homogenously with carbon black and PVDF particles and disperse inside the slurry. As observed in Section 4.2.3.2, the size of the NMC particles increases as *y* in $LiNi_{0.8-y}Mn_yCo_{0.2}O_2$ increases. As a result of inhomogeneous mixing, more carbon and PVDF particles are agglomerated on the surface during coating process. It seems that the coating process needs to be optimized for NMC662, 712 and 802 so that the particles are better distributed in the PVDF and carbon black matrix. The inhomogeneous coating may affect the delivered capacity as some particles of active material may not be available for redox reactions. The inhomogeneous coating will also adversely affect the rate capability. However, these are not thermodynamic-related properties of the electrode. As the aim of the measurements is the evaluation of electrochemical properties of the active material close to thermodynamic equilibrium state, the imperfection of coated electrodes could be neglected. Therefore, the present electrodes are utilized for the cell assembly and electrochemical measurements.

7.2 Initial galvanostatic coulometry with potential limitations (GCPL)

Figure 7.2 shows the voltage profile of five initial charge and discharge cycles of GCPL measurement of $LiNi_{0.8-y}Mn_yCo_{0.2}O_2$ (NMC802, 712, 622, 532 and 442) as well as $LiNi_{0.5}Mn_{0.5}O_2$ (NMC110) half cells using a nominal C/10 charge/discharge rate at 25 °C. In order to guarantee the reproducibility of the electrochemical performance through the measurements, at least three cells for each sample were fabricated and tested. The measured data of all the cells for a specific composition were almost identical. Thus in the present section, only one typical datum for each composition is presented.

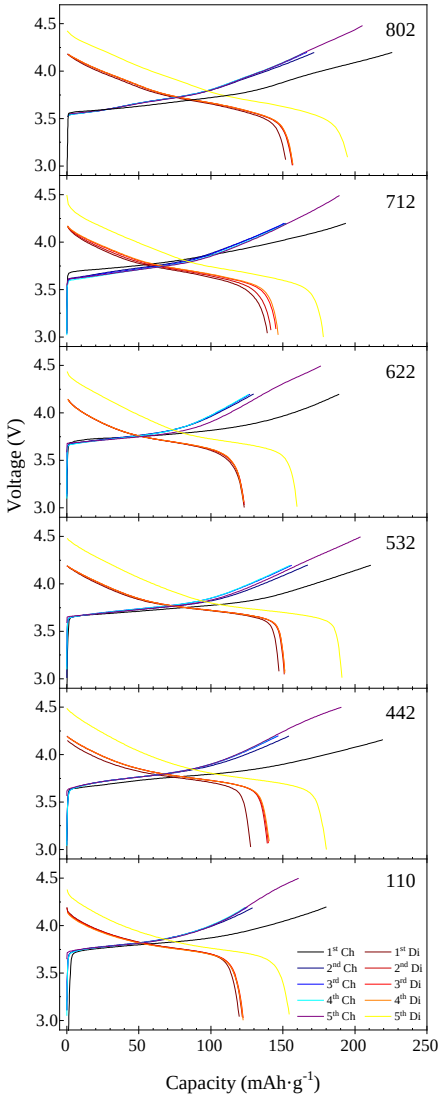

Figure 7.2: Voltage profile of five initial charge and discharge cycles of $LiNi_{0.8-y}Mn_yCo_{0.2}O_2$ and $LiNi_{0.5}Mn_{0.5}O_2$ half cells using a nominal C/10 charge/discharge rate at 25 °C. The first four cycles are performed in the potential range of 3-4.2 V, and the fifth cycle in the range of 3-4.5 V. For quantitative data please see Table 7.1.

The first four cycles are performed in the potential range of 3-4.2 V. Cells are cycled four times to realize the formation of SEI (solid-electrolyte-interface). These cycles are therefore known as “formation cycles”. The fifth cycle is performed in the voltage range of 3-4.5 V to determine the capacity of the cell up to 4.5 V cut-off voltage. Knowing this capacity is essential for calculating the applied current in the following step of the measurement, which is GITT. The four initial cycles where however performed using a lower cut-off voltage to avoid the degradation of the cell electrodes and electrolyte by exposure to high voltages, while still allowing the formation of the protective layers.

As described in Section 2.3, the evolution of cell voltage versus lithium content, or similarly the cell capacity, provides an insight about the cell reactions and the thermodynamic behavior of the electrode material. As can be seen in Figure 7.2, except the first charge curve that is discussed in the following text, the voltage profile of all studied cell compositions during charge and discharge have a smooth shape. By charging, the voltages of all samples quickly increase to 3.5-3.8 V, and then follow the slopes to the cutoff voltage of 4.3 V or 4.5 V without any obvious plateaus. The almost monotonous variation of the potential against capacity reflects the existence of a solid solution region over the whole experimented composition range. The behavior observed for the NMC samples here is very different from those of LCO or LNO [84, 134] half cells with many plateaus on the voltage curves and corresponding strong peaks in the derivative curve which are associated with the biphased domains.

The charge and discharge capacities of investigated cells are listed in Table 7.1. As can be seen for all compositions, the first charge capacity is much higher than the capacity obtained in the following charges. The reason is that during the first cycle some of the applied current, and consequently some of the calculated capacity, is used by the side reactions, other than the redox reaction. The side reactions include the formation of an SEI layer. The other reason may be the intercalation of Li ions not only from the 3a sites in the initial hexagonal structure, but also from excess Li atoms outside of the octahedral sites. However, during the first discharging, the latter Li ions cannot insert the cathode material again, resulting in larger first cycle’s irreversible

capacity. The first discharge capacities of $LiNi_{0.8-y}Mn_yCo_{0.2}O_2$ are 128.5, 147.7, 123.1, 139.5, 152.7 mAh·g^{-1} for x = 0.4, 0.3, 0.2, 0.1 and 0, respectively. The first discharge capacity of $LiNi_{0.5}Mn_{0.5}O_2$ is measured as 120 mAh·g^{-1}. However, after the first cycles, the cells start to stabilize and deliver an almost constant capacity by charging and discharging.

Table 7.1: The charge (Ch) and discharge (Di) capacities delivered during GCPL measurement of $LiNi_{0.8-y}Mn_yCo_{0.2}O_2$ as well as $LiNi_{0.5}Mn_{0.5}O_2$ half cells. The first four cycles are performed in the potential range of 3-4.2 V, and the fifth cycle in the range of 3-4.5 V. m in mg is the amount of active material in each investigated cathode.

Composi-tion	Cell No.	m (mg)	Capacity (mAh·g^{-1})									
			1st		2nd		3rd		4th		5th	
			Ch	Di	Ch	Di	Ch	Di	Ch	Di	Ch	Di
NMC110	03	4.477	180.7	120.0	130.2	122.2	126.0	122.6	124.6	122.4	160.9	154.9
NMC442	06	4.241	219.7	128.5	155.0	139.7	147.0	140.5	145.7	141.2	190.6	180.1
NMC532	04	3.676	211.7	147.7	167.3	151.3	156.7	151.8	155.4	151.8	204.5	191.0
NMC622	07	4.087	189.4	123.1	129.9	123.3	127.7	123.3	127.0	123.1	176.3	159.2
NMC712	10	5.165	193.9	139.5	152.3	142.4	151.2	145.8	153.0	146.9	189.2	178.2
NMC802	01	3.197	226.8	152.7	172.4	156.4	166.7	157.0	165.8	157.0	205.2	194.8

A firm relationship between the delivered cell capacities and the cell composition was not found here. This might be due to the fact that for the initial cycles, the applied currents are calculated based on some rough estimated capacity values taken from the literature [250] for the corresponding cell composition. These values were not necessarily similar to the obtained capacities of our examined cells. Therefore, not all of the cells are actually cycled with the same charge/discharge rate and charge/discharge rate directly affects the capacity value. The absence of a clear relationship between the delivered cell capacities and the cell composition may also be due to the different coating qualities. As observed in Section 7.1, the quality of electrode coating was not similar for all the investigated cell compositions. The quality of the coated electrode including homogenous distribution of active material

in the matrix and the existence of a good connection between the particles of active material and carbon black particles is important in realizing the extraction of maximum capacity and avoiding dead weight of active material.

As mentioned earlier in Section 2.3, in the voltage profile versus lithium amount or eventually, versus capacity, the high-slope parts reflect single-phase solid solution domains, plateaus show first-order phase transition resulted in two-phase regions, and inflection points represent the continuous phase transitions with no region of two-phase coexistence [57, 84]. These features are more visible in the derivative curve or differential capacity curve, where strong peaks associate with the plateaus showing the biphased domains.

The derivative of the cycling curve, the dq/dV curve, for $LiNi_{0.8-y}Mn_yCo_{0.2}O_2$ and $LiNi_{0.5}Mn_{0.5}O_2$ half cells in the voltage window of 3.0 V and 4.5 V are presented in Figure 7.3. The curves corresponding to the first charges are shown by dotted black lines in Figure 7.3. In almost all graphs, the curves of first charge are different from the curves of following charges, showing larger or even extra peaks. The oxidation of water is an unlikely reason for the peaks on first charge differential curves because this reaction takes place at much lower potentials (about 1.23 V). Besides, all the cell components were well vacuum dried before the assembly. The extra peaks here might show the side reactions of the electrolyte and the SEI formation reaction, which happens during the first charge and are different from the main redox reaction of the cell. In addition, in the first cycle the lithium ion are extracted not only from the lithium layer of the O3 phase, but also from the possible impurity phases and thus may yield extra peaks on the corresponding differential curve. The capacity used for these extra reactions appears as irreversible capacity of the first cycle.

As can be seen in Figure 7.3 the derivative of the cycling curve for all samples show no strong peaks indicating the absence of any biphased domains upon cycling. However, although no strong peak is present, there are still weaker peaks on the derivate curves of Figure 7.3. These peaks represent inflection points on the respective cycling curves indicating second order phase transitions upon lithium extraction/ reinsertion.

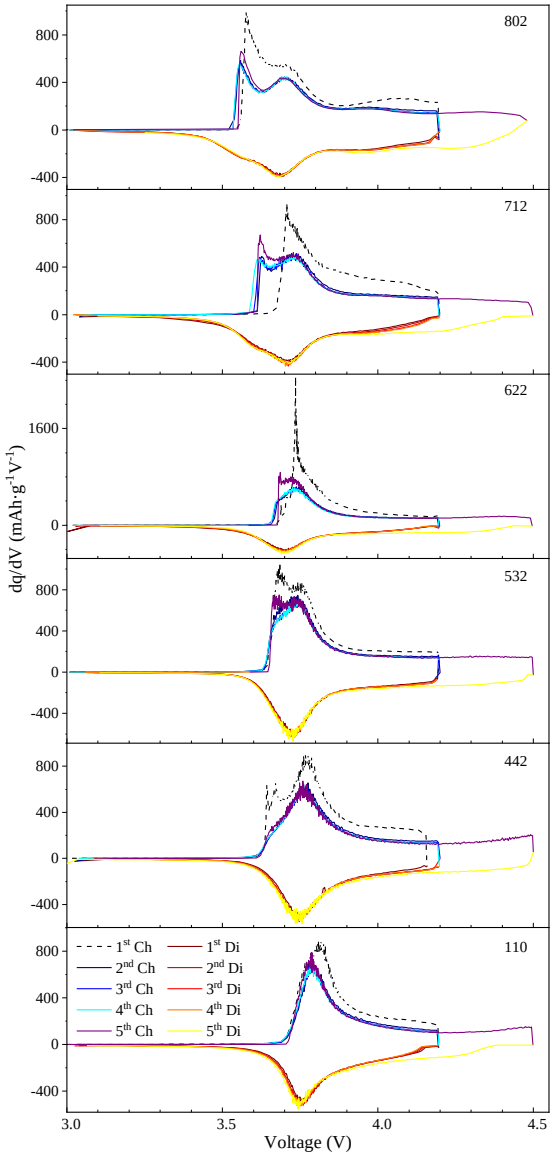

Figure 7.3: The derivative of the cycling curve, the dq/dV curve, for $LiNi_{0.8-y}Mn_yCo_{0.2}O_2$ and $LiNi_{0.5}Mn_{0.5}O_2$ half cells in the voltage window of 3.0 V and 4.5 V.

It has been described in Section 2.3 that the phase transitions which happen during the (de)intercalation of $LiNiO_2$ or $LiCoO_2$ are basically caused by the lithium/vacancy ordering. Saadoune and Delmas [134] have shown that by substitution of at least 20% of Ni in Li_xNiO_2 with Co, the monoclinic distortion upon lithium extraction is suppressed. They suggest that there is a tendency for ordering of the lithium ions upon (de)lithiation, but due to the random distribution of transition metals in the slabs, a long range ordering is prevented. Therefore only a second order transition takes place and all new phases maintain the rhombohedral symmetry. It seems that the same phenomena is taking place here. In this work, in the examined half cells with different NMC compositions, the transition metal layer is occupied by various cations instead of pure Ni or Co. This introduces a disorder within the slabs and prevents the lithium/vacancy ordering at different state of charges. Therefore, the peaks that appear on the derivative curves of Figure 7.3 are possibly due to the second order phase transitions happening to the initial O3 phases.

The differential capacity curves during the charging of NMC802 and NMC712 exhibit a couple-peak. The peaks are less separated from each other in the discharge differential curves. The peaks on charging are at around 3.56 and 3.70 V for NMC802 and at about 3.62 V and 3.73 V for NMC712. In the differential capacity curves of NMC622, NMC532, NMC442 and NMC110 only one peak is to observe which is located at approximately 3.74 V, 3.74 V, 3.76 V and 3.79 V on charging, respectively. Accordingly, it seems that the peak appears at lower voltage of about 3.6 V in NMC802 and NMC712 curves disappear by increasing Mn content, in NMC622, NMC532, NMC442 and NMC110 graphs. The shape of the differential capacity vs. voltage profiles and the values of peaks for NMC532 and NMC622 in the present work (Figure 7.3) are in a very good agreement with those observed by Noh et al. [250] (shown in Figure 2.13).

It seems that by increasing Mn content in $LiNi_{0.8-y}Mn_yCo_{0.2}O_2$, the disorder in transition metal layer increases and thus the tendency for ordering of the lithium ions upon (de)lithiation decreases.

7.3 Galvanostatic intermittent titration technique (GITT)

The variation of the open circuit voltage (OCV) versus lithium amount in $Li_xNi_{0.8-y}Mn_yCo_{0.2}O_2$ and $Li_xNi_{0.5}Mn_{0.5}O_2$ are determined using GITT measurements on the half cells in the voltage range of 3.0 V and 4.5 V. The open circuit voltages and the respective lithium contents, eventually state of charge, are extracted from the voltage versus time graphs of GITT measurements as described in Section 3.5.3.2. The results including the recorded voltage of the cells during intermittent charge/discharge and relaxation periods and the extracted open circuit voltages for two examined cells of each NMC composition are plotted in the voltage versus x in Li_xMO_2 graphs, as shown in Figure 7.4. For a more clear view, the NMC110 graph in Figure 7.4 is shown in Figure 7.5 separately.

As can be seen, in all cells, the difference between the closed circuit voltage (CCV, the voltage at the end of each intermittent charge/discharge step) and the respective OCV value is higher when x in Li_xMO_2 is close to one. This means that the cells deviate more from the equilibrium state at the beginning of charging and the end of discharging process. In the case of all investigated cells, the NMC starting phase is not completely restored during the lithium reinsertion reaction. This behavior is probably due to the increasing lithium-lithium electrostatic repulsion when lithium layer is becoming fully occupied and x becomes close to one. Therefore, the kinetics of inserting more lithium into the structure becomes slower.

In Figure 7.4, except for NMC802 sample, a very good agreement is observed between the first and the second cells of the same cell composition. In the case of NMC802 sample, due to a damaged measurement program of the second cell, the last step of the intermittent charging takes too long and therefore, the equilibrium is probably not completely accomplished at the high delithiated states of this sample.

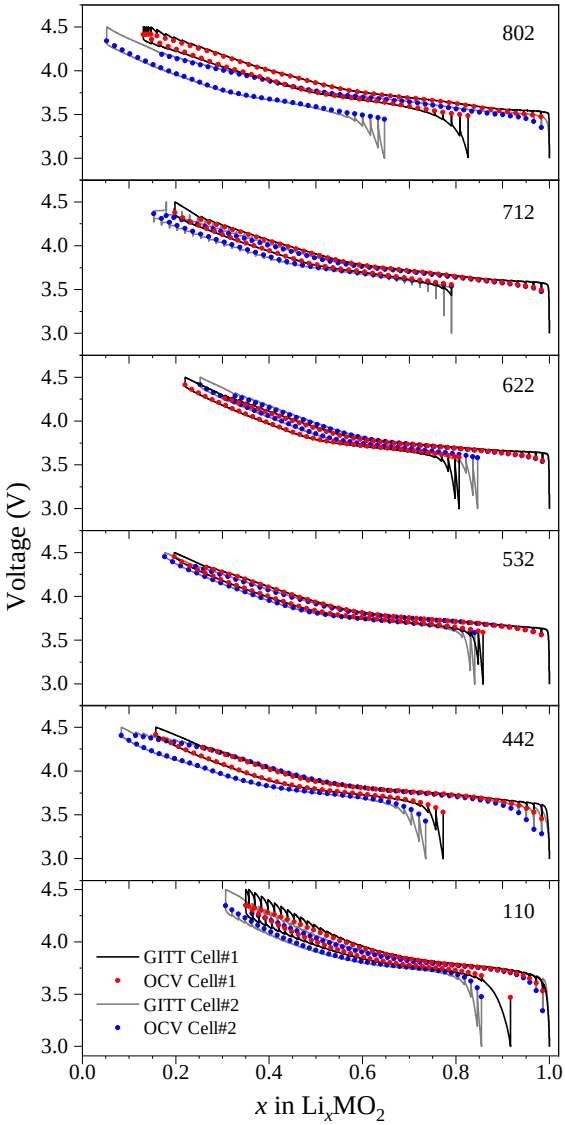

Figure 7.4: Voltage versus x in Li_xMO_2 graphs showing the voltage of the cells during intermittent charge/discharge and relaxation periods and the extracted open circuit voltages for two examined cells of each NMC composition.

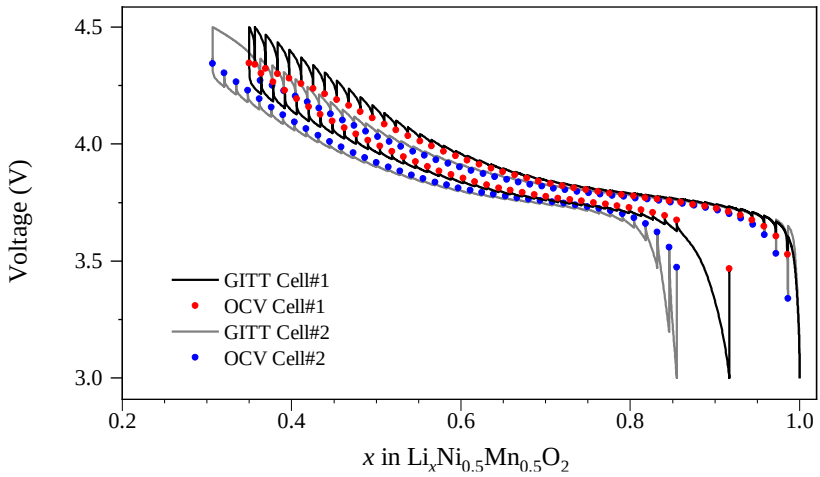

Figure 7.5: Enlarged voltage versus x in Li_xMO_2 graphs for NMC110 from Figure 7.4, showing the voltage of the cells during intermittent charge/discharge and relaxation periods and the extracted open circuit voltages for two examined cells.

For a better comparison, open circuit voltage values versus x in Li_xMO_2 for charging of the first cell of each studied composition are presented in Figure 7.6. By intermittent charging to 4.5 V, 0.85, 0.80, 0.78, 0.80 and 0.84 of one mole lithium are extracted from NMC802, NMC712, NMC622, NMC532, NMC442 half cells, respectively. This value is 0.65 mole of lithium for NMC110 half-cell. So it seems that $LiNi_{0.8-y}Mn_yCo_{0.2}O_2$ samples deliver higher capacity in comparison to Co free $Li_xNi_{0.5}Mn_{0.5}O_2$ sample in the same voltage window. This could be attributed to a lower redox potential of Ni cations in the presence of Co.

One interesting feature to notice in the interpretation of voltage curves in Figure 7.6, is the presence of a shift in the voltage curves. In general, the open circuit voltage of $LiNi_{0.8-y}Mn_yCo_{0.2}O_2$ increases by increasing y. In NMC802, intercalation occurs at voltages up to 0.12 V lower than those of NMC442. It should be mentioned that NMC442 follow this trend in a smaller range of $0.6 \leq x \leq 0.88$ while other $LiNi_{0.8-y}Mn_yCo_{0.2}O_2$ keep the same order for the

whole range of x. The observed behavior could be described considering the increased effect of Ni redox reaction with lower potential on the overall cell reaction by increasing nickel content. In fact, by increasing Ni content in $LiNi_{0.8-y}Mn_yCo_{0.2}O_2$, the cell tends to perform more like $LiNiO_2$ than $LiCoO_2$. Nickel redox reactions include e_g orbitals rather than t_{2g} orbitals [37].

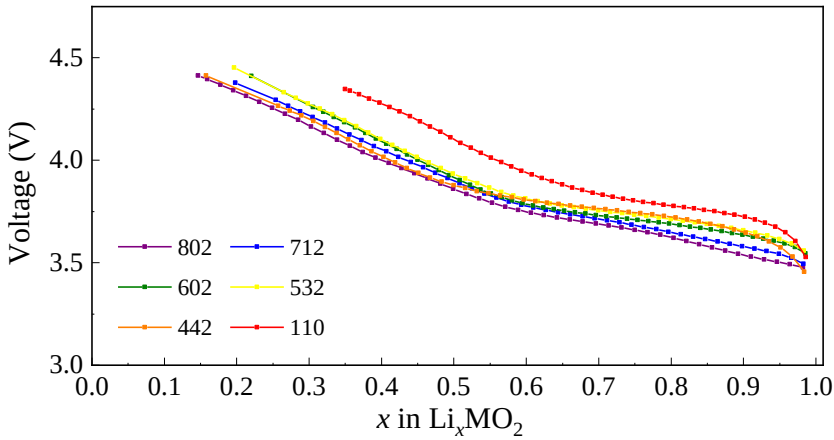

Figure 7.6: Open circuit voltage versus x in Li_xMO_2 for charging of the first cell of each studied composition.

As can be seen in Figure 7.4 and Figure 7.6, similar to Section 7.2, the voltage profile of all studied cell compositions during charge and discharge have an almost monotonous shape. Here also the differential curve could reveal the features of the cycling curve more clearly. Figure 7.7 shows the derivative of x (lithium amount in $LiMO_2$) to open circuit voltage (OCV) against x value in $LiMO_2$ for both examined half cells of each NMC composition.

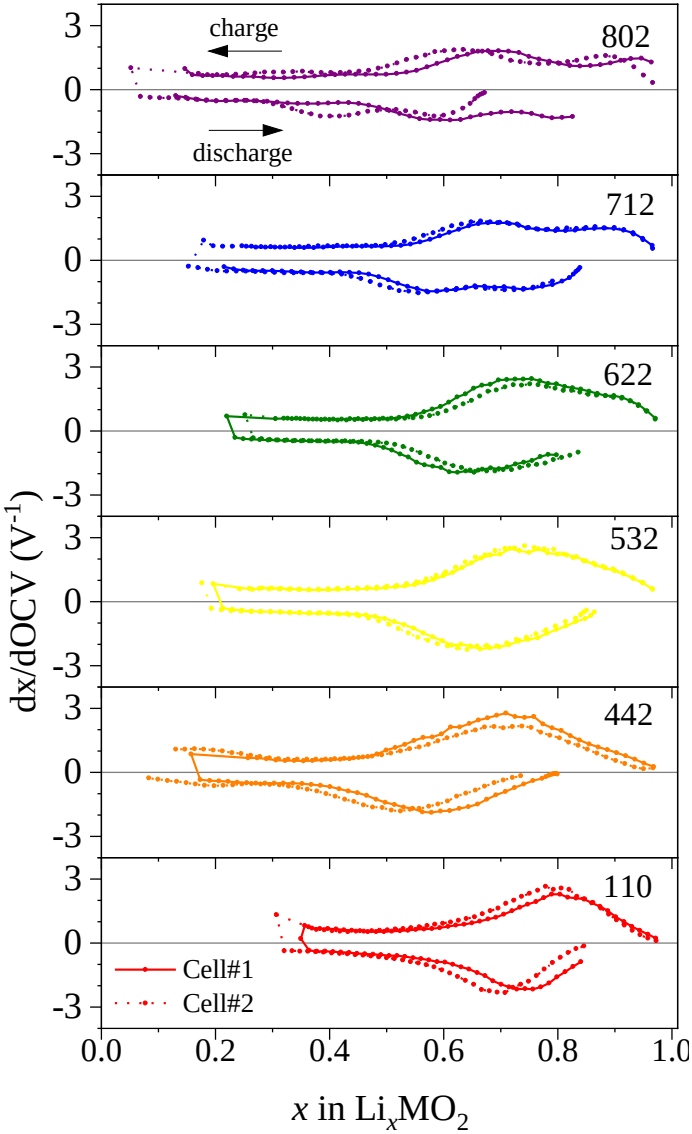

Figure 7.7: Derivative of x (lithium amount in Li_xMO_2) to open circuit voltage (OCV) against x value in $LiMO_2$ for both examined half cells of each NMC composition.

As can be observed in Figure 7.7, the derivative of the OCV curves for all samples show no sharp peaks but weaker peaks representing inflection points on the respective OCV versus *x* curves. Therefore, it could be concluded that upon lithium intercalation/deintercalation which are close to the equilibrium, one or two second order phase transitions occur. As mentioned earlier, transition metals are randomly distributed in the transition metal layer of rhombohedral O3 structure of NMC compounds. Therefore, by changing the amount of lithium in lithium layers, a long range ordering may not take place and presumably the new phases maintain the rhombohedral symmetry.

The differential OCV curves during charge and discharge of NMC802 and NMC712 exhibit two peaks while only one peak appears on the differential OCV curve of NMC622, NMC532, NMC442 and NMC110 . The first and the second cell of all NMC compounds, except NMC802, show a quite good agreement. By NMC802, as mentioned earlier, the measurements program of the second cell did not meet the equilibrium condition completely and therefore, the *x* values corresponding to the two cells differ from each other.

For all compositions, a hysteresis is observed between charge and discharge curves; the *x* values of the observed peaks in discharge lag behind those of charge curves. However, when d*x*/dOCV is plotted against voltage (V) instead of *x*, as shown in Figure 7.8, interesting results are to observe. First, the first and the second cell of each composition, show an almost identical behavior. Second, the hysteresis between charge and discharge curves is less obvious. Therefore, it seems that when the variations of the curve features with respect to voltage are considered, the cell reactions are easier to detect.

The peaks on charging are at around 3.51 and 3.69 V for NMC802 and at approximately 3.59 V and 3.72 V for NMC712. In the differential OCV curves of NMC622, NMC532, NMC442 and NMC110 one peak appear which is located at around 3.72 V, 3.74 V, 3.75 V and 3.77 V on charging, respectively. Hence, it seems that the peak observed at lower voltage of about 3.5 V in NMC802 and NMC712 graphs disappear by increasing Mn content, in NMC622, NMC532, NMC442 and NMC110 curves. This could be attributed to the increased disorder in transition metal layer by increasing *y* in $Li_xNi_{0.8-y}Mn_yCo_{0.2}O_2$, and thus the decreased tendency for ordering of the

lithium ions upon cycling. However, to determine the structure of the phases emerged after the phase transitions, extensive in-situ or ex-situ structural investigations are necessary. In particular, the respective cell parameters need to be measured to determine if any destructive hexagonal phase with shorter interslab distances, similar to H3 phase which appears during deep delithiation of $LiNiO_2$ phase [84], appears in any of the investigated NMC half cells upon cycling.

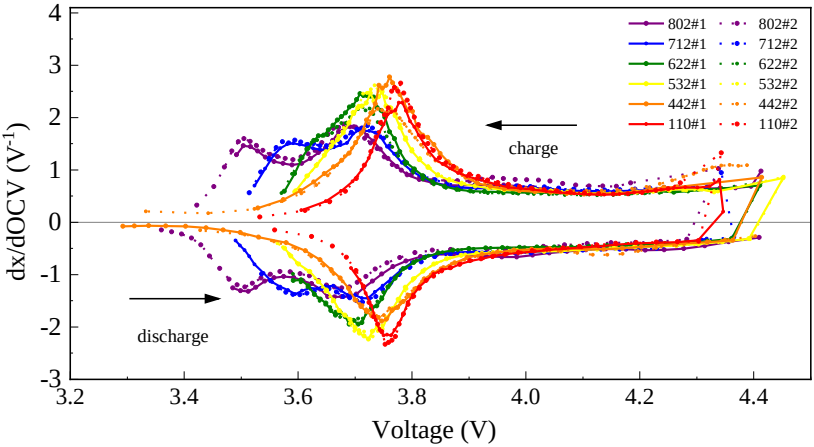

Figure 7.8: Derivative of *x* (lithium amount in $LiMO_2$) to open circuit voltage (OCV) against voltage (V) for both examined half cells of each NMC composition.

7.4 Cyclic voltammetry

Figure 7.9 shows the cyclic voltammogram (CV) of $LiNi_{0.8-y}Mn_yCo_{0.2}O_2$ (y = 0, 0.1, 0.2. 0.3 and 0.4) and $LiNi_{0.5}Mn_{0.5}O_2$ half cells. The measurements are performed with a sweep rate of 0.01 mv·s^{-1} over the potential range of 3.0 and 4.5 V for four cycles, according to Figure 3.10.

The cyclic voltammetry has started after 5 hours of open circuit voltage stand, therefore, the first charge curves begin from the respective OCV values and

differ from the following charge curves. In general, the CV patterns show one distinct redox process. A sharp and intense anodic peak equal to the extraction of Li ions from the lattice is identified at approximately 3.63 , 3.71, 3.72, 3.72, 3.75 and 3.78 V (vs. Li/Li^+) for NMC802, NMC712, NMC622, NMC532, NMC442 and NMC110 CV curves, respectively. A well-defined cathodic peak corresponding to the insertion of Li ions is centered at about 3.63, 3.68, 3.68, 3.70, 3.73 and 3.72 (vs. Li/Li^+) in NMC802, NMC712, NMC622, NMC532, NMC442 and NMC110 curves, respectively.

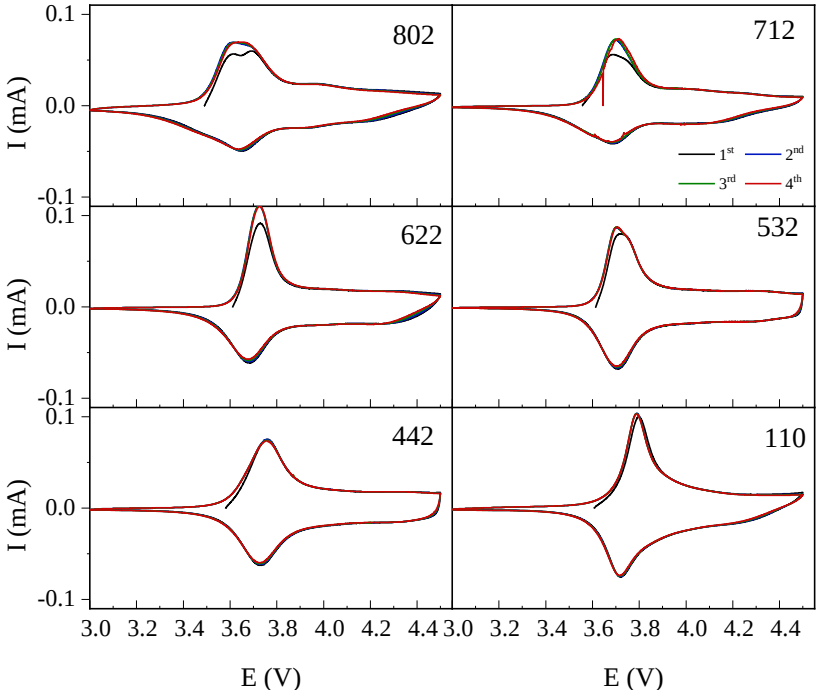

Figure 7.9: Cyclic voltammogram (CV) of $LiNi_{0.8-y}Mn_yCo_{0.2}O_2$ (y = 0, 0.1, 0.2. 0.3 and 0.4) and $LiNi_{0.5}Mn_{0.5}O_2$ half cells with a sweep rate of 0.01 mv·s^{-1} over the potential range of 3.0 and 4.5 V for four cycles.

In all samples, it can be seen that during the second, third and fourth cycles, both anodic and cathodic peaks get very slightly lowered in intensity, which indicates good capacity retention in spite of some fading with the process of cycling. Among all samples, NMC110 shows the best capacity retention behavior, with almost constant redox peak intensity over four cycles.

In the case of NMC712 and NMC802, the anodic peak shifts to higher voltage side by up to 0.02 V during four cycles. The cathodic peak shifts to the same extent to lower voltages upon progressive cycling. Thus there is a slight increase in the hysteresis between the anodic and cathodic peaks by cycling, which indicates inferior electrochemical reversibility of the electrode. Second order phase transitions that was discussed in previous section might be responsible for this behavior. For the other compositions, the positions of oxidation and reduction peaks remain at constant potential with the cycle number, confirming good reversibility of the electrochemical reactions of the cell and excellent cyclic stability.

The observed redox peaks could be attributed to the Ni^{2+}/Ni^{4+} redox reaction. It was shown that in the case of $Li(Ni_xCo_{1-2x}Mn_x)O_2$ systems [337] a two-electron transfer pertinent to Ni^{2+}/Ni^{4+} couple is active near 3.75, in the same voltage range where the intense redox process is observed in the present NMC samples.

7.5 Rate capability and cyclability

The rate capability and cyclability of $LiNi_{0.8-y}Mn_yCo_{0.2}O_2$ (y = 0, 0.1, 0.2. 0.3 and 0.4) and $LiNi_{0.5}Mn_{0.5}O_2$ half cells at different C-rates are evaluated after GITT and CV tests. As shown in the step No. 10 in Figure 3.10, the cells are galvanostatically cycled with C/20, C/10, C/5, C/2, C, 2C, 5C charge/ discharge rates, for 5 cycles at each rate, over the potential range of 3.0 and 4.5 V at 25 °C. Then the C/5 rate was used again from 36th cycles and after that.

Figure 7.10 illustrates the discharge capacities versus cycle number of different NMC half cells at the investigated C-rates. The evaluation of rate capability

may not be realized through comparison of absolute capacity values, as for the reasons mentioned in Section 7.2, the absolute value of discharge capacities may not be actually compared between samples of the present work with different loading of active material in coated electrodes. However, one interesting property to notice is the capacity retention of the half cells at different C-rates. For this purpose the capacity retention is calculated as the ratio of respective discharge capacity to the first discharge capacity with C/20 charge/discharge rate. Figure 7.11 compares the capacity retention of $LiNi_{0.8-y}Mn_yCo_{0.2}O_2$ (y = 0, 0.1, 0.2. 0.3 and 0.4) and $LiNi_{0.5}Mn_{0.5}O_2$ half cells versus cycle number. It should be mentioned that the results of NMC622 are not included in Figure 7.11. This was due to the unsatisfactory performance of NMC622 half cells, probably due to low quality of electrode coating, as mentioned earlier in this chapter.

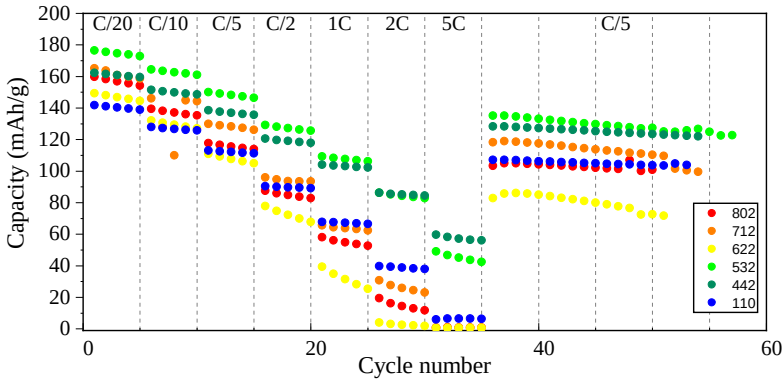

Figure 7.10: Discharge capacities vs. cycle number of $LiNi_{0.8-y}Mn_yCo_{0.2}O_2$ (y = 0, 0.1, 0.2. 0.3 and 0.4) and $LiNi_{0.5}Mn_{0.5}O_2$ (NMC110) half cells cycled using C/20, C/20, C/5, C/2, C, 2C, 5C charge/ discharge rates, over the potential range of 3.0 and 4.5 V at 25 °C.

As can be seen in Figure 7.11, NMC442 exhibits the highest capacity retention at all C-rates, followed by NMC532, NMC110, NMC712 and NMC802. In general by increasing the C-rate, i.e. in faster charge and discharge processes,

the capacity retention of all cells decreases, mainly due to the slower kinetics of lithium diffusion. Yet, the diminishing of capacity retention is less severe by increasing *y* in $LiNi_{0.8-y}Mn_yCo_{0.2}O_2$, indicating an improved rate capability. At 1C rate, NMC442 and NMC532 show just above 60% of their respective capacity at C/20 rate. This value is just below 50% for NMC110 and less than 40% for NMC712 and NMC802. NMC110 shows a moderate rate capability behavior, somewhere between the behavior of NMC442 and NMC802. At a C-rate as high as 5C, NMC110 delivers very little capacity, similar to NMC712 and NMC802, while NMC442 and NMC532 still exhibit about 35% and 25% of their discharge capacity at C/20 rate, respectively.

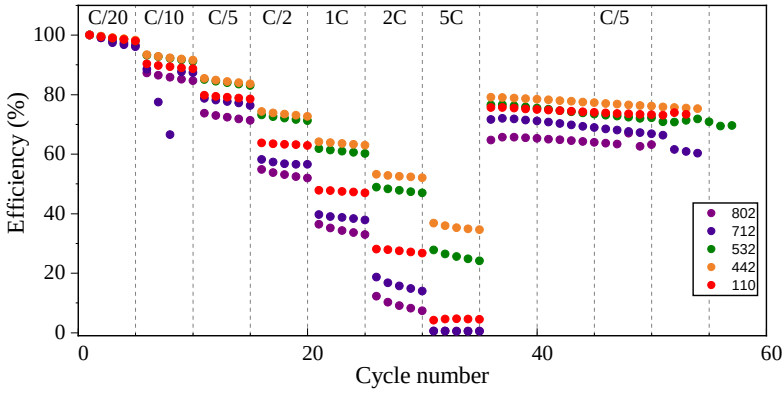

Figure 7.11: Capacity retention (%, with respect to the initial capacity at C/20) vs. cycle number of $LiNi_{0.8-y}Mn_yCo_{0.2}O_2$ (y = 0, 0.1, 0.2, 0.3 and 0.4) and $LiNi_{0.5}Mn_{0.5}O_2$ (NMC110) half cells cycled using C/20, C/20, C/5, C/2, C, 2C, 5C charge/ discharge rates, over the potential range of 3.0 and 4.5 V at 25 °C.

The cyclability of the cell can be evaluated based on the persevering the same capacity (retention) over cycling. Therefore, a steep decrease in capacity retention versus cycle number graph indicates a deterioration of cyclability. For the purpose of a more careful evaluation of the cyclability, the behavior of different cell compositions at the C/5 rate from $10^{th-15th}$ and 30th-50th cycles is observed while the data related to other C-rates are eliminated. The results are

depicted in Figure 7.12. It should be noted that capacity retention here has a different definition from that of Figure 7.11. In Figure 7.12 the capacity retention is calculated as the ratio of respective capacity of each cycle to the discharge capacity of 10th cycle, the first cycle performed at C/5 rate.

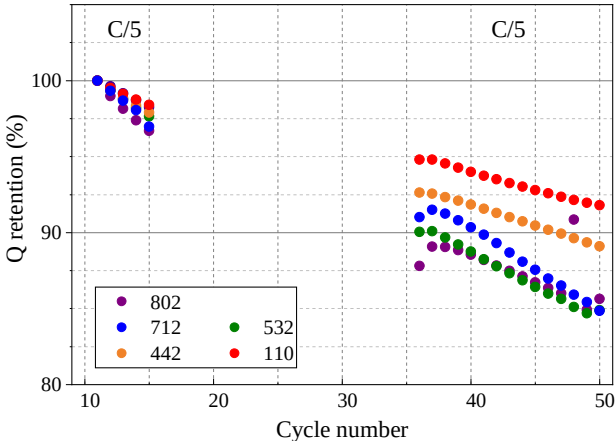

Figure 7.12: Capacity retention (%, with respect to the initial capacity at C/5) vs. cycle number of $LiNi_{0.8-y}Mn_yCo_{0.2}O_2$ (y = 0, 0.1, 0.3 and 0.4) and $LiNi_{0.5}Mn_{0.5}O_2$ (NMC110) half cells cycled C/5 charge/ discharge rates, over the potential range of 3.0 and 4.5 V at 25 °C.

Although NMC110 exhibited lowest capacity at C/5, its capacity retention is the highest among other samples and shows the best cyclability. At the end of 50th cycle, it still delivers about 92% of the capacity that was delivered at 10th cycle. This trend in capacity retention is followed by NMC442 with 89% capacity retention at the 50th cycle. NMC532, NMC712 and NMC802 show inferior performance with about 85% of capacity retention. Therefore, it seems that in $LiNi_{0.8-y}Mn_yCo_{0.2}O_2$ series, NMC442 with the highest Mn content demonstrates the best cyclability. The cyclability of NMC110 is even better than NMC442. The observed enhanced capacity retention and improved electrochemical stability of the investigated NMC cells is consistent with the

energetic stabilities determined through thermochemical experiments in Section 6.4.

Summary and Conclusions

The goal of the present dissertation was the synthesis, characterization and investigation of thermochemistry and electrochemistry of $Li(Ni_xMn_yCo_z)O_2$ ($x + y + z = 1$) or NMC layer structured compounds as positive electrode material for Li-ion batteries. In the course of this work, two compositional series including 1) manganese and nickel equimolar $LiNi_xMn_xCo_{1-2x}O_2$ (x = 0, 0.167, 0.333, 0.4 and 0.5) and 2) Ni-rich $LiNi_{0.8-y}Mn_yCo_{0.2}O_2$ (y = 0, 0.1, 0.2, 0.3 and 0.4) were studied. The synthesis of different NMC compositions were successfully performed by a sol-gel method using metal acetates and adipic acid and through high temperature heat treatment in air. A method for deriving the chemical formula from the results of chemical analysis was introduced. The oxygen coefficient in chemical formula was determined by direct measurement using carrier gas hot extraction as well as through determination of average oxidation state of transition metals using redox titration. A good agreement between two very different methods with a maximum difference of 8.7% was observed. For the $LiNi_{0.7}Mn_{0.1}Co_{0.2}O_2$ and $LiNi_{0.8}Co_{0.2}O_2$ samples, the optimum heat treatment temperatures were determined considering different criteria such as minimum lithium loss and carbon residual (probably in the form of Li_2CO_3 impurity phase) as well as best layered structure's features including larger I(003) / I(104) ratio and c/a ratio. The optimum temperatures were found as 850 °C and 800 °C, for $LiNi_{0.7}Mn_{0.1}Co_{0.2}O_2$ and $LiNi_{0.8}Co_{0.2}O_2$, respectively. The optimum heat treatment temperature of $LiNi_{0.5}Mn_{0.5}O_2$ was found to be 1000 °C, as by heat treatment at 900 °C Li_2MnO_3 was found as the impurity phase. For all the other investigated compositions, a final heat treatment at 900 °C yield to single phase O3 layer structured samples with chemical formula very close to the nominal stoichiometry. However, it seems that when samples with higher Ni content are heat treated in air, Li and O coefficient deviate more from the ideal values, i.e. it is more difficult to reach the average oxidation state of three in transition metals and obtain a stoichiometric sample through heat treatment under air. The lattice parameters of the synthesized samples were determined by Rietveld

refinement and found in a very good agreement with the literature data. The changes in the lattice parameters with the compositional changes in each studied series of samples was observed to be almost linear, which is common for a substitution mechanism that is not accompanied by significant attractive or repulsive electronic effects.

Simultaneous differential thermal analysis - thermal gravimetry (DTA / TG) studies of $LiNi_{0.8-y}Mn_yCo_{0.2}O_2$ compounds for y = 0, 0.1, 0.2, 0.3 and 0.4 in argon showed that all samples remain stable until approximately 720 °C. The initial O3 phase in NMC442 was stable up to 1000 °C under flowing argon while the onset temperatures of the decomposition reaction for NMC532, NMC622, NMC712 and NMC802 are determined to be about 865 °C, 823 °C, 748 °C and 719 °C, respectively. The corresponding weight losses during heating from room temperature to 1000°C with 10 $K \cdot min^{-1}$ heating rate for the above-mentioned samples were also observed as 0.69%, 1.37%, 3.14% and 3.71 %, respectively. Powder-XRD and Rietveld refinement investigations of the samples after DTA / TG experiments showed that NMC442, NMC532 and NMC622 samples remain single phase with $R\bar{3}m$ structures. However, the integrated intensity ratio of (003) to (104) Bragg peaks were 1.73, 1.08 and 1.00 for NMC442, NMC532 and NMC622 samples, respectively showing an increased Li and Ni site mixing and the decreased layered characteristics of the initial O3 phase by increasing Ni content in the sample from NMC442 to NMC622. Furthermore, the refined oxygen occupancy decreases from NMC442 (0.97) to NMC622 (0.74). In the case of NMC712 and NMC802 samples, the initial rhombohedral phase (O3) decomposed and a new rock-salt cubic phase with $Fm\bar{3}m$ space group formed. A decomposition reaction involving oxygen gas release, similar to the decomposition of $LiNiO_2$ in the absence of oxygen, was proposed in this regard. This result combined with the observed mass losses which were attributed to the weight of released oxygen, suggest that the sample with higher nickel content starts releasing oxygen and partially reducing Ni^{3+} to Ni^{2+} at a lower temperature and is chemically and structurally less stable.

The enthalpies of formation of two synthesized series of the NMC samples were determined by high temperature oxide melt drop solution calorimetry in

$3Na_2O{\cdot}4MoO_3$ solvent at 701 °C under argon atmosphere. The obtained enthalpy values for $LiCoO_2$ were in good agreement with the available literature data. The standard enthalpies of formation of $LiNi_xMn_xCo_{1-2x}O_2$ from the elements became more exothermic by increasing *x*. Thus, by substitution of Co^{3+} with equimolar amounts of Mn^{4+} and Ni^{2+} cations on 3(*b*) sites (the transition metal layer), the layer structured compound becomes energetically more stable. By increasing *y*, the standard enthalpies of formation of $LiNi_{0.8-y}Mn_yCo_{0.2}O_2$ from the elements became also more exothermic. Therefore, by substitution of Ni^{3+} with equimolar amounts of Mn^{4+} and Ni^{2+} cations on 3(*b*) sites (the transition metal layer), the layer structured compound became energetically more stable. When the experimental error was taken into account, for compositions along the line from $LiNi_{0.5}Mn_{0.5}O_2$ to $LiCoO_2$, the relationship between the enthalpies of formation from elements and *x* was linear. The relationship between the enthalpies of formation from elements and *y* for $LiNi_{0.8-y}Mn_yCo_{0.2}O_2$ compositions along the line from $LiNi_{0.8}Co_{0.2}O_2$ to $LiNi_{0.4}Mn_{0.4}Co_{0.2}O_2$ could also be considered as linear. A ternary contour plot of the standard enthalpy of formation from elements was presented for the left side of the NMC triangle; the compositions lie between the $LiNiO_2$, $LiCoO_2$ and $LiNi_{0.5}Mn_{0.5}O_2$ end members. The contour lines were almost linear, indicating a near-linear relationship between the standard enthalpy of formation value and the composition of the NMC compound in this region. The path of composition variation which led to the maximum changes in the enthalpy of formation values and indicated the improvement of energetic stability of the layer structured compound was shown on the ternary contour graph. $LiNi_{0.5}Mn_{0.5}O_2$ and $LiNiO_2$ were found as the most and the least energetically stable compounds, in the investigated area, respectively.

The results of electrochemical experiments on $LiNi_{0.8-y}Mn_yCo_{0.2}O_2$ and $LiNi_{0.5}Mn_{0.5}O_2$ half cells actually verified that the NMC compounds with higher thermodynamic stabilities possess improved structural stability and cyclability upon electrochemical lithium intercalation. The differential curves resulted from GCPL measurements as well as from GITT measurements exhibited no sharp peaks but weaker peaks representing inflection points on the respective cycling. The derivates curves showed two peaks during charge and discharge of NMC802 and NMC712 while only one peak became

noticeable on the differential curves of NMC622, NMC532, NMC442 and NMC110. The weak peaks were attributed to the occurrence of one or two second order phase transitions upon lithium extraction/ reinsertion. As transition metals were randomly distributed in the transition metal layer of rhombohedral O3 structure of the NMC compounds, a disorder was introduced within the slabs which prevented a long range lithium/vacancy ordering at different state of charges.

Based on the derivative curves of intermittent cycling, the peaks on charging appeared at around 3.51 and 3.69 V for NMC802 and at about 3.59 V and 3.72 V for NMC712. In the differential OCV curves of NMC622, NMC532, NMC442 and NMC110 one peak was observed which was positioned at approximately 3.72 V, 3.74 V, 3.75 V and 3.77 V on charging, respectively. It could be concluded that by increasing Mn content in $LiNi_{0.8-y}Mn_yCo_{0.2}O_2$, the phase transition happened at higher voltages because the disorder in transition metal layer increased and therefore the tendency for ordering of the lithium ions upon (de)lithiation decreased. In addition, by increasing *y*, the occupation of octahedrally coordinated Mn^{4+} cations increased, which serves as an electrochemically inactive filler, making the structure more stable by preventing the transformation to spinel structure.

GITT measurements showed that $LiNi_{0.8-y}Mn_yCo_{0.2}O_2$ samples deliver higher capacity in comparison to Co free $Li_xNi_{0.5}Mn_{0.5}O_2$ sample in the same voltage window due to lower redox potential of Ni cations in the presence of Co. By intermittent charging to 4.5 V, 0.85, 0.80, 0.78, 0.80 and 0.84 of one mole lithium were extracted from NMC802, NMC712, NMC622, NMC532, NMC442 half cells, respectively while this value was 0.65 mole of lithium for NMC110 half-cell. However, it was observed that by increasing *y*, the open circuit voltage of $LiNi_{0.8-y}Mn_yCo_{0.2}O_2$ in general increases up to 0.12 V. This was attributed to the increased effect of Ni redox reaction with lower potential on the overall cell reaction.

It was also observed that when the differential curves were plotted against voltage (V) instead of lithium content (*x*), the hysteresis between charge and discharge curves was smaller.

Cyclic voltammograms showed one distinct redox process attributed to the Ni^{2+}/Ni^{4+} redox reaction. The anodic peak was recognized at about 3.63 , 3.71, 3.72, 3.72, 3.75 and 3.78 V (vs. Li/Li^{+}) for NMC802, NMC712, NMC622, NMC532, NMC442 and NMC110 CV curves, respectively. The cathodic peak was identified at approximately 3.63, 3.68, 3.68, 3.70, 3.73 and 3.72 (vs. Li/Li^{+}) in NMC802, NMC712, NMC622, NMC532, NMC442 and NMC110 curves, respectively.

The rate capability evaluations showed that in general by increasing the C-rate the capacity retention of all cells decreases, mainly because of slower lithium diffusion. Yet, by increasing y in $LiNi_{0.8-y}Mn_yCo_{0.2}O_2$ the deteriorating of capacity retention is less severe, indicative of an improved rate capability. At 1C rate, NMC442 and NMC532 delivered just above 60% of their respective capacity at C/20 rate. This value was just below 50% for NMC110 and less than 40% for NMC712 and NMC802. At a C-rate as high as 5C, NMC110 exhibited very little capacity, similar to NMC712 and NMC802, while NMC442 and NMC532 still delivered about 35% and 25% of their discharge capacity at C/20 rate, respectively.

By cyclability evaluations at C/5 rate, NMC110 exhibited the highest capacity retention (approx. 92%) and the best cyclability among other samples. This trend in capacity retention is followed by NMC442, NMC532, NMC712 and NMC802 with 85% - 89% capacity retention at the 50th cycle showing an inferior performance. Therefore, in $LiNi_{0.8-y}Mn_yCo_{0.2}O_2$ series, NMC442 with the highest Mn content showed the best cyclability.

The following topics could be suggested for future investigations:

1- The experimental thermochemical data obtained in this work could be used as input data for the development of CALPHAD-based thermodynamic descriptions of the Li–Ni-Mn-Co–O system, which can then be used to calculate open circuit voltages based on the Gibbs free energy descriptions of the assessed phases in the multi-component systems.

2- Base on the differential cycling curves, we predicted one or two second order phase transitions upon lithium extraction/ reinsertion of NMC compounds. In-situ or ex-situ structural investigations could be used to determine the structure of the phases emerging after the phase transitions. In particular, the respective cell parameters need to be measured to see if any destructive hexagonal phase with shorter interslab distances, similar to H3 phase which appears during deep delithiation of $LiNiO_2$ phase, appears in any of the investigated NMC half cells upon cycling.

Appendix

In this appendix the calculation process used in the present work for the determination of the enthalpy of drop solution based on the results of high temperature oxide solution calorimetry are described for one sample as an example. The sample is NMC622 (see Section 3.1 and Figure 3.2 for the sample notations). As described in Section 3.4.1, multiple samples were prepared from the as-synthesized powder in the form of pressed pellets with 3 mm diameter and the pellets were dropped from ambient temperature into liquid sodium molybdate inside the calorimeter cell. Adequate time intervals between the drops were considered for the heat flow signal to stabilize after each drop and to ensure complete dissolution of the sample in molten sodium molybdate. Figure A.1 shows the results as heat flow signal (ϕ in µV) against time (in h) curves for NMC622 sample measured over three successive days of calorimetry experiments. When every second samples were dropped into the calorimeter's right/ left cells, the signal deviated from the baseline, reached an extremum, slowly returned to the baseline level and created consecutive peaks, as can be seen in Figure A.1. As described in Section 3.4.1, Equation (3.17) was used to determine the enthalpy of drop solution from the measured heat flow signal through measuring the area under the peaks, which are highlighted in yellow in Figure A.1. The values of the area under the peaks measured on the left and right cells of the calorimeter are listed in Table A.1 and Table A.2, respectively. The values of the masses of the pellets, the room temperature and the temperature inside the platinum crucibles located inside the calorimeter cells are listed as well. Having the formula weight of NMC622, the mole number of each sample was obtained and the heat effect per mole of sample was calculated. In case that the measured heat effect for one drop was very far from the others, the drop is considered as unacceptable. For NMC622 sample, 12 good drops, five drops on the left side and seven drops on the right side of the calorimeter were obtained.

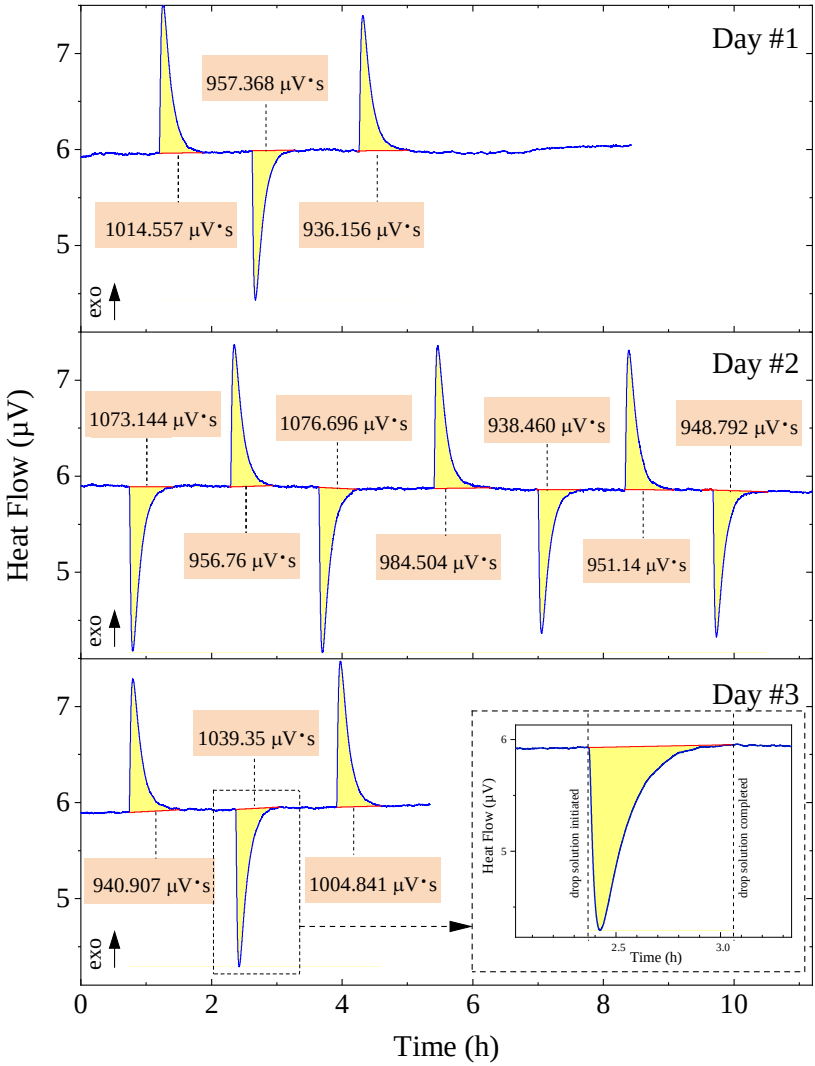

Figure A.1: Repeated calorimetric measurement curves of NMC622 sample showing heat flow signal against time. The base line (in red) linearly connects the beginning and the end point of each drop's peak. The peak area is shown in yellow. Inset graph: overview of the determination of the baseline and area under the peak.

The calibration factors listed in Table A.1 and Table A.2 (K/R_{th}) in Equation (3.17)) were independently determined for both calorimetric chambers through calibration by 7 mg sapphire spheres without any oxide melt at 974 K (origin and purity of sapphire in Table 3.3). The measured heat content of sapphire with known heat capacity is then used to determine the calibration factor.

Table A.1: Measured experimental parameters during drop solution calorimetry of NMC6222 sample on the left cell.

Sample number	1	2	3	4	5	6	7
Day	1	1	2	2	2	3	3
Pellet mass (mg)	5.73	5.16	5.39	5.53	5.42	5.25	5.76
T (Room) (°C)	22.0	21.7	21.9	21.7	21.3	21.6	21.9
T (Calor.) (°C)	701	701	701	701	701	701	701
Formula weight ($g \cdot mol^{-1}$)	96.930						
Moles of NMC ($\times 10^{-4}$ mol)	591	532	556	571	559	542	594
Peak area ($\mu V \cdot s$)	1014.557	936.1560	956.7600	984.5040	951.1400	940.9070	1004.841
Calibration factor ($J \cdot (\mu Vs)^{-1}$)	0.00464650						
Measured heat effect ($kJ \cdot mol^{-1}$)	79.7456	81.7116	79.9465	80.1821	79.0369	80.7184	78.5706
Accepted measurement	1	1	1	1	1	1	1

Table A.2: Measured experimental parameters during drop solution calorimetry of NMC6222 sample on the right cell.

Sample number	1	2	3	4	5	6
Day	1	2	2	2	2	3
Pellet mass (mg)	5.69	5.92	5.93	5.31	5.45	5.88
T (Room) (°C)	22.1	21.8	21.8	21.5	21.8	21.9
T (Calor.) (°C)	701	701	701	701	701	701
Formula weight ($g \cdot mol^{-1}$)	96.930					
Moles of NMC ($\times 10^{-4}$ mol)	587	611	612	548	562	607
Peak area ($\mu V \cdot s$)	957.368	1073.144	1076.690	938.460	948.792	1039.350
Calibration factor ($J \cdot (\mu Vs)^{-1}$)	0.00467593					
Measured heat effect ($kJ \cdot mol^{-1}$)	76.2594	82.0336	82.1663	79.9791	78.7825	79.9908
Accepted measurement	0	1	1	1	1	1

Table A.3 summarizes the average values of heat effect on both sides and the total value, as well as the uncertainty calculations, using Equations (3.24) to (3.28). The uncertainty here relates to the repeatability of the experiments.

Table A.3: Average values of heat effect on both sides and the total value, as well as the uncertainty calculations.

	Left cell	Right Cell	**Total**
Accepted drops number	7	5	12
Average heat effect ($kJ \cdot mol^{-1}$)	79.99	80.59	**80.24**
Standard deviation (s)	1.05	1.47	1.22
Overall uncertainty (U)	0.79	1.31	**0.70**
% Error	0.99	1.63	0.88

References

1. Huggins RA (2010) Energy Storage, vol 406. Springer, New York.
2. Chu S, Majumdar A (2012) Opportunities and challenges for a sustainable energy future. *nature* 488(7411): 294. doi: 10.1038/nature11475
3. U.S. Department of Energy (2011) Quadrennial Technology Review: An Assessment of Energy Technologies and Research Opportunities. https://www.energy.gov/sites/prod/files/QTR_report.pdf. Accessed 08 Oct 2019.
4. Tarascon J-M, Armand M (2011) Issues and challenges facing rechargeable lithium batteries. In: Dusastre V (ed) Materials For Sustainable Energy: A Collection of Peer-Reviewed Research and Review Articles from Nature Publishing Group. Nature Publishing Group, UK, pp 171–179.
5. Tarascon JM, Grugeon S, Laruelle S, Larcher D et al. (2009) The key role of nanoparticles in reactivity of 3d metal oxides toward lithium. In: Nazri G-A, Pistoia G (eds) Lithium Batteries: Science and Technology. Springer Science & Business Media, Boston, MA, pp 220–246.
6. Huggins R (2008) Advanced batteries: Materials science aspects. Springer-Verlag US, New York.
7. van den Bossche P, Vergels F, van Mierlo J, Matheys J et al. (2006) SUBAT: An assessment of sustainable battery technology. *J. Power Sources* 162(2): 913–919. doi: 10.1016/j.jpowsour.2005.07.039
8. Whittingham MS (1976) Electrical energy storage and intercalation chemistry. *Science* 192(4244): 1126–1127. doi: 10.1126/science.192.4244.1126
9. Whittingham MS (2014) Ultimate limits to intercalation reactions for lithium batteries. *Chem. Rev.* 114(23): 11414–11443. doi: 10.1021/cr5003003
10. Scrosati B (1992) Lithium Rocking Chair Batteries: An Old Concept? *J. Electrochem. Soc* 139(10): 2776–2781. doi: 10.1149/1.2068978

11. Armand MB (1980) Intercalation electrodes. In: Materials for advanced batteries. Springer, Boston, MA, pp 145–161.
12. Mizushima K, Jones PC, Wiseman PJ, Goodenough J.B. (1981) LixCoO2 (0< x ≤ 1): A new cathode material for batteries of high energy density. *Solid State Ion.* 3: 171–174. doi: 10.1016/0167-2738(81)90077-1
13. Nagaura T, Tozawa K (1990) Lithium ion rechargeable battery. *Prog. Batteries Solar Cells* 9: 209
14. Imanishi N, Luntz AC, Bruce P (2014) The lithium air battery: Fundamentals. Springer, New York.
15. Zhang Z, Zhang SS (eds) (2015) Rechargeable Batteries: Green Energy and Technology, vol 4. Springer Cham, Heidelberg New York Dordrecht London.
16. Thackeray MM, Wolverton C, Isaacs ED (2012) Electrical energy storage for transportation—approaching the limits of, and going beyond, lithium-ion batteries. *Energy Environ. Sci.* 5(7): 7854–7863. doi: 10.1039/C2EE21892E
17. Manthiram A, Fu Y, Chung S-H, Zu C et al. (2014) Rechargeable lithium-sulfur batteries. *Chem. Rev.* 114(23): 11751–11787. doi: 10.1021/cr500062v
18. Nazar LF, Cuisinier M, Pang Q (2014) Lithium-sulfur batteries. *MRS Bull* 39(5): 436–442. doi: 10.1557/mrs.2014.86
19. Han MH, Gonzalo E, Singh G, Rojo T (2015) A comprehensive review of sodium layered oxides: Powerful cathodes for Na-ion batteries. *Energy Environ. Sci.* 8(1): 81–102. doi: 10.1039/C4EE03192J
20. Yabuuchi N, Kubota K, Dahbi M, Komaba S (2014) Research development on sodium-ion batteries. *Chem. Rev.* 114(23): 11636–11682. doi: 10.1021/cr500192f
21. Yoo HD, Shterenberg I, Gofer Y, Gershinsky G et al. (2013) Mg rechargeable batteries: An on-going challenge. *Energy Environ. Sci.* 6(8): 2265–2279. doi: 10.1039/C3EE40871J
22. Song Y, Zavalij PY, Whittingham MS (2005) ε-VOPO4: Electrochemical synthesis and enhanced cathode behavior. *J. Electrochem. Soc.* 152(4): A721-A728. doi: 10.1149/1.1862265

23. Gallagher KG, Goebel S, Greszler T, Mathias M et al. (2014) Quantifying the promise of lithium-air batteries for electric vehicles. *Energy Environ. Sci.* 7(5): 1555–1563. doi: 10.1039/C3EE43870H
24. Goodenough JB, Park K-S (2013) The Li-ion rechargeable battery: A perspective. *J. Am. Chem. Soc.* 135(4): 1167–1176. doi: 10.1021/ja3091438
25. Aydinol MK, Kohan AF, Ceder G, Cho K et al. (1997) Ab initio study of lithium intercalation in metal oxides and metal dichalcogenides. *Phys. Rev. B* 56(3): 1354. doi: 10.1103/PhysRevB.56.1354
26. Ceder G, van der Ven A (1999) Phase diagrams of lithium transition metal oxides: Investigations from first principles. *Electrochim. Acta* 45(1-2): 131–150. doi: 10.1016/S0013-4686(99)00199-1
27. Gulbinska MK (2014) Lithium-ion Battery Materials and Engineering: Current Topics and Problems from the Manufacturing Perspective. Springer, London.
28. Huggins RA (2016) Energy Storage: Fundamentals, Materials and Applications, 2nd edn. Springer Cham, Heidelberg New York Dordrecht London.
29. Ellis BL, Lee KT, Nazar LF (2010) Positive electrode materials for Li-ion and Li-batteries. *Chem. Mater.* 22(3): 691–714. doi: 10.1021/cm902696j
30. Nitta N, Wu F, Lee JT, Yushin G (2015) Li-ion battery materials: Present and future. *Mater. Today* 18(5): 252–264. doi: 10.1016/j.mattod.2014.10.040
31. Julien CM, Mauger A, Zaghib K, Groult H (2014) Comparative Issues of Cathode Materials for Li-Ion Batteries. *Inorganics* 2(1): 132–154. doi: 10.3390/inorganics2010132
32. He P, Yu H, Li D, Zhou H (2012) Layered lithium transition metal oxide cathodes towards high energy lithium-ion batteries. *J. Mater. Chem.* 22(9): 3680. doi: 10.1039/c2jm14305d
33. Daniel C, Mohanty D, Li J, Wood DL (2014) Cathode materials review. *AIP Conference Proceedings* 1597(1): 26–43. doi: 10.1063/1.4878478
34. Daniel C, Besenhard JO (eds) (2011) Handbook of Battery Materials, 2nd edn. Wiley-VCH Verlag, Weinheim, Germany.

35. Rougier A, Saadoune I, Gravereau P, Willmann P et al. (1996) Effect of cobalt substitution on cationic distribution in LiNi1- y CoyO2 electrode materials. *Solid State Ion.* 90(1-4): 83–90. doi: 10.1016/S0167-2738(96)00370-0
36. Delmas C, Fouassier C, Hagenmuller P (1980) Structural classification and properties of the layered oxides. *Physica B+ C* 99(1-4): 81–85. doi: 10.1016/0378-4363(80)90214-4
37. Radin MD, Hy S, Sina M, Fang C et al. (2017) Narrowing the Gap between Theoretical and Practical Capacities in Li-Ion Layered Oxide Cathode Materials. *Adv. Energy Mater. doi:* 10.1002/aenm.201602888
38. Delmas C, Braconnier J-J, Hagenmuller P (1982) A new variety of LiCoO2 with an unusual oxygen packing obtained by exchange reaction. *Mater. Res. Bull.* 17(1): 117–123. doi: 10.1016/0025-5408(82)90192-1
39. Ben Yahia H, Shikano M, Kobayashi H (2013) Phase Transition Mechanisms in Li x CoO2 (0.25≤ x≤ 1) Based on Group-Subgroup Transformations. *Chem. Mater.* 25(18): 3687–3701. doi: 10.1021/cm401942t
40. van der Ven A, Aydinol MK, Ceder G (1998) First-Principles Evidence for Stage Ordering in Li x CoO2. *J. Electrochem. Soc* 145(6): 2149–2155. doi: 10.1149/1.1838610
41. van der Ven A, Aydinol MK, Ceder G, Kresse G et al. (1998) First-principles investigation of phase stability in Li x CoO 2. *Phys. Rev. B* 58(6): 2975. doi: 10.1103/PhysRevB.58.2975
42. Chen Z, Lu Z, Dahn, JR (2002) Staging Phase Transitions in Li x CoO2. *J. Electrochem. Soc.* 149(12): A1604-A1609. doi: 10.1149/1.1519850
43. Mendiboure A, Delmas C, Hagenmuller P (1984) New layered structure obtained by electrochemical deintercalation of the metastable LiCoO2 (O2) variety. *Mater. Res. Bull.* 19(10): 1383–1392. doi: 10.1016/0025-5408(84)90204-6
44. Carlier D, van der Ven A, Delmas C, Ceder G (2003) First-principles investigation of phase stability in the O2-LiCoO2 system. *Chem. Mater.* 15(13): 2651–2660. doi: 10.1021/cm030002t

45. Delmas C, Braconnier J-J, Fouassier C, Hagenmuller P (1981) Electrochemical intercalation of sodium in NaxCoO2 bronzes. *Solid State Ion.* 3: 165–169. doi: 10.1016/0167-2738(81)90076-X
46. Marianetti CA, Morgan D, Ceder G (2001) First-principles investigation of the cooperative Jahn-Teller effect for octahedrally coordinated transition-metal ions. *Phys. Rev. B* 63(22): 224304. doi: 10.1103/PhysRevB.63.224304
47. Reimers JN, Dahn, JR (1992) Electrochemical and In Situ X-Ray Diffraction Studies of Lithium Intercalation in Li x CoO2. *J. Electrochem. Soc.* 139(8): 2091–2097. doi: 10.1149/1.2221184
48. van der Ven A, Ceder G (1999) Electrochemical properties of spinel Li x CoO 2: A first-principles investigation. *Phys. Rev. B* 59(2): 742. doi: 10.1103/PhysRevB.59.742
49. Thackeray MM (1997) Manganese oxides for lithium batteries. *Prog. Solid State Chem.* 25(1-2): 1–71. doi: 10.1016/S0079-6786(97)81003-5
50. Reed J, Ceder G (2004) Role of electronic structure in the susceptibility of metastable transition-metal oxide structures to transformation. *Chem. Rev.* 104(10): 4513–4534. doi: 10.1021/cr020733x
51. Reed J, Ceder G, van der Ven A (2001) Layered-to-Spinel Phase Transition in Li x MnO2. *Electrochem. Solid-State Lett.* 4(6): A78-A81. doi: 10.1149/1.1368896
52. Ménétrier M, Saadoune I, Levasseur S, Delmas C (1999) The insulator-metal transition upon lithium deintercalation from LiCoO2: Electronic properties and 7Li NMR study. *J. Mater. Chem.* 9(5): 1135–1140. doi: 10.1039/A900016J
53. Marianetti CA, Kotliar G, Ceder G (2004) A first-order Mott transition in Li x CoO 2. *Nat. Mater.* 3(9): 627. doi: 10.1038/nmat1178
54. Milewska A, Świerczek K, Tobola J, Boudoire F et al. (2014) The nature of the nonmetal-metal transition in LixCoO2 oxide. *Solid State Ion.* 263: 110–118. doi: 10.1016/j.ssi.2014.05.011
55. Arroyo y de Dompablo, M. E., van der Ven A, Ceder G (2002) First-principles calculations of lithium ordering and phase stability on LixNiO2. *Phys. Rev. B* 66(6). doi: 10.1103/PhysRevB.66.064112

56. Delmas C, Menetrier M, Croguennec L, Levasseur S et al. (1999) Lithium batteries: A new tool in solid state chemistry. *Int. J. Inorg. Mater.* 1(1): 11–19. doi: 10.1016/S1463-0176(99)00003-4
57. Ohzuku T, Ueda A, Nagayama M (1993) Electrochemistry and structural chemistry of LiNiO2 (R3m) for 4 volt secondary lithium cells. *J. Electrochem. Soc.* 140(7): 1862–1870. doi: 10.1149/1.2220730
58. Chang K, Hallstedt B, Music D (2012) Thermodynamic description of the LiNiO2–NiO2 pseudo-binary system and extrapolation to the Li(Co,Ni)O2–(Co,Ni)O2 system. *Calphad* 37: 100–107. doi: 10.1016/j.calphad.2012.02.006
59. Levi E, Aurbach D (2014) Lattice strains in the layered Mn, Ni and Co oxides as cathode materials in Li and Na batteries. *Solid State Ion.* 264: 54–68. doi: 10.1016/j.ssi.2014.06.020
60. Rozier P, Tarascon JM (2015) Li-rich layered oxide cathodes for next-generation Li-ion batteries: Chances and challenges. *J. Electrochem. Soc.* 162(14): A2490-A2499. doi: 10.1149/2.0111514jes
61. Ohzuku T, Ueda A, Nagayama M, Iwakoshi Y et al. (1993) Comparative study of LiCoO2, LiNi12Co12O2 and LiNiO2 for 4 volt secondary lithium cells. *Electrochim. Acta* 38(9): 1159–1167. doi: 10.1016/0013-4686(93)80046-3
62. Norrish K, Taylor R_M (1962) Quantitative analysis by X-ray diffraction. *Clay Miner. Bull* 5(28): 98–109. doi: 10.1180/claymin.1962.005.28.06
63. Whittingham MS (2004) Lithium Batteries and Cathode Materials. *Chem. Rev.* 104(10): 4271–4302. doi: 10.1021/cr020731c
64. Amatucci GG, Tarascon JM, Klein LC (1996) CoO2, the end member of the LixCoO2 solid solution. *J. Electrochem. Soc.* 143(3): 1114-1123. doi: 10.1149/1.1836594
65. Yazami R, Ozawa Y, Gabrisch H, Fultz B (2004) Mechanism of electrochemical performance decay in LiCoO2 aged at high voltage. *Electrochim. Acta* 50(2-3): 385–390. doi: 10.1016/j.electacta.2004.03.048
66. Wang H, Jang YI, Huang B, Sadoway DR et al. (1999) TEM Study of Electrochemical Cycling-Induced Damage and Disorder in LiCoO 2

Cathodes for Rechargeable Lithium Batteries. *J. Electrochem. Soc.* 146(2): 473. doi: 10.1149/1.1391631

67. Wang H, Jang Y-I, Huang B, Sadoway DR et al. (1999) Electron microscopic characterization of electrochemically cycled LiCoO2 and Li (Al, Co) O2 battery cathodes. *J. Power Sources* 81: 594–598. doi: 10.1016/S0378-7753(99)00108-1
68. Yano A, Shikano M, Ueda A, Sakaebe H et al. (2017) LiCoO2 degradation behavior in the high-voltage phase transition region and improved reversibility with surface coating. *J. Electrochem. Soc.* 164(1): A6116-A6122. doi: 10.1149/2.0181701jes
69. Woodford WH, Carter WC, Chiang Y-M (2012) Design criteria for electrochemical shock resistant battery electrodes. *Energy Environ. Sci.* 5(7): 8014–8024. doi: 10.1039/C2EE21874G
70. Amatucci GG, Tarascon JM, Klein LC (1996) Cobalt dissolution in LiCoO,-based non-aqueous rechargeable batteries. *Solid State Ion.* 83: 167–173. doi: 10.1016/0167-2738(95)00231-6
71. Edström K, Gustafsson T, THOMAS J (2004) The cathode-electrolyte interface in a Li-ion battery. In: Balbuena PB, Wang Y (eds) Lithium-ion Batteries: Solid-electrolyte Interphase, pp 337–364.
72. Vetter J, Novák P, Wagner, Veit C et al. (2005) Ageing mechanisms in lithium-ion batteries. *J. Power Sources* 147(1-2): 269–281. doi: 10.1016/j.jpowsour.2005.01.006
73. Manthiram A, Murugan AV, Sarkar A, Muraliganth T (2008) Nanostructured electrode materials for electrochemical energy storage and conversion. *Energy Environ. Sci.* 1(6): 621–638. doi: 10.1039/B811802G
74. Dahn JR, Fuller EW, Obrovac M, Sacken U von (1994) Thermal stability of LixCoO2, LixNiO2 and λ-MnO2 and consequences for the safety of Li-ion cells. *Solid State Ionics* 69(3-4): 265–270
75. Ceder G, Chiang Y-M, Sadoway, Aydinol MK et al. (1998) Identification of cathode materials for lithium batteries guided by first-principles calculations. *nature* 392(6677): 694. doi: 10.1038/33647
76. Alcantara R, Jumas JC, Lavela P, Olivier-Fourcade J et al. (1999) X-ray diffraction, 57Fe Mössbauer and step potential electrochemical

spectroscopy study of LiFeyCo1- yO2 compounds. *J. Power Sources* 81: 547–553. doi: 10.1016/S0378-7753(99)00213-X

77. Madhavi S, Rao GS, Chowdari BVR, Li SFY (2002) Effect of Cr dopant on the cathodic behavior of LiCoO2. *Electrochim. Acta* 48(3): 219–226. doi: 10.1016/S0013-4686(02)00594-7
78. Stoyanova R, Zhecheva E, Zarkova L (1994) Effect of Mn-substitution for Co on the crystal structure and acid delithiation of LiMnyCo1- yO2 solid solutions. *Solid State Ion.* 73(3-4): 233–240. doi: 10.1016/0167-2738(94)90039-6
79. Cho J, Kim YJ, Kim T-J, Park B (2001) Zero-strain intercalation cathode for rechargeable Li-Ion cell. *Angew. Chem.* 40(18): 3367–3369. doi: 10.1002/1521-3757(20010917)113:18<3471:AID-ANGE3471>3.0.CO;2-Y
80. Scott ID, Jung YS, Cavanagh AS, Yan Y et al. (2010) Ultrathin coatings on nano-LiCoO2 for Li-ion vehicular applications. *Nano Lett.* 11(2): 414–418. doi: 10.1021/nl1030198
81. Dahn, JR, Sacken U von, Michal CA (1990) Structure and electrochemistry of Li1±yNiO2 and a new Li2NiO2 phase with the Ni (OH) 2 structure. *Solid State Ionics* 44(1-2): 87–97
82. Kalyani P, Kalaiselvi N (2005) Various aspects of LiNiO2 chemistry: A review. *Sci. Technol. Adv. Mater.* 6(6): 689–703. doi: 10.1016/j.stam.2005.06.001
83. Ting-Kuo Fey G, Chen J-G, Wang Z-F, Yang H-Z et al. (2004) Saturated linear dicarboxylic acids as chelating agents for the sol–gel synthesis of LiNi0.8Co0.2O2. *Mater. Chem. Phys.* 87(2-3): 246–255. doi: 10.1016/j.matchemphys.2003.12.018
84. Li W, Reimers JN, Dahn JR (1993) In situ x-ray diffraction and electrochemical studies of Li1- xNiO2. *Solid State Ion.* 67(1-2): 123–130. doi: 10.1016/0167-2738(93)90317-V
85. Li W, Reimers JN, Dahn JR (1992) Crystal structure of Li x Ni 2− x O 2 and a lattice-gas model for the order-disorder transition. *Phys. Rev. B* 46(6): 3236. doi: 10.1103/PhysRevB.46.3236
86. Reimers JN, Dahn JR, Greedan JE, Stager CV et al. (1993) Spin glass behavior in the frustrated antiferromagnetic LiNiO2. *J. Solid State Chem.* 102(2): 542–552. doi: 10.1006/jssc.1993.1065

87. Delmas C, Menetrier M, Croguennec L, Saadoune I et al. (1999) An overview of the Li (Ni, M) O2 systems: Syntheses, structures and properties. *Electrochim. Acta* 45(1-2): 243–253. doi: 10.1016/S0013-4686(99)00208-X
88. Delmas C, Peres JP, Rougier A, Demourgues A et al. (1997) On the behavior of the LixNiO2 system: An electrochemical and structural overview. *J. Power Sources* 68(1): 120–125. doi: 10.1016/S0378-7753(97)02664-5
89. Croguennec L, Pouillerie C, Delmas C (2000) NiO2 obtained by electrochemical lithium deintercalation from lithium nickelate: Structural modifications. *J. Electrochem. Soc.* 147(4): 1314–1321. doi: 10.1149/1.1393356
90. Rougier A, Gravereau P, Delmas C (1996) Optimization of the Composition of the Li1- z Ni1+ z O 2 Electrode Materials: Structural, Magnetic, and Electrochemical Studies. *J. Electrochem. Soc.* 143(4): 1168–1175. doi: 10.1149/1.1836614
91. Hirano A, Kanno R, Kawamoto Y, Takeda Y et al. (1995) Relationship between non-stoichiometry and physical properties in LiNiO2. *Solid State Ion.* 78(1-2): 123–131. doi: 10.1016/0167-2738(95)00005-Q
92. Kanno R, Kubo H, Kawamoto Y, Kamiyama T et al. (1994) Phase relationship and lithium deintercalation in lithium nickel oxides. *J. Solid State Chem.* 110(2): 216–225. doi: 10.1006/jssc.1994.1162
93. Shannon RD (1976) Revised effective ionic radii and systematic studies of interatomic distances in halides and chalcogenides. *Acta Crystallogr. A: crystal physics, diffraction, theoretical and general crystallography* 32(5): 751–767. doi: 10.1107/S0567739476001551
94. Caurant D, Baffier N, Garcia B, Pereira-Ramos JP (1996) Synthesis by a soft chemistry route and characterization of LiNixCo1- xO2 (0≤ x≤ 1) cathode materials. *Solid State Ion.* 91(1-2): 45–54. doi: 10.1016/S0167-2738(96)00418-3
95. Arai H, Okada S, Sakurai Y, Yamaki J-i (1997) Reversibility of LiNiO2 cathode. *Solid State Ion.* 95(3-4): 275–282. doi: 10.1016/S0167-2738(96)00598-X
96. Peres JP, Delmas C, Rougier A, Broussely M et al. (1996) The relationship between the composition of lithium nickel oxide and the

loss of reversibility during the first cycle. *J. Phys. Chem. Solids* 57(6-8): 1057–1060. doi: 10.1016/0022-3697(95)00395-9

97. Choi YM, Pyun SI, Bae JS, Moon SI (1995) Effects of lithium content on the electrochemical lithium intercalation reaction into LiNiO2 and LiCoO2 electrodes. *J. Power Sources* 56(1): 25–30. doi: 10.1016/0378-7753(95)02206-V
98. Nakamura K, Ohno H, Okamura K, Michihiro Y et al. (2000) On the diffusion of Li+ defects in LiCoO2 and LiNiO2. *Solid State Ion.* 135(1-4): 143–147. doi: 10.1016/S0167-2738(00)00293-9
99. Strobel P, Levy J-P, Joubert J-C (1984) Hydrothermal and flux synthesis of Li・ Mn・ O compounds: Crystal growth of LiMnO2 and Li2MnO3. *J Cryst Growth* 66(2): 257–261. doi: 10.1016/0022-0248(84)90208-2
100. Dittrich G, Hoppe R (1969) Zur Kristallstruktur von LiMnO2. *Z. Anorg. Allg. Chem* 368(5-6): 262–270. doi: 10.1002/zaac.19693680507
101. Mishra SK, Ceder G (1999) Structural stability of lithium manganese oxides. *Phys. Rev. B* 59(9): 6120. doi: 10.1103/PhysRevB.59.6120
102. Reimers JN, Fuller EW, Rossen E, Dahn, JR (1993) Synthesis and electrochemical studies of LiMnO2 prepared at low temperatures. *J. Electrochem. Soc.* 140(12): 3396–3401. doi: 10.1149/1.2221101
103. Armstrong AR, Bruce PG (1996) Synthesis of layered LiMnO2 as an electrode for rechargeable lithium batteries. *nature* 381(6582): 499. doi: 10.1038/381499a0
104. Capitaine F, Gravereau P, Delmas C (1996) A new variety of LiMnO2 with a layered structure. *Solid State Ion.* 89(3-4): 197–202. doi: 10.1016/0167-2738(96)00369-4
105. Wang M, Navrotsky A (2005) LiMO2 (M= Mn, Fe, and Co): Energetics, polymorphism and phase transformation. *J. Solid State Chem.* 178(4): 1230–1240. doi: 10.1016/j.jssc.2005.01.028
106. Jang Y-I, Chiang Y-M (2000) Stability of the monoclinic and orthorhombic phases of LiMnO2 with temperature, oxygen partial pressure, and Al doping. *Solid State Ion.* 130(1-2): 53–59. doi: 10.1016/S0167-2738(00)00310-6
107. Jang Y-I, Moorehead WD, Chiang Y-M (2002) Synthesis of the monoclinic and orthorhombic phases of LiMnO2 in oxidizing

atmosphere. *Solid State Ion.* 149(3-4): 201–207. doi: 10.1016/S0167-2738(02)00176-5

108. Shao-Horn Y, Hackney SA, Armstrong AR, Bruce PG et al. (1999) Structural characterization of layered LiMnO2 electrodes by electron diffraction and lattice imaging. *J. Electrochem. Soc.* 146(7): 2404–2412. doi: 10.1149/1.1391949
109. Vitins G, West K (1997) Lithium intercalation into layered LiMnO2. *J. Electrochem. Soc.* 144(8): 2587–2592. doi: 10.1149/1.1837869
110. Gu M, Belharouak I, Zheng J, Wu H et al. (2012) Formation of the spinel phase in the layered composite cathode used in Li-ion batteries. *ACS nano* 7(1): 760–767. doi: 10.1021/nn305065u
111. Thackeray MM (1997) A Comment on the Structure of Thin-Film LiMn2 O 4 Electrodes. *J. Electrochem. Soc.* 144(5): L100-L102. doi: 10.1149/1.1837624
112. Paulsen JM, Thomas CL, Dahn, JR (1999) Layered Li-Mn-Oxide with the O2 Structure: A Cathode Material for Li-Ion Cells Which Does Not Convert to Spinel. *J. Electrochem. Soc.* 146(10): 3560–3565. doi: 10.1149/1.1392514
113. Tu J, Zhao XB, Cao GS, Zhuang DG et al. (2006) Enhanced cycling stability of LiMn2O4 by surface modification with melting impregnation method. *Electrochim. Acta* 51(28): 6456–6462. doi: 10.1016/j.electacta.2006.04.031
114. Choi W, Manthiram A (2006) Comparison of metal ion dissolutions from lithium ion battery cathodes. *J. Electrochem. Soc.* 153(9): A1760-A1764. doi: 10.1149/1.2219710
115. Wohlfahrt-Mehrens M, Vogler C, Garche J (2004) Aging mechanisms of lithium cathode materials. *J. Power Sources* 127(1-2): 58–64. doi: 10.1016/j.jpowsour.2003.09.034
116. Gowda SR, Gallagher KG, Croy JR, Bettge M et al. (2014) Oxidation state of cross-over manganese species on the graphite electrode of lithium-ion cells. *Phys. Chem. Chem. Phys.* 16(15): 6898–6902. doi: 10.1039/C4CP00764F
117. Zheng H, Sun Q, Liu G, Song X et al. (2012) Correlation between dissolution behavior and electrochemical cycling performance for

LiNi1/3Co1/3Mn1/3O2-based cells. *J. Power Sources* 207: 134–140. doi: 10.1016/j.jpowsour.2012.01.122

118. Abraham DP, Spila T, Furczon MM, Sammann E (2008) Evidence of transition-metal accumulation on aged graphite anodes by SIMS. *Electrochem. Solid State Lett.* 11(12): A226-A228. doi: 10.1149/1.2987680
119. Koyama Y, Makimura Y, Tanaka I, Adachi H et al. (2004) Systematic Research on Insertion Materials Based on Superlattice Models in a Phase Triangle of LiCoO2 LiNiO2 LiMnO2 I. First-Principles Calculation on Electronic and Crystal Structures, Phase Stability and New LiNi 1/2 Mn 1/2 O 2 Material. *J. Electrochem. Soc.* 151(9): A1499-A1506. doi: 10.1149/1.1783908
120. Park KS, Cho MH, Jin SJ, Song CH et al. (2005) Design and analysis of triangle phase diagram for preparation of new lithium manganese oxide solid solutions with stable layered crystal structure. *J. Power Sources* 146(1-2): 281–286. doi: 10.1016/j.jpowsour.2005.03.029
121. Brown CR, McCalla E, Watson C, Dahn, JR (2015) Combinatorial study of the Li-Ni-Mn-Co oxide pseudoquaternary system for use in Li-Ion battery materials research. *ACS Comb. Sci.* 17(6): 381–391. doi: 10.1021/acscombsci.5b00048
122. Brown ID (1992) Chemical and steric constraints in inorganic solids. *Acta Crystallogr., Sect. B: Struct. Sci* 48(5): 553–572. doi: 10.1107/S0108768192002453
123. Brown ID (2016) The chemical bond in inorganic chemistry: The bond valence model, 2nd edn., vol 27. Oxford University Press, Oxford [u.a.].
124. Brown ID (2009) Recent developments in the methods and applications of the bond valence model. *Chem. Rev.* 109(12): 6858–6919. doi: 10.1021/cr900053k
125. Levi E, Aurbach D (2014) Crystal chemistry and valence determinations for Mn, Ni and Co oxides as cathode materials in Li batteries. *Solid State Ion.* 257: 1–8. doi: 10.1016/j.ssi.2014.01.024
126. Delmas C, Saadoune I (1992) Electrochemical and physical properties of the LixNi1- yCoyO2 phases. *Solid State Ion.* 53: 370–375. doi: 10.1016/0167-2738(92)90402-B

127. Manthiram A, Song B, Li W (2017) A perspective on nickel-rich layered oxide cathodes for lithium-ion batteries. *Energy Storage Mater.* 6: 125–139. doi: 10.1016/j.ensm.2016.10.007
128. Alcantara R, Morales J, Stoyanova R, Tirado JL et al. (1995) Chemically deintercalated cathode materials for lithium cells. *Ionics* 1(3): 246–250. doi: 10.1007/BF02426025
129. Alcantara R, Morales J, Tirado JL, Stoyanova R et al. (1995) Structure and Electrochemical Properties of Li1- x (Ni y Co1- y) 1+ x O 2 Effect of Chemical Delithiation at 0° C. *J. Electrochem. Soc.* 142(12): 3997–4005. doi: 10.1149/1.2048453
130. Delmas C, Saadoune I, Rougier A (1993) The cycling properties of the LixNi1- yCoyO2 electrode. *J. Power Sources* 44(1-3): 595–602. doi: 10.1016/0378-7753(93)80208-7
131. Wang C, Ma X, Zhou L, Cheng J et al. (2007) Study on the rapid synthesis of LiNi1- xCoxO2 cathode material for lithium secondary battery. *Electrochim. Acta* 52(9): 3022–3027. doi: 10.1016/j.electacta.2006.09.047
132. Sun Y-K, Oh I-H, Kim KY (1997) Synthesis of LiCo 0.5 Ni> 0.5 O 2 powders by a sol-gel method. *J. Mater. Chem.* 7(8): 1481–1485. doi: 10.1039/A607550I
133. Idemoto Y, Takanashi Y, Kitamura N (2009) Dependence of property, crystal structure and electrode characteristics on Li content for LixNi0. 8Co0. 2O2 as a cathode active material for Li secondary battery. *J. Power Sources* 189(1): 269–278
134. Saadoune I, Delmas C (1998) On the LixNi0. 8Co0. 2O2System. *J. Solid State Chem.* 136(1): 8–15. doi: 10.1006/jssc.1997.7599
135. Armstrong AR, Robertson AD, Bruce PG (1999) Structural transformation on cycling layered Li (Mn1- yCoy) O2 cathode materials. *Electrochim. Acta* 45(1-2): 285–294. doi: 10.1016/S0013-4686(99)00211-X
136. Armstrong AR, Robertson AD, Gitzendanner R, Bruce PG (1999) The Layered Intercalation Compounds Li (Mn1- yCoy) O2: Positive Electrode Materials for Lithium-Ion Batteries. *J. Solid State Chem.* 145(2): 549–556. doi: 10.1006/jssc.1999.8216

137. Robertson AD, Armstrong AR, Bruce PG (2001) Layered Li x Mn1-y Co y O2 Intercalation Electrodes Influence of Ion Exchange on Capacity and Structure upon Cycling. *Chem. Mater.* 13(7): 2380–2386. doi: 10.1021/cm000965h
138. Rossen E, Jones CDW, Dahn, JR (1992) Structure and electrochemistry of LixMnyNi1- yO2. *Solid State Ion.* 57(3-4): 311–318. doi: 10.1016/0167-2738(92)90164-K
139. Spahr ME, Novák P, Schnyder B, Haas O et al. (1998) Characterization of layered lithium nickel manganese oxides synthesized by a novel oxidative coprecipitation method and their electrochemical performance as lithium insertion electrode materials. *J. Electrochem. Soc.* 145(4): 1113–1121. doi: 10.1149/1.1838425
140. Paulsen JM, Dahn, JR (1999) Studies of the layered manganese bronzes, Na2/3 [Mn1- xMx] O2 with M= Co, Ni, Li, and Li2/3 [Mn1- xMx] O2 prepared by ion-exchange. *Solid State Ion.* 126(1-2): 3–24. doi: 10.1016/S0167-2738(99)00147-2
141. Caurant D, Baffler N, Bianchi V, Grégoire G et al. (1996) Preparation by a ‘chimie douce’route and characterization of (LiNi z Mn 1-z O 2)(0.5⩽ z⩽ 1) cathode materials. *J. Mater. Chem.* 6(7): 1149–1155. doi: 10.1039/JM9960601149
142. Arai H, Okada S, Sakurai Y, Yamaki J-i (1997) Electrochemical and Thermal Behavior of LiNi1- z M z O 2 (M= Co, Mn, Ti). *J. Electrochem. Soc.* 144(9): 3117–3125. doi: 10.1149/1.1837968
143. Ohzuku T, Makimura Y (2001) Layered lithium insertion material of LiNi1/2Mn1/2O2: A possible alternative to LiCoO2 for advanced lithium-ion batteries. *Chem. Lett.* 30(8): 744–745. doi: 10.1246/cl.2001.744
144. Makimura Y, Ohzuku T (2003) Lithium insertion material of LiNi1/2Mn1/2O2 for advanced lithium-ion batteries. *J. Power Sources* 119-121: 156–160. doi: 10.1016/S0378-7753(03)00170-8
145. Lu Z, MacNeil DD, Dahn, JR (2001) Layered cathode materials Li [Ni x Li (1/3- 2x/3) Mn (2/3- x/3)] O 2 for lithium-ion batteries. *Electrochem. Solid State Lett.* 4(11): A191-A194. doi: 10.1149/1.1407994

146. Yoon W-S, Paik Y, Yang X-Q, Balasubramanian M et al. (2002) Investigation of the Local Structure of the LiNi0. 5Mn0. 5 O 2 Cathode Material during Electrochemical Cycling by X-Ray Absorption and NMR Spectroscopy. *Electrochem. Solid State Lett.* 5(11): A263-A266. doi: 10.1149/1.1513001
147. Reed J, Ceder G (2002) Charge, Potential, and Phase Stability of Layered Li(Ni0.5Mn0.5)O2. *Electrochem. Solid-State Lett.* 5(7): A145-A148. doi: 10.1149/1.1480135
148. Ammundsen B, Paulsen J (2001) Novel lithium-ion cathode materials based on layered manganese oxides. *Adv. Mater.* 13(12-13): 943-956. doi: 10.1002/1521-4095(200107)13:12/13<943:AID-ADMA943>3.0.CO;2-J
149. Arachi Y, Kobayashi H, Emura S, Nakata Y et al. (2003) Structural Change of Li1- x Ni0. 5Mn0. 5O2 Cathode Materials for Lithium-ion Batteries by Synchrotron Radiation. *Chem. Lett.* 32(1): 60–61. doi: 10.1246/cl.2003.60
150. Venkatraman S, Manthiram A (2003) Structural and Chemical Characterization of Layered Li1-x Ni1-y Mn y O2-\delta (y= 0.25 and 0.5, and 0≤(1- x)≤ 1) Oxides. *Chem. Mater.* 15(26): 5003–5009. doi: 10.1021/cm034757b
151. Abdel-Ghany A, Zaghib K, Gendron F, Mauger A et al. (2007) Structural, magnetic and electrochemical properties of LiNi0. 5Mn0. 5O2 as positive electrode for Li-ion batteries. *Electrochim. Acta* 52(12): 4092–4100. doi: 10.1016/j.electacta.2006.11.044
152. Kang K, Meng YS, Bréger J, Grey CP et al. (2006) Electrodes with high power and high capacity for rechargeable lithium batteries. *Science* 311(5763): 977–980. doi: 10.1126/science.1122152
153. Kobayashi H, Sakaebe H, Kageyama H, Tatsumi K et al. (2003) Changes in the structure and physical properties of the solid solution LiNi 1- x Mn x O 2 with variation in its composition. *J. Mater. Chem.* 13(3): 590–595. doi: 10.1039/B211558A
154. Sun Y-K, Lee D-J, Lee YJ, Chen Z et al. (2013) Cobalt-free nickel rich layered oxide cathodes for lithium-ion batteries. *ACS Appl. Mater. Interfaces* 5(21): 11434–11440. doi: 10.1021/am403684z

155. Liu Z, Yu A, Lee JY (1999) Synthesis and characterization of LiNi1- x- yCoxMnyO2 as the cathode materials of secondary lithium batteries. *J. Power Sources* 81-82: 416–419. doi: 10.1016/S0378-7753(99)00221-9
156. Yoshio M, Noguchi H, Itoh J-i, Okada M et al. (2000) Preparation and properties of LiCoyMnxNi1- x- yO2 as a cathode for lithium ion batteries. *J. Power Sources* 90(2): 176–181. doi: 10.1016/S0378-7753(00)00407-9
157. Lu Z, MacNeil DD, Dahn JR (2001) Layered Li [Ni x Co1- 2x Mn x] O 2 cathode materials for lithium-ion batteries. *Electrochem. Solid State Lett.* 4(12): A200-A203. doi: 10.1149/1.1413182
158. Ohzuku T, Makimura Y (2001) Layered Lithium Insertion Material of LiCo1/3Ni1/3Mn1/3O2 for Lithium-Ion Batteries. *Chem. Lett.* 30(7): 642–643. doi: 10.1246/cl.2001.642
159. Hoang K, Johannes M (2016) Defect physics and chemistry in layered mixed transition metal oxide cathode materials:(Ni, Co, Mn) vs (Ni, Co, Al). *Chem. Mater.* 28(5): 1325–1334. doi: 10.1021/acs.chemmater.5b04219
160. Yabuuchi N, Ohzuku T (2003) Novel lithium insertion material of LiCo1/3Ni1/3Mn1/3O2 for advanced lithium-ion batteries. *J. Power Sources* 119: 171–174. doi: 10.1016/S0378-7753(03)00173-3
161. Hwang BJ, Tsai YW, Carlier D, Ceder G (2003) A combined computational/experimental study on LiNi1/3Co1/3Mn1/3O2. *Chem. Mater.* 15(19): 3676–3682. doi: 10.1021/cm030299v
162. Chen C-H, Wang C-J, Hwang B-J (2005) Electrochemical performance of layered Li [NixCo1- 2xMnx] O2 cathode materials synthesized by a sol-gel method. *J. Power Sources* 146(1-2): 626–629. doi: 10.1016/j.jpowsour.2005.03.079
163. Shaju KM, Rao GS, Chowdari BVR (2004) Li-ion kinetics and polarization effect on the electrochemical performance of Li (Ni1/2Mn1/2) O2. *Electrochim. Acta* 49(9-10): 1565–1576. doi: 10.1016/j.electacta.2003.11.018
164. Xu J, Lin F, Doeff MM, Tong W (2017) A review of Ni-based layered oxides for rechargeable Li-ion batteries. *J. Mater. Chem. A* 5(3): 874–901. doi: 10.1039/C6TA07991A

165. Shaju KM, Rao GS, Chowdari BVR (2002) Performance of layered Li (Ni1/3Co1/3Mn1/3) O2 as cathode for Li-ion batteries. *Electrochim. Acta* 48(2): 145–151. doi: 10.1016/S0013-4686(02)00593-5
166. Belharouak I, Sun Y-K, Liu J, Amine K (2003) Li (Ni1/3Co1/3Mn1/3) O2 as a suitable cathode for high power applications. *J. Power Sources* 123(2): 247–252. doi: 10.1016/S0378-7753(03)00529-9
167. Yabuuchi N, Makimura Y, Ohzuku T (2007) Solid-State Chemistry and Electrochemistry of LiCo1/ 3Ni1/ 3Mn1/ 3O2 for Advanced Lithium-Ion Batteries III. Rechargeable Capacity and Cycleability. *J. Electrochem. Soc.* 154(4): A314-A321. doi: 10.1149/1.2455585
168. Wu S-L, Zhang W, Song X, Shukla AK et al. (2012) High rate capability of Li (Ni1/3Mn1/3Co1/3) O2 electrode for Li-ion batteries. *J. Electrochem. Soc.* 159(4): A438-A444. doi: 10.1149/2.062204jes
169. Koyama Y, Tanaka I, Adachi H, Makimura Y et al. (2003) Crystal and electronic structures of superstructural Li1- x [Co1/3Ni1/3Mn1/3] O2 (0≤ x≤ 1). *J. Power Sources* 119: 644–648. doi: 10.1016/S0378-7753(03)00194-0
170. Yabuuchi N, Koyama Y, Nakayama N, Ohzuku T (2005) Solid-state chemistry and electrochemistry of LiCo1/ 3Ni1/ 3Mn1/ 3O2 for advanced lithium-ion batteries II. Preparation and characterization. *J. Electrochem. Soc.* 152(7): A1434-A1440. doi: 10.1149/1.1924227
171. Whitfield PS, Davidson IJ, Cranswick LMD, Swainson IP et al. (2005) Investigation of possible superstructure and cation disorder in the lithium battery cathode material LiMn1/3Ni1/3Co1/3O2 using neutron and anomalous dispersion powder diffraction. *Solid State Ion.* 176(5-6): 463–471. doi: 10.1016/j.ssi.2004.07.066
172. Yoon W-S, Grey CP, Balasubramanian M, Yang X-Q et al. (2004) Combined NMR and XAS Study on Local Environments and Electronic Structures of Electrochemically Li-Ion Deintercalated Li1- x Co1/3Ni1/3Mn1/3 O 2 Electrode System. *Electrochem. Solid State Lett.* 7(3): A53-A55. doi: 10.1149/1.1643592
173. Lee S, Park SS (2012) Atomistic simulation study of mixed-metal oxide (LiNi1/3Co1/3Mn1/3O2) cathode material for lithium ion battery. *J. Phys. Chem. C* 116(10): 6484–6489. doi: 10.1021/jp2122467

174. Zeng D, Cabana J, Bréger J, Yoon W-S et al. (2007) Cation Ordering in Li [Ni x Mn x Co (1-2 x)] O2-Layered Cathode Materials: A Nuclear Magnetic Resonance (NMR), Pair Distribution Function, X-ray Absorption Spectroscopy, and Electrochemical Study. *Chem. Mater.* 19(25): 6277–6289. doi: 10.1021/cm702241a
175. Li X, Wei YJ, Ehrenberg H, Du F et al. (2008) Characterizations on the structural and electrochemical properties of LiNi1/3Mn1/3Co1/3O2 prepared by a wet-chemical process. *Solid State Ion.* 178(39-40): 1969–1974. doi: 10.1016/j.ssi.2008.01.048
176. Kim J-M, Chung H-T (2004) The first cycle characteristics of Li [Ni1/3Co1/3Mn1/3] O2 charged up to 4.7 V. *Electrochim. Acta* 49(6): 937–944. doi: 10.1016/j.electacta.2003.10.005
177. Kobayashi H, Arachi Y, Emura S, Kageyama H et al. (2005) Investigation on lithium de-intercalation mechanism for Li1-yNi1/3Mn1/3Co1/3O2. *J. Power Sources* 146(1-2): 640–644. doi: 10.1016/j.jpowsour.2005.03.081
178. Tsai YW, Hwang BJ, Ceder G, Sheu HS et al. (2005) In-situ X-ray absorption spectroscopic study on variation of electronic transitions and local structure of LiNi1/3Co1/3Mn1/3O2 cathode material during electrochemical cycling. *Chem. Mater.* 17(12): 3191–3199. doi: 10.1021/cm048027v
179. Labrini M, Saadoune I, Scheiba F, Almaggoussi A et al. (2013) Magnetic and structural approach for understanding the electrochemical behavior of LiNi0. 33Co0. 33Mn0. 33O2 positive electrode material. *Electrochim. Acta* 111: 567–574. doi: 10.1016/j.electacta.2013.08.051
180. Koyama Y, Yabuuchi N, Tanaka I, Adachi H et al. (2004) Solid-State Chemistry and Electrochemistry of LiCo1/3Ni1/3Mn1/3 O 2 for Advanced Lithium-Ion Batteries I. First-Principles Calculation on the Crystal and Electronic Structures. *J. Electrochem. Soc.* 151(10): A1545-A1551. doi: 10.1149/1.1784823
181. Meng YS, Arroyo-de Dompablo ME (2009) First principles computational materials design for energy storage materials in lithium ion batteries. *Energy Environ. Sci.* 2(6): 589–609. doi: 10.1039/B901825E

182. Ngala JK, Chernova NA, Ma M, Mamak M et al. (2004) The synthesis, characterization and electrochemical behavior of the layered LiNi0.4Mn0.4Co0.2O2 compound. *J. Mater. Chem.* 14(2): 214. doi: 10.1039/b309834f
183. Li Z, Chernova NA, Roppolo M, Upreti S et al. (2011) Comparative Study of the Capacity and Rate Capability of LiNi y Mn y Co1-2y O2 (y= 0.5, 0.45, 0.4, 0.33). *J. Electrochem. Soc.* 158(5): A516-A522. doi: 10.1149/1.3562212
184. Oh SW, Park SH, Park C-W, Sun Y-K (2004) Structural and electrochemical properties of layered Li[Ni0.5Mn0.5]1−xCoxO2 positive materials synthesized by ultrasonic spray pyrolysis method. *Solid State Ion.* 171(3-4): 167–172. doi: 10.1016/j.ssi.2004.04.012
185. Ma M, Chernova NA, Toby BH, Zavalij PY et al. (2007) Structural and electrochemical behavior of LiMn0. 4Ni0. 4Co0. 2O2. *J. Power Sources* 165(2): 517–534. doi: 10.1016/j.jpowsour.2006.10.022
186. Shu J, Ma R, Shao L, Shui M et al. (2014) In-situ X-ray diffraction study on the structural evolutions of LiNi0. 5Co0. 3Mn0. 2O2 in different working potential windows. *J. Power Sources* 245: 7–18. doi: 10.1016/j.jpowsour.2013.06.049
187. Li D, Sasaki Y, Kageyama M, Kobayakawa K et al. (2005) Structure, morphology and electrochemical properties of LiNi0. 5Mn0. 5-xCoxO2 prepared by solid state reaction. *J. Power Sources* 148: 85–89. doi: 10.1016/j.jpowsour.2005.02.006
188. Li D, Sasaki Y, Kobayakawa K, Sato Y (2006) Impact of cobalt substitution for manganese on the structural and electrochemical properties of LiNi0. 5Mn0. 5O2. *Electrochim. Acta* 51(18): 3809–3813. doi: 10.1016/j.electacta.2005.10.046
189. Yang S, Wang X, Yang X, Bai Y et al. (2012) Determination of the chemical diffusion coefficient of lithium ions in spherical Li [Ni0. 5Mn0. 3Co0. 2] O2. *Electrochim. Acta* 66: 88–93. doi: 10.1016/j.electacta.2012.01.061
190. Wu L, Nam K-W, Wang X, Zhou Y et al. (2011) Structural origin of overcharge-induced thermal instability of Ni-containing layered-cathodes for high-energy-density lithium batteries. *Chem. Mater.* 23(17): 3953–3960. doi: 10.1021/cm201452q

191. Konishi H, Yoshikawa M, Hirano T (2013) The effect of thermal stability for high-Ni-content layer-structured cathode materials, LiNi0. 8Mn0. 1- xCo0. 1MoxO2 (x= 0, 0.02, 0.04). *J. Power Sources* 244: 23–28. doi: 10.1016/j.jpowsour.2013.05.004
192. Bak S-M, Hu E, Zhou Y, Yu X et al. (2014) Structural changes and thermal stability of charged LiNi x Mn y Co z O2 cathode materials studied by combined in situ time-resolved XRD and mass spectroscopy. *ACS Appl. Mater. Interfaces* 6(24): 22594–22601. doi: 10.1021/am506712c
193. Kim Y (2012) Lithium nickel cobalt manganese oxide synthesized using alkali chloride flux: Morphology and performance as a cathode material for lithium ion batteries. *ACS Appl. Mater. Interfaces* 4(5): 2329–2333. doi: 10.1021/am300386j
194. Konishi H, Yuasa T, Yoshikawa M (2011) Thermal stability of Li1- yNixMn (1- x)/2Co (1- x)/2O2 layer-structured cathode materials used in Li-Ion batteries. *J. Power Sources* 196(16): 6884–6888. doi: 10.1016/j.jpowsour.2011.01.016
195. Liang L, Du K, Lu W, Peng Z et al. (2014) Synthesis and characterization of LiNi0. 6CoxMn0. 4-xO2 (x= 0.05, 0.1, 0.15, 0.2, 0.25 and 0.3) with high-electrochemical performance for lithium-ion batteries. *Electrochim. Acta* 146: 207–217. doi: 10.1016/j.electacta.2014.09.063
196. Li J, Wang L, Zhang Q, He X (2009) Synthesis and characterization of LiNi0. 6Mn0. 4- xCoxO2 as cathode materials for Li-ion batteries. *J. Power Sources* 189(1): 28–33. doi: 10.1016/j.jpowsour.2008.12.046
197. Liao PY, Duh JG, Sheen, SR (2005) Microstructure and electrochemical performance of LiNi0. 6Co0. 4- xMnxO2 cathode materials. *J. Power Sources* 143(1-2): 212–218. doi: 10.1016/j.jpowsour.2004.12.001
198. Ahn W, Lim SN, Jung K-N, Yeon S-H et al. (2014) Combustion-synthesized LiNi0. 6Mn0. 2Co0. 2O2 as cathode material for lithium ion batteries. *J. Alloys Compd.* 609: 143–149. doi: 10.1016/j.jallcom.2014.03.123
199. Liang L, Du K, Peng Z, Cao Y et al. (2014) Co-precipitation synthesis of Ni0. 6Co0. 2Mn0. 2 (OH) 2 precursor and characterization of LiNi0.

6Co0. 2Mn0. 2O2 cathode material for secondary lithium batteries. *Electrochim. Acta* 130: 82–89. doi: 10.1016/j.electacta.2014.02.100

200. Yue P, Wang Z, Guo H, Wu F et al. (2012) Effect of synthesis routes on the electrochemical performance of Li [Ni 0.6 Co 0.2 Mn 0.2] O 2 for lithium ion batteries. *J Solid State Electrochem* 16(12): 3849–3854. doi: 10.1007/s10008-012-1823-3
201. Sun Y-K, Kim D-H, Jung H-G, Myung S-T et al. (2010) High-voltage performance of concentration-gradient Li [Ni0. 67Co0. 15Mn0. 18] O2 cathode material for lithium-ion batteries. *Electrochim. Acta* 55(28): 8621–8627. doi: 10.1016/j.electacta.2010.07.074
202. Liang L, Hu G, Cao Y, Du K et al. (2015) Synthesis and characterization of full concentration-gradient LiNi0. 7Co0. 1Mn0. 2O2 cathode material for lithium-ion batteries. *J. Alloys Compd.* 635: 92–100. doi: 10.1016/j.jallcom.2015.02.032
203. Fu C, Li G, Luo D, Li Q et al. (2014) Nickel-rich layered microspheres cathodes: Lithium/nickel disordering and electrochemical performance. *ACS Appl. Mater. Interfaces* 6(18): 15822–15831. doi: 10.1021/am5030726
204. Cheralathan KK, Kang NY, Park HS, Lee YJ et al. (2010) Preparation of spherical LiNi0. 80Co0. 15Mn0. 05O2 lithium-ion cathode material by continuous co-precipitation. *J. Power Sources* 195(5): 1486–1494. doi: 10.1016/j.jpowsour.2009.08.101
205. Shim J-H, Kim C-Y, Cho S-W, Missiul A et al. (2014) Effects of heat-treatment atmosphere on electrochemical performances of Ni-rich mixed-metal oxide (LiNi0. 80Co0. 15Mn0. 05O2) as a cathode material for lithium ion battery. *Electrochim. Acta* 138: 15–21. doi: 10.1016/j.electacta.2014.06.079
206. Kim M-H, Shin H-S, Shin D, Sun Y-K (2006) Synthesis and electrochemical properties of Li [Ni0. 8Co0. 1Mn0. 1] O2 and Li [Ni0. 8Co0. 2] O2 via co-precipitation. *J. Power Sources* 159(2): 1328–1333. doi: 10.1016/j.jpowsour.2005.11.083
207. Eom J, Kim MG, Cho J (2008) Storage characteristics of LiNi0. 8Co0. 1+ x Mn0. 1- x O2 (x= 0, 0.03, and 0.06) cathode materials for lithium batteries. *J. Electrochem. Soc.* 155(3): A239-A245. doi: 10.1149/1.2830946

208. Zheng J, Kan WH, Manthiram A (2015) Role of Mn Content on the Electrochemical Properties of Nickel-Rich Layered LiNi0. 8-x Co0. 1Mn0. 1+ x O2 (0.0≤ x≤ 0.08) Cathodes for Lithium-Ion Batteries. *ACS Appl. Mater. Interfaces* 7(12): 6926–6934. doi: 10.1021/acsami.5b00788
209. Ju SH, Kang YC (2009) Fine-sized LiNi0. 8Co0. 15Mn0. 05O2 cathode particles prepared by spray pyrolysis from the polymeric precursor solutions. *Ceram. Int.* 35(4): 1633–1639. doi: 10.1016/j.ceramint.2008.09.002
210. Idris MS, West AR (2012) The effect on cathode performance of oxygen non-stoichiometry and interlayer mixing in layered rock salt LiNi0. 8Mn0. 1Co0. 1O2-\delta. *J. Electrochem. Soc.* 159(4): A396-A401. doi: 10.1149/2.037204jes
211. Sun Y-K, Myung S-T, Park B-C, Prakash J et al. (2009) High-energy cathode material for long-life and safe lithium batteries. *Nat. Mater.* 8(4): 320. doi: 10.1038/nmat2418
212. Xiong X, Wang Z, Yue P, Guo H et al. (2013) Washing effects on electrochemical performance and storage characteristics of LiNi0. 8Co0. 1Mn0. 1O2 as cathode material for lithium-ion batteries. *J. Power Sources* 222: 318–325. doi: 10.1016/j.jpowsour.2012.08.029
213. Lin F, Nordlund D, Li Y, Quan MK et al. (2016) Metal segregation in hierarchically structured cathode materials for high-energy lithium batteries. *Nat. Energy* 1(1): 15004. doi: 10.1038/nenergy.2015.4
214. Thackeray MM, Kang S-H, Johnson CS, Vaughey JT et al. (2007) Li 2 MnO 3-stabilized LiMO 2 (M= Mn, Ni, Co) electrodes for lithium-ion batteries. *J. Mater. Chem.* 17(30): 3112–3125. doi: 10.1039/B702425H
215. Andre D, Kim S-J, Lamp P, Lux SF et al. (2015) Future generations of cathode materials: An automotive industry perspective. *J. Mater. Chem. A* 3(13): 6709–6732. doi: 10.1039/C5TA00361J
216. Ohzuku T, Ueda A (1994) Solid-State Redox Reactions of LiCoO2 ($R\bar{3}m$) for 4 Volt Secondary Lithium Cells. *J. Electrochem. Soc.* 141(11): 2972–2977. doi: 10.1149/1.2059267
217. Chen Z, Dahn, JR (2004) Methods to obtain excellent capacity retention in LiCoO2 cycled to 4.5 V. *Electrochim. Acta* 49(7): 1079–1090. doi: 10.1016/j.electacta.2003.10.019

218. Yang XQ, Sun X, McBreen J (2000) New phases and phase transitions observed in Li1- xCoO2 during charge: In situ synchrotron X-ray diffraction studies. *Electrochem commun* 2(2): 100–103. doi: 10.1016/S1388-2481(99)00155-1
219. Abe T, Koyama T (2011) Thermodynamic modeling of the LiCoO2-CoO2 pseudo-binary system. *Calphad* 35(2): 209–218. doi: 10.1016/j.calphad.2011.02.006
220. Chang K, Hallstedt B, Music D, Fischer J et al. (2013) Thermodynamic description of the layered O3 and O2 structural LiCoO2-CoO2 pseudo-binary systems. *Calphad* 41: 6–15. doi: 10.1016/j.calphad.2013.01.001
221. Kawaji H, Takematsu M, Tojo T, Atake T et al. (2002) Low temperature heat capacity and thermodynamic functions of LiCoO 2. *J. Therm. Anal. Calorim.* 68(3): 833–839. doi: 10.1023/A:1016169917912
222. Emelina AL, Bykov MA, Kovba ML, Senyavin BM et al. (2011) Thermochemical properties of lithium cobaltate. *Russ. J. Phys. Chem. A* 85(3): 357–363. doi: 10.1134/S0036024411030071
223. Ménétrier M, Carlier D, Blangero M, Delmas C (2008) On “really” stoichiometric LiCoO2. *Electrochem. Solid-State Lett.* 11(11): A179-A182. doi: 10.1149/1.2968953
224. Paulsen JM, Mueller-Neuhaus, JR, Dahn, JR (2000) Layered LiCoO2 with a different oxygen stacking (O2 structure) as a cathode material for rechargeable lithium batteries. *J. Electrochem. Soc.* 147(2): 508–516. doi: 10.1149/1.1393225
225. Tarascon JM, Vaughan G, Chabre Y, Seguin L et al. (1999) In situ structural and electrochemical study of Ni1- xCoxO2 metastable oxides prepared by soft chemistry. *J. Solid State Chem.* 147(1): 410–420. doi: 10.1006/jssc.1999.8465
226. Wolverton C, Zunger A (1998) First-principles prediction of vacancy order-disorder and intercalation battery voltages in Li x CoO 2. *Phys. Rev. Lett.* 81(3): 606. doi: 10.1103/PhysRevLett.81.606
227. Ohzuku T, Ueda A (1994) Why transition metal (di)oxides are the most attractive materials for batteries. *Solid State Ion.* 69: 201–211. doi: 10.1016/0167-2738(94)90410-3
228. Arai H, Okada S, Ohtsuka H, Ichimura M et al. (1995) Characterization and cathode performance of Li1− xNi1+ xO2 prepared with the excess

lithium method. *Solid State Ion.* 80(3-4): 261–269. doi: 10.1016/0167-2738(95)00144-U

229. Guilmard M, Croguennec L, Denux D, Delmas C (2003) Thermal Stability of Lithium Nickel Oxide Derivatives. Part I: Li x Ni 1.02 O 2 and Li x Ni 0.89 Al 0.16 O 2 (x = 0.50 and 0.30). *Chem. Mater.* 15(23): 4476–4483. doi: 10.1021/cm030059f
230. Chazel C, Ménétrier M, Carlier D, Croguennec L et al. (2007) DFT modeling of NMR contact shift mechanism in the ideal LiNi2O4 spinel and application to thermally treated layered Li0. 5NiO2. *Chem. Mater.* 19(17): 4166–4173. doi: 10.1021/cm070324n
231. Arai H, Tsuda M, Saito K, Hayashi M et al. (2002) Structural and thermal characteristics of nickel dioxide derived from LiNiO2. *J. Solid State Chem.* 163(1): 340–349. doi: 10.1006/jssc.2001.9428
232. Yang X-Q, McBreen J, Yoon W-S, Grey CP (2002) Crystal structure changes of LiMn0. 5Ni0. 5O2 cathode materials during charge and discharge studied by synchrotron based in situ XRD. *Electrochem commun* 4(8): 649–654. doi: 10.1016/S1388-2481(02)00406-X
233. Yang XQ, Sun X, McBreen J (1999) New findings on the phase transitions in Li1- xNiO2: In situ synchrotron X-ray diffraction studies. *Electrochem commun* 1(6): 227–232. doi: 10.1016/S1388-2481(99)00046-6
234. Chebiam RV, Prado F, Manthiram A (2001) Structural Instability of Delithiated Li1- x Ni1- y Co y O2 Cathodes. *J. Electrochem. Soc.* 148(1): A49-A53. doi: 10.1149/1.1339029
235. Chebiam RV, Prado F, Manthiram A (2001) Soft Chemistry Synthesis and Characterization of Layered Li1-x Ni1-y Co y O2-\delta (0≤ x≤ 1 and 0≤ y≤ 1). *Chem. Mater.* 13(9): 2951–2957. doi: 10.1021/cm0102537
236. Yabuuchi N, Kumar S, Li HH, Kim Y-T et al. (2007) Changes in the crystal structure and electrochemical properties of Li x Ni0. 5Mn0. 5O2 during electrochemical cycling to high voltages. *J. Electrochem. Soc.* 154(6): A566-A578. doi: 10.1149/1.2724734
237. Bréger J, Meng YS, Hinuma Y, Kumar S et al. (2006) Effect of high voltage on the structure and electrochemistry of LiNi0. 5Mn0. 5O2: A

joint experimental and theoretical study. *Chem. Mater.* 18(20): 4768–4781. doi: 10.1021/cm060886r

238. Li HH, Yabuuchi N, Meng YS, Kumar S et al. (2007) Changes in the Cation Ordering of Layered O3 Li x Ni0. 5Mn0. 5O2 during Electrochemical Cycling to High Voltages: An Electron Diffraction Study. *Chem. Mater.* 19(10): 2551–2565. doi: 10.1021/cm070139+
239. Kobayashi H, Arachi Y, Kageyama H, Tatsumi K (2004) Structural determination of Li 1- y Ni 0.5 Mn 0.5 O 2 (y= 0.5) using a combination of Rietveld analysis and the maximum entropy method. *J. Mater. Chem.* 14(1): 40–42. doi: 10.1039/B311827D
240. Arachi Y, Kobayashi H, Emura S, Nakata Y et al. (2005) Li de-intercalation mechanism in LiNi0. 5Mn0. 5O2 cathode material for Li-ion batteries. *Solid State Ion.* 176(9-10): 895–903. doi: 10.1016/j.ssi.2004.10.024
241. Yin S-C, Rho Y-H, Swainson I, Nazar LF (2006) X-ray/Neutron Diffraction and Electrochemical Studies of Lithium De/Re-Intercalation in Li1-x Co1/3Ni1/3Mn1/3O2 (x= 0→ 1). *Chem. Mater.* 18(7): 1901–1910. doi: 10.1021/cm0511769
242. Choi J, Manthiram A (2005) Role of chemical and structural stabilities on the electrochemical properties of layered LiNi1/ 3Mn1/ 3Co1/ 3O2 cathodes. *J. Electrochem. Soc.* 152(9): A1714-A1718. doi: 10.1149/1.1954927
243. Manthiram A, Choi J (2006) Chemical and structural instabilities of lithium ion battery cathodes. *J. Power Sources* 159(1): 249–253. doi: 10.1016/j.jpowsour.2006.04.028
244. Jung S-K, Gwon H, Hong J, Park K-Y et al. (2014) Understanding the degradation mechanisms of LiNi0. 5Co0. 2Mn0. 3O2 cathode material in lithium ion batteries. *Adv. Energy Mater.* 4(1). doi: 10.1002/aenm.201300787
245. Hua W, Zhang J, Zheng Z, Liu W et al. (2014) Na-doped Ni-rich LiNi 0.5 Co 0.2 Mn 0.3 O 2 cathode material with both high rate capability and high tap density for lithium ion batteries. *Dalton Trans.*, 43(39): 14824–14832. doi: 10.1039/C4DT01611D

246. Liao PY, Duh JG, Sheu HS (2007) In Situ Synchrotron X-Ray Studies of LiNi1- x- y Co y Mn x O2 Cathode Materials. *Electrochem. Solid-State Lett.* 10(4): A88-A92. doi: 10.1149/1.2432943
247. Saavedra-Arias JJ, Karan NK, Pradhan DK, Kumar A et al. (2008) Synthesis and electrochemical properties of Li (Ni0. 8Co0. 1Mn0. 1) O2 cathode material: Ex situ structural analysis by Raman scattering and X-ray diffraction at various stages of charge-discharge process. *J. Power Sources* 183(2): 761–765. doi: 10.1016/j.jpowsour.2008.05.068
248. Yang J, Hou M, Haller S, Wang Y et al. (2016) Improving the cycling performance of the layered Ni-rich oxide cathode by introducing low-content Li2MnO3. *Electrochim. Acta* 189: 101–110. doi: 10.1016/j.electacta.2015.12.080
249. Yang J, Xia Y (2016) Suppressing the phase transition of the layered Ni-rich oxide cathode during high-voltage cycling by introducing low-content Li2MnO3. *ACS Appl. Mater. Interfaces* 8(2): 1297–1308. doi: 10.1021/acsami.5b09938
250. Noh H-J, Youn S, Yoon CS, Sun Y-K (2013) Comparison of the structural and electrochemical properties of layered Li[NixCoyMnz]O2 (x = 1/3, 0.5, 0.6, 0.7, 0.8 and 0.85) cathode material for lithium-ion batteries. *J. Power Sources* 233: 121–130. doi: 10.1016/j.jpowsour.2013.01.063
251. Lin F, Nordlund D, Markus IM, Weng T-C et al. (2014) Profiling the nanoscale gradient in stoichiometric layered cathode particles for lithium-ion batteries. *Energy Environ. Sci.* 7(9): 3077–3085. doi: 10.1039/C4EE01400F
252. Lin F, Markus IM, Doeff MM, Xin HL (2014) Chemical and structural stability of lithium-ion battery electrode materials under electron beam. *Sci. Rep.* 4: 5694. doi: 10.1038/srep05694
253. Andreu N, Flahaut D, Dedryvère R, Minvielle M et al. (2015) XPS investigation of surface reactivity of electrode materials: Effect of the transition metal. *ACS Appl. Mater. Interfaces* 7(12): 6629–6636. doi: 10.1021/am5089764
254. Lee E-J, Chen Z, Noh H-J, Nam SC et al. (2014) Development of microstrain in aged lithium transition metal oxides. *Nano Lett.* 14(8): 4873–4880. doi: 10.1021/nl5022859

255. Lukas HL, Suzana G. Fries, Bo Sundman (2007) Computational thermodynamics: The Calphad method, vol 131. Cambridge Univ. Press, Cambridge.
256. Hertz JT, Huang Q, Mcqueen T, Klimczuk T et al. (2008) Magnetism and structure of Li x Co O 2 and comparison to Na x Co O 2. *Phys. Rev. B* 77(7): 75119. doi: 10.1103/PhysRevB.77.075119
257. Miyoshi K, Iwai C, Kondo H, Miura M et al. (2010) Magnetic and electronic properties of Li x CoO 2 single crystals. *Phys. Rev. B* 82(7): 75113. doi: 10.1103/PhysRevB.82.075113
258. Gotcu-Freis P, Cupid DM, Rohde M, Seifert HJ (2015) New experimental heat capacity and enthalpy of formation of lithium cobalt oxide. *J. Chem. Thermodyn.* 84: 118–127. doi: 10.1016/j.jct.2014.12.007
259. Jankovsky O, Kovarik J, Leitner J, Ruzicka K et al. (2016) Thermodynamic properties of stoichiometric lithium cobaltite LiCoO 2. *Thermochim Acta* 634: 26–30. doi: 10.1016/j.tca.2016.04.018
260. Wu L, Lee WH, Zhang J (2014) First principles study on the electrochemical, thermal and mechanical properties of LiCoO2 for thin film rechargeable battery. *Mater Today Proc.* 1(1): 82–93. doi: 10.1016/j.matpr.2014.09.017
261. Du T, Xu B, Wu M, Liu G et al. (2016) Insight into the vibrational and thermodynamic properties of layered lithium transition-metal oxides LiMO2 (M= Co, Ni, Mn): A first-principles study. *J. Phys. Chem. C* 120(11): 5876–5882. doi: 10.1021/acs.jpcc.5b11891
262. Zhang YC, Tagawa H, Asakura S, Mizusaki J et al. (1997) Solid-State CO 2 Sensor with Li2 CO 3-Li3 PO 4-LiAlO2 Electrolyte and LiCoO2-Co3 O 4 as Solid Reference Electrode. *J. Electrochem. Soc.* 144(12): 4345–4350. doi: 10.1149/1.1838190
263. Kawaji H, Oka T, Tojo T, Atake T et al. (2002) Low-temperature heat capacity of layer structure lithium nickel oxide. *Solid State Ion.* 152-153: 195–198. doi: 10.1016/S0167-2738(02)00300-4
264. Chang K, Hallstedt B, Music D (2011) Thermodynamic and Electrochemical Properties of the Li-Co-O and Li-Ni-O Systems. *Chem. Mater.* 24(1): 97–105. doi: 10.1021/cm201964r

265. Chernova NA, Ma M, Xiao J, Whittingham MS et al. (2007) Layered Li x Ni y Mn y Co 1-2y O 2 Cathodes for Lithium Ion Batteries: Understanding Local Structure via Magnetic Properties. *Chem. Mater.* 19(19): 4682–4693. doi: 10.1021/cm0708867
266. Liu B, Wang HW, Ouyang CY (2017) Vibrational and Thermodynamic Properties of Layered LiM0. 5Ni0. 5O2 (M= Mn, Co) Cathode Materials for Li Ion Batteries. *Int. J. Electrochem. Sci.* 12(4): 2963–2972. doi: 10.20964/2017.04.05
267. Cupid DM, Li D, Gebert C, Reif A et al. (2016) Enthalpy of formation and heat capacity of Li2MnO3. *J. Ceram. Soc. Japan* 124(10): 1072–1082. doi: 10.2109/jcersj2.124.P10-1
268. Gotcu P, Pfleging W, Smyrek P, Seifert HJ (2017) Thermal behaviour of Li x MeO 2 (Me= Co or Ni+ Mn+ Co) cathode materials. *Phys. Chem. Chem. Phys.* 19(19): 11920–11930. doi: 10.1039/C7CP00513J
269. Wang M, Navrotsky A, Venkatraman S, Manthiram et al. (2005) Enthalpy of Formation of Li x CoO2 (0.5⩽ x⩽ 1.0). *J. Electrochem. Soc.* 152(7): J82-J84. doi: 10.1149/1.1931292
270. Wang M, Navrotsky A (2004) Enthalpy of formation of LiNiO2, LiCoO2 and their solid solution, LiNi1−xCoxO2. *Solid State Ion.* 166(1-2): 167–173. doi: 10.1016/j.ssi.2003.11.004
271. Kramer D, Ceder G (2009) Tailoring the morphology of LiCoO2: A first principles study. *Chem. Mater.* 21(16): 3799–3809. doi: 10.1021/cm9008943
272. Chang K, Hallstedt B, Music D (2012) Thermodynamic and Electrochemical Properties of the Li–Co–O and Li–Ni–O Systems. *Chem. Mater.* 24(1): 97–105. doi: 10.1021/cm201964r
273. Cupid DM, Gotcu P, Beutl A, Bergfeldt T et al. (2017) Interlaboratory study of the heat capacity of LiNi1/3Mn1/3Co1/3O2 (NMC111) with layered structure. *Int. J. Mater. Res.* 108(11): 1008–1021. doi: 10.3139/146.111571
274. Idemoto Y, Matsui T (2008) Thermodynamic stability, crystal structure, and cathodic performance of Lix(Mn1/3Co1/3Ni1/3)O2 depend on the synthetic process and Li content. *Solid State Ion.* 179(17-18): 625–635. doi: 10.1016/j.ssi.2008.03.024

275. Martha SK, Sclar H, Szmuk Framowitz Z, Kovacheva D et al. (2009) A comparative study of electrodes comprising nanometric and submicron particles of LiNi0.50Mn0.50O2, LiNi0.33Mn0.33Co0.33O2, and LiNi0.40Mn0.40Co0.20O2 layered compounds. *J. Power Sources* 189(1): 248–255. doi: 10.1016/j.jpowsour.2008.09.090
276. Wang M, Navrotsky A (2005) Thermochemistry of Li1+ xMn2−xO4 (0⩽ x⩽ 1/3) spinel. *J. Solid State Chem.* 178(4): 1182–1189. doi: 10.1016/j.jssc.2004.12.007
277. Cupid DM, Reif A, Seifert HJ (2015) Enthalpy of formation of Li1+xMn2−xO4 (0<x<0.1) spinel phases. *Thermochimica Acta* 599: 35–41. doi: 10.1016/j.tca.2014.11.003
278. Bach S, Pereira-Ramos JP, Baffier N, Messina R (1992) Thermodynamic data of electrochemical lithium intercalation in LixMn2O4. *Electrochim. Acta* 37(7): 1301–1305. doi: 10.1016/0013-4686(92)85071-R
279. Yazami R (2009) Thermodynamics of Electrode Materials for Lithium-Ion Batteries. In: Ozawa K (ed) Lithium Ion Rechargeable Batteries: Materials, Technology, and New Applications. Wiley-VCH, Weinheim, Germany
280. Reynier Y, Graetz J, Swan-Wood T, Rez P et al. (2004) Entropy of Li intercalation in Li x CoO 2. *Phys. Rev. B* 70(17): 174304. doi: 10.1103/PhysRevB.70.174304
281. Lepple M (2016) Kupfer-und Eisenoxide als Konversions-Elektrodenmaterialien für Lithium-Ionen-Batterien: Thermodynamische und Elektrochemische Untersuchungen, vol 56. KIT Scientific Publishing, Karlsruhe, Germany.
282. Viswanathan VV, Choi D, Wang D, Xu W et al. (2010) Effect of entropy change of lithium intercalation in cathodes and anodes on Li-ion battery thermal management. *J. Power Sources* 195(11): 3720–3729. doi: 10.1016/j.jpowsour.2009.11.103
283. Williford RE, Viswanathan VV, Zhang J-G (2009) Effects of entropy changes in anodes and cathodes on the thermal behavior of lithium ion batteries. *J. Power Sources* 189(1): 101–107. doi: 10.1016/j.jpowsour.2008.10.078

284. Eddahech A, Briat O, Vinassa J-M (2013) Thermal characterization of a high-power lithium-ion battery: Potentiometric and calorimetric measurement of entropy changes. *Energy* 61: 432–439. doi: 10.1016/j.energy.2013.09.028
285. Schmidt JP, Weber A, Ivers-Tiffée E (2014) A novel and precise measuring method for the entropy of lithium-ion cells: \DeltaS via electrothermal impedance spectroscopy. *Electrochim. Acta* 137: 311–319. doi: 10.1016/j.electacta.2014.05.153
286. Tarascon JM, Wang E, Shokoohi FK, McKinnon WR et al. (1991) The spinel phase of LiMn2 O 4 as a cathode in secondary lithium cells. *J. Electrochem. Soc.* 138(10): 2859–2864
287. FU L, Liu H, LI C, WU Y et al. (2005) Electrode materials for lithium secondary batteries prepared by sol–gel methods. *Prog. Mater. Sci.* 50(7): 881–928. doi: 10.1016/j.pmatsci.2005.04.002
288. Julien C, Letranchant C, Rangan S, Lemal M et al. (2000) Layered LiNi0. 5Co0. 5O2 cathode materials grown by soft-chemistry via various solution methods. *Mater. Sci. Eng., B* 76(2): 145–155. doi: 10.1016/S0921-5107(00)00431-1
289. Julien C, El-Farh L, Rangan S, Massot S (1999) Studies of LiNi0. 6Co0. 4O2 cathode material prepared by the citric acid-assisted sol-gel method for lithium batteries. *J. Sol-Gel Sci. Technol.* 15(1): 63–72. doi: 10.1023/A:1008765030990
290. Livage J, Henry M, Sanchez C (1988) Sol-gel chemistry of transition metal oxides. *Prog. Solid State Chem.* 18(4): 259–341
291. Barboux P, Tarascon JM, Shokoohi FK (1991) The use of acetates as precursors for the low-temperature synthesis of LiMn2O4 and LiCoO2 intercalation compounds. *J. Solid State Chem.* 94(1): 185–196
292. Lee Y-S, Sun Y-K, Nahm K-S (1998) Synthesis of spinel LiMn2O4 cathode material prepared by an adipic acid-assisted sol-gel method for lithium secondary batteries. *Solid State Ion.* 109: 285–294. doi: 10.1016/S0167-2738(98)00085-X
293. Cupid DM, Lehmann T, Bergfeldt T, Berndt H et al. (2013) Investigation of the lithium-rich boundary of the Li1+x Mn2−x O4 cubic spinel phase in air. *J. Mater. Sci.* 48(9): 3395–3403. doi: 10.1007/s10853-012-7126-3

294. Wang GX, Zhong S, Bradhurst DH, Dou SX et al. (1998) Synthesis and characterization of LiNiO2 compounds as cathodes for rechargeable lithium batteries. *J. Power Sources* 76(2): 141–146. doi: 10.1016/S0378-7753(98)00153-0
295. Dahn JR, Fong R, Sacken U von (1993) Lithiated nickel dioxide and secondary cells prepared therefrom.(US5264201A)
296. Li W (1992) Crystal structure of $Li_xNi_{2-x}O_2$ and a lattice-gas model for the order-disorder transition. Master of Science, Dept. of Physics.
297. Choi JW (2006) Crystal chemistry, chemical stability, and electrochemical properties of layered oxide cathodes of lithium ion batteries. Doctoral dissertation, The University of Texas at Austin.
298. Wu Y (2008) Structural and electrochemical characterization and surface modification of layered solid solution oxide cathodes of lithium ion batteries. Doctoral Thesis, The University of Texas at Austin.
299. Rietveld HM (1967) Line profiles of neutron powder-diffraction peaks for structure refinement. *Acta Crystallogr.* 22(1): 151–152. doi: 10.1107/S0365110X67000234
300. Rietveld H (1969) A profile refinement method for nuclear and magnetic structures. *J. Appl. Crystallogr.* 2(2): 65–71. doi: 10.1107/S0021889869006558
301. Bruker AXS (2009) TOPAS 4.2 User manual. http://algol.fis.uc.pt/jap/TOPAS%204-2%20Users%20Manual.pdf. Accessed 25 Jan 2019.
302. Pfaffmann L, Jaiser S, Müller M, Scharfer P et al. (2017) New method for binder and carbon black detection at nanometer scale in carbon electrodes for lithium ion batteries. *J. Power Sources* 363: 460–469. doi: 10.1016/j.jpowsour.2017.07.102
303. Garitagoitia Cid A, Rosenkranz R, Zschech E (2016) Optimization of the SEM working conditions: EsB detector at low voltage. *Adv. Eng. Mater.* 18(2): 185–193. doi: 10.1002/adem.201500161
304. Azmi R, Masoumi M, Ehrenberg H, Trouillet V et al. (2018) Surface analytical characterization of LiNi0. 8-yMnyCo0. 2O2 (0≤ y≤ 0.4) compounds for lithium-ion battery electrodes. *Surf. Interface Anal. doi:* 10.1002/sia.6415

305. Parry KL, Shard AG, Short RD, White RG et al. (2006) ARXPS characterisation of plasma polymerised surface chemical gradients. *Surf. Interface Anal.* 38(11): 1497–1504. doi: 10.1002/sia.2400
306. Haines PJ (ed) (2002) Principles of Thermal Analysis and Calorimetry. The Royal Society of Chemistry, Cambridge, UK.
307. Hemminger W, Cammenga HK (1989) Methoden der thermischen Analyse. Anleitungen für die chemische Laboratoriumspraxis, vol 24. Springer, Berlin.
308. Sarge SM, Höhne GWH, Hemminger W (2014) Calorimetry: fundamentals, instrumentation and applications. Wiley-VCH, Weinheim.
309. SETARAM Instrumentation Brochure-SETSYS Evolution. https://www.setaram.com/wp-content/uploads/2018/10/SETSYS-Evolution-EN.pdf. Accessed 13 Jan 2019.
310. Gmelin E, Sarge SM (1995) Calibration of differential scanning calorimeters. *Pure Appl. Chem.* 67(11): 1789–1800. doi: 10.1351/pac199567111789
311. Della Gatta G, Richardson MJ, Sarge SM, Stølen S (2006) Standards, calibration, and guidelines in microcalorimetry. Part 2. Calibration standards for differential scanning calorimetry* (IUPAC Technical Report). *Pure Appl. Chem.* 78(7). doi: 10.1351/pac200678071455
312. Preston-Thomas H (1990) The international temperature scale of 1990 (ITS-90). *metrologia* 27(1): 3
313. Boettinger WJ, Kattner UR, Moon K-W et al. (2006) DTA and Heat-Flux DSC Measurements of Alloy Melting and Freezing: Recommended Practice Guide. https://www.nist.gov/publications/nist-recommended-practice-guide-dta-and-heat-flux-dsc-measurements-alloy-melting-and. Accessed 08 Oct 2019.
314. Navrotsky A (1977) Progress and new directions in high temperature calorimetry. *Phys. Chem. Miner.* 2(1-2): 89–104. doi: 10.1007/BF00307526
315. Calvet E, Prat H (1963) Recent progress in microcalorimetry. Elsevier Pergamon Pr, Oxford [u.a.].

316. Navrotsky A (2014) Progress and new directions in calorimetry: A 2014 perspective. *J. Am. Ceram. Soc.* 97(11): 3349–3359. doi: 10.1111/jace.13278
317. Navrotsky A (1997) Progress and new directions in high temperature calorimetry revisited. *Phys. Chem. Miner.* 24(3): 222–241. doi: 10.1007/s002690050035
318. Yokokawa T, Kleppa OJ (1964) A calorimetric study of the transformation of some metastable modifications of alumina to \alpha-alumina. *J. Phys. Chem.* 68(11): 3246–3249. doi: 10.1021/j100793a028
319. Navrotsky A, Kleppa OJ (1968) Thermodynamics of formation of simple spinels. *J. Inorg. Nucl. Chem.* 30(2): 479–498. doi: 10.1016/0022-1902(68)80475-0
320. Holm JL, Kleppa OJ (1966) The thermodynamic properties of the aluminum silicates. *Am. Mineral.: Earth Planet. Mater.* 51(11-12): 1608–1622
321. Kleppa OJ (1972) Oxide melt solution calorimetry. *Colloques internationaux du CNRS, Thermochimie* 201: 119–127
322. SETARAM Instrumentation Brochure-AlexSys: High Temperature Calvet Calorimeter by Setaram. https://www.setaram.com/wp-content/uploads/2018/10/ALEXSYS-EN.pdf. Accessed 13 Jan 2019.
323. Wen CJ, Boukamp BA, Huggins RA, Weppner W (1979) Thermodynamic and mass transport properties of “LiAl”. *J. Electrochem. Soc.* 126(12): 2258–2266. doi: 10.1149/1.2128939
324. Weppner W, Huggins R. A. (1977) Determination of the kinetic parameters of mixed-conducting electrodes and application to the system Li3Sb. *J. Electrochem. Soc.* 124(10): 1569–1578. doi: 10.1149/1.2133112
325. Deiss E (2002) Spurious potential dependence of diffusion coefficients in Li+ insertion electrodes measured with PITT. *Electrochim. Acta* 47(25): 4027–4034. doi: 10.1016/S0013-4686(02)00363-8
326. Garcia-Belmonte G, Pomerantz Z, Bisquert J, Lellouche J-P et al. (2004) Analysis of ion diffusion and charging in electronically conducting polydicarbazole films by impedance methods. *Electrochim. Acta* 49(20): 3413–3417. doi: 10.1016/j.electacta.2004.03.009

327. Lindström H, Södergren S, Solbrand A, Rensmo H et al. (1997) Li+ ion insertion in TiO2 (anatase). 2. Voltammetry on nanoporous films. *J. Phys. Chem. B* 101(39): 7717–7722. doi: 10.1021/jp970490q
328. BIPM IEC, IFCC I, IUPAC I, ISO O (2008) Evaluation of measurement data—guide for the expression of uncertainty in measurement. JCGM 100: 2008. *Citado en las* 167
329. Jiang J, Eberman KW, Krause LJ, Dahn JR (2005) Reactivity of Li y [Ni x Co1− 2x Mn x] O 2 (x= 0.1, 0.2, 0.35, 0.45, and 0.5; y= 0.3, 0.5) with Nonaqueous Solvents and Electrolytes Studied by ARC. *J. Electrochem. Soc.* 152(3): A566-A569. doi: 10.1149/1.1859611
330. Thomas MGSR, David WIF, Goodenough J (1985) Synthesis and structural characterization of the normal spinel Li [Ni2] O4. *Mater. Res. Bull.* 20(10): 1137–1146. doi: 10.1016/0025-5408(85)90087-X
331. Liu W, Oh P, Liu X, Lee M-J et al. (2015) Nickel-rich layered lithium transition-metal oxide for high-energy lithium-ion batteries. *Angew. Chem.* 54(15): 4440–4457. doi: 10.1002/anie.201409262
332. Zhou F, Zhao X, Smith AJ, Dahn JR (2010) Studies of LiNi2/3Mn1/3O2: A Positive Electrode Material That Cycles Well to 4.6 V. *J. Electrochem. Soc* 157(4): A399-A406. doi: 10.1149/1.3294792
333. Xiao J, Chernova NA, Whittingham MS (2008) Layered mixed transition metal oxide cathodes with reduced cobalt content for lithium ion batteries. *Chem. Mater.* 20(24): 7454–7464. doi: 10.1021/cm802316d
334. Xiao J, Chernova NA, Whittingham MS (2009) Influence of Manganese Content on the Performance of LiNi0. 9- y Mn y Co0. 1O2 (0.45≤ y≤ 0.60) as a Cathode Material for Li-Ion Batteries. *Chem. Mater.* 22(3): 1180–1185. doi: 10.1021/cm902627w
335. Gao Y, Yakovleva MV, Ebner WB (1998) Novel LiNi1-xTix/2Mgx/2O2 Compounds as Cathode Materials for Safer Lithium-Ion Batteries. *Electrochem. Solid-State Lett.* 1(3): 117–119. doi: 10.1149/1.1390656
336. Morales J, Perez-Vicente C, Tirado JL (1990) Cation distribution and chemical deintercalation of Li1-xNi1+ xO2. *Mater. Res. Bull.* 25(5): 623–630. doi: 10.1016/0025-5408(90)90028-Z

337. MacNeil DD, Lu Z, Dahn JR (2002) Structure and Electrochemistry of Li[NixCo1− 2xMnx]O2 (0⩽ x⩽ 1/2). *J. Electrochem. Soc.* 149(10): A1332-A1336. doi: 10.1149/1.1505633
338. Hinuma Y, Meng YS, Kang K, Ceder G (2007) Phase transitions in the LiNi0. 5Mn0. 5O2 system with temperature. *Chem. Mater.* 19(7): 1790–1800. doi: 10.1021/cm062903i
339. Yoshio M, Todorov Y, Yamato K, Noguchi H et al. (1998) Preparation of LiyMnxNi1- xO2 as a cathode for lithium-ion batteries. *J. Power Sources* 74(1): 46–53. doi: 10.1016/S0378-7753(98)00011-1
340. Akimoto J, Gotoh Y, Oosawa Y (1998) Synthesis and Structure Refinement of LiCoO2 Single Crystals. *J. Solid State Chem.* 141(1): 298–302. doi: 10.1006/jssc.1998.7966
341. Shizuka K, Kobayashi T, Okahara K, Okamoto K et al. (2005) Characterization of Li1+yNixCo1−2xMnxO2 positive active materials for lithium ion batteries. *J. Power Sources* 146(1-2): 589–593. doi: 10.1016/j.jpowsour.2005.03.046
342. Choi J, Manthiram A (2006) Crystal chemistry and electrochemical characterization of layered LiNi0. 5- yCo0. 5- yMn2yO2 and LiCo0. 5- yMn0. 5- yNi2yO2 (0≤ 2y≤ 1) cathodes. *J. Power Sources* 162(1): 667–672. doi: 10.1016/j.jpowsour.2006.06.031
343. Jouanneau S, Eberman KW, Krause LJ, Dahn, JR (2003) Synthesis, Characterization, and Electrochemical Behavior of Improved Li [Ni x Co1- 2x Mn x] O 2 (0.1⩽ x⩽ 0.5). *J. Electrochem. Soc.* 150(12): A1637-A1642. doi: 10.1149/1.1622956
344. Chen JG, Vries BD de, Lewandowski JT, Hall RB (1994) Direct differentiation of surface and bulk compositions of powder catalysts: application of electron-yield and fluorescence-yield NEXAFS to Li x Ni 1- x O. *Catal. Lett.* 23(1-2): 25–35. doi: 10.1007/BF00812128
345. Nohma T, Kurokawa H, Uehara M, Takahashi M et al. (1995) Electrochemical characteristics of LiNiO2 and LiCoO2 as a positive material for lithium secondary batteries. *J. Power Sources* 54(2): 522–524. doi: 10.1016/0378-7753(94)02140-X
346. Chang C-C, Scarr N, Kumta PN (1998) Synthesis and electrochemical characterization of LiMO2 (M= Ni, Ni0. 75Co0. 25) for rechargeable

lithium ion batteries. *Solid State Ion.* 112(3-4): 329–344. doi: 10.1016/S0167-2738(98)00183-0

347. Cho D-H, Jo C-H, Cho W, Kim Y-J et al. (2014) Effect of residual lithium compounds on layer Ni-rich Li [Ni0. 7Mn0. 3] O2. *J. Electrochem. Soc.* 161(6): A920-A926. doi: 10.1149/2.042406jes
348. Gu Y-J, Chen Y-B, Liu H-Q, Wang Y-M et al. (2011) Structural characterization of layered LiNi0. 85- xMnxCo0. 15O2 with x= 0, 0.1, 0.2 and 0.4 oxide electrodes for Li batteries. *J. Alloys Compd.* 509(30): 7915–7921. doi: 10.1016/j.jallcom.2011.05.024
349. Kim D, Lim J-M, Lim Y-G, Yu J-S et al. (2015) Design of nickel-rich layered oxides using d electronic donor for redox reactions. *Chem. Mater.* 27(18): 6450–6456. doi: 10.1021/acs.chemmater.5b02697
350. Dou S, Wang W (2011) Synthesis and electrochemical properties of layered LiNi0.5 − x Mn0.5 − x Co2x O2 for lithium-ion battery from nickel manganese cobalt oxide precursor. *J Solid State Electrochem.* 15(2): 399–404. doi: 10.1007/s10008-010-1101-1
351. Lee K-S, Myung S-T, Prakash J, Yashiro H et al. (2008) Optimization of microwave synthesis of Li [Ni0. 4Co0. 2Mn0. 4] O2 as a positive electrode material for lithium batteries. *Electrochim. Acta* 53(7): 3065–3074. doi: 10.1016/j.electacta.2007.11.042
352. Kosova NV, Devyatkina ET, Kaichev VV (2007) Optimization of Ni2+/Ni3+ ratio in layered Li (Ni, Mn, Co) O2 cathodes for better electrochemistry. *J. Power Sources* 174(2): 965–969. doi: 10.1016/j.jpowsour.2007.06.051
353. Tang H, Zhao F, Chang Z-r, Yuan X-Z et al. (2009) Synthesis and Electrochemical Properties of High Density LiNi0. 8Co0. 2- x Ti x O2 for Lithium-Ion Batteries. *J. Electrochem. Soc.* 156(6): A478-A482. doi: 10.1149/1.3116244
354. Ban C, Li Z, Wu Z, Kirkham MJ et al. (2011) Extremely Durable High-Rate Capability of a LiNi0. 4Mn0. 4Co0. 2O2 Cathode Enabled with Single-Walled Carbon Nanotubes. *Adv. Energy Mater.* 1(1): 58–62. doi: 10.1002/aenm.201000001
355. Soo SP, Idris MS, Am Osman R, Rahmat A (2015) The Effect of Synthesis Temperature on Interlayer Mixing in Layered Rock Salt

Cathode Materials LiNi 0.7 Mn 0.1 Co 0.2 O 2 for Li-ion Batteries Application. In: Materials Science Forum, vol 819, pp 155–160.
356. Earnest CM (ed) (1988) Compositional analysis by thermogravimetry: Proceeding of the Symposium on Compositional Analysis by Thermogravimetry, vol 997. ASTM International, Baltimore, MD.
357. Lin S-P, Fung K-Z, Hon Y-M, Hon M-H (2001) Crystallization mechanism of LiNiO2 synthesized by Pechini method. *J. Cryst. Growth* 226(1): 148–157. doi: 10.1016/S0022-0248(01)01363-X
358. Tao S, Wu Q, Zhan Z, Meng G (1999) Preparation of LiMO 2 (M= Co, Ni) cathode materials for intermediate temperature fuel cells by sol-gel processes. *Solid State Ion.* 124(1): 53–59. doi: 10.1016/S0167-2738(99)00137-X
359. Li W, Currie JC, Wolstenholme J (1997) Influence of morphology on the stability of LiNiO2. *J. Power Sources* 68(2): 565–569. doi: 10.1016/S0378-7753(96)02566-9
360. Masoumi M, Cupid DM, Reichmann TL, Chang K et al. (2017) Enthalpies of formation of layeredLiNixMnxCo1–2xO2 ($0 \leq x \leq 0.5$) compoundsas lithium ion battery cathode materials. *Int. J. Mater. Res.* 108(11): 869–878. doi: 10.3139/146.111553
361. Navrotsky A, Kleppa OJ (1967) Calorimetric study of molten sodium molybdate-molybdenum trioxide mixtures at 970 degree K. *Inorg. Chem.* 6(11): 2119–2121. doi: 10.1021/ic50057a047
362. Wang L, Navrotsky A, Stevens R, Woodfield BF et al. (2003) Thermodynamics of CoO–MgO solid solutions. *J. Chem. Thermodyn.* 35(7): 1151–1159. doi: 10.1016/S0021-9614(03)00083-1
363. Le S-N, Navrotsky A, Pralong V (2008) Energetics of copper diphosphates-Cu2P2O7 and Cu3 (P2O6OH) 2. *Solid State Sci* 10(6): 761–767
364. McHale JM, Navrotsky A, Kowach GR, Balbarin VE et al. (1997) Energetics of Ternary Nitrides: Li- Ca- Zn- N and Ca- Ta- N Systems. *Chem. Mater.* 9(7): 1538–1546. doi: 10.1021/cm970244r
365. Birkner N, Navrotsky A (2012) Thermodynamics of manganese oxides: Effects of particle size and hydration on oxidation-reduction equilibria among hausmannite, bixbyite, and pyrolusite. *Am. Mineral* 97(8-9): 1291–1298. doi: 10.2138/am.2012.3982

366. Mayer NA, Cupid DM, Adam R, Reif A et al. (2017) Standard enthalpy of reaction for the reduction of Co3O4 to CoO. *Thermochim Acta* 652: 109–118. doi: 10.1016/j.tca.2017.03.011
367. Ma C, Navrotsky A (2012) Thermodynamics of the CoO-ZnO System at Bulk and Nanoscale. *Chem. Mater.* 24(12): 2311–2315. doi: 10.1021/cm3005198
368. Dinsdale AT (1991) SGTE data for pure elements. *Calphad* 15(4): 317–425. doi: 10.1016/0364-5916(91)90030-N
369. Chase Jr MW (1998) NIST-JANAF thermochemical tables. *J. Phys. Chem. Ref. Data, Monograph* 9: 12
370. Glushko VP, Medvedev VA (1990) Thermal constants of substances. Hemisphere Publishing Company, New York.
371. Chase MW, Davies CA, Downey, JR., Frurip DJ et al. (1985) Janaf thermochemical tables-2. *J. Phys. Chem. Ref. Data* 14: 927-1856
372. Makimura Y, Ohzuku T (2003) Lithium insertion material of LiNi1/2Mn1/2O2 for advanced lithium-ion batteries. *J. Power Sources* 119-121: 156–160. doi: 10.1016/S0378-7753(03)00170-8
373. Myung ST, Ogata A, Lee KS, Komaba S et al. (2008) Structural, Electrochemical, and Thermal Aspects of Li [(Ni0. 5Mn0. 5) 1− x Co x] O2 (0≤ x≤ 0.2) for High-Voltage Application of Lithium-Ion Secondary Batteries. *J. Electrochem. Soc.* 155(5): A374-A383. doi: 10.1149/1.2883733
374. Choi J, Manthiram A (2005) Structural and electrochemical characterization of the layered LiNiMnCoO (0≤2≤1) cathodes. *Solid State Ion.* 176(29-30): 2251–2256. doi: 10.1016/j.ssi.2005.06.004
375. Moshtev R, Zlatilova P, Vasilev S, Bakalova I et al. (1999) Synthesis, XRD characterization and electrochemical performance of overlithiated LiNiO2. *J. Power Sources* 81: 434–441. doi: 10.1016/S0378-7753(99)00247-5